

Correlations between ligand field Δ_o , spin crossover $T_{1/2}$ and redox potential E_{pa} in a family of five dinuclear helicates

Sandhya Singh and Sally Brooker*

Electronic Supplementary Information (ESI)

Contents

Instrumentation.....	S3
General organic synthesis scheme	S4
Experimental section	S4
Previously reported SCO-active Fe ^{II} ₂ L ₃ dinuclear helicates.....	S12
Previously reported SCO <i>and</i> redox active complexes.....	S14
X-ray crystallography	S15
VT- ¹ H NMR Evans method	S44
VT-UV vis studies in acetonitrile solution.....	S55
Cyclic voltammetry	S66
¹ H DOSY NMR spectra.....	S69
Mass spectra.....	S71
NMR spectra	S98
Overlaid crystal structures.....	S114
Solid state magnetic studies.....	S116

Instrumentation

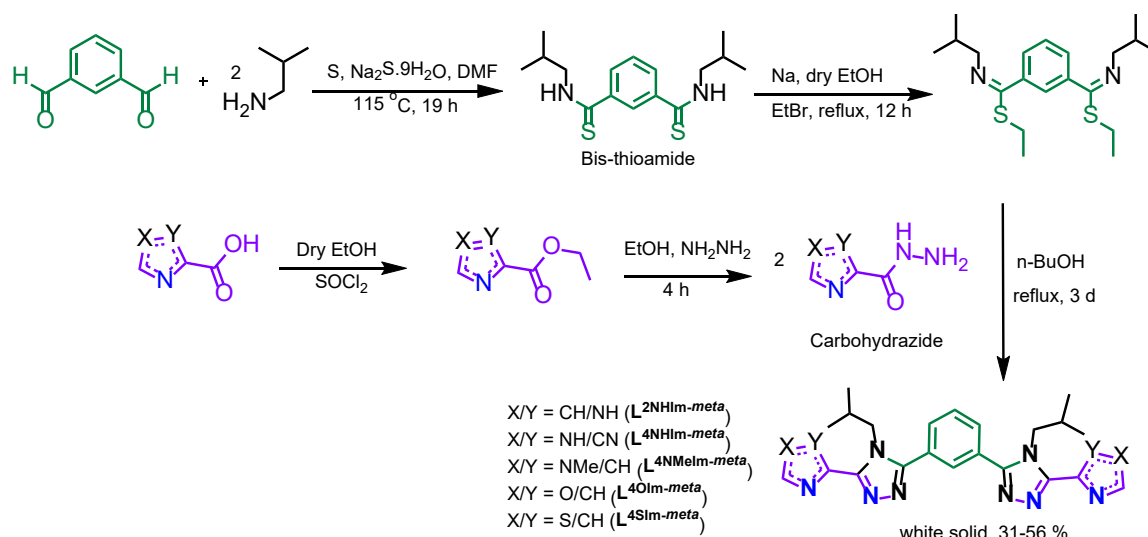
Elemental analyses (C, H, N, S) were measured at the Campbell Microanalytical Laboratory, University of Otago. ^1H and ^{13}C NMR spectra were recorded on a Varian 400 MHz NMR spectrometer at 298 K. ^{15}N (referenced to nitromethane, +380 ppm) and ^1H DOSY NMR spectra at 298 K, and the ^1H VT-NMR ranging from 243 K to 343 K, in CD_3CN were recorded on a Varian 500 MHz NMR spectrometer. High resolution ESI-MS were recorded at 293 K (with heating of the source and nebuliser gas switched off), at Bio21, in house, using a Shimadzu LCMS_9030 mass spectrometer; the m/z values have a standard error of ± 1 ppm. Variable temperature UV-Vis spectra were recorded, in house, from 253 K to 303 K on a PerkinElmer Lambda 950 UV-Vis/NIR spectrometer. Electrochemistry measurements were performed with a two electrode electrochemical cell using an Iviumstat.XRe potentostat, on 1 mM of **1-5**, in degassed, freshly distilled MeCN (over CaH_2), with TBAClO_4 (0.1 mol L^{-1}) except for **5** where TBAPF_6 is used (for solubility reasons), as the supporting electrolyte and $0.01 \text{ mol L}^{-1} \text{ Ag/AgNO}_3$. Both the counter electrode and working electrode were Pt. The potential values are referred to Fc/Fc^+ redox couple, is observed at $E_m = 0.08 \pm 0.01 \text{ V}$ with $\Delta E = 0.08 \text{ V}$ at 200 mV s^{-1} scan rate.

The solid-state magnetic susceptibilities were measured from 300–50–400 K for **1-5** in settle mode (measuring in 5 K steps, ramping between steps at 5 K min^{-1} , with the instrument considering the temperature “settled” after 1 min of the temperature being within the smaller value of $\pm 0.5 \text{ K}$ or $\pm 0.5\%$ of the target value) and an applied field of 0.1 T with a Quantum Design Physical Property Measurement System equipped with a vibrating sample mount (VersaLab). The data were corrected for the diamagnetism of the capsule, and of the sample ($-M \times 0.5 \times 10^{-6} \text{ cm}^3 \text{ mol}^{-1}$).¹

The single-crystal X-ray diffraction measurements were performed on an Oxford Diffraction SuperNova diffractometer with Atlas CCD, equipped with a Cryostream N_2 open-flow cooling device using mirror monochromated micro-focus $\text{Cu-K}\alpha$ radiation source ($\lambda = 1.56 \text{ \AA}$) at 100 K, except for **4·5·NO₂CH₃** and **4·4·NO₂CH₃** (253 K) where the $\text{Mo-K}\alpha$ radiation source was used (as the Cu radiation source was blown and could not be replaced due to COVID19 restrictions). A series of scans was performed in such a way as to collect a complete set of unique reflections (and many equivalents) to a maximum

θ of 72° (Cu) and 26° (Mo). Raw frame data (including data reduction, inter-frame scaling, unit cell refinement and absorption corrections)² for all structures were processed using CrysAlis Pro.³ Structures were solved using ShelXT⁴ and using intrinsic phasing and refined using all data by least-squares techniques with SHELXL⁵ and olex2⁶ program. All hydrogen atoms were placed in calculated positions and rode on the attached carbon atom, with $U(H) = 1.2U$ (attached C) except for –NH substituted for which $U(H) = 1.5U$ (attached atom). All non-H atoms were refined anisotropically, otherwise stated. For further details, see Table S1 and cif files (CCDC: 2061247-2061253 and 2090518-2090519).

General organic synthesis scheme



Scheme S1. General synthetic route used to synthesise ditopic azole-triazole **Rat** ligands.⁷

Experimental section

Synthesis

All chemicals were used as commercially available without further purification. Dry ethanol was prepared by distilling absolute ethanol from Mg/I₂. *N,N'*-(1,3-phenylenebis((ethylthio)methylene))bis(2-methyl-propan-1-amine),⁸

1-methyl-1*H*-imidazole-4-carbohydrazide⁹ and thiazole-4-carbohydrazide⁹ synthesised as previously reported.

Ethyl 1*H*-imidazole-4-carboxylate. To a dry ethanol (30 mL) solution of 4-imidazolecarboxylic acid (1 g, 8.9 mmol) heated at 80 °C was added thionyl chloride (3 mL, 45 mmol) dropwise with continuous stirring. The light yellow solution was stirred at 80 °C overnight. After it was cooled to room temperature, the yellow reaction mixture was taken to dryness under vacuum. The resulting yellow oil was dissolved in water (5 mL) and 1 mM aq. NaOH (20 mL) was added dropwise with continuous stirring to reach pH 9. The product was then extracted with dichloromethane (5x 10 mL), the combined organic layer was dried over MgSO₄ and then concentrated under reduced pressure, giving a crystalline white powder (950 mg, 76%). Anal. calcd for C₆H₈N₂O₂: C 51.42, H 5.75, N 19.99; found C 51.48, H 5.67, N 19.86. ¹H NMR (CDCl₃, 400 MHz) ppm: 7.79 (s, 1H), 7.76 (s, 1H), 4.37 (q, 2H), 1.36 (t, 3H).

1*H*-imidazole-4-carbohydrazide. Ethyl 1*H*-imidazole-4-carboxylate (1 g, 7.1 mmol) was dissolved in 8 mL of ethanol, then 80% hydrazine hydrate (4 mL, 80 mmol) was added dropwise. Behind an explosion shield, the reaction mixture was refluxed for 4 h, cooled down to room temperature, then refrigerated at 4 °C. The resulting white solid was filtered off, washed with chilled ethanol, and dried for 2 h in air (800 mg, 78%). Anal. calcd for C₄H₆N₄O₁·1.6H₂O·0.1C₂H₅OH: C 31.62, H 6.19, N 35.12; found: C 31.90, H 6.28, N 35.02. ¹H NMR (D₂O, 400 MHz) ppm: 7.80 (s, 1H); 7.75 (s, 1H).

1*H*-imidazole-2-carbohydrazide. Ethyl 1*H*-imidazole-2-carboxylate (3 g, 21 mmol) was dissolved in 10 mL of ethanol, then 80% hydrazine hydrate (10 mL, 200 mmol) was added dropwise. Behind an explosion shield, the reaction mixture was refluxed for 4 h and cooled down to room temperature. The resulting white solid was filtered off, washed with chilled ethanol, and dried for 2 h in air (2.6 g, 96%). Anal. calcd for C₄H₆N₄O: C 38.09, H 4.80, N 44.42; found: C 38.03, H 4.53, N 45.03. ¹H NMR (DMSO-*d*₆, 400 MHz) ppm: 12.96 (b, 1H), 9.53 (s, 1H), 7.24 (d, 2H), 4.43 (b, 2H).

Oxazole-4-carbohydrazide. Methyl oxazole-4-carboxylate (2.1 g, 14.8 mmol) was dissolved in 4 mL of ethanol, then 80% hydrazine hydrate (4 mL, 80 mmol) was added. The reaction mixture was stirred at room temperature for 4 h. The resulting white

precipitate was filtered off, washed with chilled ethanol, and dried for 2 h in air (1.3 g, 68%). Anal. calcd for C₄H₅N₃O₂: C 37.80, H 3.97, N 33.06; found: C 37.71, H 3.96, N 33.71. ¹H NMR (DMSO-d₆, 400 MHz) ppm: 9.54 (s, 1H), 8.60 (s, 1H), 8.48 (s, 1H), 4.46 (d, 2H).

1,3-bis(5-(1H-imidazol-2-yl)-4-isobutyl-4H-1,2,4-triazol-3-yl)benzene (L^{2NHIm-meta}). An *n*-butanol (10 mL) solution of *N,N'*-(1,3-phenylenebis((ethylthio)methylene))bis(2-methyl-propan-1-amine) (1.3 g, 3.2 mmol) and 1*H*-imidazole-2-carbohydrazide (720 mg, 5.7 mmol) was refluxed at 108 °C for 3 days. The resulting pale yellow precipitates was cooled to room temperature and the product isolated as a white solid by filtration, washed with diethyl ether (3 x 5mL), then with water (3 x 5mL), and air dried overnight (596 mg, 31%). Anal. calcd for C₂₄H₂₈N₁₀: C 63.14, H 6.18, N 30.68; found: C 62.92, H 6.72, N 31.03. MS (*m/z*) [(C₂₄H₂₈N₁₀) Na]⁺: calcd 479.2396, found 479.2365; [(C₂₄H₂₈N₁₀)₂ Na]⁺: calcd 935.4895, found 935.4878. ¹H NMR (CDCl₃, 400 MHz) ppm: 13.00 (b, 2H), 7.98 (s, 1H), 7.84 (d, 2H), 7.75 (t, 1H), 7.31 (s, 4H), 4.67 (d, 4H), 1.99 (sep, 2H), 0.73 (d, 12H). ¹³C NMR (CDCl₃, 100 MHz) ppm: 154.88, 147.36, 135.54, 130.78, 129.87, 129.79, 128.52, 52.27, 29.29, 19.47.

1,3-Bis(5-(1H-imidazol-4-yl)-4-isobutyl-4H-1,2,4-triazol-3-yl)benzene (L^{4NHIm-meta}). An *n*-butanol (10 mL) solution of *N,N'*-(1,3-phenylenebis((ethylthio)methylene))bis(2-methyl-propan-1-amine) (1.3 g, 3.2 mmol) and 4*H*-imidazole-2-carbohydrazide (730 mg, 5.8 mmol) was refluxed at 108 °C for 3 days. The resulting pale yellow precipitate was cooled to room temperature and the product isolated as a white solid by filtration, washed with diethyl ether (3 x 5 mL), then with water (3 x 5 mL), and air dried overnight (850 mg, 44%). Anal. calcd for C₂₄H₂₈N₁₀·2H₂O: C 58.52, H 6.55, N 28.44; found: C 58.82, H 7.78, N 28.30. MS (*m/z*) [(C₂₄H₂₈N₁₀) H]⁺: calcd 457.2532, found 457.25712; [(C₂₄H₂₈N₁₀) Na]⁺: calcd 479.2396, found 479.23906; [(C₂₄H₂₈N₁₀) Na]⁺: calcd 479.23906, found 479.24030. ¹H NMR (DMSO-D₆, 400 MHz) ppm: 7.99 (s, 1H), 7.90 (s, 2H), 7.86 (d, 2H), 7.79 (b, 2H), 7.75 (t, 1H), 4.49 (d, 4H), 1.70 (sep, 2H), 0.57 (d, 12H). ¹³C NMR (DMSO-d₆, 100 MHz) ppm: 154.06, 150.66, 136.82, 130.49, 130.02, 129.39, 129.31, 125.80, 118.02, 51.30, 29.08, 29.08, 19.61.

1,3-Bis(4-isobutyl-5-(1-methyl-1H-imidazol-4-yl)-4H-1,2,4-triazol-3-yl)benzene (L^{4NMelm-meta}). An *n*-butanol (10 mL) solution of *N,N'*-(1,3-phenylenebis((ethylthio)methylene))bis(2-methyl-propan-1-amine) (1 g, 3.2 mmol) and

1-methyl-1*H*-imidazole-4-carbohydrazide (620 mg, 4.4 mmol) added as solid in reaction mixture and refluxed at 108 °C for 3 days. The resulting pale yellow precipitate was cooled to room temperature and the product isolated as a white solid by filtration, washed with diethyl ether (3 x 5 mL), then with water (3 x 5 mL), and air dried overnight (720 mg, 46%). Anal. calcd for C₂₆H₃₂N₁₀·0.5H₂O: C 63.27, H 6.74, N 28.38; found: C 63.49, H 6.68, N 28.10. MS (*m/z*) [(C₂₆H₃₂N₁₀) Na]⁺: calcd 507.2709, found 507.2715; [(C₂₆H₃₂N₁₀)₂ Na]⁺: calcd 991.5521, found 991.5440. ¹H NMR (CDCl₃, 400 MHz) ppm: 7.85 (s, 1H), 7.78 (d, 2H), 7.69 (s, 2H), 7.66 (t, 1H), 7.50 (s, 2H), 4.45 (d, 4H), 3.78 (s, 6H), 1.78 (sep, 2H), 0.63 (d, 12H). ¹³C NMR (CDCl₃, 100 MHz) ppm: 154.55, 150.23, 138.04, 130.87, 130.72, 129.63, 129.37, 128.78, 122.10, 51.91, 33.73, 29.28, 19.43.

1,3-Bis(4-isobutyl-5-(oxazol-4-yl)-4*H*-1,2,4-triazol-3-yl)benzene (L^{40Im-meta}). An *n*-butanol (10 mL) solution of *N,N'*-(1,3-phenylenebis((ethylthio)methylene))bis(2-methylpropan-1-amine) (1 g, 3.2 mmol) and oxazole-4-carbohydrazide (864 mg, 6.8 mmol) was refluxed at 108 °C for 3 days. The resulting off-white precipitate was cooled to room temperature and the product isolated as a off-white solid by filtration, washed with diethyl ether (3 x 5 mL), then with water (3 x 5 mL), and air dried overnight (514 mg, 35%). Anal. calcd for C₂₄H₂₆N₈O₂: C 62.87, H 5.72, N 24.44; found: C 61.95, H 6.78, N 24.81. MS (*m/z*) [(C₂₄H₂₆N₈O₂) Na]⁺: calcd 481.2076, found 481.2079; [(C₂₄H₂₆N₈O₂)₂ Na]⁺: calcd 939.4255, found 939.4153. ¹H NMR (CDCl₃, 400 MHz) ppm: 8.45 (s, 2H), 8.03 (s, 2H), 7.87 (s, 1H), 7.81 (d, 2H), 7.71 (t, 1H), 4.39 (d, 4H), 1.79 (sep, 2H), 0.67 (d, 12 H). ¹³C NMR (CDCl₃, 100 MHz) ppm: 155.12, 151.32, 147.59, 139.37, 130.86, 129.94, 129.73, 129.60, 128.56, 51.85, 29.57, 19.38. ¹⁵N NMR (CDCl₃, 50MHz) ppm: 317.33, 314.07, 253.61, 169.53.

1,3-Bis(4-isobutyl-5-(thiazol-4-yl)-4*H*-1,2,4-triazol-3-yl)benzene (L^{45Im-meta}). An *n*-butanol (10 mL) solution of *N,N'*-(1,3-phenylenebis((ethylthio)methylene))bis(2-methylpropan-1-amine) (1 g, 3.2 mmol) and thiazole-4-carbohydrazide (804 mg, 5.6 mmol) was refluxed at 108 °C for 3 days. The resulting pale yellow precipitate was cooled to room temperature and the product isolated as a white solid by filtration, washing with diethyl ether (3 x 5 mL), then with water (3 x 5 mL), and air dried overnight (900 mg, 56%). Anal. calcd for C₂₄H₂₆N₈S₂: C 58.75, H 5.34, N 22.84; found: C 58.53, H 5.40, N 22.97. MS (*m/z*) [(C₂₄H₂₆N₈S₂) Na]⁺: calcd 513.1620, found 513.1614; [(C₂₄H₂₆N₈S₂)₂ Na]⁺: calcd

1003.3341, found 1003.3352. ^1H NMR (CDCl_3 , 400 MHz) ppm: 8.93 (s, 2H), 8.29 (s, 2H), 7.88 (s, 1H), 7.82 (d, 2H), 7.71 (t, 1H), 4.44 (d, 4H), 1.71 (sep, 2H), 0.63 (d, 12H). ^{13}C NMR (CDCl_3 , 100 MHz) ppm: 155.16, 153.24, 150.26, 144.69, 130.93, 129.73, 129.71, 128.70, 120.69, 52.16, 29.61, 19.40. ^{15}N NMR (CDCl_3 , 50 MHz) ppm: 316.60, 316.10, 315.12, 169.12.

$\text{Fe}_2(\text{L}^{2\text{NHIm-meta}})_3(\text{BF}_4)_4 \cdot 4\text{H}_2\text{O}$ (1·4H₂O). To a white suspension of $\text{L}^{2\text{NHIm-meta}}$ (30 mg, 0.06 mmol) in acetonitrile (5 mL), solid $\text{Fe}(\text{BF}_4)_2 \cdot 6\text{H}_2\text{O}$ (15 mg, 0.04 mmol) was added, resulting in an orange clear solution which was stirred for 4 h at room temperature. Vapour diffusion of diethyl ether into this solution gave, within a week, a few block shaped orange crystals of **1**-solvents which were suitable for X-ray crystallography. The orange crystals were filtered off, washed with diethyl ether and air dried, giving as the hydrate, **1**·4H₂O (30 mg, 73%). Anal. calcd for **1**·4H₂O: C 45.50, H 4.88, N 22.11; found: C 45.33, H 4.78, N 22.31. Cryo-MS (m/z) [$\text{Fe}_2(\text{C}_{24}\text{H}_{28}\text{N}_{10})_3$]⁴⁺: calcd 370.15443, found 370.15571; [$\text{Fe}_2(\text{C}_{24}\text{H}_{28}\text{N}_{10})_3$](F)³⁺: calcd 499.87222, found 499.87145; [$\text{Fe}_2(\text{C}_{24}\text{H}_{28}\text{N}_{10})_3$](BF₄)³⁺: calcd 522.54075, found 522.54071; [$\text{Fe}_2(\text{C}_{24}\text{H}_{28}\text{N}_{10})_3$](F)₂²⁺: calcd 759.30780, found 759.30687. ^1H DOSY (CD_3CN) diffusion coefficient: $6.7 \times 10^{-6} \text{ cm}^2 \text{ s}^{-1}$.

$\text{Fe}_2(\text{L}^{4\text{NHIm-meta}})_3(\text{BF}_4)_4 \cdot 6\text{H}_2\text{O}$ (2·6H₂O). To a white suspension of $\text{L}^{4\text{NHIm-meta}}$ (30 mg, 0.06 mmol) in nitromethane (5 mL), solid $\text{Fe}(\text{BF}_4)_2 \cdot 6\text{H}_2\text{O}$ (15 mg, 0.04 mmol) was added, resulting in a greenish-brown clear solution which was stirred for 4 h at room temperature. Vapour diffusion of diethyl ether into this solution gave, within a week, a few block shaped greenish brown crystals of **2**-solvents which were suitable for X-ray crystallography. The brown crystals were filtered off, washed with diethyl ether and air dried, giving as the hydrated **2**·6H₂O (12 mg, 30%). Anal. calcd for **2**·6H₂O: C 44.65, H 5.00, N 21.70; found: C 43.36, H 4.95, N 21.40. Cryo-MS (m/z) [$\text{Fe}_2(\text{C}_{24}\text{H}_{28}\text{N}_{10})_3$]⁴⁺: calcd 370.15443, found 370.15105; [$\text{Fe}_2(\text{C}_{24}\text{H}_{28}\text{N}_{10})_3$](F)³⁺: calcd 499.87222, found 499.87225; [$\text{Fe}_2(\text{C}_{24}\text{H}_{28}\text{N}_{10})_3$](BF₄)³⁺: calcd 522.54075, found 522.54038; [$\text{Fe}_2(\text{C}_{24}\text{H}_{28}\text{N}_{10})_3$](BF₄)₂²⁺: calcd 827.31331, found 827.31229. ^1H DOSY (CD_3CN) diffusion coefficient: $6.5 \times 10^{-6} \text{ cm}^2 \text{ sec}^{-1}$.

$[\text{Fe}_2(\text{L}^{4\text{NMelm-meta}})_3(\text{BF}_4)_4 \cdot 5\text{H}_2\text{O}$ (3·5H₂O). To a white suspension of $\text{L}^{4\text{NMelm-meta}}$ (44 mg, 0.09 mmol) in acetonitrile (4 mL), solid $\text{Fe}(\text{BF}_4)_2 \cdot 6\text{H}_2\text{O}$ (20 mg, 0.06 mmol) was added, resulting in a brownish orange clear solution which was stirred for 4 h at room

temperature. Vapour diffusion of diethyl ether into this solution gave, within a week, a few irregular shaped orange/yellow crystals of **3·6MeCN·C₄H₁₀O** which were suitable for X-ray crystallography. The orange crystals were filtered off, washed with diethyl ether and air dried, giving as the hydrated **3·5H₂O** (48 mg, 87%). Anal. calcd for **3·5H₂O**: C 46.78 H 5.33 N 20.98; found: C 46.89 H 5.63 N 21.28. TGA for **3·5H₂O** calcd: 4.49 %, found: 5.27 %. Cryo MS (*m/z*) [**Fe₂(C₂₆H₃₂N₁₀)₃**]⁴⁺: calcd 391.17812, found 391.17892; [**Fe₂(C₂₆H₃₂N₁₀)₃**](F)³⁺: calcd 527.90354, found 527.90272; [**Fe₂(C₂₆H₃₂N₁₀)₃**](BF₄)³⁺: calcd 550.57209, found 550.57183; [**Fe₂(C₂₆H₃₂N₁₀)₃**](F₂)²⁺: calcd 801.35479, found 801.35297; [**Fe₂(C₂₆H₃₂N₁₀)₃**](BF₄)₂²⁺: calcd 869.36035, found 869.35841. ¹H DOSY (CD₃CN) diffusion coefficient: 6.6 x 10⁻⁶ cm² sec⁻¹.

Fe₂(L^{40Im-meta})₃(BF₄)₄·6H₂O (4·6H₂O). To a white suspension of **L^{40Im-meta}** (80 mg, 0.17 mmol) in acetonitrile (10 mL), solid Fe(BF₄)₂·6H₂O (40 mg, 0.12 mmol) was added, resulting in a violet clear solution which was stirred for 4 h at room temperature. Vapour diffusion of diethyl ether into this solution gave, within a week, a few needle shaped light pinkish-violet crystals of **4·solvents** which were suitable for X-ray crystallography. The light violet crystals were filtered off, washed with diethyl ether and air dried, giving as hydrated greyish powder **4·6H₂O**, (40 mg, 37%). Anal. calcd for **4·6H₂O**: C 44.52, H 4.67, N 17.30; found: C 44.39, H 4.47, N 17.58. TGA for **4·6H₂O** calcd: 5.56 %, found: 5.63 %. Cryo-MS (*m/z*) [**Fe₂(C₂₆H₂₆N₈O₂)₃**]⁴⁺: calcd 371.63045, found 371.63271; [**Fe₂(C₂₆H₂₆N₈O₂)₃**](BF₄)³⁺: calcd 524.50878, found 524.50888; [**Fe₂(C₂₆H₂₆N₈O₂)₃**](F₂)²⁺: calcd 762.25952, found 762.25985; [**Fe₂(C₂₆H₂₆N₈O₂)₃**](BF₄)(F)²⁺: calcd 796.26234, found 796.26265. ¹H DOSY (CD₃CN) diffusion coefficient: 6.4 x 10⁻⁶ cm² sec⁻¹.

Fe₂(L^{40Im-meta})₃(BF₄)₄·3.5H₂O·2NO₂CH₃ (4·3.5H₂O·2NO₂CH₃). To a white suspension of **L^{40Im-meta}** (30 mg, 0.06 mmol) in nitromethane (5 mL), solid Fe(BF₄)₂·6H₂O (15 mg, 0.04 mmol) was added, resulting in a violet clear solution which was stirred for 4 h at room temperature. Vapour diffusion of diethyl ether into this solution gave, within a week, a few needle shaped light pinkish-violet crystals of **4·5.5NO₂CH₃** which were suitable for X-ray crystallography. The light violet crystals were filtered off, washed with diethyl ether and air dried, giving a greyish powder, **4·3.5H₂O·2NO₂CH₃**, (26 mg, 70%). Anal. calcd for **4·3.5H₂O·2NO₂CH₃**: C 44.01, H 4.54, N 18.03; found: C 44.25, H 4.24, N 17.64.

Fe₂(L^{4SIm-meta})₃(BF₄)₄·2.5H₂O (5·2.5H₂O). To a white suspension of L^{4SIm-meta} (86 mg, 0.18 mmol) in acetonitrile (10 mL), solid Fe(BF₄)₂·6H₂O (46 mg, 0.14 mmol) was added, resulting in an orange clear solution which was stirred for 4 h at room temperature. Vapour diffusion of diethyl ether into this solution gave, within a week, a few block shaped orange crystals of 5·solvent which were suitable for X-ray crystallography. The orange crystals were filtered off, washed with diethyl ether and air dried, giving as hydrated 5·2.5H₂O, (98 mg, 87%). Anal. calcd for 5·2.5H₂O: C 43.77, H 4.23, N 17.01; found: C 43.62, H 3.92, N 17.23. Cryo-MS (*m/z*) [Fe₂(C₂₆H₂₆N₈S₂)₃]⁴⁺: calcd 395.84672, found 395.84795; [Fe₂(C₂₆H₂₆N₈S₂)₃](F)³⁺: calcd 533.79487, found 533.79484; [Fe₂(C₂₆H₂₆N₈S₂)₃](BF₄)³⁺: calcd 556.46310, found 556.46302; [Fe₂(C₂₆H₂₆N₈S₂)₃](F₂)²⁺: calcd 810.19133, found 810.19066; [Fe₂(C₂₆H₂₆N₈S₂)₃](BF₄)(F)²⁺: calcd 844.19413, found 844.19324; [Fe₂(C₂₆H₂₆N₈S₂)₃](BF₄)₂²⁺: calcd 878.19685, found 878.19685. ¹H DOSY (CD₃CN) diffusion coefficient: 6.6 x 10⁻⁶ cm² sec⁻¹.

[Ni₂(L^{2NHIm-meta})₃(BF₄)₄·6H₂O (1^{Ni}·6H₂O). To a white suspension of L^{2NHIm-meta} (30.2 mg, 0.06 mmol) in acetonitrile (5 mL), solid Ni(BF₄)₂·6H₂O (16 mg, 0.04 mmol) was added, resulting in a pale violet clear solution which was stirred for 4 h at room temperature. Vapour diffusion diethyl ether into this solution gave, within a week, a few plate shaped violet crystals of 1^{Ni}·CH₃CN·solvents which were suitable for X-ray crystallography. The violet crystals were filtered off and washed with diethyl ether, air dried, giving as the hydrate, 1^{Ni}·6H₂O, (25 mg, 62%). Anal. calcd for 1^{Ni}·6H₂O: C 44.52, H 4.98, N 21.63; found: C 44.43, H 4.68, N 21.43. Cryo-MS (*m/z*) [Ni₂(C₂₄H₂₈N₁₀)₃]⁴⁺: calcd 371.6542, found 371.6545; [[Ni₂(C₂₄H₂₈N₁₀)₃](BF₄)₁]³⁺: calcd 524.5403, found 524.5399. [[Ni₂(C₂₄H₂₈N₁₀)₃](BF₄)₂]²⁺: calcd 830.3125, found 830.3123.

[Ni₂(L^{4NHIm-meta})₃(BF₄)₄·4H₂O (2^{Ni}·4H₂O). To a white suspension of L^{4NHIm-meta} (30 mg, 0.06 mmol) in acetonitrile (5 mL), solid Ni(BF₄)₂·6H₂O (16 mg, 0.04 mmol) was added, resulting in a pale violet clear solution which was stirred for 4 h at room temperature. Vapour diffusion diethyl ether into this solution gave, within a week, a few block shaped violet crystals of 2^{Ni}·4CH₃CN·solvents which were suitable for X-ray crystallography. The violet crystals were filtered off and washed with diethyl ether, air dried, giving as the hydrate, 2^{Ni}·4H₂O, (20 mg, 50%). Anal. calcd for 2^{Ni}·4H₂O: C 44.33, H 4.86, N 22.04; found: C 44.29, H 4.64, N 21.76. Cryo-MS (*m/z*) [Ni₂(C₂₄H₂₈N₁₀)₃]⁴⁺: calcd 371.6542, found

371.6547: $[[\text{Ni}_2(\text{C}_{24}\text{H}_{28}\text{N}_{10})_3](\text{BF}_4)_1]^{3+}$: calcd 524.5403, found 524.5398. $[[\text{Ni}_2(\text{C}_{24}\text{H}_{28}\text{N}_{10})_3](\text{BF}_4)]^{2+}$: calcd 830.3125, found 830.3117.

$[\text{Ni}_2(\text{L}^{4\text{NMelm-meta}})_3](\text{BF}_4)_4 \cdot 5\text{H}_2\text{O}$ ($3^{\text{Ni}} \cdot 5\text{H}_2\text{O}$). To a white suspension of $\text{L}^{4\text{NMelm-meta}}$ (70 mg, 0.14 mmol) in acetonitrile (8 mL), solid $\text{Ni}(\text{BF}_4)_2 \cdot 6\text{H}_2\text{O}$ (35 mg, 0.10 mmol) was added, resulting in a pale violet clear solution which was stirred for 4 h at room temperature. Vapour diffusion diethyl ether into this solution gave, within a week, a few block shaped violet crystals, none of which were suitable for X-ray crystallography. The violet crystals were filtered off and washed with diethyl ether, air dried, giving as the hydrate, $3^{\text{Ni}} \cdot 5\text{H}_2\text{O}$, (85 mg, 92%). Anal. calcd for $3^{\text{Ni}} \cdot 5\text{H}_2\text{O}$: C 46.64, H 5.32, N 20.92; found: C 46.61, H 5.31, N 21.00. Cryo-MS (m/Z) $[\text{Ni}_2(\text{C}_{26}\text{H}_{32}\text{N}_{10})_3]^{4+}$: calcd 392.68412, found 392.67776: $[[\text{Ni}_2(\text{C}_{26}\text{H}_{32}\text{N}_{10})_3](\text{BF}_4)_1]^{3+}$: calcd 552.56987, found 552.57172. $[[\text{Ni}_2(\text{C}_{26}\text{H}_{32}\text{N}_{10})_3](\text{BF}_4)]^{2+}$: calcd 872.35644, found 872.35960.

$[\text{Ni}_2(\text{L}^{4\text{OIm-meta}})_3](\text{BF}_4)_4 \cdot 2.5\text{H}_2\text{O}$ ($4^{\text{Ni}} \cdot 2.5\text{H}_2\text{O}$). To a brown suspension of $\text{L}^{4\text{OIm-meta}}$ (30.6 mg, 0.06 mmol) in acetonitrile (5 mL), solid $\text{Ni}(\text{BF}_4)_2 \cdot 6\text{H}_2\text{O}$ (15 mg, 0.04 mmol) was added, resulting in a violet clear solution which was stirred for 4 h at room temperature. Vapour diffusion diethyl ether into this solution gave, within a week, a few needle shaped violet crystals, none of which were suitable for X-ray crystallography. The violet crystals were filtered off and washed with diethyl ether, air dried, giving as the hydrate, $4^{\text{Ni}} \cdot 2.5\text{H}_2\text{O}$, (25 mg, 62%). Anal. calcd for $4^{\text{Ni}} \cdot 2.5\text{H}_2\text{O}$: C 45.87, H 4.44, N 17.83; found: C 45.73, H 4.29, N 18.11. Cryo-MS (m/Z) $[\text{Ni}_2(\text{C}_{24}\text{H}_{26}\text{N}_8\text{O}_2)_3]^{4+}$: calcd 373.12549, found 373.13023: $[[\text{Ni}_2(\text{C}_{24}\text{H}_{26}\text{N}_8\text{O}_2)_3](\text{BF}_4)]^{3+}$: calcd 526.50835, found 526.50545. $[[\text{Ni}_2(\text{C}_{24}\text{H}_{26}\text{N}_8\text{O}_2)_3](\text{BF}_4)_2]^{2+}$: calcd 833.26011, found 833.76454.

$[\text{Ni}_2(\text{L}^{4\text{SIm-meta}})_3](\text{BF}_4)_4 \cdot 3\text{H}_2\text{O}$ ($5^{\text{Ni}} \cdot 3\text{H}_2\text{O}$). To a white suspension of $\text{L}^{4\text{SIm-meta}}$ (60 mg, 0.12 mmol) in acetonitrile (5 mL), solid $\text{Ni}(\text{BF}_4)_2 \cdot 6\text{H}_2\text{O}$ (30 mg, 0.09 mmol) was added, resulting in a pale violet clear solution which was stirred for 4 h at room temperature. Vapour diffusion diethyl ether into this solution gave, within a week, a few needle shaped violet crystals, none of which were suitable for X-ray crystallography. The violet crystals were filtered off and washed with diethyl ether, air dried, giving as the hydrate, $5^{\text{Ni}} \cdot 3\text{H}_2\text{O}$, (75 mg, 96%). Anal. calcd for $5^{\text{Ni}} \cdot 3\text{H}_2\text{O}$: C 43.44, H 4.25, N 16.89, S 9.66; found: C 43.57, H 4.01, N 16.76, S 9.61. Cryo-MS (m/Z) $[\text{Ni}_2(\text{C}_{24}\text{H}_{26}\text{N}_8\text{S}_2)_3]^{4+}$: calcd 397.09197,

found 397.09584: $[[\text{Ni}_2(\text{C}_{24}\text{H}_{26}\text{N}_8\text{S}_2)_3](\text{BF}_4)]^{3+}$: calcd 558.46251, found 558.45965. $[[\text{Ni}_2(\text{C}_{24}\text{H}_{26}\text{N}_8\text{S}_2)_3](\text{BF}_4)_2]^{2+}$: calcd 881.19582, found 881.19198.

Previously reported SCO-active $\text{Fe}^{\text{II}}_2\text{L}_3$ dinuclear helicates

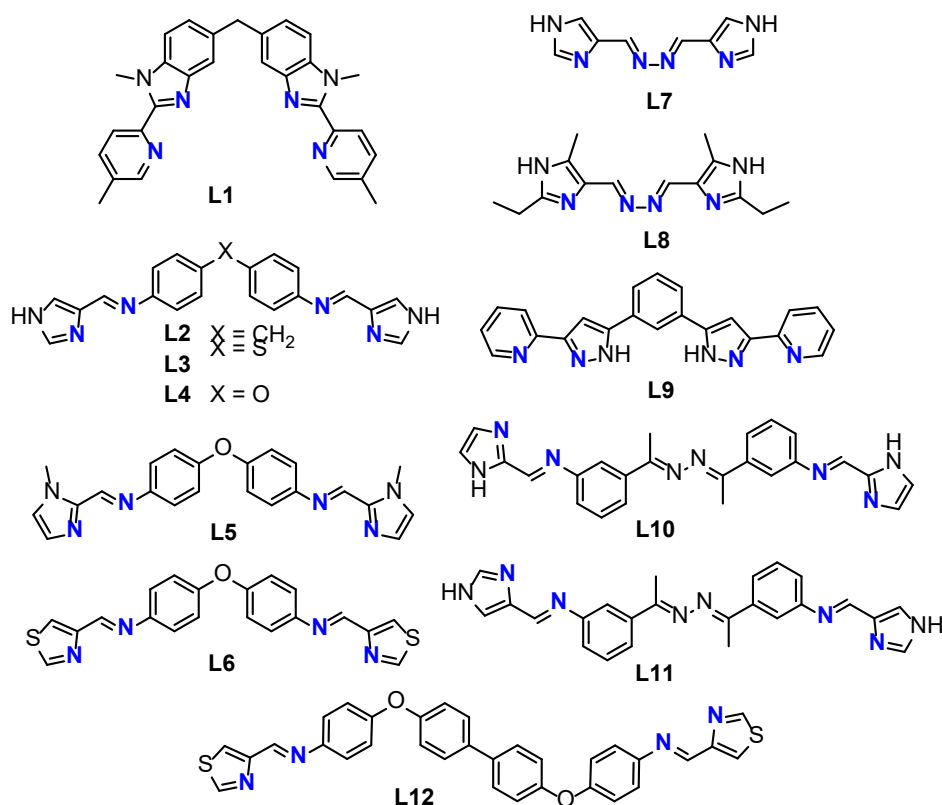


Figure S1.1 The 12 ligands, **L1–L12**, reported in the literature to form dinuclear SCO active triply bridged Fe_2L_3 helicates (see also Figure 1, main paper).¹⁰⁻²⁰

The first example of a SCO-active dinuclear helicate, $[\text{Fe}_2\text{L}_3]^{4+}$ (Figure S1) reported by Williams and co-workers in 1998,¹¹ undergoes a gradual and incomplete SCO in CD_3CN solution (240-330 K). Then in 2004 Hannon and co-workers²¹ showed that the solid state SCO of the family of $[\text{Fe}_2\text{L}_3](\text{X})_4$ ($\text{X} = \text{PF}_6$, BF_4 and ClO_4) differed with counter-anion choice. The PF_6 and BF_4 analogues undergo gradual SCO from fully HS to ~80% LS at ~200 K and 150 K, respectively, whilst the ClO_4 analogue undergoes half SCO at ~180 K.²¹ A subsequent Mössbauer spectroscopy study showed that half of the $[\text{Fe}_2\text{L}_3](\text{ClO}_4)_4$

undergo a two-step SCO, with $T_{1/2}$ values of 240 K and 120 K for the [HS-HS] \leftrightarrow [LS-LS] conversion, whilst the other half remains HS-HS.²² Li and co-workers went on to show that the choice of heteroatom, methylene vs thioether vs ether, at the ‘hinge’ in such ligands, **L2-L4** (Figure S1), modified the half-SCO for the resulting [Fe₂L₃](BF₄)₄ helicates, $T_{1/2}\downarrow$ values (switching temperature in cooling mode) of 155 K, 115 K and 150 K, respectively, with a 15 K wide thermal hysteresis in all cases¹² whereas [Fe₂L₄](I₃)₄ undergoes full SCO at 210 K.²⁰ Maintaining an ether hinge, but changing the terminal 4-imidazole group of **L4** to a 1-methyl-2-imidazole in **L5**, Kruger and co-workers reported the doubly switchable (temperature and light) and solvent sensitive SCO of [Fe₂(**L5**)₃](ClO₄)₄.¹³ The desolvated helicate undergoes full SCO [HS-HS] \rightarrow [LS-LS] in the solid state, with $T_{1/2} = 140$ K.¹³ In contrast, the hydrated analogues [Fe₂(**L5**)₃](ClO₄)₄·xH₂O (x=1-4), exhibit moisture sensitive half SCO, with $T_{1/2}$ value between 210-265 K.²³ Further modification of **L4**, changing the 4-imidazole to 4-thiazole **L6** (Figure S1), by Li and co-workers, resulted in [Fe₂(**L6**)₃](BF₄)₄, which undergoes full SCO at $T_{1/2} = 348$ K.¹⁴ Sunatsuki and Kojima and co-workers showed that short spacer ligands **L7** and ethyl/methyl substituted analogue **L8** (Figure S1) resulted in tightly wound dinuclear helicates that exhibited abrupt half-SCO in the solid state.¹⁵ The complex [Fe₂(**L7**)₃](ClO₄)₄ undergoes $T_{1/2} = 240$ K and similarly the analogue BF₄ showed lower $T_{1/2} = 190$ K,¹⁵ whereas the plate crystals of [Fe₂(**L8**)₃](ClO₄)₄·H₂O undergoes $T_{1/2} = 120$ K.¹⁸ Aromi and co-workers reported two helicates based on the *meta*-phenylene linked **L9** ligand (Figure S1), X@[Fe₂(**L9**)₃]X(PF₆)₂, that could be triply switched by guests (X = Cl or Br), temperature or light.¹⁶ Due to the presence of a pair of ‘spare’ NH moieties on each **L9** strand, the helicates encapsulate a halide ion guest, X = Cl or Br, with the choice of guest, shown to tune the $T_{1/2}$ by about 40 K, from 302 K for Cl to 258 K for Br. Kruger, Clérac and co-workers showed that the solid state $T_{1/2}$ for the thermally induced full SCO of two solvated dinuclear helicates formed from a pair of isomeric ligands, **L10** and **L11** (Figure S1), featuring imidazole-imine binding pockets, was modified from 355 K to 148 K on changing from stronger 2-imidazole (**L10**) to weaker 4-imidazole (**L11**).¹⁷ Very recently, Li and co-workers reported the longest dinuclear helicate, of Fe...Fe length 19.322 Å, formed using a long semi-flexible ligand **L12** (Figure S1). It undergoes incomplete two-step SCO at $T_{1/2} = 335$ K and $T_{1/2} = 91$ K.¹⁹

Previously reported SCO *and* redox active complexes

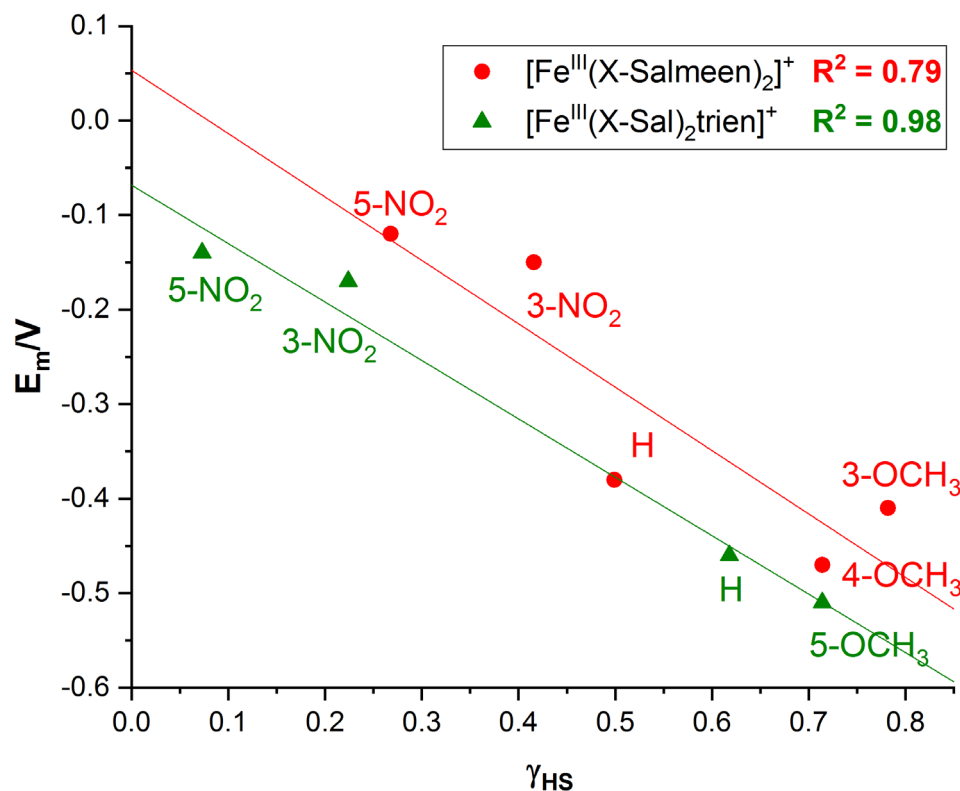


Figure S1.2 A strong linear plot between E_m and γ_{HS} for nine mononuclear $[\text{Fe}^{\text{III}}(\mathbf{X}\text{-Salmeen})_2]\text{PF}_6$ and $[\text{Fe}^{\text{III}}(\mathbf{X}\text{-Sal})_2\text{trien}]\text{PF}_6$ complexes reported by Kadish and co-workers.^{24, 25}

In 1975 Drago and co-workers studied four mononuclear Fe(II) complexes, showing that HS was the hardest to oxidise, but steric factors were also at play in that case.²⁶ The biggest family we are aware of contains nine mononuclear $[\text{Fe}^{\text{III}}(\mathbf{X}\text{-Salmeen})_2]\text{PF}_6$ and $[\text{Fe}^{\text{III}}(\mathbf{X}\text{-Sal})_2\text{trien}]\text{PF}_6$ complexes and was published in 1984 by Kadish and co-workers: they observed a linear correlation of decreasing fraction HS (γ_{HS}) with increasing redox potential (hence increasing ease of reduction), both measured in acetone solution (Figure S1.2).^{24, 25} The only case involving SCO-active dinuclear iron(II) helicates was reported by Sunatsuki and co-workers in 2009, in which a pair of helicates differing by ligand substituent X underwent irreversible oxidation, with the HS (at 300 K in the solid state) complex of the X = H ligand slightly harder to oxidise (0.70 V) than the LS complex of the electron donating X = Me ligand (0.69 V).¹⁵ In 2017, Kuroda-Sowa and co-workers studied a family of four $[\text{Fe}^{\text{II}}(\mathbf{qsal}^{\text{X}})_2]$ complexes varying in halide substituent X (F, Cl, Br and I): X = F remained HS in the solid state (but with a small needle component

undergoing SCO at 144 K) and was the easiest to oxidise in MeCN solution (-0.35 V), whilst the other three complexes were SCO active with $T_{1/2}$ 308-341 K, and had redox potentials of -0.27 to -0.26 V.²⁷ More recently, Sunatsuki and co-workers reported that a pair of tetrahedral cages $[\text{Fe}^{\text{II}}_4(\text{H}_2\text{L}^{\text{R}})_6]\text{X}_8$ (R = H, X = ClO₄; R = Me, X = BF₄) showed gradual incomplete SCO in the solid state, starting below 150 K for the former (weaker ligand field) and below 200 K for the latter, stronger field complex, with the former, more HS complex, significantly harder to oxidise in MeCN solution ($E_{\text{pa}} = 0.68$ V vs 0.54 V).²⁸ Of these, only the Drago²⁶ and Kadish^{24, 25} studies involved monitoring the SCO in solution, which is the most relevant option for comparison with the redox potential, also determined in solution.

X-ray crystallography

$[\text{Fe}_2(\text{L}^{\text{2NHIm-meta}})_3](\text{BF}_4)_4 \cdot 2\text{CH}_3\text{CN} \cdot \text{solvent}$ (**1-solvents**): The asymmetric unit consists of cationic Fe_2L_3 , two acetonitrile, three BF₄ and fourth disordered BF₄ anion at two positions with half occupancies. All hydrogen atoms were placed in calculated positions and rode on the attached atom with $U(\text{H}) = 1.2U(\text{attached atom, C})$ and $U(\text{H}) = 1.5U(\text{attached atom, N})$. All non-H atoms were refined anisotropically. One of the counteranion, BF₄ had positional disordered with half occupancy (B4, F41, F42, F43 and F44) and (B5, F51, F52, F53 and F54). The command SAME was applied on isobutyl group C65, C66, C67 and C68. The electron density found by SQUEEZE²⁹ was 231 electrons/cell i.e. 115.5 electrons per helicate ($Z = 2$). This is in agreement with the presence of five molecules of acetonitrile ($5 \times 22 = 110$ electrons) per helicate. For further details, see Table S2 and the cif file.

$[\text{Fe}_2(\text{L}^{\text{4NHIm-meta}})_3](\text{BF}_4)_4 \cdot \text{solvent}$ (**2-solvents**): The asymmetric unit consists of cationic Fe_2L_3 and four BF₄ counteranions. All hydrogen atoms were placed in calculated positions and rode on the attached atom with $U(\text{H}) = 1.2U(\text{attached atom, C})$ and $U(\text{H}) = 1.5U(\text{attached atom, N})$. All non-H atoms were refined anisotropically. Carbon atoms (and associated H atoms) of an isobutyl group were disordered across two positions with 0.6 occupancy (C66, C67) and 0.4 (C69, C70). In another not well behaved isobutyl group RIGU was applied C53 C54 C56 C55. One of the counteranion, BF₄ was disordered at two

positions with occupancy 0.8 (F41, F42, F43 and F44) and 0.2 (F45, F46, F47 and F48). The seven molecules of nitromethane were highly disordered so SQUEEZE²⁹ was applied. The electron density found by SQUEEZE was 2136 electrons/cell i.e. 267 electrons per helicate (Z = 8). This is in agreement with the presence of approximately 8 molecules of nitromethane (8 x 32 = 256) per helicate. For further details, see Table S2 and the cif file.

[Fe₂(L^{4NMeIm-meta})₃](BF₄)₄·6CH₃CN·C₄H₁₀O (**3**·6CH₃CN·C₄H₁₀O): The asymmetric unit constituting of the whole cation Fe₂L₃, six acetonitrile, one diethyl ether and four BF₄⁻ anions. All hydrogen atoms were placed in calculated positions and rode on the attached carbon atom with U(H) = 1.2U (attached atom, C). All non-H atoms were refined anisotropically. No disorder was present. For further details, see Table S2 and the cif file.

[Fe₂(L^{4OIm-meta})₃](BF₄)₄·6CH₃CN·solvent (**4**·solvents): The asymmetric unit consist of Fe₂L₃ cationic unit, four BF₄ and six CH₃CN molecules. All hydrogen atoms were placed in calculated positions and rode on the attached carbon atom with U(H) = 1.2U(attached atom, C). All non-H atoms were refined anisotropically otherwise mentioned. Carbon atoms (and associated H atoms) of one isobutyl group were disordered with half occupancy (C18, C19, C20 and C21, C22, C23). One of the counteranion, BF₄ was disordered at two positions with occupancy 0.5 and RIGU was applied (F41, F42, F43 and F44) and (F45, F46, F47 and F48, and left isotropically). The command SAME was applied on isobutyl group C56, C57, C58 and C59. The electron density found by SQUEEZE²⁹ was 179 electrons/cell i.e. 89.5 electrons per helicate (Z = 2). This is in agreement with the presence of four molecules of acetonitrile (4 x 22 = 88) per helicate. For further details, see Table S2 and the cif file.

[Fe₂(L^{4OIm-meta})₃](BF₄)₄·5.5NO₂CH₃ (**4**·5.5NO₂CH₃): The asymmetric unit consists of the Fe₂L₃ cationic unit, four BF₄, five and half NO₂CH₃ molecules. All hydrogen atoms were placed in calculated positions and rode on the attached carbon atom with U(H) = 1.2U(attached atom, C). All non-H atoms were refined anisotropically. Carbon atoms (and associated H atoms) of one isobutyl group were disordered with 0.7 (C30A, C31A, C32A) and 0.3 (C30B, C31B, C32B) occupancy. Two of the BF₄ counteranions was 'twirl' disordered around the B2-F21 and B4-F41 bond, over two positions with occupancy 0.8 (F22, F23, F24) and 0.2 (F25, F26, F27) and second BF₄ with 0.5 occupancy (F42, F43,

F44) and (F45, F46, F47). The RIGU command was applied to the nitromethane molecule O600, N600 and C600. For further details, see Table S2 and the cif file.

[Fe₂(L^{40Im-meta})₃](BF₄)₄·4NO₂CH₃ (**4**·5NO₂CH₃): The asymmetric unit consists of the Fe₂L₃ cationic unit, four BF₄, four NO₂CH₃ molecules. All hydrogen atoms were placed in calculated positions and rode on the attached carbon atom with U(H) = 1.2U(attached atom, C). All non-H atoms were refined anisotropically otherwise mentioned. Carbon atoms (and associated H atoms) of three isobutyl group were disordered with 0.6 (C30A, C31A, C32A) and 0.4 (C30B, C31B, C32B) occupancy, 0.7 (C43A, C44A, C45A) and 0.3 (C43B, C44B, C45B, and left isotropic) occupancy and 0.6 (C55A, C56A, C57A) and 0.4 (C43B, C44B, C45B). One of the BF₄ counteranions was 'twirl' disordered around the B4-F41 bond, over two positions with occupancy 0.5 (F42, F43, F44) and (F46, F47, F48). The unit cell contains solvent accessible voids of 240 Å³ so SQUEEZE²⁹ was applied. The electron density found by SQUEEZE was 59 electrons/cell i.e. 29.5 electrons per helicate (Z = 2). This is in agreement with the presence of approximately one molecule of nitromethane (1 x 32 = 32) per helicate. For further details, see Table S2 and the cif file.

[Fe₂(L^{45Sim-meta})₃](BF₄)₄·solvent (**5**·solvents): The asymmetric unit consists of half cationic unit, FeL_{1.5}, and two BF₄ in an asymmetric unit. All hydrogen atoms were placed in calculated positions and rode on the attached carbon atom with U(H) = 1.2U(attached atom, C). All non-H atoms were refined anisotropically otherwise mentioned. Out of three isobutyl groups one was disordered. Carbon atoms (and associated H atoms) of one isobutyl group were disordered across two positions but there was not enough electron density to resolve it so left as isotropic (C6, C7 and C8). One of the counteranion, BF₄ was disordered at two positions with occupancy 0.6 (F22, F23 and F24) and 0.4 (F25, F26 and F27). Three acetonitrile molecules were highly disordered so SQUEEZE²⁹ was applied. The electron density found by SQUEEZE was 362 electrons/cell i.e. 90.5 electrons per helicate (Z = 4). This is in agreement with the presence of approximately four molecules of acetonitrile (4 x 22 = 88) per helicate. For further details, see Table S2 and the cif file.

[Ni₂(L^{2NHIm-meta})₃](BF₄)₄·solvent (**1**^{Ni}·solvents): The asymmetric unit consists of cation Ni₂L₃, two BF₄ and six CH₃CN molecules. All hydrogen atoms were placed in calculated positions and rode on the attached carbon atom with U(H) = 1.2U(attached atom, C) and

$U(H) = 1.5U(\text{attached atom, N})$. Carbon atoms (and associated H atoms) of one isobutyl group were disordered with occupancy of 0.7 (C66, C67, C68) and 0.3 (C69, C70, C71). Two of the counteranions, BF_4 , two diethyl ether and other four acetonitrile were highly disordered so SQUEEZE²⁹ was applied. The electron density found by SQUEEZE was 1044 electrons/cell i.e. 261 electrons per helicate ($Z = 4$). This is in good agreement with the presence of two BF_4 ($2 \times 41 = 82$) and two molecules diethyl ether molecules ($2 \times 42 = 84$) and four molecules of acetonitrile ($4 \times 22 = 88$) per helicate. For further details, see Table S3 and the cif file.

$[\text{Ni}_2(\text{L}^{\text{4NHIm-meta}})_3](\text{BF}_4)_4 \cdot \text{solvent}$ (2^{Ni} -solvents): The asymmetric unit consists of cation $\text{Ni}_{1.5}$, two acetonitrile, one BF_4 and two BF_4 with half occupancy. All hydrogen atoms were placed in calculated positions and rode on the attached carbon atom with $U(H) = 1.2U(\text{attached atom, C})$ and $U(H) = 1.5U(\text{attached atom, N})$. All non-H atoms were refined anisotropically. The electron density found by SQUEEZE²⁹ was 820 electrons/cell i.e. 102.5 electrons per helicate ($Z = 8$). This is in agreement with the presence of five molecules of acetonitrile ($5 \times 22 = 110$) per helicate. For further details, see Table S3 and the cif file.

In all cases, the stereochemistry around the M(II) (M: Fe and Ni) centre is *facial*, as seen in other *ditopic* azine-triazole helicates and cages.⁸ This is in contrast to the *meridional* binding mode of the *monotopic* azine-triazole/azole-triazole **Rdpt** or **Rat** analogues observed in the mononuclear $[\text{FeL}_3]^{2+}$ complexes.³⁰⁻³³

All of the Fe–N distances fall in the range of 1.934–2.000 Å (Table S1), which is consistent with LS Fe(II). There are two distinct sets of *cis* N–Fe–N angle: the intraligand bite angles are restricted by the 5-membered chelate ring formed by the azole-azole binding pocket, so fall well below 90° (79.9–81.2°, Table S4) whereas the interligand *cis*-N-Fe-N angles are much less constrained, so are larger and closer to 90° (88.9–98.3°, Table S5). The *trans*-N–Fe–N angles, 168.1–173.0°, are all ~below the ideal 180° for an octahedral geometry (Table S6).¹⁰

Table S1. Selected structural parameters at 100 K, otherwise mentioned, of the following complexes: the new azole-triazole dinuclear Fe(II) helicates **1-5**, a pair of azole-triazole dinuclear Ni(II) helicates, the pair of analogous literature azine-triazole dinuclear helicates, and the pair of analogous mononuclear azole-triazole complexes. The distances and angles given are the averages for each independent Fe(II) centre. HS and mixedHS/LS Fe(II) in red text. Octahedral Ni(II) in blue text.

Complexes	Space group	<Fe–N _{azole} > (Å)	<Fe–N _{triazole} > (Å)	Σ°	Spin state	M···M (Å)	Intraligand <N _{azole} –Fe–N _{triazole} > (°)
1 ·solvents	$P\bar{1}$	1.984, 1.978	1.949, 1.948	60.9, 59.7	LS	10.0361(6)	80.1, 80.5
1 ^{Ni} ·solvents	$P2_1/n$	2.103, 2.083	2.091, 2.069	75.2, 70.2	S=1	10.313(1)	78.3, 78.7
2 ·solvents	$Pbca$	1.988, 1.993	1.956, 1.949	58.7, 57.8	LS	10.1619(9)	80.5, 80.6
2 ^{Ni} ·solvents	$lbca$	2.097	2.069	69.7	S=1	10.3891(8)	78.8
3 ·6CH ₃ CN·C ₄ H ₁₀ O	$P\bar{1}$	2.000, 1.997	1.961, 1.964	62.0, 61.5	LS	10.3227(7)	80.3, 80.4
4 ·solvents	$P\bar{1}$	1.999, 1.987	1.948, 1.940	57.0, 56.8	LS	10.018(1)	80.6, 80.8
4 ·5.5NO ₂ CH ₃	$P\bar{1}$	1.988, 2.075	1.945, 2.042	62, 77.2	LS, mixLS/HS	10.1554(7)	80.7, 78.5
4 ·5NO ₂ CH ₃ (253K)	$P\bar{1}$	2.002, 2.202	1.957, 2.159	63, 95.3	LS, HS	10.2281(9)	80.3, 75.8
5 ·solvents	$C2/c$	1.975	1.931	57.0	LS	9.9711(9)	80.9
[Fe ₂ (L ^{2pym-meta}) ₃](BF ₄) ₄ ·6CH ₃ CN ⁸	$P\bar{3}1c$	1.999	1.926	56.7	LS	10.132	80.7
[Fe ₂ (L ^{4pym-meta}) ₃](BF ₄) ₄ ·6CH ₃ CN ⁸	$P\bar{3}1c$	2.008	1.915	60.3	LS	10.320	80.3
[Fe(L ^{4NMelm}) ₃](BF ₄) ₂ ·solvents ⁹	$P\bar{1}$	2.175	2.197	92.9°	HS	–	75.7
[Fe(L ^{4Sim}) ₃](BF ₄) ₂ ·solvents ⁹	$P\bar{1}$	1.997, 1.988	1.976, 1.958	58.2, 58.2°	LS	–	80.6, 80.6

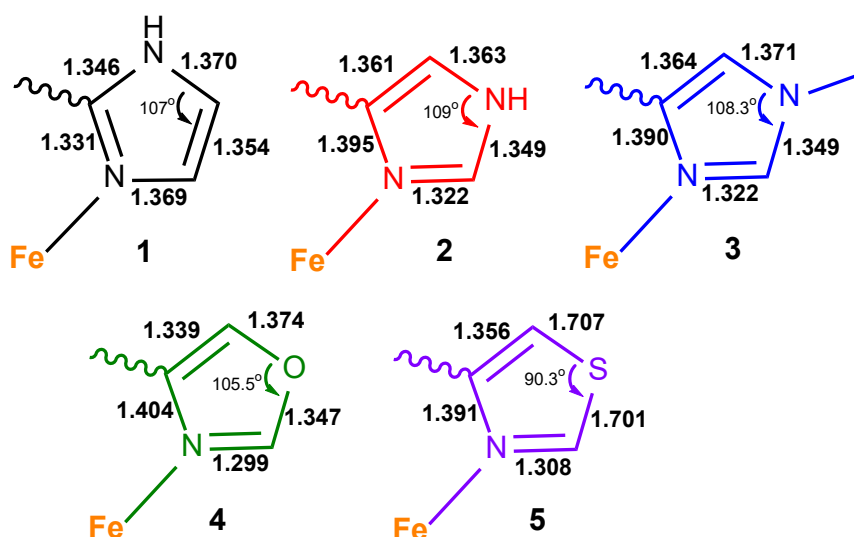


Figure S2. Selected structural parameters (average bond lengths (Å), av. C–X–C angles (°)) associated with the azole ring in the dinuclear helicates: **1**·solvents (black), **2**·solvents (red), **3**·6CH₃CN·C₄H₁₀O (blue), **4**·solvents (green) and **5**·solvents (purple).

The average C–X–C angle and C–X bond length in the azole of these helicates varies (Figure S2): for X = CH (**1**·solvents), NH (**2**·solvents), NMe (**3**·6CH₃CN·C₄H₁₀O) and O (**4**·solvents) they lie in a very narrow range (105–109°, 1.35–1.37 Å), whereas for the larger X = S heteroatom (**5**·solvents) they are significantly lower (90°) and longer (1.70 Å), respectively. The overlaid structures of the 4–imidazole (**2**·solvents) and 4–thiazole (**5**·solvents) helicates highlights both of these differences (Figure S3).

The angle between the centroids of the triazole–phenylene–triazole rings in all of these helicates (116–120°) remains close to 120°, irrespective of changing from a six membered diazine to a five membered azole ring (Table S8), as it is largely controlled by the *meta*-phenylene linker employed in all of these ditopic ligands. Unsurprisingly, given that both rings coordinate, the azole and attached triazole ring are close to co-planar (2.84–5.77°, Table S7) in all helicates **1–5**, as were the analogous n-pyrimidine and triazole rings for [Fe₂(L^{2/4pym-*meta*})₃](BF₄)₄·6CH₃CN (1.80/1.20°).⁸ This is usual for such **Rat** complexes.^{9, 32, 34–36} Interestingly, the twist angle between the triazole and phenylene linker drops slightly, by ~4°, from 50.22–51.33° for the azine-triazoles to 45.40–48.18° for the azole-triazoles (Table S7).

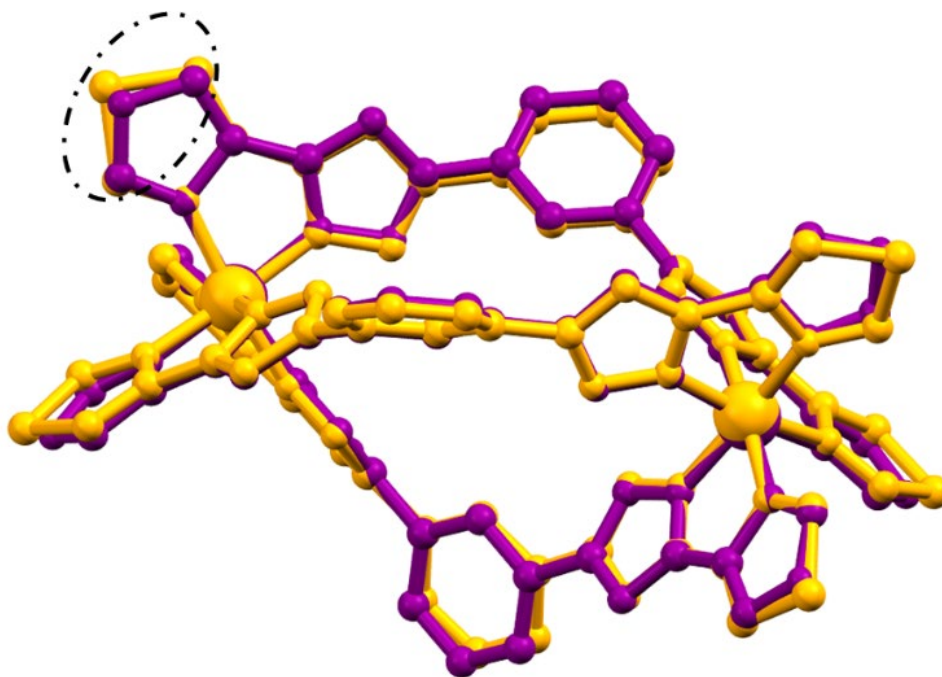


Figure S3. Overlay (fit of Fe, N, C and S) of the cationic structures of $[\text{Fe}_2(\text{L}^{4\text{NHim-meta}})_3](\text{BF}_4)_4$ (**2**, purple) and $[\text{Fe}_2(\text{L}^{4\text{SIm-meta}})_3](\text{BF}_4)_4$ (**5**, golden yellow); emphasising of the differences in C–X bond length and C–X–C angle (X = S vs N; black dashed circle). For clarity, hydrogen atoms, counter-anions, solvents and iso-butyl groups are not shown.

Table S2. Crystal data and structure refinement details for the complexes. †SQUEEZE applied.

	1-solvents†	2-solvents†	3-6CH ₃ CN·C ₄ H ₁₀ O	4-solvents†	4-5.5NO ₂ CH ₃	4-5NO ₂ CH ₃ †	5-solvents†
T [K]	100	100	100	100	100	253	100
Empirical formula	C ₇₆ H ₉₀ B ₄ F ₁₆ Fe ₂ N ₃₂	C ₇₂ H ₈₄ B ₄ F ₁₆ Fe ₂ N ₃₀	C ₉₄ H ₁₂₄ B ₄ F ₁₆ Fe ₂ N ₃₆ O	C ₈₄ H ₉₆ B ₄ F ₁₆ Fe ₂ N ₃₀ O ₆	C ₁₅₅ H ₁₈₉ B ₈ F ₃₂ Fe ₄ N ₅₉ O ₃₄	C ₇₆ H ₉₀ B ₄ F ₁₆ Fe ₂ N ₂₈ O ₁₄	C ₇₂ H ₇₈ B ₄ F ₁₆ Fe ₂ N ₂₄ S ₆
M _r	1910.73	1828.63	2233.22	2080.84	4340.52	2078.69	1926.85
CCDC No.	2061247	2061248	2061249	2061250	2090518	2090519	2061251
Crystal system	triclinic	orthorhombic	triclinic	triclinic	triclinic	triclinic	monoclinic
Space group	<i>P</i> -1	<i>Pbca</i>	<i>P</i> -1	<i>P</i> -1	<i>P</i> -1	<i>P</i> -1	<i>C</i> 2/ <i>c</i>
a [Å]	14.5969(3)	20.0164(7)	17.7970(4)	14.0743(3)	12.7611(3)	12.9427(4)	13.1754(4)
b [Å]	18.8022(3)	30.0399(5)	18.8632(5)	15.1211(6)	15.2423(5)	15.5781(6)	25.7678(7)
c [Å]	19.7107(3)	36.9150(16)	19.2290(3)	27.2280(8)	25.9116(7)	26.0851(9)	29.1091(9)
α [°]	84.573(2)	90	66.217(2)	105.634(3)	92.820(2)	93.702(3)	90
β [°]	81.247(2)	90	73.980(2)	91.620(2)	101.815(2)	101.308(3)	94.743(3)
γ [°]	89.600(2)	90	74.493(2)	96.749(3)	93.092(2)	93.154(3)	90
V [Å ³]	5322.56(16)	22196.6(13)	5587.7(2)	5530.7(3)	4916.7(2)	5134.2(3)	9848.7(5)
Z	2	8	2	2	1	2	4
ρ _{calcd.} [g/cm ³]	1.192	1.094	1.327	1.250	1.466	1.345	1.300
μ [mm ⁻¹]	2.877	2.734	2.835	2.848	0.403	0.380	4.249
F(000)	1972.0	7536.0	2328.0	2148.0	2236.0	2140.0	3944.0
Crystal Size (mm)	0.1 × 0.08 × 0.05	0.1 × 0.08 × 0.02	0.2 × 0.1 × 0.09	0.08 × 0.05 × 0.03	0.09 × 0.05 × 0.012	0.09 × 0.05 × 0.012	0.09 × 0.03 × 0.02
2θ range for data collection	7.708 to 154.666	7.148 to 153.272	8.002 to 152.934	6.992 to 153.868	6.462 to 58.928	6.588 to 58.592	7.508 to 153.194
Reflections collected	57200	93118	49438	45905	59625	57448	20758
Independent reflections	22044	23026	22943	22571	23153	23784	10075
R(int)	0.0392	0.0915	0.0343	0.0839	0.0408	0.0373	0.0389
Data / restraints / parameters	22044/26/1230	23026/24/1184	22943/0/140	22571/15/1337	23153/18/1434	23784/17/1413	10075/0/578
Goof (F ²)	1.014	0.999	1.063	1.074	1.046	1.059	1.063
R _i [I>2σ(I)]	0.0681	0.0795	0.0722	0.0916	0.0645	0.0871	0.0914
wR ₂ [all data]	0.1981	0.2399	0.2137	0.2546	0.1701	0.2745	0.2612
Max/min res. e density [eÅ ⁻³]	1.27 and -0.72	0.90 and -0.48	1.94 and -0.92	0.88 and -0.62	1.28/-0.66	1.20/-0.58	2.24 and -0.86



Figure S4. Crystals of **1**, **2**, **3**, **4** and **5** at 100 K (on diffractometer).

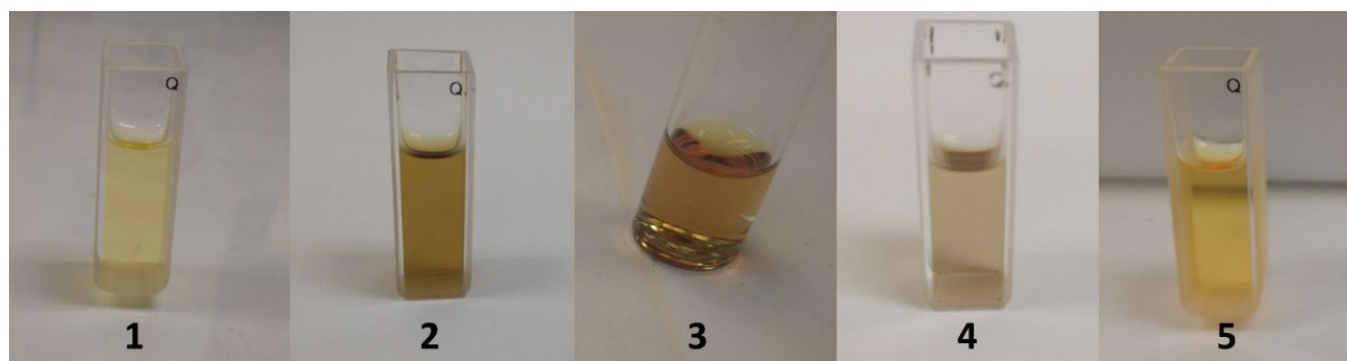


Figure S5. Solution of **1** (0.032 mM; Yellow), **2** (1.6 mM; Brown), **3** (2 mM, Dark yellow), **4** (1.4 mM; Greyish) and **5** (0.01 mM; Yellow) in acetonitrile used in VT-UV-vis studies.



Figure S6. Solid sample of **1** (orange), **2** (brown), **3** (orange), **4** (greyish) and **5** (orange) at RT under optical microscope.

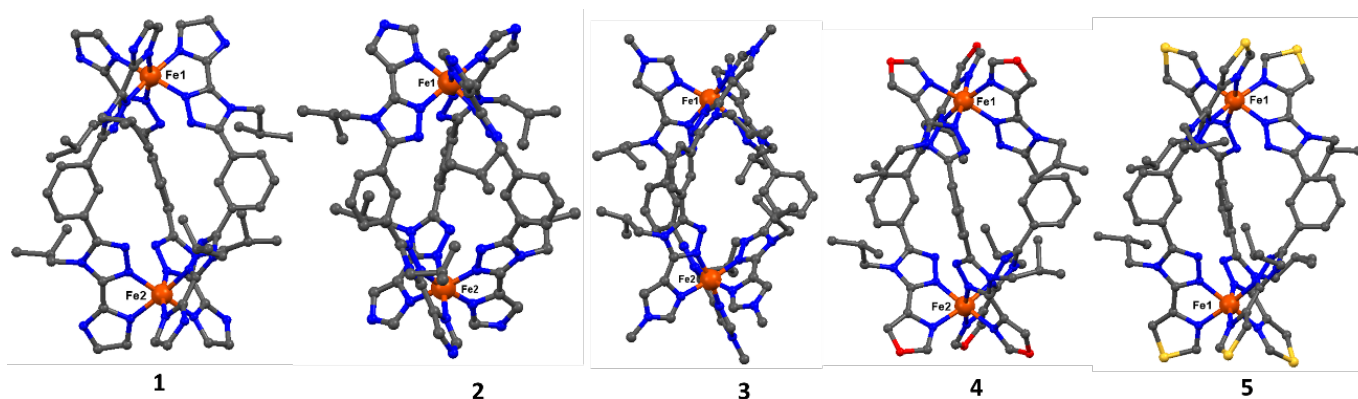


Figure S7. Crystal structure of cationic $[\text{Fe}_2(\text{L}^{2\text{NHIm-meta}})_3](\text{BF}_4)_4 \cdot 2\text{CH}_3\text{CN} \cdot \text{solvent}$ (**1**·solvents), $[\text{Fe}_2(\text{L}^{4\text{NHIm-meta}})_3](\text{BF}_4)_4 \cdot \text{solvent}$ (**2**·solvents), $[\text{Fe}_2(\text{L}^{4\text{NMIm-meta}})_3](\text{BF}_4)_4 \cdot 6\text{CH}_3\text{CN} \cdot \text{C}_4\text{H}_{10}\text{O}$ (**3**· $6\text{CH}_3\text{CN} \cdot \text{C}_4\text{H}_{10}\text{O}$), $[\text{Fe}_2(\text{L}^{4\text{OIm-meta}})_3](\text{BF}_4)_4 \cdot 6\text{CH}_3\text{CN} \cdot \text{solvent}$ (**4**·solvents) and $[\text{Fe}_2(\text{L}^{4\text{SIm-meta}})_3](\text{BF}_4)_4 \cdot \text{solvent}$ (**5**·solvents); solvent molecules, counter-anions and hydrogens are not shown for clarity.

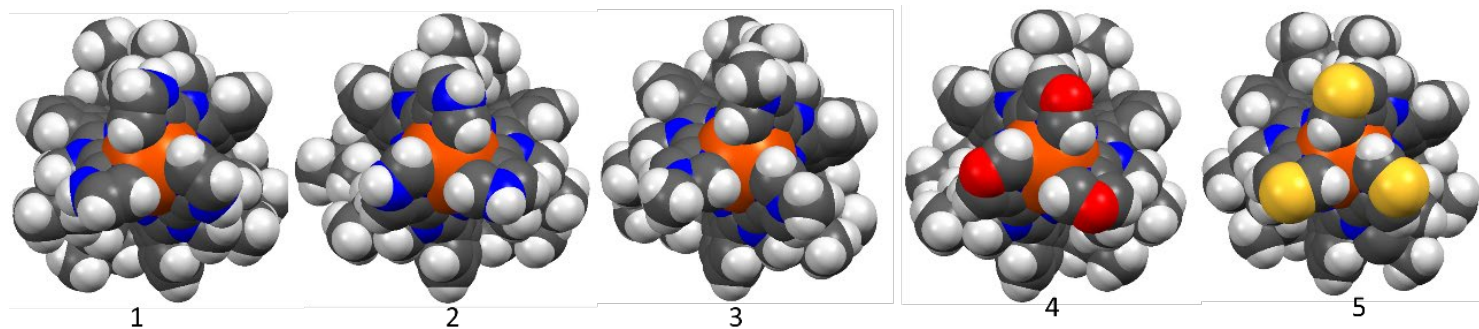


Figure S8. Space filled representation of dinuclear helicites of $[\text{Fe}_2(\text{L}^{2\text{NHIm-meta}})_3](\text{BF}_4)_4 \cdot 2\text{CH}_3\text{CN} \cdot \text{solvent}$ (**1**·solvents), $[\text{Fe}_2(\text{L}^{4\text{NHIm-meta}})_3](\text{BF}_4)_4 \cdot \text{solvent}$ (**2**·solvents), $[\text{Fe}_2(\text{L}^{4\text{NMelm-meta}})_3](\text{BF}_4)_4 \cdot 6\text{CH}_3\text{CN} \cdot \text{C}_4\text{H}_{10}\text{O}$ (**3**· $6\text{CH}_3\text{CN} \cdot \text{C}_4\text{H}_{10}\text{O}$), $[\text{Fe}_2(\text{L}^{4\text{OIm-meta}})_3](\text{BF}_4)_4 \cdot 6\text{CH}_3\text{CN} \cdot \text{solvent}$ (**4**·solvents) and $[\text{Fe}_2(\text{L}^{4\text{SIm-meta}})_3](\text{BF}_4)_4 \cdot \text{solvent}$ (**5**·solvents).



Figure S9. Solid sample of **1**^{Ni} (violet), **2**^{Ni} (pink), **3**^{Ni} (violet), **4**^{Ni} (pink) and **5**^{Ni} (pink) at RT under the optical microscope.

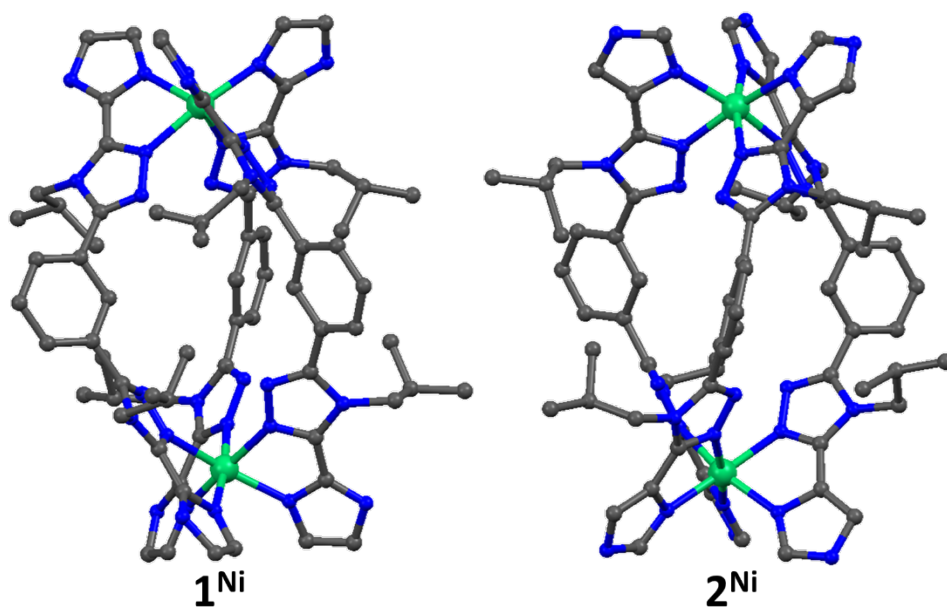


Figure S10. Crystal structure of cationic $[\text{Ni}_2(\text{L}^{2\text{NHIm-meta}})_3](\text{BF}_4)_4 \cdot \text{CH}_3\text{CN} \cdot \text{solvent}$ (**1**^{Ni}-solvents) and $[\text{Ni}_2(\text{L}^{4\text{NHIm-meta}})_3](\text{BF}_4)_4 \cdot 4\text{CH}_3\text{CN} \cdot \text{solvent}$ (**2**^{Ni}-solvents); solvent molecules, counter-anions and hydrogens are not shown for clarity.

Table S3. Crystal data and structure refinement details for the Ni(II) helicates.

	1 ^{Ni} .solvents	2 ^{Ni} .solvents
T [K]	100	100
Empirical formula	C ₇₄ H ₈₇ B ₂ F ₈ N ₃₁ Ni ₂	C ₈₀ H ₉₆ B ₄ F ₁₆ N ₃₄ Ni ₂
M _r	1701.78	1998.56
CCDC no.	2061253	2061252
Crystal system	monoclinic	orthorhombic
Space group	<i>P</i> 2 ₁ / <i>n</i>	<i>lbca</i>
a [Å]	14.3289(4)	19.9782(4)
b [Å]	22.2707(6)	29.8827(5)
c [Å]	35.2655(11)	37.7594(8)
α [°]	90	90
β [°]	96.353(3)	90
γ [°]	90	90
V [Å ³]	11184.6(6)	22542.5(8)
Z	4	8
ρ _{calcd.} [g/cm ³]	1.011	1.178
μ [mm ⁻¹]	0.918	1.093
F(000)	3544.0	8272.0
Crystal Size (mm)	0.04 × 0.02 × 0.005	0.01 × 0.009 × 0.008
2θ range for data collection	7.368 to 153.33	7.088 to 153.222
Reflections collected	54658	30243
Independent reflections	23003	11551
R(int)	0.0558	0.0230
Data / restraints / parameters	23003/9/1096	11551/0/623
Goof (F ²)	1.048	1.108
R ₁ [I>2σ(I)]	0.1241	0.0679
wR ₂ [all data]	0.3406	0.2175
Max/min res. e density [eÅ ⁻³]	1.50/-1.07	0.98/-0.64

Table S4. Bite angle and torsion angle dinuclear tris-L Fe(II) **1-5** complex.

angle within ligand N _{triazole} -Fe ^{II} -N _{azole}	(°)	Torsion angle	(°)
1·solvents			
N1-Fe1-N3	79.9(1)	N1-C3-C4-N3	-1.9(3)
N11-Fe1-N13	80.28(9)	N11-C53-C54-N13	-5.3(3)
N21-Fe1-N23	80.2(1)	N21-C51-C52-N23	-3.4(4)
N7-Fe2-N9	80.5(1)	N7-C21-C22-N9	-6.0(4)
N17-Fe2-N20	80.5(1)	N17-C45-C46-N20	-1.9(4)
N27-Fe2-N29	80.4(1)	N27-C69-C70-N29	-1.0(4)
2·solvents			
N1-Fe1-N3	80.4(1)	N1-C3-C4-N3	3.8(5)
N11-Fe1-N13	80.6(1)	N11-C27-C28-N13	4.3(5)
N21-Fe1-N23	80.4(1)	N21-C51-C52-N23	2.2(5)
N7-Fe2-N9	80.3(1)	N7-C21-C22-N9	0.6(5)
N17-Fe2-N19	80.3(1)	N17-C44-C45-N19	7.9(5)
N27-Fe2-N29	81.2(1)	N27-C71-C72-N29	3.9(5)
3·6CH₃CN·C₄H₁₀O			

N1-Fe1-N3	80.1 (1)	N1-C49-C48-N3	-4.2(4)
N11-Fe1-N13	80.3 (1)	N11-C23-C22-N13	-0.4(4)
N21-Fe1-N23	80.5 (1)	N21-C74-C75-N23	-4.4(4)
N8-Fe2-N9	80.4 (1)	N8-C31-C30-N9	-4.9(4)
N18-Fe2-N19	80.6 (1)	N18-C4-C5-N19	-3.3(4)
N28-Fe2-N29	80.3 (1)	N28-C56-C57-N29	-6.0(4)
4·solvents			
N1-Fe1-N2	80.4(2)	N1-C3-C4-N2	-1.5(7)
N9-Fe1-N10	81.0(2)	N9-C30-C31-N10	0.8(7)
N17-Fe1-N18	80.6(2)	N17-C54-C55-N18	2.2(7)
N6-Fe2-N8	80.9(2)	N6-C24-C25-N8	-1.1(8)
N14-Fe2-N16	80.9(2)	N14-C48-C49-N16	-0.4(7)
N22-Fe2-N24	80.7(2)	N22-C72-C73-N24	1.9(7)
4·5.NO₂CH₃			
N1-Fe1-N2	80.8(1)	N1-C3-C4-N2	-0.1(4)
N9-Fe1-N10	80.8(1)	N9-C27-C28-N10	-3.6(4)
N17-Fe1-N18	80.4(1)	N17-C51-C52-N18	-3.6(4)
N6-Fe2-N8	78.7(1)	N6-C21-C22-N8	-3.5(4)
N14-Fe2-N16	78.5(1)	N14-C45-C46-N16	-7.0(4)
N22-Fe2-N24	78.4(1)	N22-C69-C70-N24	-8.5(4)
4·5NO₂CH₃ (253 K)			
N1-Fe1-N2	80.2(1)	N1-C3-C4-N2	3.4(5)
N9-Fe1-N10	80.4(1)	N9-C27-C28-N10	4.3(5)
N17-Fe1-N18	80.3(1)	N17-C52-C53-N18	0.2(5)
N6-Fe2-N8	75.6(1)	N6-C21-C22-N8	8.8(6)
N14-Fe2-N16	75.6(1)	N14-C46-C47-N16	8.3(6)
N22-Fe2-N24	76.1(1)	N22-C70-C71-N24	6.1(5)
5·solvents			
N1-Fe1-N2	81.0(1)	N1-C3-C4-N2	-1.5(4)
N5-Fe1-N8	80.6(1)	N5-C21-C22-N8	-1.9(5)
N9-Fe1-N10	81.0(1)	N9-C27-C28-N10	-2.5(4)

Table S5. Remaining cis-angles between ligands N–Fe–N for the [Fe₂L₃]⁴⁺ complexes 1-5.

	(°)	Fe2	(°)
1·solvents			
N1–Fe1–N11	96.1(1)	N7–Fe2–N17	89.8(1)
N1–Fe1–N21	95.3(1)	N7–Fe2–N27	93.3(1)
N1–Fe1–N23	91.8(1)	N7–Fe2–N29	95.3(1)
N3–Fe1–N11	92.55(9)	N9–Fe2–N17	92.8(1)
N3–Fe1–N13	90.77(9)	N9–Fe2–N20	93.4(1)
N3–Fe1–N23	91.86(9)	N9–Fe2–N29	95.1(1)
N11–Fe1–N21	96.0(1)	N17–Fe2–N27	92.2(1)
N13–Fe1–N21	94.47(9)	N20–Fe2–N27	93.6(1)
N13–Fe1–N23	92.43(9)	N20–Fe2–N29	95.2(1)
2·solvents			
N1–Fe1–N11	96.1(1)	N7–Fe2–N17	91.0(1)
N1–Fe1–N13	91.7(1)	N7–Fe2–N19	93.5(1)
N1–Fe1–N21	98.3(1)	N7–Fe2–N27	91.5(1)
N3–Fe1–N13	90.4(1)	N9–Fe2–N19	96.9(1)
N3–Fe1–N21	97.0(2)	N9–Fe2–N27	93.0(1)
N3–Fe1–N23	92.9(1)	N9–Fe2–N29	97.5(1)
N11–Fe1–N21	92.5(2)	N17–Fe2–N27	90.4(1)
N13–Fe1–N23	90.4(1)	N17–Fe2–N29	91.6(1)
N11–Fe1–N23	90.8(1)	N19–Fe2–N29	94.2(1)
3·6CH₃CN·C₄H₁₀O			
N1–Fe1–N11	98.1 (1)	N8–Fe2–N18	90.7 (1)
N1–Fe1–N13	93.2 (1)	N8–Fe2–N19	95.1 (1)
N1–Fe1–N21	96.4 (1)	N8–Fe2–N28	89.1 (1)
N3–Fe1–N13	90.0 (1)	N9–Fe2–N19	94.3 (1)
N3–Fe1–N21	95.1 (1)	N9–Fe2–N28	95.4 (1)
N3–Fe1–N23	88.9 (1)	N9–Fe2–N29	95.2 (1)
N11–Fe1–N21	94.8 (1)	N18–Fe2–N28	90.3 (1)
N11–Fe1–N23	93.4 (1)	N18–Fe2–N29	94.6 (1)
N13–Fe1–N23	90.8 (1)	N19–Fe2–N29	96.3 (1)
4·solvents			
N1–Fe1–N9	95.6(2)	N6–Fe2–N14	91.5(2)
N1–Fe1–N10	91.0(2)	N6–Fe2–N16	91.9(2)
N1–Fe1–N17	97.5(2)	N6–Fe2–N22	92.2(2)
N2–Fe1–N10	92.1(2)	N8–Fe2–N16	97.6(2)
N2–Fe1–N17	91.8(2)	N8–Fe2–N22	91.9(2)
N2–Fe1–N18	90.7(2)	N8–Fe2–N24	95.3(2)
N9–Fe1–N17	95.6(2)	N14–Fe2–N22	90.1(2)
N9–Fe1–N18	93.4(2)	N14–Fe2–N24	92.4(2)
N10–Fe1–N18	91.3(2)	N16–Fe2–N24	95.8(2)
4·5.5NO₂CH₃			
N1–Fe1–N9	96.6(1)	N6–Fe2–N14	95.4(1)
N1–Fe1–N10	96.9(1)	N6–Fe2– N16	95.9(1)
N1–Fe1–N17	95.6(1)	N6–Fe2– N22	92.8(1)
N2–Fe1–N10	94.8(1)	N8–Fe2– N16	102.7(1)

N2-Fe1-N17	91.2(1)	N8-Fe2- N22	92.3(1)
N2-Fe1-N18	91.1(1)	N8-Fe2- N24	90.6(1)
N9-Fe1-N17	93.8(1)	N14-Fe2- N22	87.2(1)
N9-Fe1-N18	91.8(1)	N14-Fe2- N24	95.1(1)
N10-Fe1-N18	87.8(1)	N16-Fe2- N24	95.2(1)
4·5NO₂CH₃ (253 K)			
N1-Fe1-N9	93.9(1)	N6-Fe2-N14	87.0(1)
N1-Fe1-N17	95.9(1)	N6-Fe2- N22	93.9(1)
N1-Fe1-N18	91.2(1)	N6-Fe2- N24	91.6(1)
N2-Fe1-N9	92.1(1)	N8-Fe2- N14	95.5(1)
N2-Fe1-N10	88.3(1)	N8-Fe2- N16	96.2(1)
N2-Fe1-N18	91.7(1)	N8-Fe2- N24	91.1(1)
N9-Fe1-N17	96.1(1)	N14-Fe2- N22	96.9(1)
N10-Fe1-N17	96.2(1)	N16-Fe2- N22	97.6(1)
N10-Fe1-N18	95.1(1)	N16-Fe2- N24	106.8(1)
5·solvents			
N2-Fe1-N10	92.2(1)	–	–
N2-Fe1-N5	91.4(1)	–	–
N2-Fe1-N8	91.7(1)	–	–
N1-Fe1-N10	93.8(1)	–	–
N1-Fe1-N9	94.2(1)	–	–
N1-Fe1-N8	94.2(1)	–	–
N5-Fe1-N10	91.9(1)	–	–
N9-Fe1-N5	94.2(1)	–	–
N9-Fe1-N8	95.8(1)	–	–

Table S6. Trans-angles between ligands N-Fe-N for the [Fe₂L₃]⁴⁺ complexes **1-5**.

Fe1	(°)	Fe2	(°)
1·solvents			
N1-Fe1-N13	169.9(1)	N7-Fe2-N20	168.3(1)
N3-Fe1-N21	170.6(1)	N9-Fe2-N27	172.0(1)
N11-Fe1-N23	171.5(1)	N17-Fe2-N29	171.2(1)
2·solvents			
N1-Fe1-N23	173.0(1)	N7-Fe2-N29	172.3(1)
N3-Fe1-N11	170.3(2)	N9-Fe2-N17	170.7(1)
N13-Fe1-N21	168.4(1)	N19-Fe2-N27	169.5(1)
3·6CH₃CN·C₄H₁₀O			
N1-Fe1-N23	168.3(1)	N8-Fe2-N29	168.1(1)
N3-Fe1-N11	170.0(1)	N9-Fe2-N18	169.3(1)
N13-Fe1-N21	169.8(1)	N19-Fe2-N28	170.0(1)
4·solvents			
N1-Fe1-N18	170.9(2)	N6-Fe2-N24	171.9(2)
N2-Fe1-N9	172.1(2)	N8-Fe2-N14	172.2(2)
N10-Fe1-N17	171.1(2)	N16-Fe2-N22	170.1(2)
4·5.5NO₂CH₃			
N1-Fe1-N18	170.9(1)	N6-Fe2-N24	166.0(1)

N2–Fe1–N9	174.5(1)	N8–Fe2–N14	174.0(1)
N10–Fe1–N17	167.0(1)	N16–Fe2–N22	163.9(1)
4·5NO₂CH₃ (253 K)			
N1–Fe1–N10	167.1(1)	N6–Fe2– N16	160.1(1)
N2–Fe1– N17	171.1(1)	N8–Fe2– N22	163.3(1)
N9 –Fe1– N18	174.0(1)	N14–Fe2– N24	172.8(1)
5·solvents			
N2–Fe1–N9	171.3(1)	–	–
N1–Fe1–N5	170.5(1)	–	–
N8–Fe1–N10	171.6(1)	–	–

Table S7. Triazole-imidazole plane angle and triazole-phenyl plane angle in the dinuclear Fe(II) complexes **1-5** and [Fe₂(L^{2/4pym-meta})₃](BF₄)₄·6CH₃CN.⁸

1·solvents			
triazole-imidazole angle	(°)	triazole-phenyl ring angle	(°)
∠ N3 C4 N5 C9 N4-C3 N2 C2 C1 N1	4.10	∠ N3 C4 N5 C9 N4-C10 C15 C14 C13 C12 C11	50.93
∠ N14 C33 N15 C28 N13- C27 N12 C26 C25 N11	6.54	∠ N13 C28 N15 C33 N14- C34 C39 C38 C37 C36 C35	46.97
∠ N24 C57 N25 C52 N23-N22 C50 C49 N21 C51	3.67	∠ N23 C52 N25 C57 N24-C58 C63 C62 C61 C60 C59	40.29
∠ N7 C21 N8 C16 N6- N9 C24 C23 N10 C22	8.77	∠ N7 C21 N8 C16 N6- C12 C13 C14 C15 C10 C11	46.15
∠ N17 C45 N18 C40 N16- N20 C48 C47 N19 C46	3.59	∠ N17 C45 N18 C40 N16-C36 C37 C38 C39 C34 C35	45.52
∠ N27 C69 N28 C64 N26- N29 C71 C72 N30 C70	2.57	∠ N27 C69 N28 C64 N26- C60 C61 C62 C63 C58 C59	42.92
Average	4.87		45.46
2·solvents			
triazole-imidazole angle	(°)	triazole-phenyl ring angle	(°)
∠ C4 N3 N5 C9 N4- N1 C3 C2 N2 C1	5.20	∠ N3 C4 N5 C9 N4- C10 C15 C14 C13 C12 C11	46.71
∠ N14 C33 N15 C28 N13- N11 C25 N12 C26 C27	4.62	∠ N13 C28 N15 C33 N14- C34 C35 C36 C37 C38 C39	50.96
∠ N23 C52 N25 C57 N24- N21 C51 C50 N22 C49	3.41	∠ N23 C52 N25 C57 N24- C58 C59 C60 C61 C62 C63	39.91
∠ N7 C21 N8 C16 N6- N9 C22 C23 N10 C24	1.23	∠ N7 C21 N8 C16 N6- C12 C13 C14 C15 C10 C11	50.42
∠ N17 C45 N18 C40 N16- N19 C46 C47 N20 C48	7.62	∠ N17 C45 N18 C40 N16- C38 C37 C36 C35 C34 C39	46.89
∠ N27 C71 N28 C64 N26- N29 C72 C73 N30 C74	3.11	∠ N27 C71 N28 C64 N26- C62 C61 C60 C59 C58 C63	44.69
Average	4.20		46.59

3·6CH₃CN·C₄H₁₀O			
triazole-imidazole angle	(°)	triazole-phenyl ring angle	(°)
└ N3 C48 N5 C43 N4- N1 C52 N2 C50 C49	6.99	└ N3 C48 N5 C43 N4-C42 C41 C40 C39 C37 C38	52.33
└ N23 C74 N25 C69 N24-N21 C78 N22 C76 C75	5.39	└ N23 C74 N25 C69 N24-C67 C66 C65 C63 C64 C68	43.93
└ C22 N13 N15 C17 N14- N11 C26 N12 C24 C23	1.31	└ N13 C22 N15 C17 N14-C15 C16 C12 C11 C13 C14	50.68
└ N8 C31 N7 C36 N6- N9 C27 N10 C29 C30	5.52	└ N8 C31 N7 C36 N6- C37 C39 C40 C41 C42 C38	45.25
└ N28 C57 N27 C62 N26- N29 C53 N30 C55 C56	9.67	└ N28 C57 N27 C62 N26- C63 C65 C66 C67 C68 C64	52.68
└ N18 C5 N17 C10 N16- N19 C1 N20 C3 C4	4.53	└ N18 C5 N17 C10 N16- C11 C13 C14 C15 C16 C12	44.20
Average	5.77		48.17
4-solvents			
triazole-imidazole angle	(°)	triazole-phenyl ring angle	(°)
└ N2 C4 N4 C9 N3- N1 C1 O1 C2 C3	1.27	└ N2 C4 N4 C9 N3- C10 C11 C12 C13 C14 C15	52.22
└ N10 C31 N12 C36 N11- N9 C28 O3 C29 C30	4.11	└ N10 C31 N12 C36 N11- C37 C38 C39 C40 C41 C42	37.82
└ C55 N18 N20 C60 N19- N17 C52 O5 C53 C54	2.96	└ N18 C55 N20 C60 N19- C61 C62 C63 C64 C65 C66	47.52
└ N6 C24 N7 C16 N5- N8 C27 O2 C26 C25	3.14	└ N6 C24 N7 C16 N5- C14 C13 C12 C11 C10 C15	43.22
└ N14 C48 N15 C43 N13- N16 C51 O4 C50 C49	2.06	└ N14 C48 N15 C43 N13- C41 C40 C39 C38 C37 C42	50.72
└ N22 C72 N23 C67 N21- N24 C74 O6 C75 C73	3.48	└ N22 C72 N23 C67 N21- C65 C64 C63 C62 C61 C66	48.52
Average	2.84		46.67
5-solvents			
triazole-imidazole angle	(°)	triazole-phenyl ring angle	(°)
└ N1 C1 S1 C2 C3- N2 C4 N4 C9 N3	2.71	└ N2 C4 N4 C9 N3- C10 C11 C12 C13 C14 C15	43.71
└ N8 C24 S2 C23 C22- N5 C21 N7 C16 N6	4.50	└ N5 C21 N7 C16 N6- C14 C13 C12 C11 C10 C15	46.96
└ N9 C25 S3 C26 C27- N10 C28 N12 C33 N11	5.27	└ N10 C28 N12 C33 N11- C34 C35 C36 C35 C34 C37	45.54
Average	4.16		45.40
[Fe ₂ (L ^{2pym-meta}) ₃](BF ₄) ₄ ·6CH ₃ CN ⁸		[Fe ₂ (L ^{4pym-meta}) ₃](BF ₄) ₄ ·6CH ₃ CN ⁸	
triazole-phenyl ring angle		triazole-phenyl ring angle	
N3 C5 N5 C6 N4- C7 C9 C10 C9 C7 C8	50.22	N3 C5 N5 C10 N4- C11 C12 C13 C12 C11 C14	51.33

Table S8. The θ angle between centroid of triazole-phenylene-triazole ring of **1-5** and $[\text{Fe}_2(\text{L}^{2\text{pym-meta}})_3](\text{BF}_4)_4 \cdot 6\text{CH}_3\text{CN}$ and $[\text{Fe}_2(\text{L}^{4\text{pym-meta}})_3](\text{BF}_4)_4 \cdot 6\text{CH}_3\text{CN}$.

Triazole–phenyl –triazole angle	(°)
1-solvents	
└ N7 C21 N8 C16 N6-C12 C13 C14 C15 C10 C11- N3 C4 N5 C9 N4	116.71
└ C69 N27 N28 C64 N26- C60 C61 C62 C63 C58 C59- N23 C52 N25 C57 N24	117.21
└ C45 N17 N18 C40 N16- C36 C37 C38 C39 C34 C35- C33 N15 C28 N13 N14	117.36
2-solvents	
└ N24 C57 N25 C52 N23- C58 C59 C60 C61 C62 C63- N27 C71 N28 C64 N26	118.21
└ C9 N4 N5 C4 N3- C10 C15 C14 C13 C12 C11- N7 C21 N8 C16 N6	117.85
└ N14 C33 N15 C28 N13- C34 C35 C36 C37 C38 C39- N17 C45 N18 C40 N16	118.36
3·6CH₃CN·C₄H₁₀O	
└ N8 C31 N7 C36 N6- C37 C39 C40 C41 C42 C38- N4 C43 N5 C48 N3	119.47
└ N18 C5 N17 C10 N16-C11 C13 C14 C15 C16 C12-N14 C17 N15 C22 N13	118.80
└ N28 C57 N27 C62 N26- C63 C65 C66 C67 C68 C64- N24 C69 N25 C74 N23	119.45
4-solvents	
└ N2 C4 N4 C9 N3- C10 C11 C12 C13 C14 C15- N5 C16 N7 C24 N6	116.21
└ N10 C31 N12 C36 N11- C37 C38 C39 C40 C41 C42- N13 C43 N15 C48 N14	116.93
└ N19 C60 N20 C55 N18- C61 C62 C63 C64 C65 C66- N21 C67 N23 C72 N22	117.17
5-solvents	
└ N2 C4 N4 C9 N3- C10 C11 C12 C13 C14 C15- N6 C16 N7 C21 N5	116.75
└ C21 N5 N7 C16 N6- C14 C13 C12 C11 C10 C15- N3 C9 N4 C4 N2	116.75
└ N10 C28 N12 C33 N11- C34 C35 C36 C35 C34 C37- N11 C33 N12 C28 N10	116.95
$[\text{Fe}_2(\text{L}^{2\text{pym-meta}})_3](\text{BF}_4)_4 \cdot 6\text{CH}_3\text{CN}^{\text{8}}$	
N3 C5 N5 C6 N4- C7 C9 C10 C9 C7 C8- N4 C6 N5 C5 N3	117.88
$[\text{Fe}_2(\text{L}^{4\text{pym-meta}})_3](\text{BF}_4)_4 \cdot 6\text{CH}_3\text{CN}^{\text{8}}$	
N3 C5 N5 C10 N4- C11 C12 C13 C12 C11 C14- N4 C10 N5 C5 N3	120.02

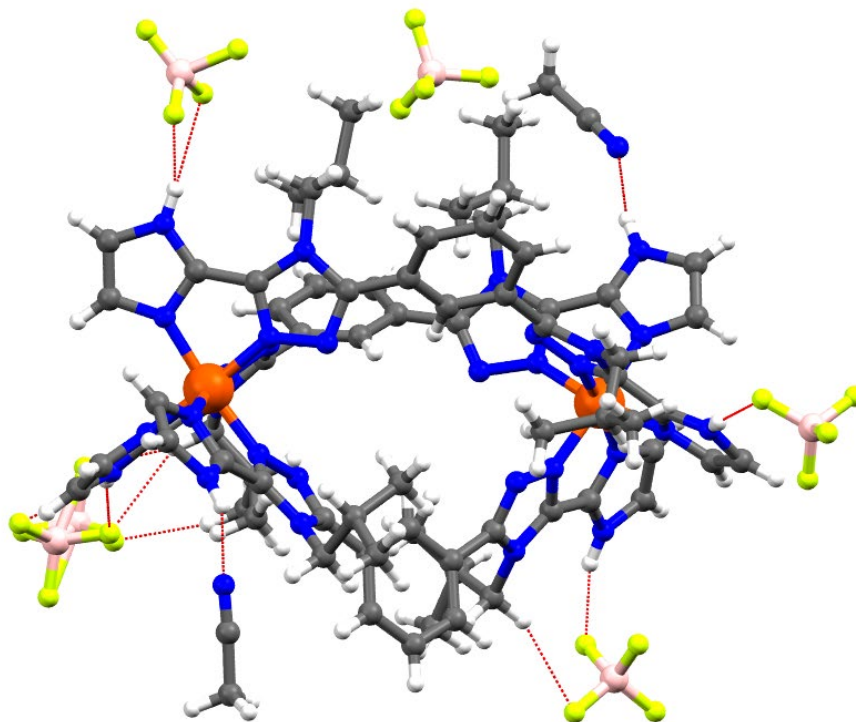


Figure S11. Intermolecular classical/non-classical hydrogen bonding through interaction of H's of acetonitrile and F's of BF_4^- anion with H's of azole rings in **1**-solvents.

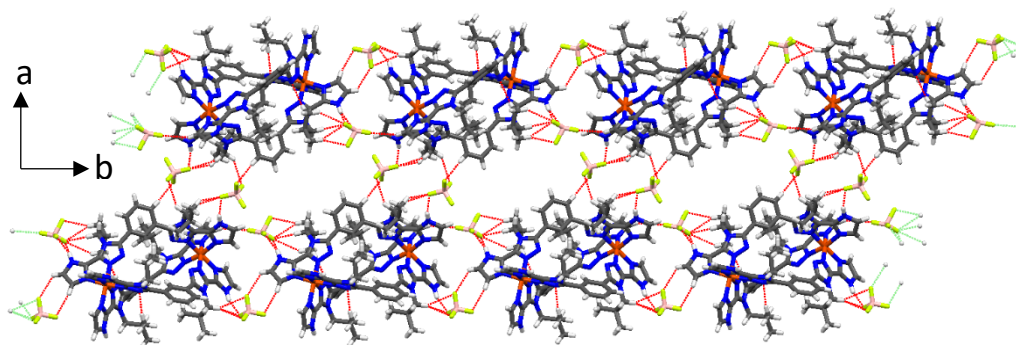


Figure S12. $-\text{NH}$ of 2-Imidazole interacting with $-\text{F}$ of BF_4^- counter-anions through hydrogen bonding in **1**-solvents; $\text{N19-H19}\cdots\text{F24}$, $\text{N30-H30}\cdots\text{F14}$, $\text{N12-H12}\cdots\text{F31}$ and $\text{N12-H12}\cdots\text{F32}$ to form 1D-chain.

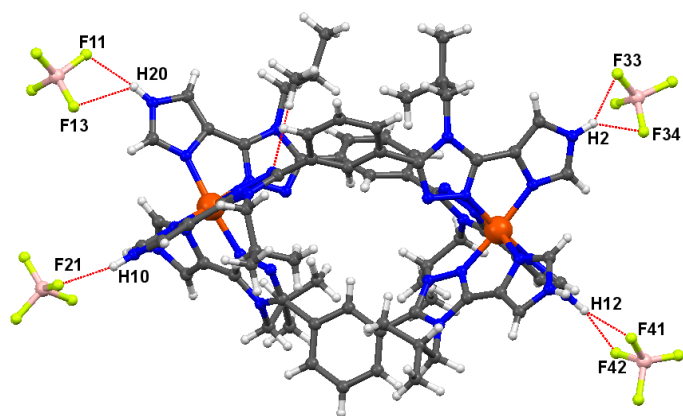


Figure S13. Intramolecular non-classical hydrogen bonding through interaction of F's of BF_4^- anion with H's of azole rings in **2**-solvents.

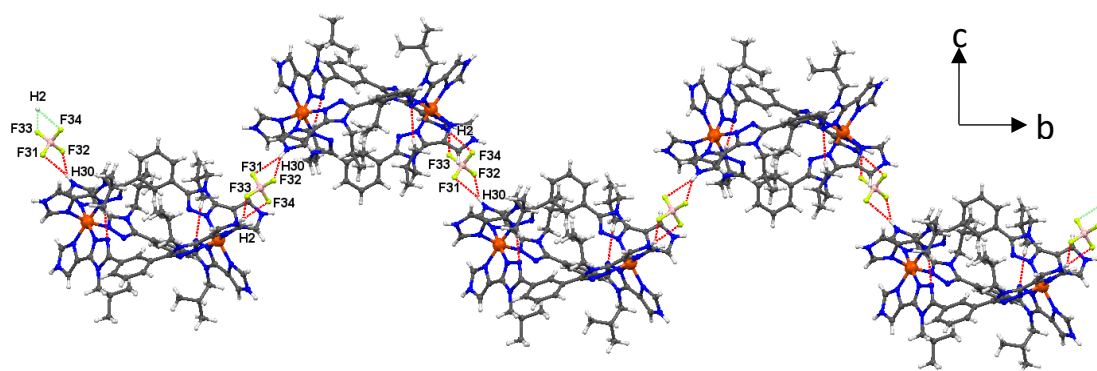


Figure S14. F's of BF_4^- counter-anion interacting with $-\text{NH}'\text{s}$ of 4-imidazole to form helical chain extended along b-axis in **2**-solvents; $\text{N30}-\text{H30}\cdots\text{F32}$, $\text{N30}-\text{H30}\cdots\text{F31}$, $\text{N2}-\text{H2}\cdots\text{F33}$ and $\text{N2}-\text{H2}\cdots\text{F34}$.

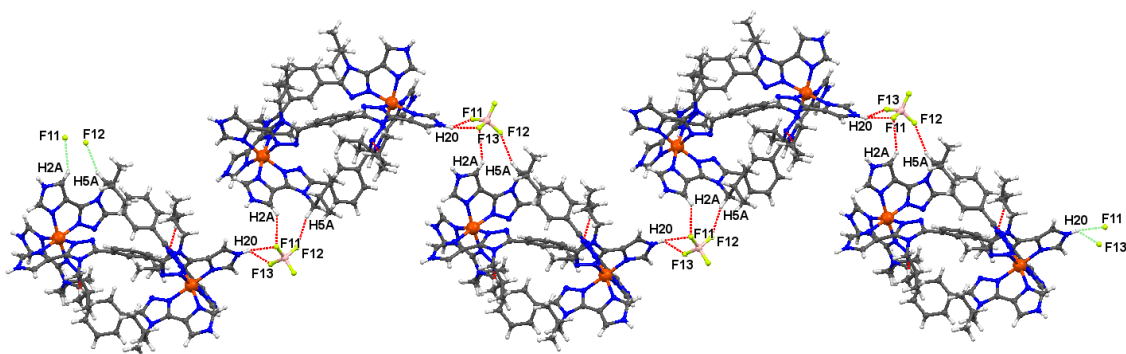


Figure S15. F's of BF_4^- counter-anion interacting with $-\text{NH}'\text{s}$ of 4-imidazole to form helical chain extended along b-axis in **2**-solvents; $\text{N20}-\text{H20}\cdots\text{F11}$, $\text{N20}-\text{H20}\cdots\text{F13}$, $\text{C2}-\text{H2A}\cdots\text{F13}$ and $\text{C5}-\text{H5A}\cdots\text{F12}$.

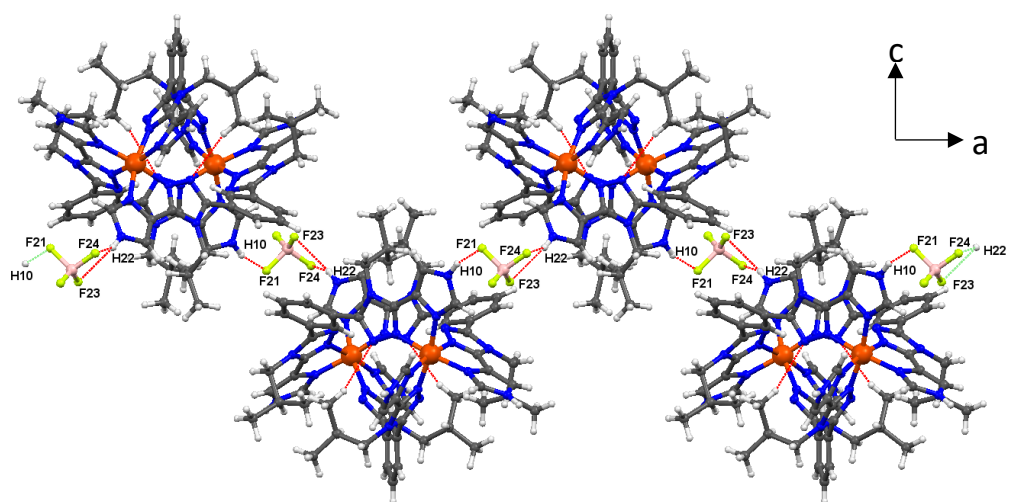


Figure S16. F's of BF_4^- counter-anion interacting with $-\text{NH}'\text{s}$ of 4-imidazole to form helical chain extended along a-axis in **2**-solvents; $\text{N10-H10}\cdots\text{F21}$, $\text{N22-H22}\cdots\text{F23}$ and $\text{N22-H22}\cdots\text{F24}$.

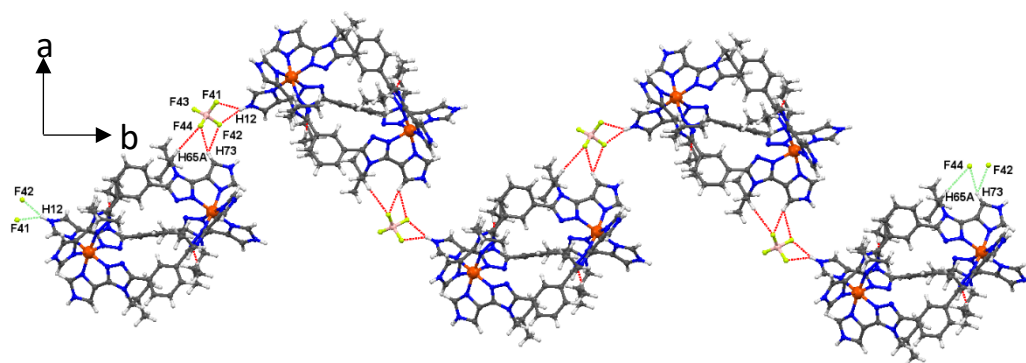


Figure S17. F's of BF_4^- counter-anion interacting with $-\text{NH}'\text{s}$ of 4-imidazole to form helical chain extended along b-axis in **2**-solvents; $\text{N12-H12}\cdots\text{F42}$, $\text{N12-H12}\cdots\text{F41}$, $\text{C73-H73}\cdots\text{F42}$, $\text{C73-H73}\cdots\text{F44}$ and $\text{C65-H65A}\cdots\text{F44}$.

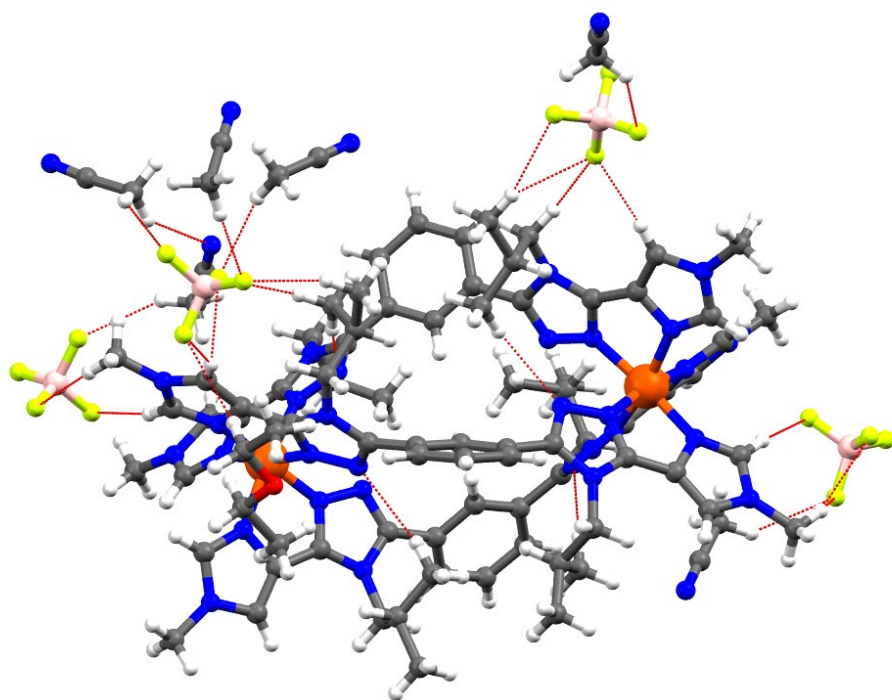


Figure S18. Intramolecular classical/non-classical hydrogen bonding through interaction of H's of six acetonitrile, H's of diethyl ether and H's of azole rings with F's of four BF_4^- anion in $\mathbf{3} \cdot 6\text{CH}_3\text{CN} \cdot \text{C}_4\text{H}_{10}\text{O}$.

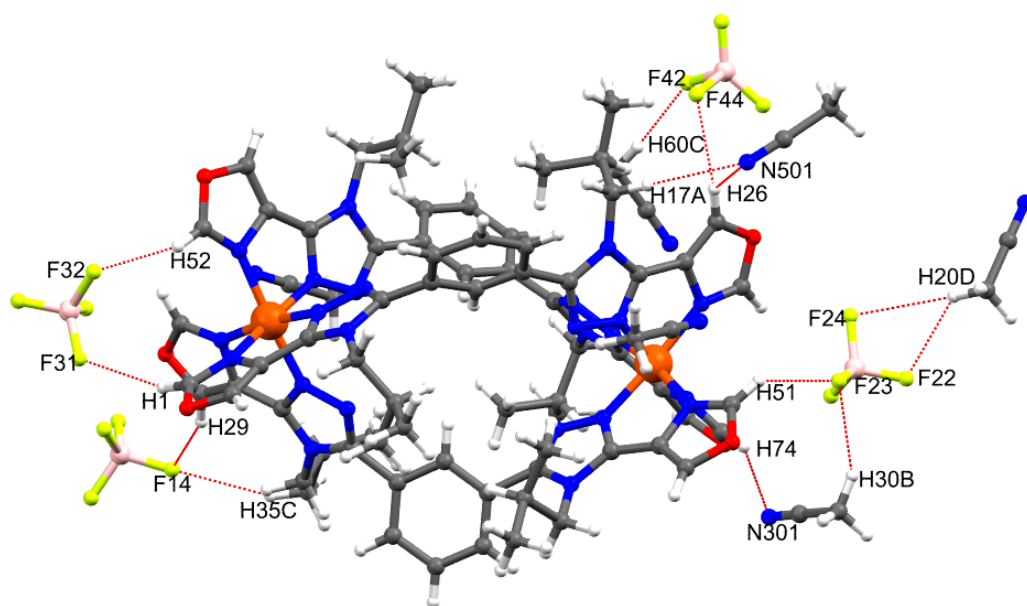


Figure S19. Intermolecular classical/non-classical hydrogen bonding through interaction of H's of four acetonitrile and F's of four BF_4^- anion with H's of azole rings in $\mathbf{4} \cdot \text{solvents}$.

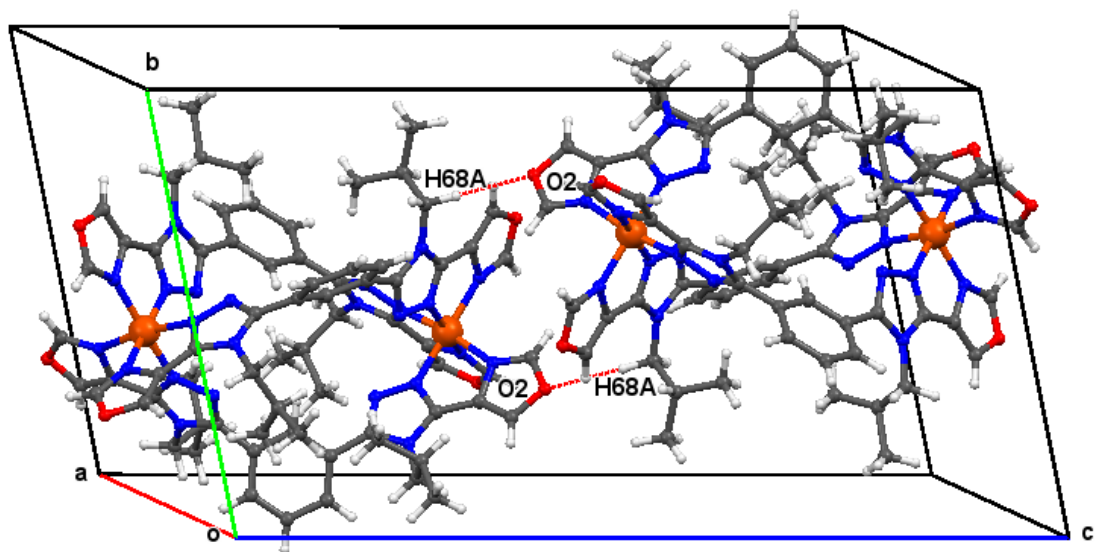


Figure S20. Two inverted dimeric units reside in a unit cell via CH...O intermolecular hydrogen bond in **4**-solvents.

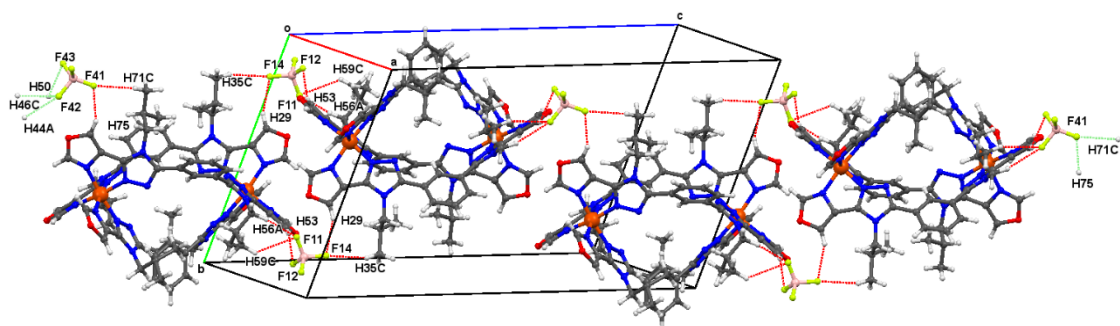


Figure S21. F's of BF_4^- counter-anion interacting with $-\text{CH}'$ s of 4-oxazol to form 1D chain extended along c-axis in **4**-solvents; two inverted dimers are connected through one BF_4^- : C29–H29...F14, C35–H35C...F14, C53–H53...F12, C59–H59C...F11 and C56–H56A...F11 and connected through other BF_4^- : C71–H71C...F41, C75–H75...F41, C44–H44A...F42, C46–H46C...F42, C50–H50...F42 and C50–H50...F43.

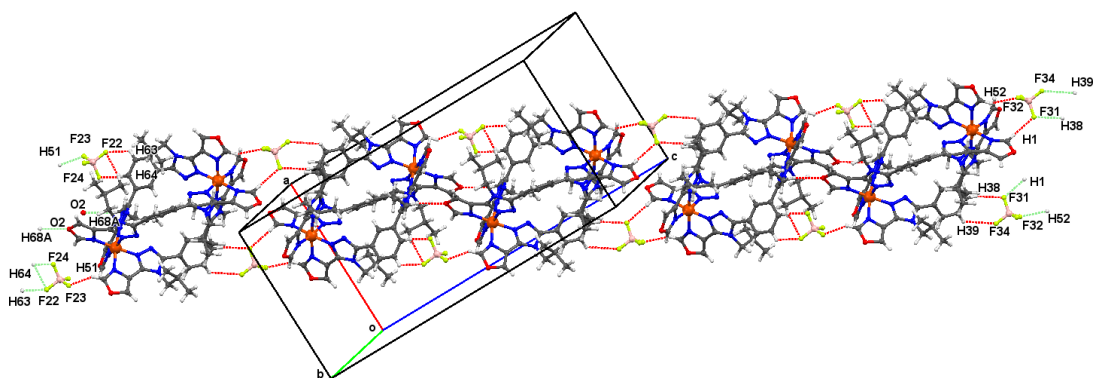


Figure S22. F's of BF_4^- counter-anion interacting with $-\text{CH}'\text{s}$ of 4-oxazol/phenylene to form 1D chain extended along ac-plane in **4**-solvents; dimers are connected through one different BF_4^- : C63–H63 \cdots F22, C64–H64 \cdots F22, C64–H64 \cdots F24, C68–H68C \cdots O2, C51–H51 \cdots F23 and, connected through other BF_4^- : C1–H1 \cdots F31, C52–H52 \cdots F32, C38–H38 \cdots F31 and C39–H39 \cdots F34.

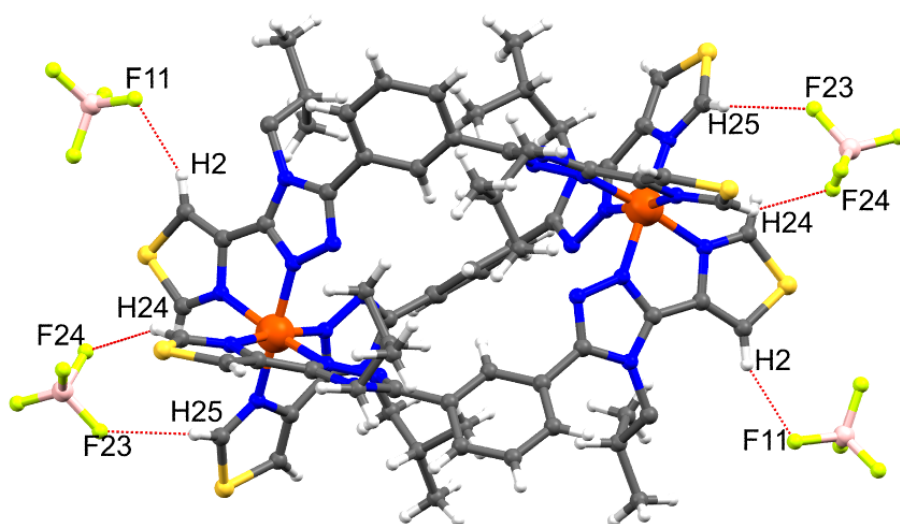


Figure S23. Intramolecular non-classical hydrogen bonding through the interaction of H's of imidazole rings and F's of four BF_4^- anion in **5**-solvents.

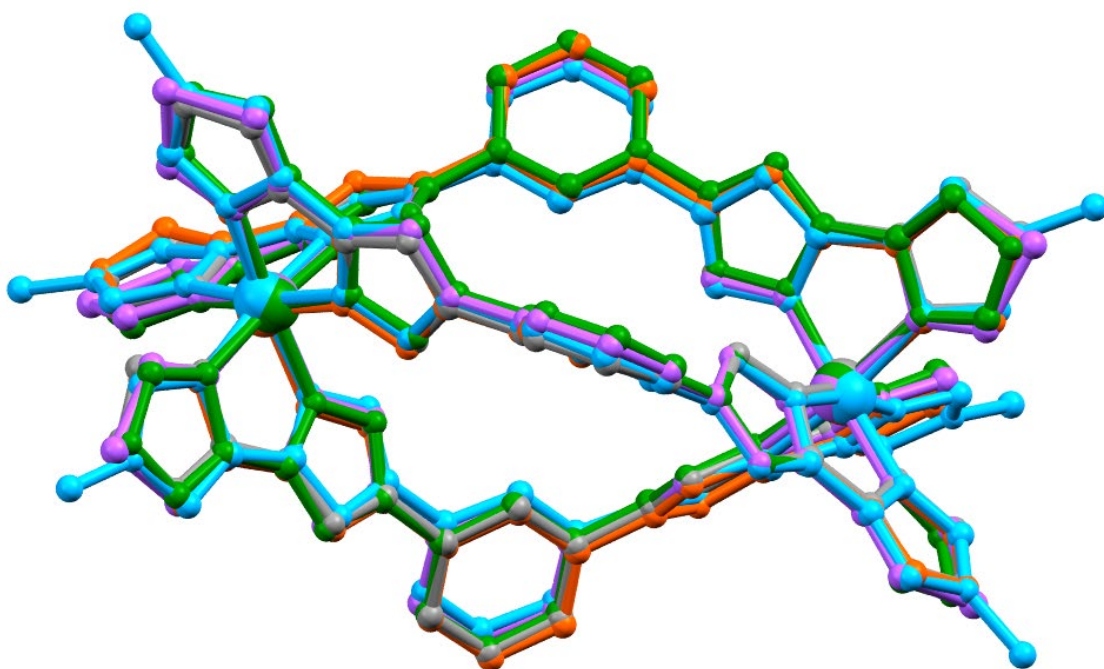


Figure S24. Overlaid structure of **1**-solvents (grey), **2**-solvents (orange), **3**-6CH₃CN·C₄H₁₀O (blue), **4**-solvents (green) and **5**-solvents (purple); emphasising all structures are similar (iso-butyl group, hydrogens and anions are removed for clarity).

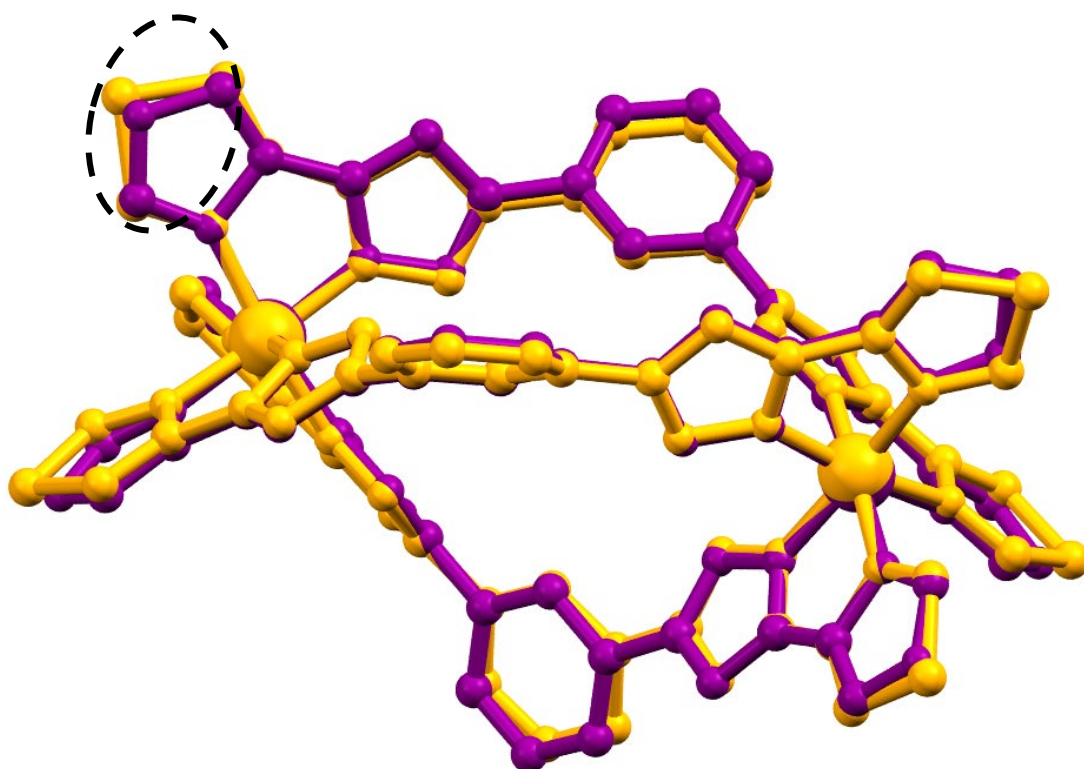


Figure S25. Overlaid structure of **2**-solvents (purple) and **5**-solvents at 100 K (orange); emphasising comparison of C–S and C–N bond length (black dashes circle) (iso-butyl group, hydrogens and anions are removed for clarity).

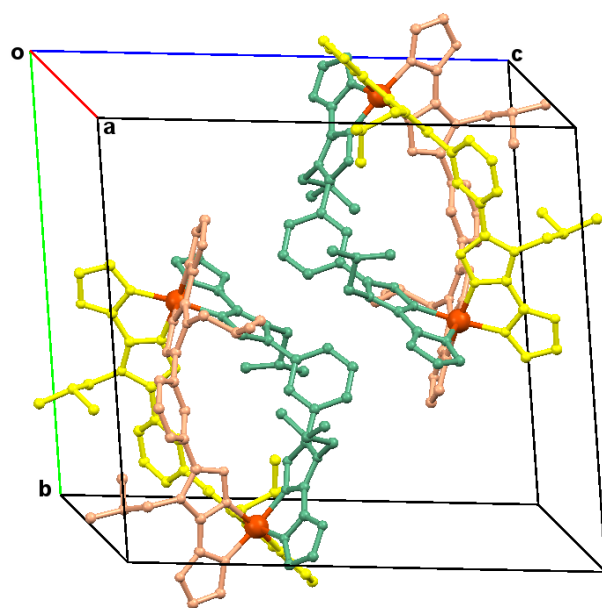


Figure S26. $[\text{Fe}_2(\text{L}^{2\text{NHIm-meta}})_3](\text{BF}_4)_4$, homochiral Δ, Λ in a crystal packing.

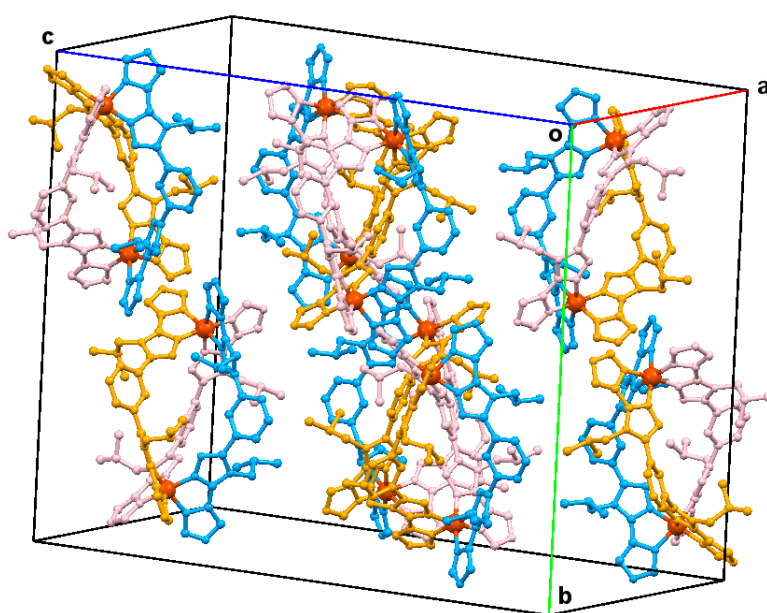


Figure S27. $[\text{Fe}_2(\text{L}^{4\text{NHIm-meta}})_3](\text{BF}_4)_4$, homochiral $\Delta\Delta\Delta, \Lambda\Lambda\Lambda$ in a crystal packing.

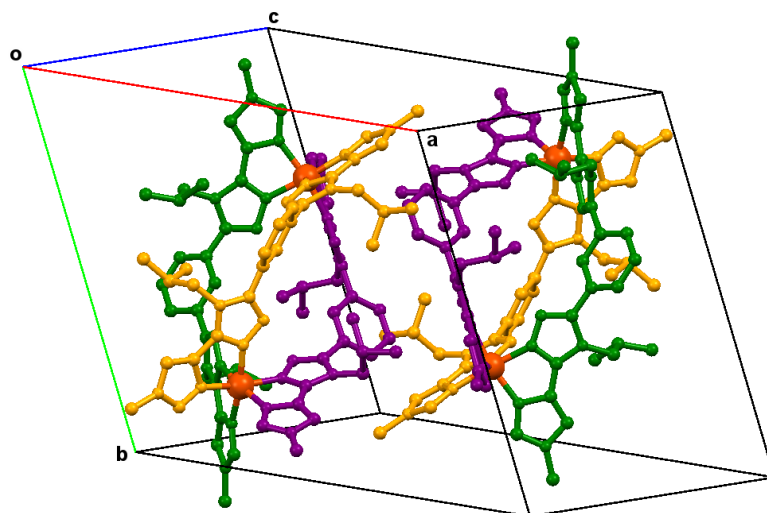


Figure S28. Unit cell packing of $[\text{Fe}_2(\text{L}^{4\text{NMelm-meta}})_3](\text{BF}_4)_4 \cdot 6\text{CH}_3\text{CN} \cdot \text{C}_2\text{H}_5\text{O}$, homochiral Δ, Λ in a crystal packing.

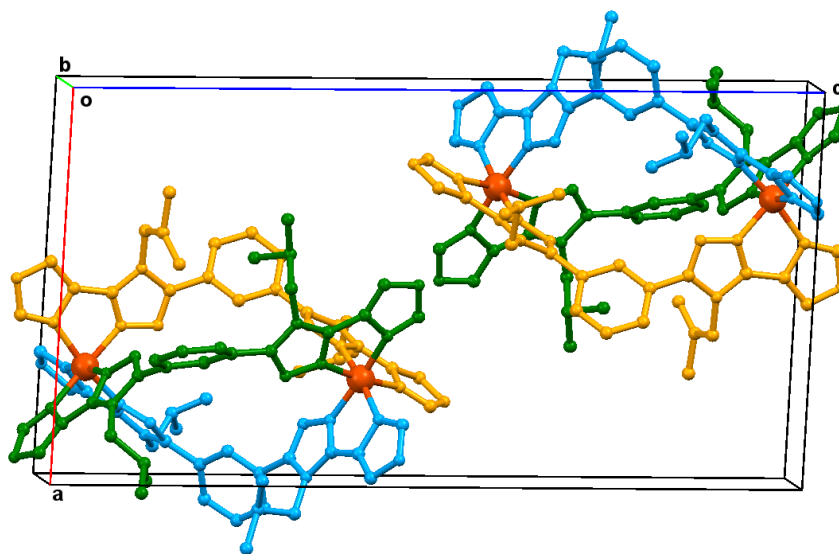


Figure S29. $[\text{Fe}_2(\text{L}^{4\text{OIm-meta}})_3](\text{BF}_4)_4$, homochiral Δ, Λ in a crystal packing.

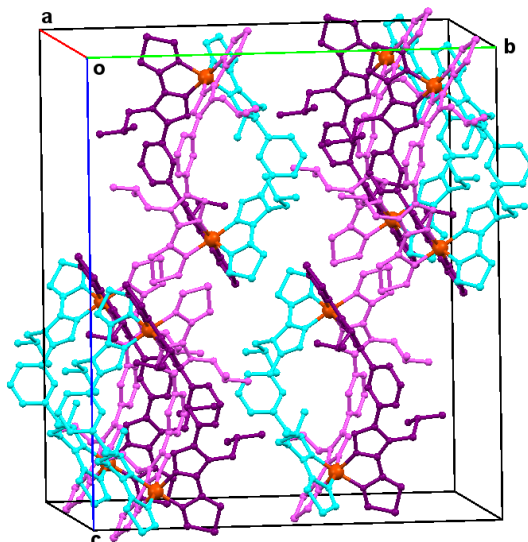


Figure S30. $[\text{Fe}_2\text{L}^{4\text{SIm-meta}}]_3(\text{BF}_4)_4$, homochiral $\Delta\Delta\Delta$, $\Lambda\Lambda\Lambda$ in a crystal packing.

VT- ^1H NMR Evans method

For the solution Evans method VT-NMR spectra, **1**·4H₂O (5.6 mM), **2**·6H₂O (6.2 mM), **3**·5H₂O (5.4 mM), **4**·6H₂O (6.1 mM) and **5**·2.5H₂O (6.0 mM) in CD₃CN solution were used. The obtained data on **1-5** helicates from variable temperature Evans NMR method were modelled with the regular solution model Equation S1 (below). The R² for all fits was 0.99 (for all solvents studied; see below Table, Figure S31-Figure S35 below). The range of ΔH (10-20 kJ·mol⁻¹) and ΔS (34-79 J·mol⁻¹·K⁻¹) values obtained from the fit (below Table) fall in the expected literature ranges for solution studies of SCO-active iron(II) complexes ($\Delta H = 4-41$ kJ·mol⁻¹ and $\Delta S = 22-146$ J·mol⁻¹·K⁻¹).³⁷⁻³⁹ The modelling to equation S1 was carried out in OriginPro 2018 from OriginLab Corporation; Excel was also employed, to determine 95% confidence intervals and help assign appropriate errors to the parameters obtained from the fit (Figure S31-Figure S35). Note that the expected error in temperature in a VT-NMR instrument is ± 1 K, and error associated with the Evans method determination of $\chi_m T(T)$ is 5-10%, so significant errors are expected in the derived parameters³⁷.

$$\chi_m T(T) = \frac{\chi_m T(\text{max})}{1 + e^{\left(\frac{\Delta H}{RT} - \frac{\Delta S}{R}\right)}} \quad (\text{Equation S1})$$

Where:

$\chi_m T(T)$ is the molar magnetic susceptibility at temperature T.

$\chi_m T_{(\max)}$ was, in all fits, set to $3.7 \text{ cm}^3 \text{ mol}^{-1} \text{ K}^{-1}$

R is the ideal gas constant ($8.314472 \text{ J mol}^{-1} \text{ K}^{-1}$).

The parameters obtained from the fit include: ΔH and ΔS , the thermodynamic enthalpy and entropy values associated with the SCO event.

$T_{1/2}$, the SCO transition temperature = $\Delta H / \Delta S$.

	$T_{1/2}$ (K)	ΔH (kJ K mol ⁻¹)	ΔS (J mol ⁻¹)	R ²
[Fe ₂ (L ^{2NHIm-meta}) ₃](BF ₄) ₄ ·4H ₂ O (1·4H ₂ O)	331 ± 17	17.558	53.0	0.99
[Fe ₂ (L ^{4NHIm-meta}) ₃](BF ₄) ₄ ·6H ₂ O (2·6H ₂ O)	267 ± 13	10.258	38.3	0.99
[Fe ₂ (L ^{4NMelm-meta}) ₃](BF ₄) ₄ ·5H ₂ O (3·5H ₂ O)	247 ± 12	17.881	72.4	0.99
[Fe ₂ (L ^{4OIm-meta}) ₃](BF ₄) ₄ ·5H ₂ O (4·6H ₂ O)	249 ± 12	19.682	79.0	0.99
[Fe ₂ (L ^{4SIm-meta}) ₃](BF ₄) ₄ ·2.5H ₂ O (5·2.5H ₂ O)	471 ± 23	23.537	50.0	0.92

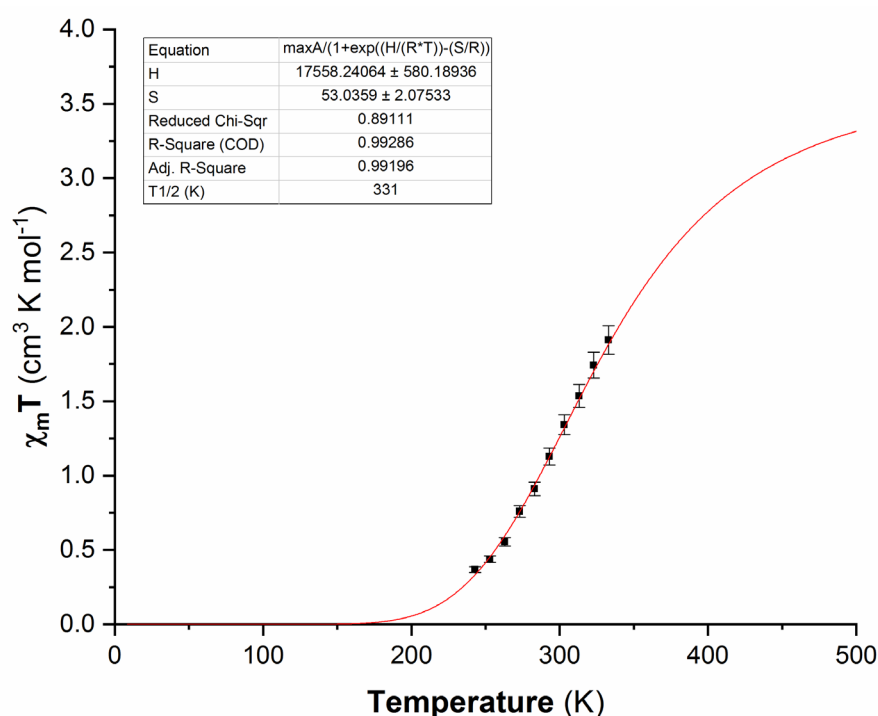


Figure S31. Plot of $\chi_m T$ vs T for 5.6 mM of [Fe₂(L^{2NHIm-meta})₃](BF₄)₄ (1·4H₂O) in CD₃CN solution from Evans method NMR studies (500 MHz); this graph displays the experimental data points (black squares) with error bar of 5%.

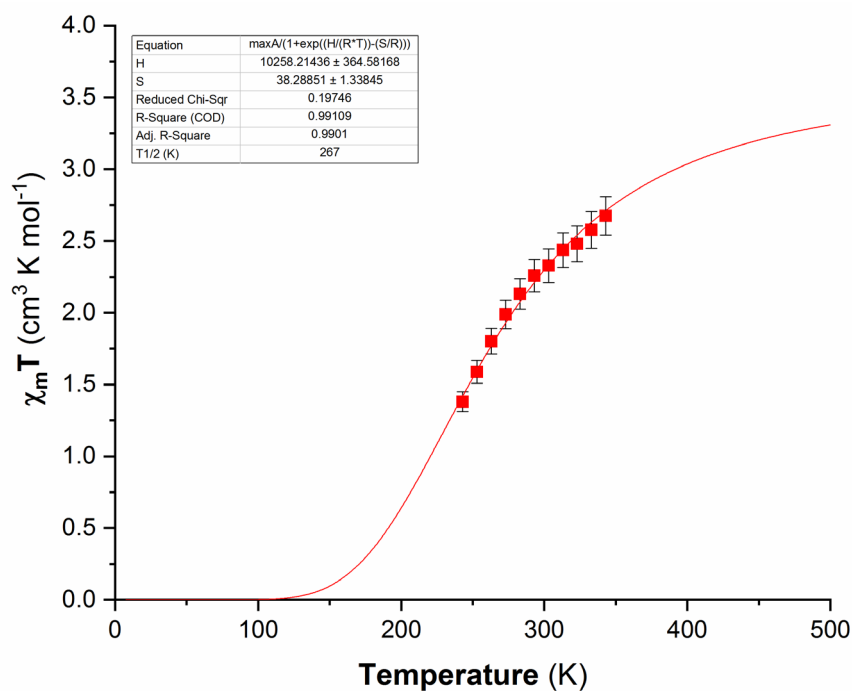


Figure S32. Plot of $\chi_m T$ vs T for 6.2 mM of $[\text{Fe}_2(\text{L}^{4\text{NHIm-meta}})_3](\text{BF}_4)_4 (2 \cdot 6\text{H}_2\text{O})$ in CD_3CN solution from Evans method NMR studies (500 MHz); this graph displays the experimental data points (red squares) with error bar of 5%.

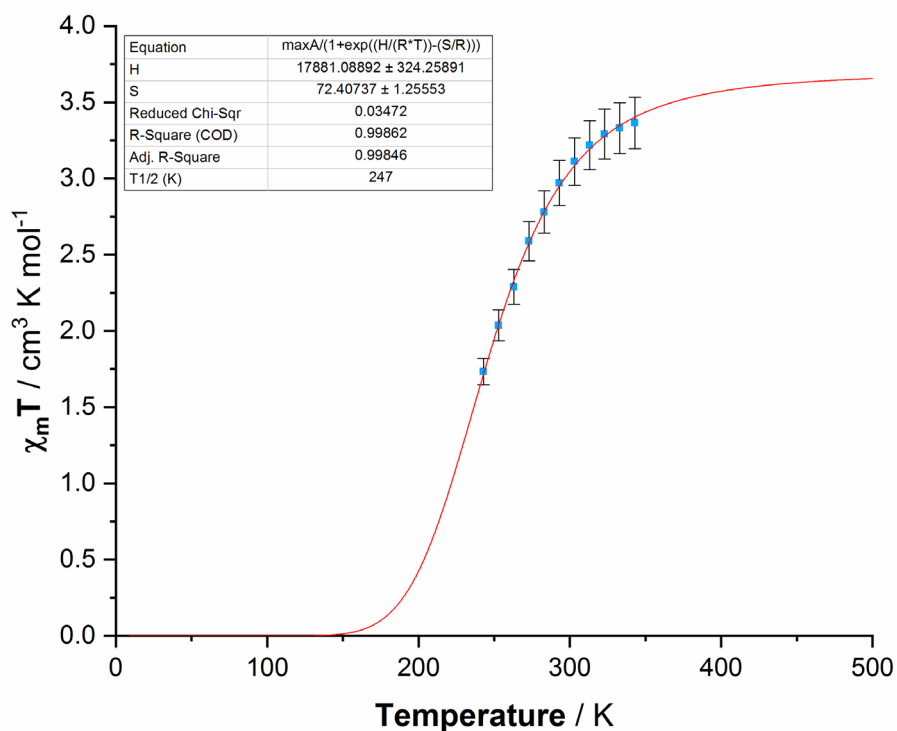


Figure S33. Plot of $\chi_m T$ vs T for 5.4 mM of $[\text{Fe}_2(\text{L}^{4\text{NMeIm-meta}})_3](\text{BF}_4)_4 (3 \cdot 5\text{H}_2\text{O})$ in CD_3CN solution from Evans method NMR studies (500 MHz); this graph displays the experimental data points (blue squares) with error bar of 5%.

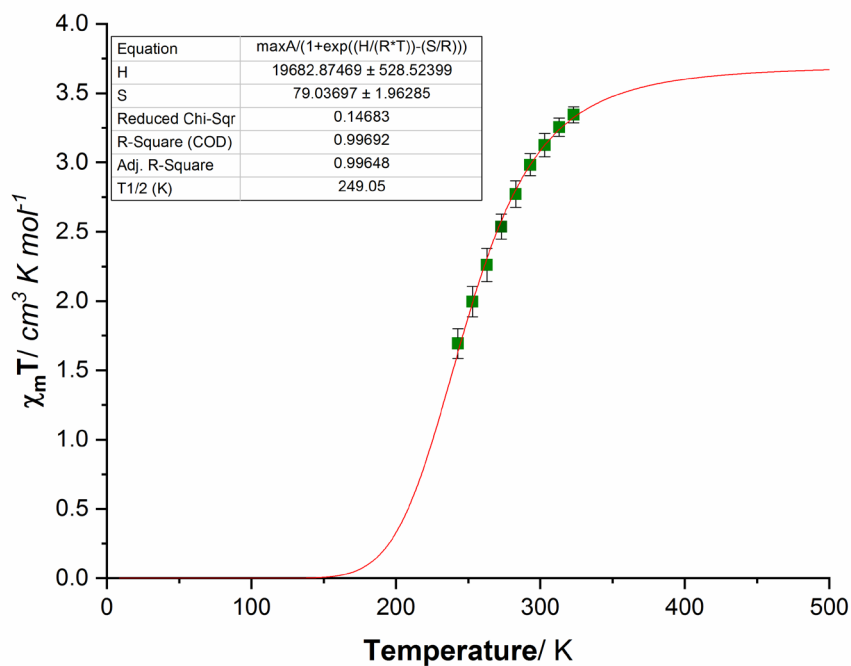


Figure S34. Plot of $\chi_m T$ vs T for 6.1 mM of $[\text{Fe}_2(\text{L}^{40\text{Im-meta}})_3](\text{BF}_4)_4 (4 \cdot 6\text{H}_2\text{O})$ in CD_3CN solution from Evans method NMR studies (500 MHz); this graph displays the experimental data points (green squares) with error bar of 5%.

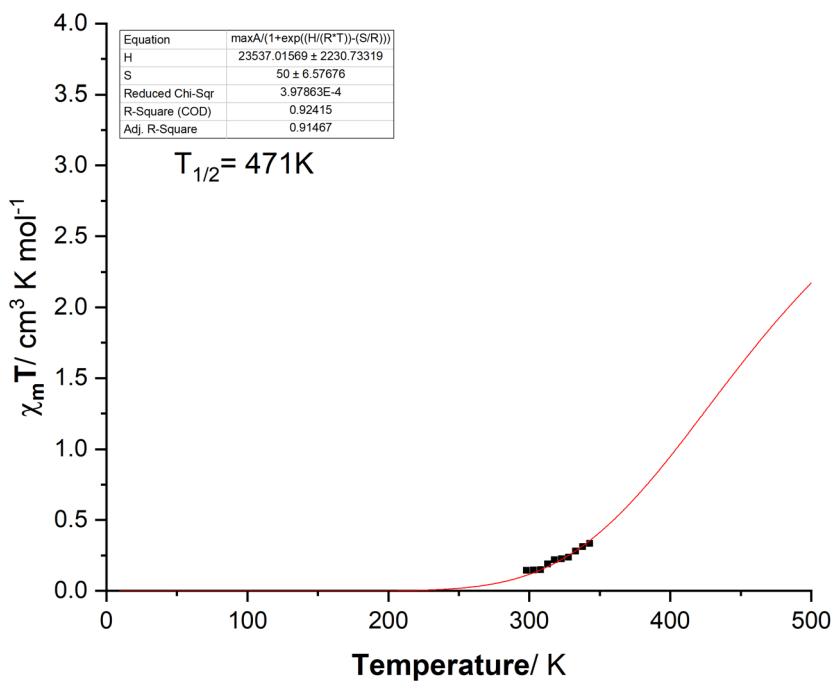


Figure S35a. Plot of $\chi_m T$ vs T for 6.0 mM of $[\text{Fe}_2(\text{L}^{45\text{Im-meta}})_3](\text{BF}_4)_4 (5 \cdot 2.5\text{H}_2\text{O})$ in CD_3CN solution from Evans method NMR studies (500 MHz).

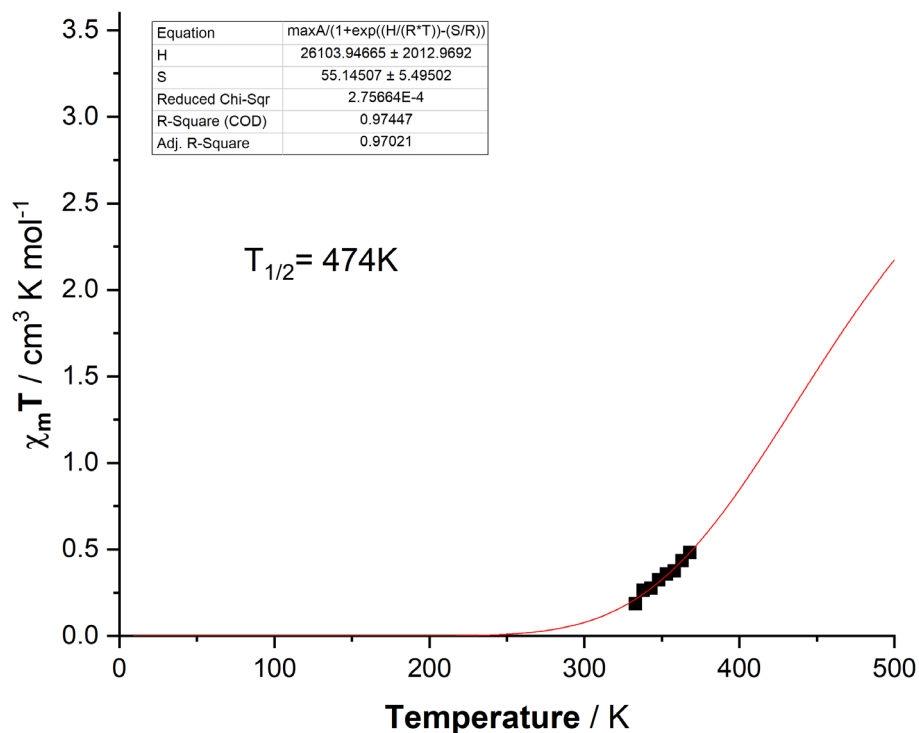


Figure S36b. Plot of $\chi_m T$ vs T for 6.0 mM of $[\text{Fe}_2(\text{L}^{4\text{SIm-meta}})_3](\text{BF}_4)_4 (5 \cdot 2.5\text{H}_2\text{O})$ in CD_3NO_2 solution from Evans method NMR studies (500 MHz).

Table S9a. Comparison of $\chi_m T$ (per Fe^{II} ion) vs T for $5 \cdot 2.5\text{H}_2\text{O}$ in CD_3CN and CD_3NO_2 solvent; calculated from ^1H NMR data by the Evans method at various temperatures.

Temperature/K	CD_3CN	CD_3NO_2
298	0.14384	-
303	0.14626	-
308	0.14867	-
313	0.18812	-
318	0.21736	-
323	0.22464	-
328	0.23626	-
333	0.27956	0.18516
338	0.31051	0.26293
343	0.33254	0.27638
348	-	0.32405
353	-	0.35627
358	-	0.37479
363	-	0.43463
368	-	0.48214

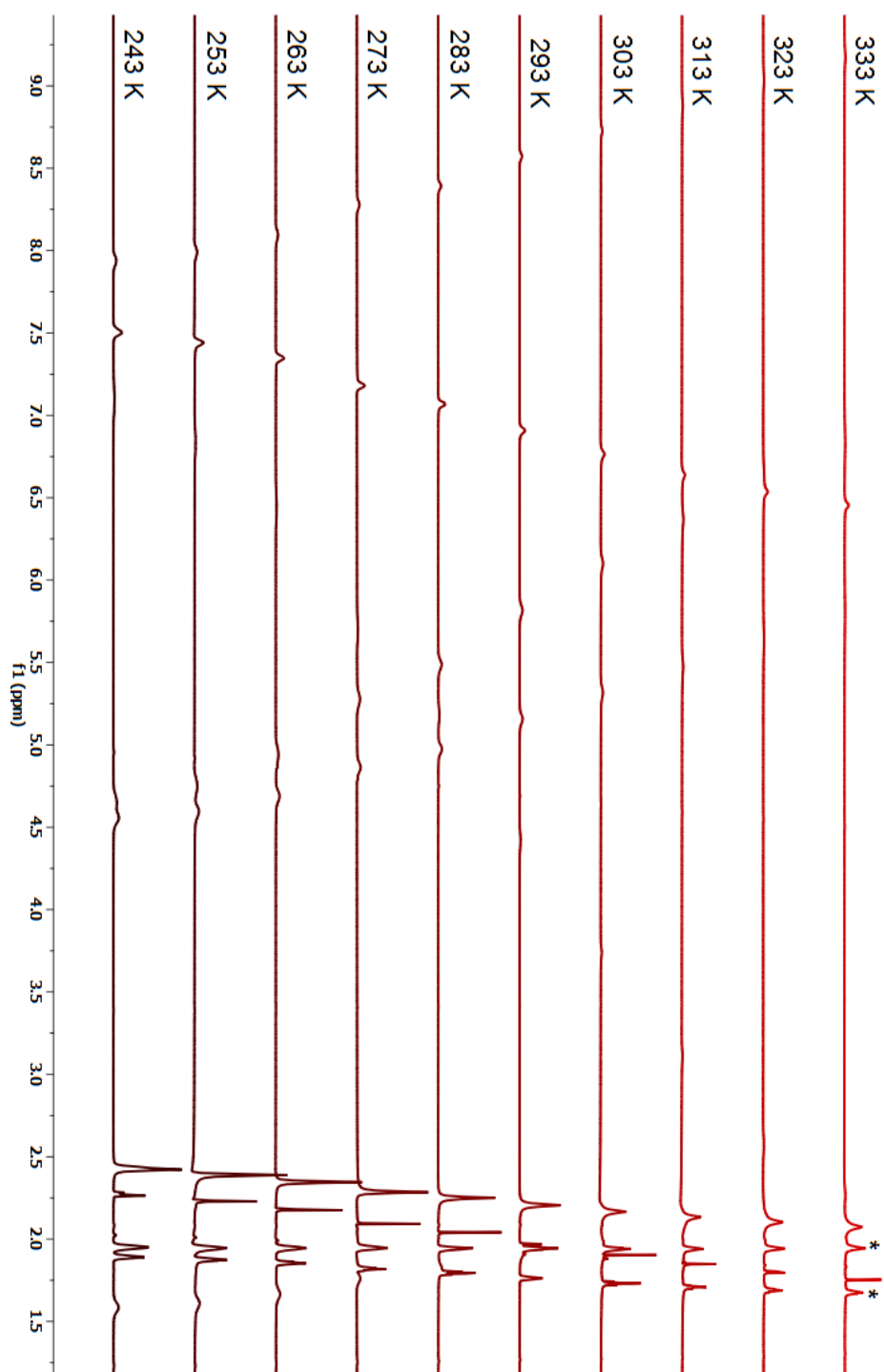


Figure S37. Stacked spectra, obtained by the Evans ¹H NMR method, from 333 to 243 K for complex $[\text{Fe}_2(\text{L}^{\text{2NHIm-meta}})_3](\text{BF}_4)_4$ (**1**) in CD₃CN (500 MHz) (* represent the solvent residual signal).

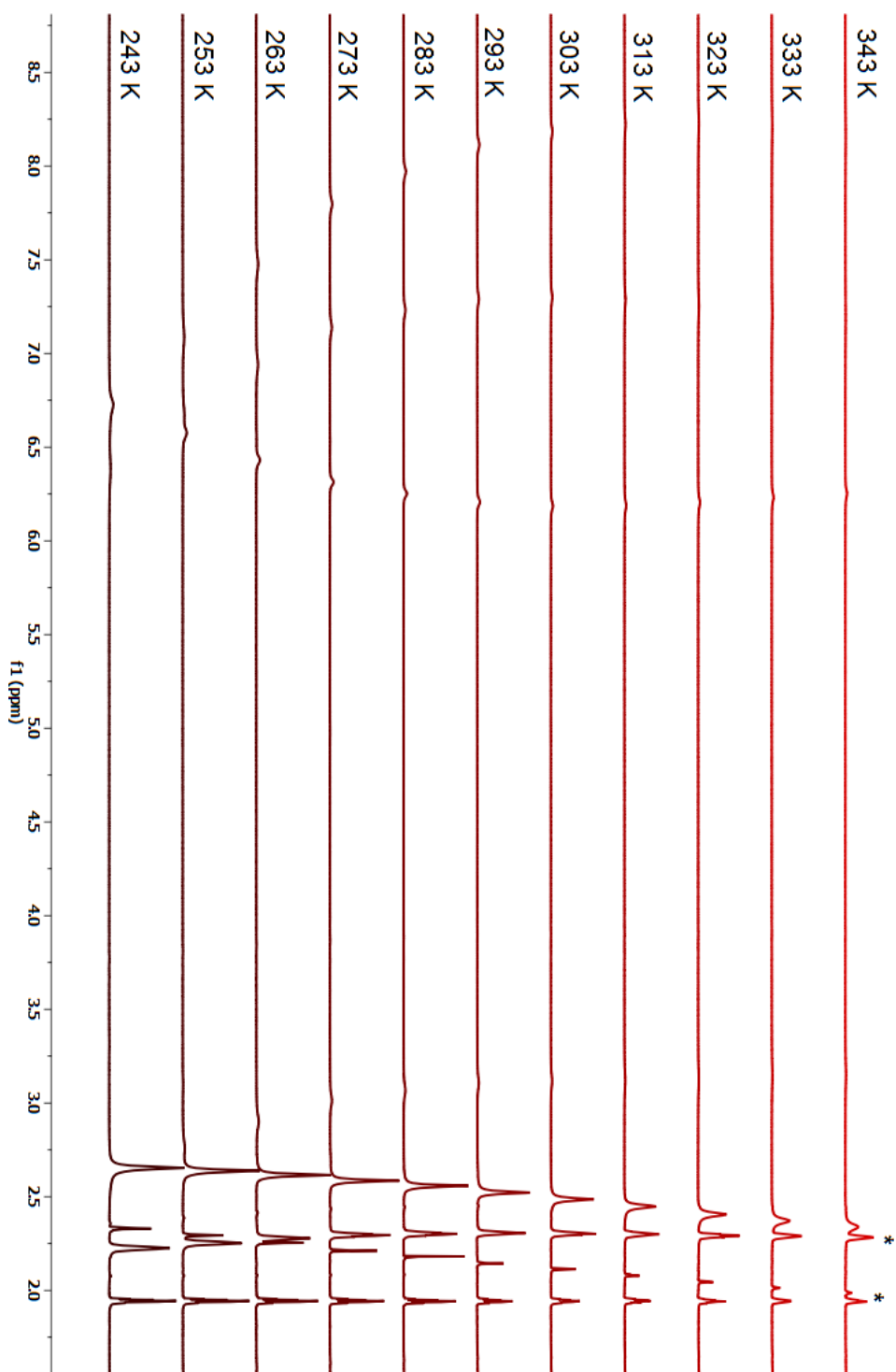


Figure S38. Stacked spectra, obtained by the Evans ¹H NMR method, from 343 to 243 K for complex [Fe₂(L^{4NHIm-meta})₃](BF₄)₄ (**2**) in CD₃CN (500 MHz) (* represent the solvent residual signal).

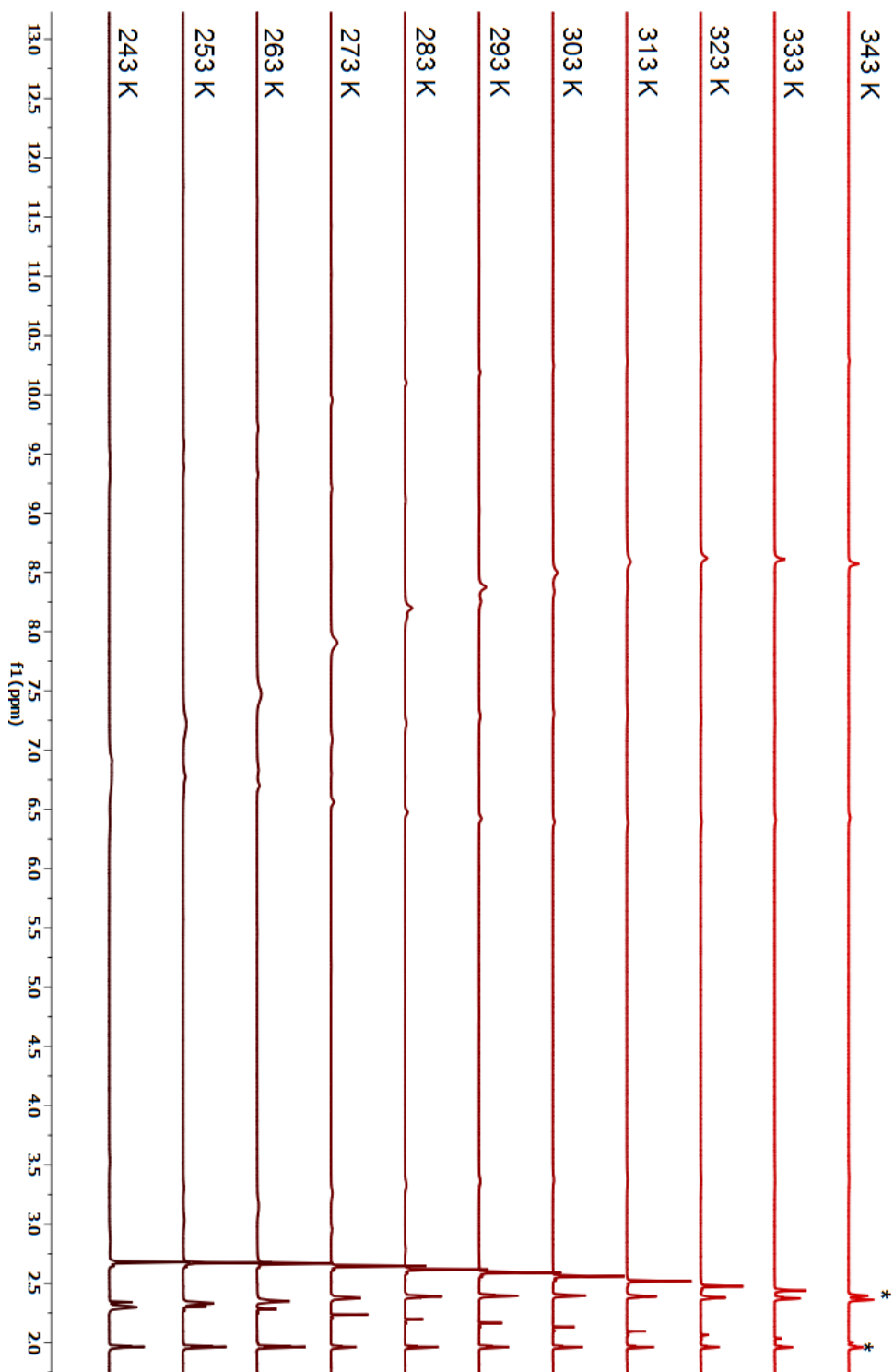


Figure S39. Stacked spectra, obtained by the Evans ^1H NMR method, from 343 to 243 K for complex $[\text{Fe}_2(\text{L}^{4\text{NMelm-meta}})_3](\text{BF}_4)_4$ (**3**) in CD_3CN (500 MHz) (* represent the solvent residual signal).

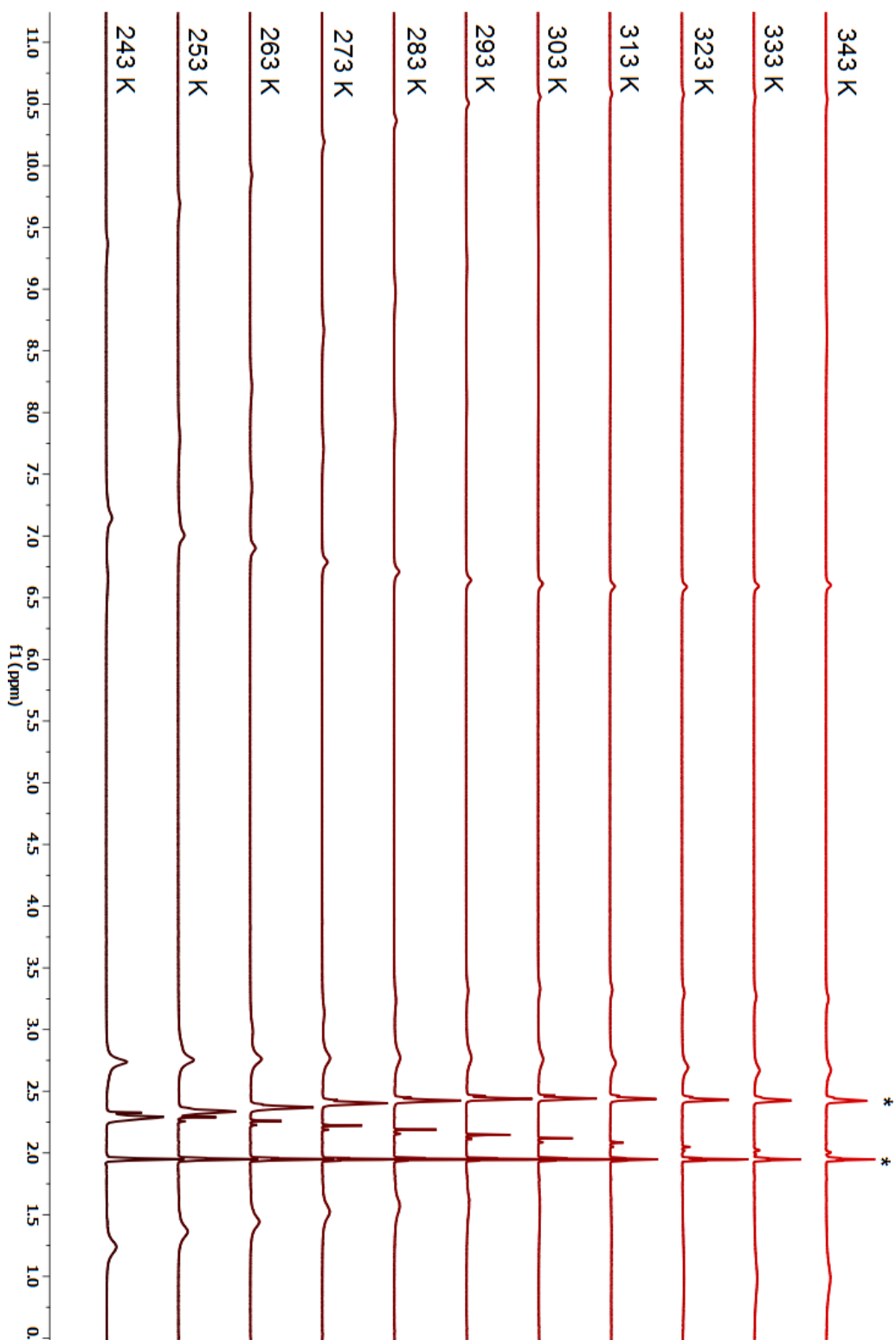


Figure S40. Stacked spectra, obtained by the Evans ¹H NMR method, from 343 to 243 K for complex [Fe₂(L^{40im-meta})₃](BF₄)₄ (**4**) in CD₃CN (500 MHz) (* represent the solvent residual signal).

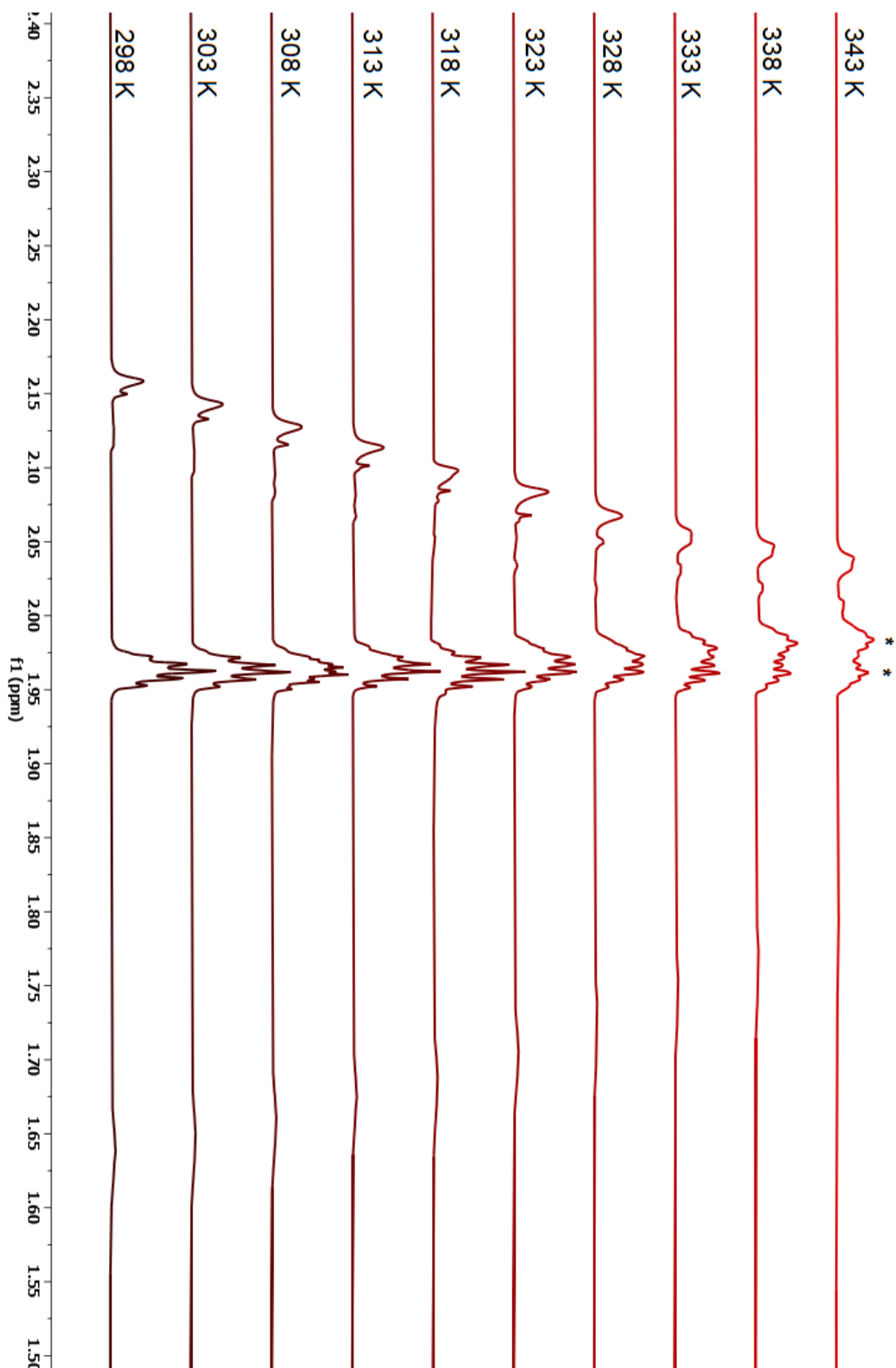


Figure S41a. Stacked spectra, obtained by the Evans ¹H NMR method, from 343 to 298 K for complex $[\text{Fe}_2(\text{L}^{4\text{SIm-meta}})_3](\text{BF}_4)_4$ (**5**) in CD_3CN (500 MHz) (* represent the solvent residual signal).

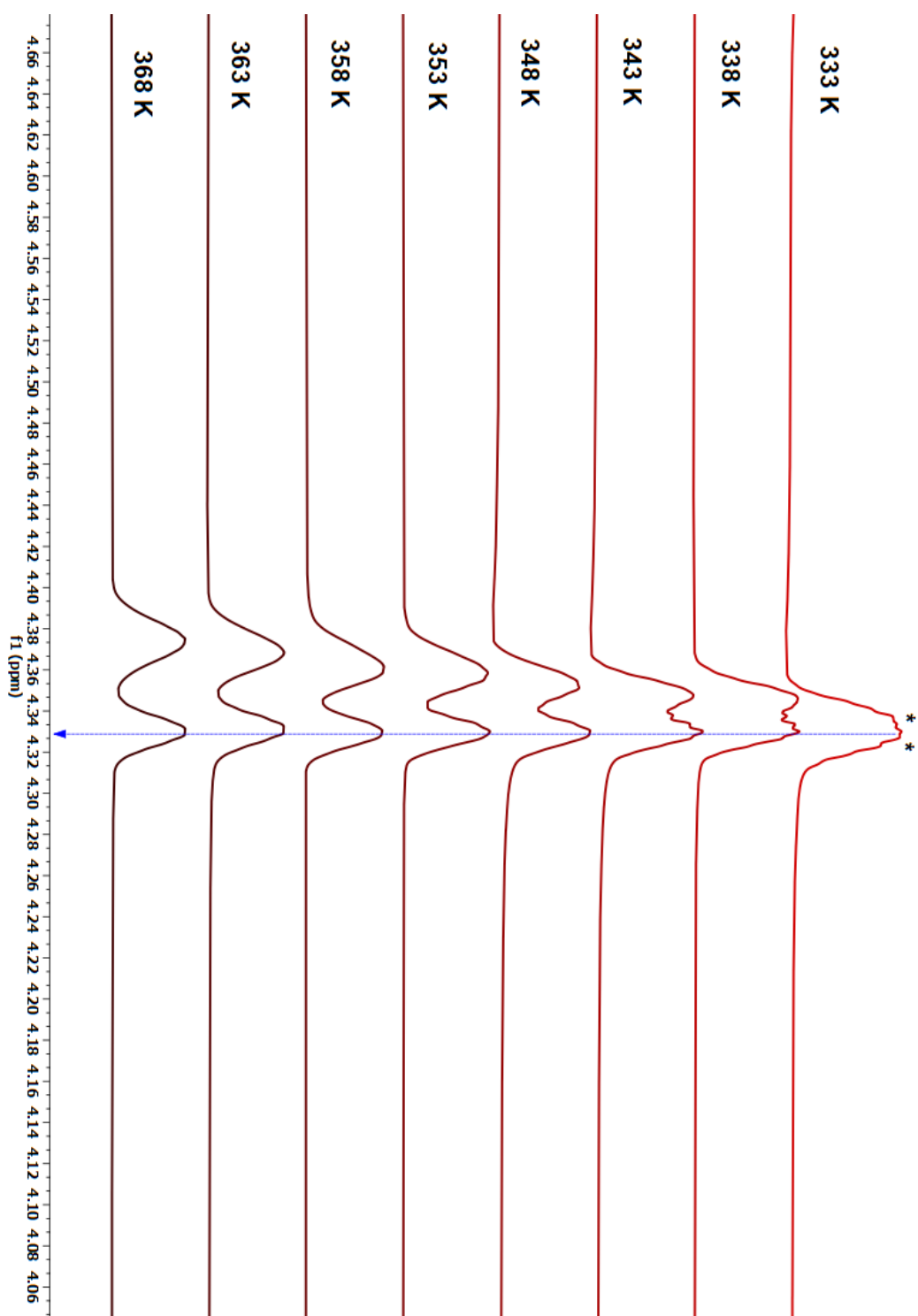


Figure S40b. Stacked spectra, obtained by the Evans ¹H NMR method, from 368 to 333 K for complex [Fe₂(L^{45Im-meta})₃](BF₄)₄ (**5**) in CD₃NO₂ (500 MHz) (* represent the solvent residual signal).

VT-UV vis studies in acetonitrile solution

The UV-vis spectra recorded from 253 K to 303 K on acetonitrile solutions of **1-5** (Figure S5). The resulting solution VT-UV-vis data were then modelled using the regular solution model (Equation S3).

The increasing absorbance with decreasing temperature directly relates to the increasing population of the Fe(II) LS state. If HS and LS fraction are in thermal equilibrium, the absorbance can be defined as a function of temperature as equation S2^{40, 41}

$$A(T) = \frac{A(0)}{1 + e^{\left(\frac{-\Delta H + \Delta S}{RT} + \frac{\Delta S}{R}\right)}} \quad \text{Equation S2}$$

According to the Beer-Lambert law, $A = \epsilon cl$, so equation S2 can be rewritten as follows, in terms of molar extinction coefficient:

$$\epsilon(T) = \frac{\epsilon(0)}{1 + e^{\left(\frac{-\Delta H + \Delta S}{RT} + \frac{\Delta S}{R}\right)}} \quad \text{Equation S3}$$

$\epsilon(T)$ is molar extinction coefficient as a function of temperature,

$\epsilon(0)$ is the extinction coefficient for fully LS (i.e. $\gamma_{\text{HS}} = 0$), estimated from the equation for the fit shown in Figure S52 and Figure S54, $\gamma_{\text{HS}} = x\epsilon + c$. For all fits to equation D3, $\epsilon(0)$ was set to this value $\epsilon_{\text{LS}}(0) = 103.3$ (**1**), 316.6 (**2**), 168.2 (**3**) and 176.8 (**4**) $\text{L mol}^{-1} \text{cm}^{-1}$ and extrapolate significantly (Figure S53 and Figure S55).

R is the ideal gas constant ($8.314472 \text{ J mol}^{-1} \text{K}^{-1}$), and the determined parameters, ΔH and ΔS , are the thermodynamic enthalpy and entropy values associated with the SCO. The transition temperature $T_{1/2}$ calculated accordingly, $\Delta H/\Delta S$.

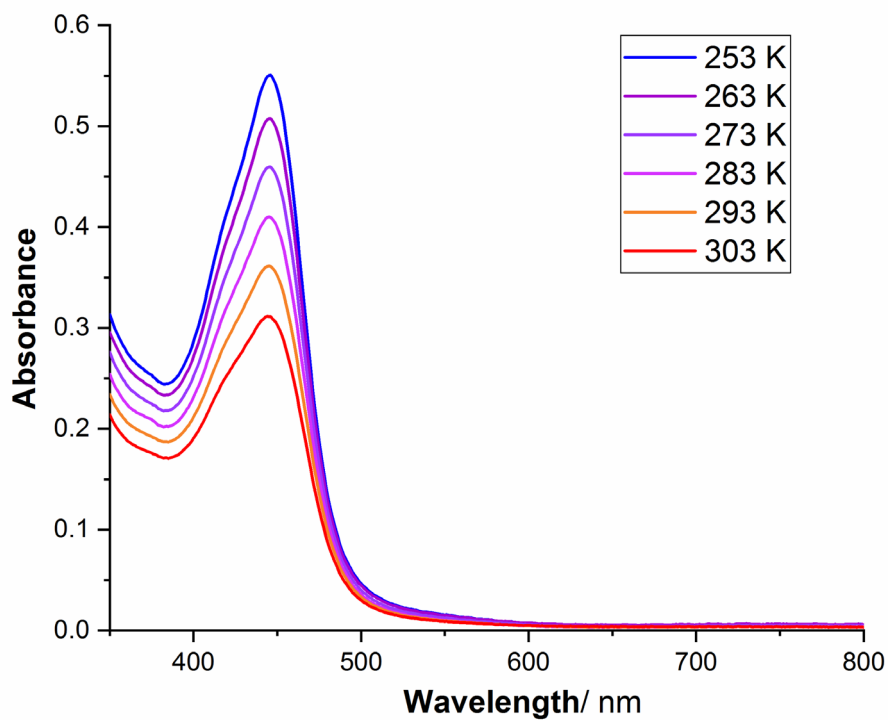


Figure S42. Variable temperature absorbance UV-vis spectra of 0.032 mM $[\text{Fe}_2(\text{L}^{2\text{NHIm-meta}})_3](\text{BF}_4)_4$ (**1**) in acetonitrile solution (charge transfer transition at 446 nm).

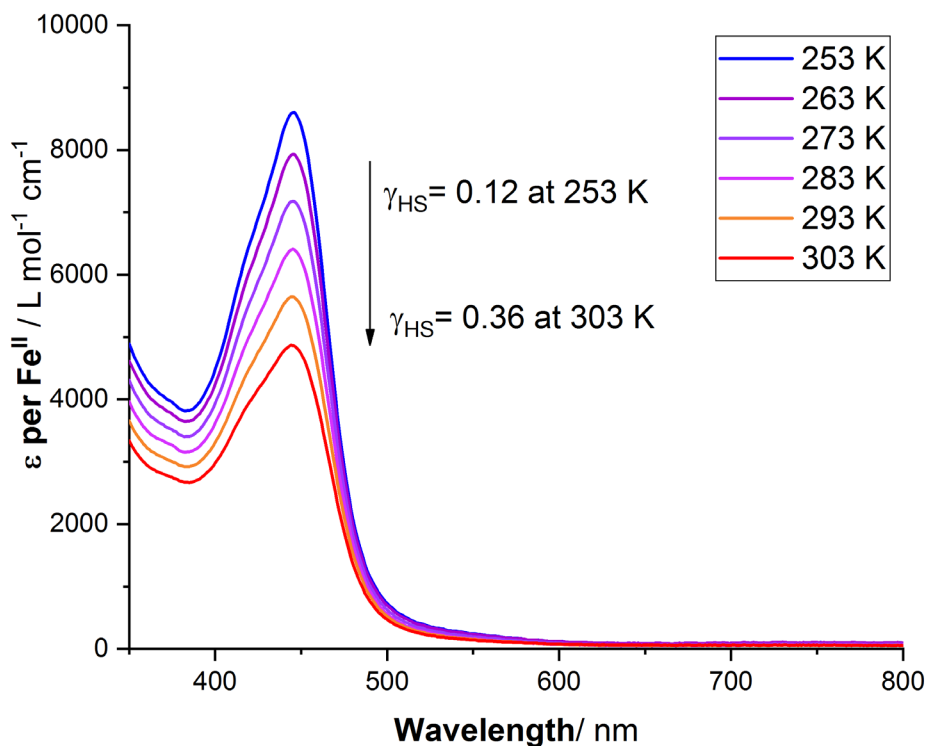


Figure S43. Variable temperature UV-vis study of a 0.032 mM acetonitrile solution of **1**. Note: ϵ is calculated per mole of Fe^{II} ion so it can be used to monitor the spin state as a function of T .

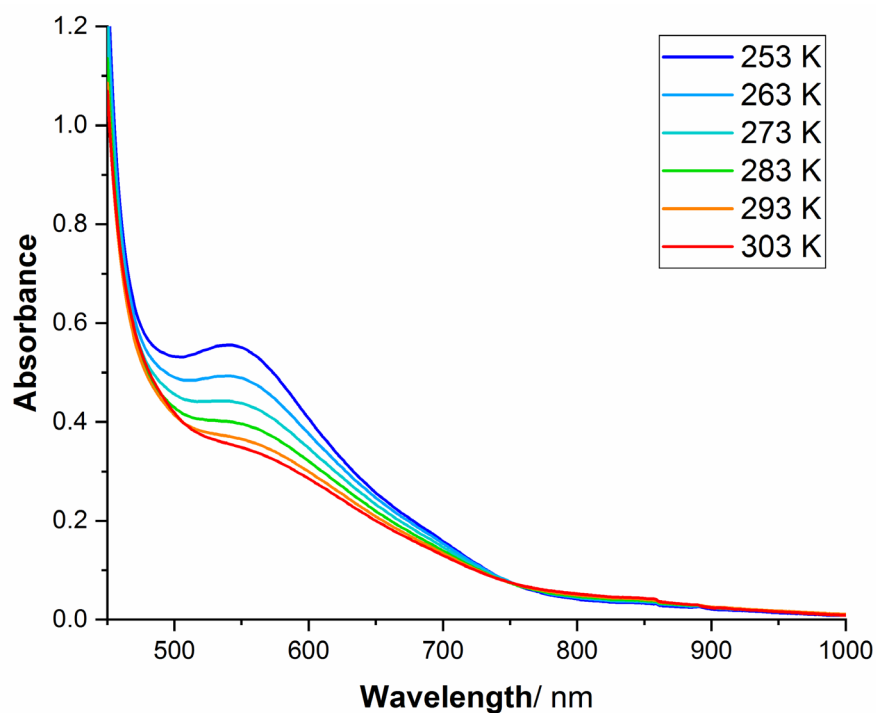


Figure S44. Variable Temperature absorbance UV-vis spectra of 1.6 mM $[\text{Fe}_2(\text{L}^{4\text{NHIm-meta}})_3](\text{BF}_4)_4$ (**2**) in acetonitrile (d-d transition at 540 nm).

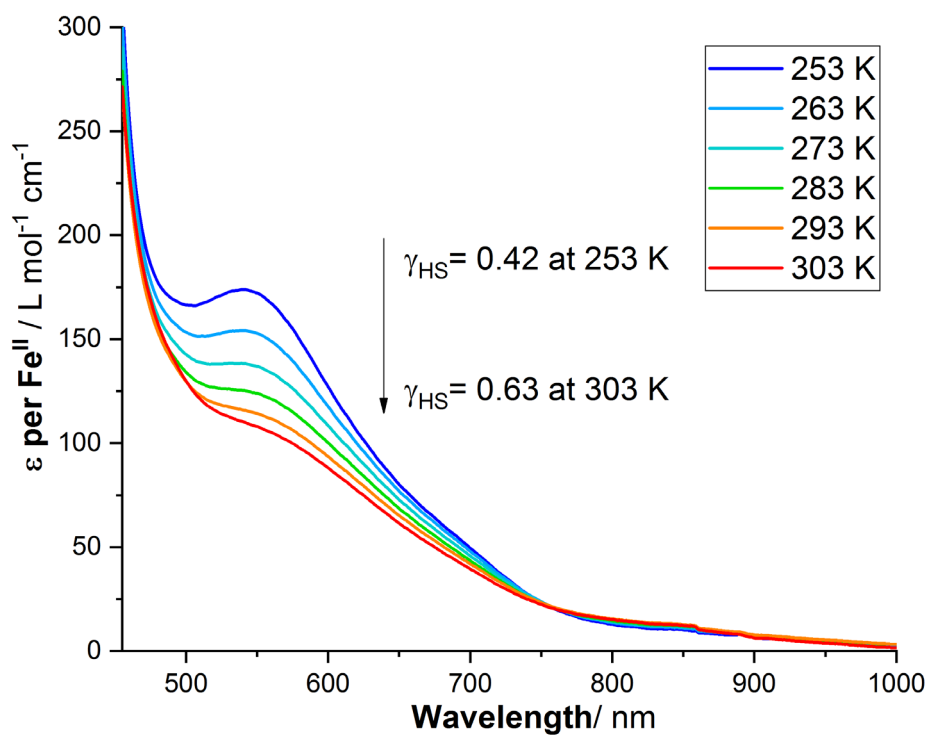


Figure S45. Variable temperature UV-vis study of a 1.6 mM acetonitrile solution of **2**. Note: ϵ is calculated per mole of Fe^{II} ion so it can be used to monitor the spin state as a function of T.

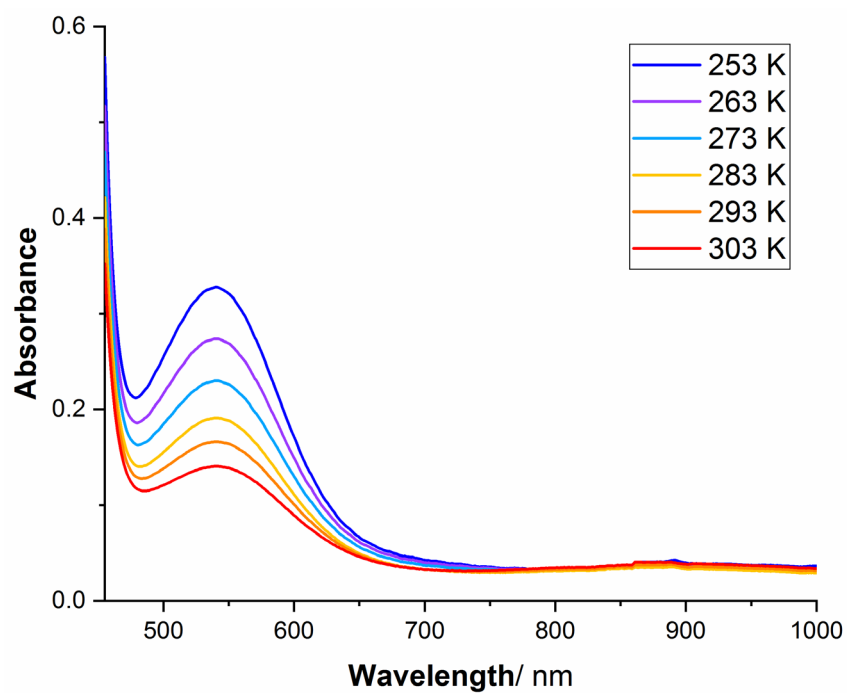


Figure S46. Variable temperature absorbance UV-vis spectra of 2 mM $[\text{Fe}_2(\text{L}^{4\text{NMeIm-meta}})_3](\text{BF}_4)_4$ (**3**) in acetonitrile (d-d transition at 540 nm).

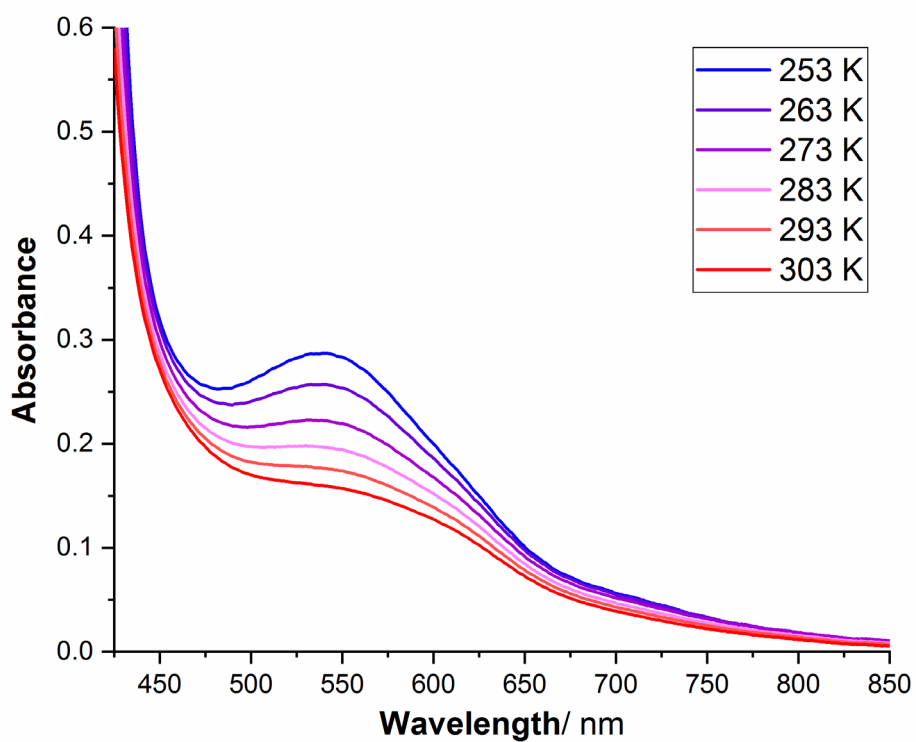


Figure S47. Variable temperature absorbance UV-vis spectra of 1.4 mM $[\text{Fe}_2(\text{L}^{4\text{OIm-meta}})_3](\text{BF}_4)_4$ (**4**) in acetonitrile (d-d transition at 540 nm).

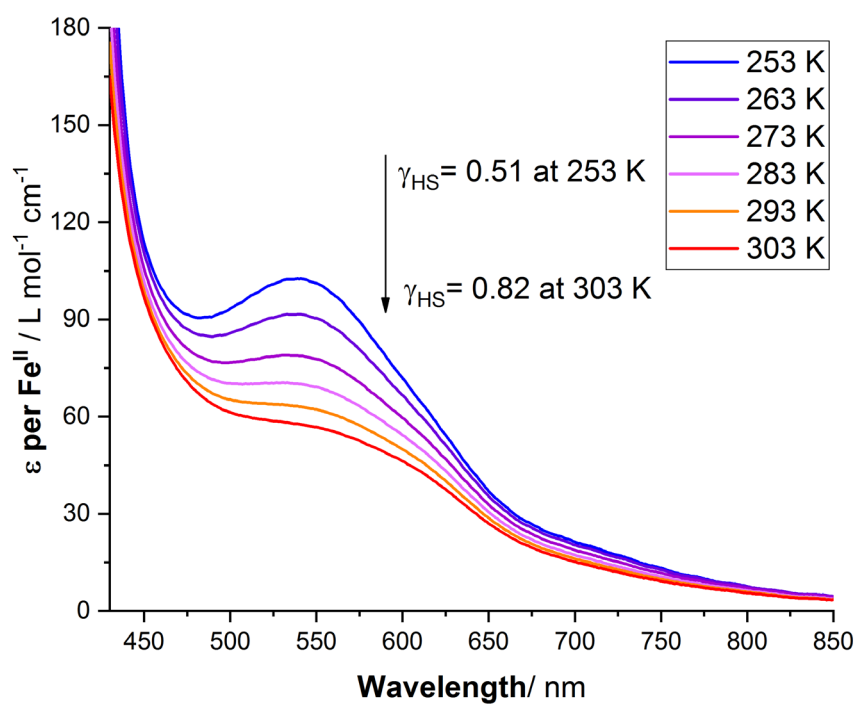


Figure S48. Variable temperature UV-vis study of a 1.4 mM acetonitrile solution of **4**. Note: ϵ is calculated per mole of Fe^{II} ion so it can be used to monitor the spin state as a function of T .

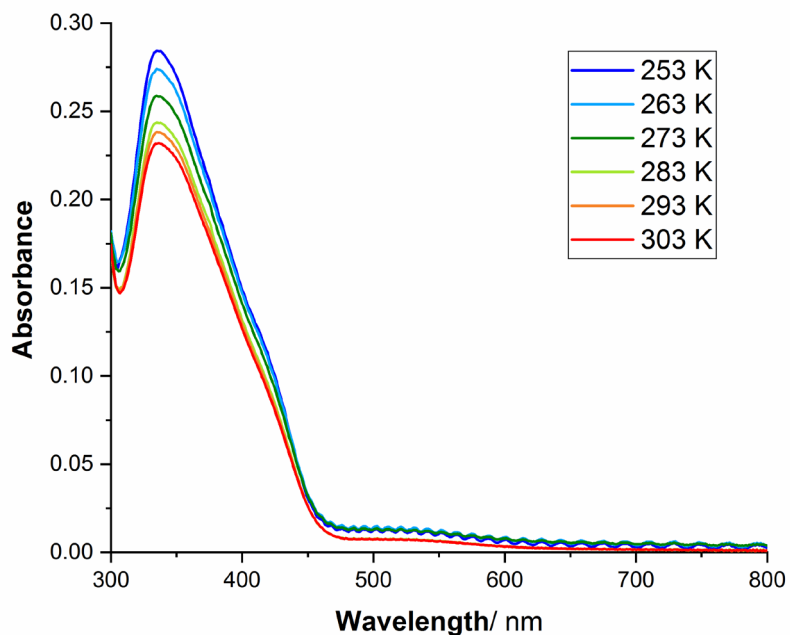


Figure S49. Variable temperature absorbance UV-vis spectra of 0.012 mM $[\text{Fe}_2(\text{L}^{4\text{SIm-meta}})_3](\text{BF}_4)_4$ (**5**) in acetonitrile (charge transfer transition at 336 nm and d-d band at 540 nm).

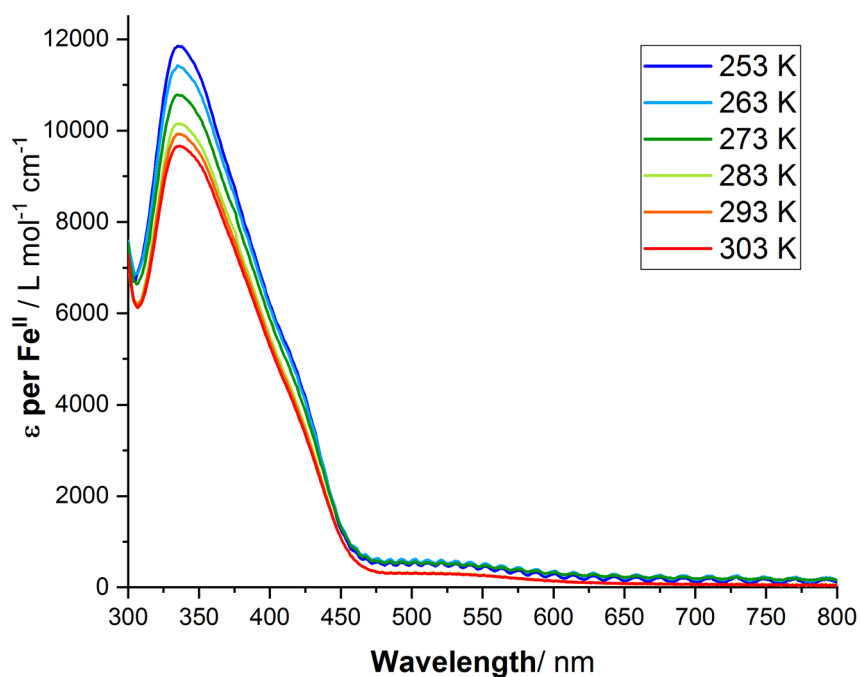


Figure S50. Variable temperature UV-vis spectra of 0.012 mM $[\text{Fe}_2(\text{L}^{4\text{Sim-meta}})_3](\text{BF}_4)_4$ (**5**) in acetonitrile (charge transfer transition at 336 nm).

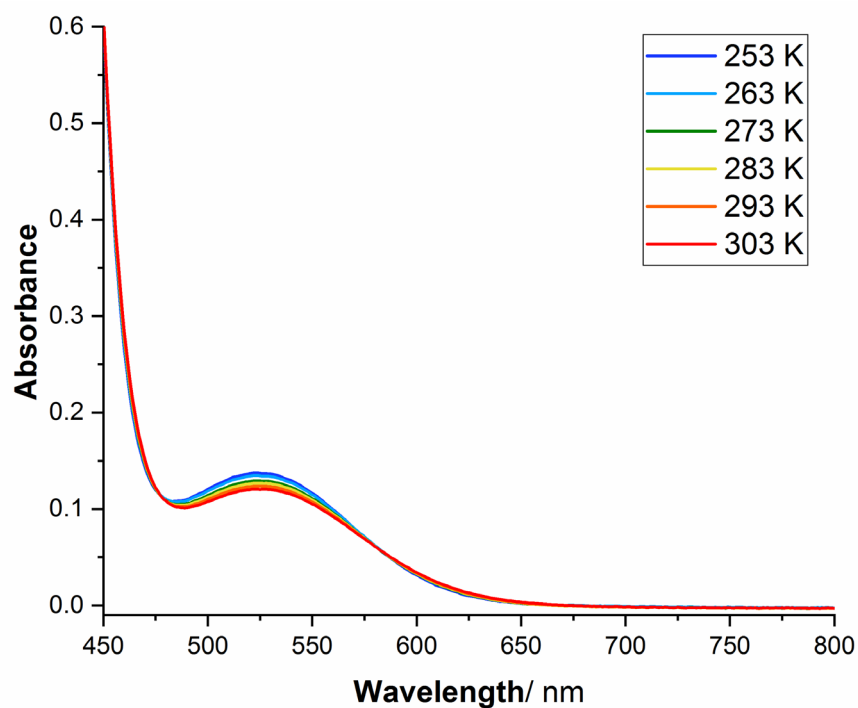


Figure S51. Variable Temperature absorbance UV-vis spectra of 0.3 mM $[\text{Fe}_2(\text{L}^{4\text{Sim-meta}})_3](\text{BF}_4)_4$ (**5**) in acetonitrile (d-d transition at 524 nm).

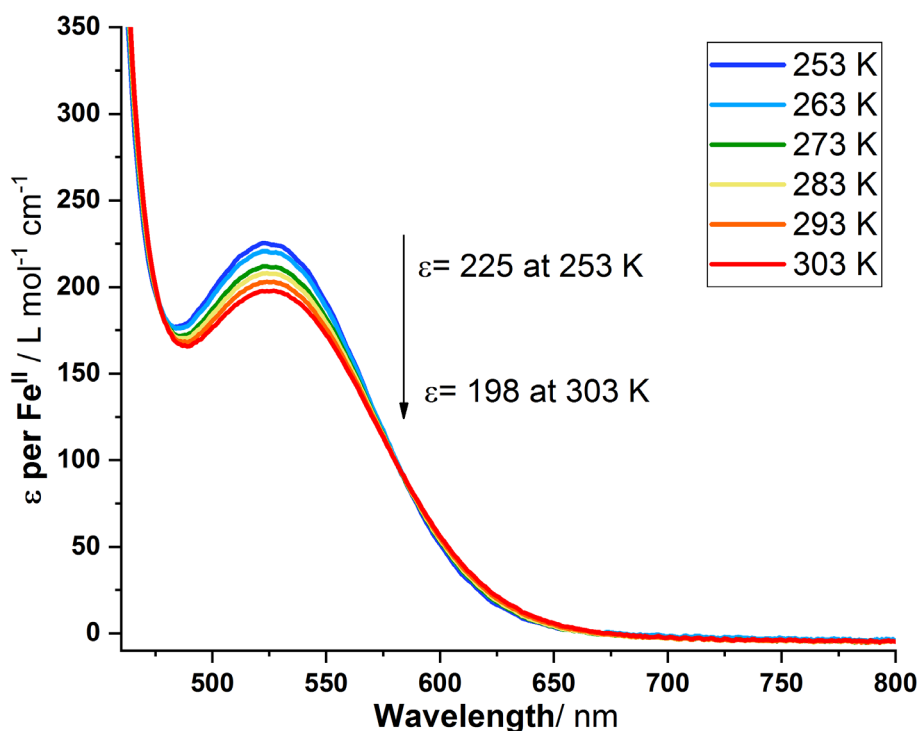


Figure S52. Variable temperature UV-vis study of a 0.3 mM acetonitrile solution of **5**. Note: ϵ is calculated per Fe^{II} ion of complex.

Estimation of HS fraction (γ_{HS}) of UV-vis data points by calibrating with Evans method data

γ_{HS} from the Evans method data (Table S11, 1st column) was calculated assuming $\chi_{\text{m}}T_{(\text{HH})} = 3.7 \text{ K cm}^3 \text{ mol}^{-1}$ for the fully [HS-HS] state and $\chi_{\text{m}}T_{(\text{LL})} = 0 \text{ K cm}^3 \text{ mol}^{-1}$ for the fully [LS-LS] state.

The $^1\text{H-NMR}$ and UV-vis spectra were both recorded at 253 K, 263 K, 273 K, 283 K, 293 K and 303 K for **1-5** complexes in acetonitrile, so the extinction coefficient (ϵ) values observed for the 540 nm band due to the LS state can be compared with the γ_{HS} obtained by $^1\text{H-NMR}$ Evans method at the same temperature. A plot of γ_{HS} versus ϵ (both per metal ion of the complex) gave the linear relationship noted in the insert (Figure S52 and Figure S54), which was then used to convert each ϵ (per metal ion of the complex) measured in UV-vis spectrum to a γ_{HS} value (green column, Table S11), and to

estimate the $\epsilon(0)$ expected for the fully LS state (i.e. $\gamma_{HS} = 0$), to be $\epsilon(0)$ (a significant extrapolation).

Table S9b. $\chi_m T$ (per Fe^{II} ion) values calculated from ¹H NMR data by the Evans method at various temperatures for each complex in the CD₃CN solution.

Temperature / K	$\chi_m T$ (cm ³ K mol ⁻¹)			
	[Fe ₂ (L ^{2NHIm-meta}) ₃] (BF ₄) ₄ (1)	[Fe ₂ (L ^{4NHIm-meta}) ₃] (BF ₄) ₄ (2)	[Fe ₂ (L ^{4NMeIm-meta}) ₃] (BF ₄) ₄ (3)	[Fe ₂ (L ^{4OIm-meta}) ₃] (BF ₄) ₄ (4)
243	0.3685	1.3806	1.7328	1.61698
253	0.43815	1.58814	2.03685	1.9183
263	0.55413	1.80158	2.28796	2.17566
273	0.75964	1.98822	2.58833	2.47243
283	0.91081	2.13116	2.77965	2.70389
293	1.12879	2.25767	2.96951	2.92644
303	1.34176	2.32796	3.11074	3.06567
313	1.53524	2.43604	3.21721	3.20861
323	1.74255	2.48000	3.29128	3.30308
333	1.91178	2.57693	3.33051	
343		2.67567	3.36465	

Table S10. Molar extinction coefficient, ϵ per Fe^{II} ion of the charge transfer for **1** (446 nm) and ¹A_{1g} → ¹T_{1g} band (540 nm) for **2**, **3** and **4** and at various temperatures for each complex in MeCN solution.

Temperature / K	ϵ (L mol ⁻¹ cm ⁻¹)			
	[Fe ₂ (L ^{2NHIm-meta}) ₃] (BF ₄) ₄ (1)	[Fe ₂ (L ^{4NHIm-meta}) ₃] (BF ₄) ₄ (2)	[Fe ₂ (L ^{4NMeIm-meta}) ₃] (BF ₄) ₄ (3)	[Fe ₂ (L ^{4OIm-meta}) ₃] (BF ₄) ₄ (4)
253	8597	173.81	81.8995	102.5
263	7928	154.21	68.46175	91.5
273	7178	138.29	57.46075	78.8
283	6405	125.38	47.7365	70.1
293	5646	113.36	41.57325	63.1
303	4863	106.9	35.1385	57.66

Table S11. Comparison of γ_{HS} values at measured temperatures both calculated from ^1H NMR (Evans method) data and estimated for UV-vis data, for **1**, **2**, **3** and **4** complex in $\text{CD}_3\text{CN}/\text{MeCN}$ solution.

T / K	$[\text{Fe}_2(\text{L}^{2\text{NHIm-meta}})_3](\text{BF}_4)_4$ (1)		$[\text{Fe}_2(\text{L}^{4\text{NHIm-meta}})_3](\text{BF}_4)_4$ (2)		$[\text{Fe}_2(\text{L}^{4\text{NHIm-meta}})_3](\text{BF}_4)_4$ (3)		$[\text{Fe}_2(\text{L}^{4\text{OIm-meta}})_3](\text{BF}_4)_4$ (4)	
	γ_{HS} (NMR)	γ_{HS} (UV-vis)	γ_{HS} (NMR)	γ_{HS} (UV-vis)	γ_{HS} (NMR)	γ_{HS} (UV-vis)	γ_{HS} (NMR)	γ_{HS} (UV-vis)
243	0.0996		0.37314		0.46832		0.43702	
253	0.11842	0.11251	0.42923	0.42857	0.5505	0.54403	0.51846	0.51275
263	0.14976	0.159	0.48691	0.48737	0.61837	0.62869	0.58802	0.58865
273	0.20531	0.21113	0.53736	0.53513	0.69955	0.698	0.66823	0.67628
283	0.24616	0.26485	0.57599	0.57386	0.75126	0.75926	0.73078	0.73631
293	0.30508	0.3176	0.61018	0.60992	0.80257	0.79809	0.79093	0.78461
303	0.36264	0.37202	0.62918	0.6293	0.84074	0.83863	0.82856	0.82215
313	0.41493		0.65839		0.86952		0.86719	
323	0.47096		0.67027		0.88954		0.89272	
333	0.5167		0.69647		0.90014			
343			0.72315		0.90936			

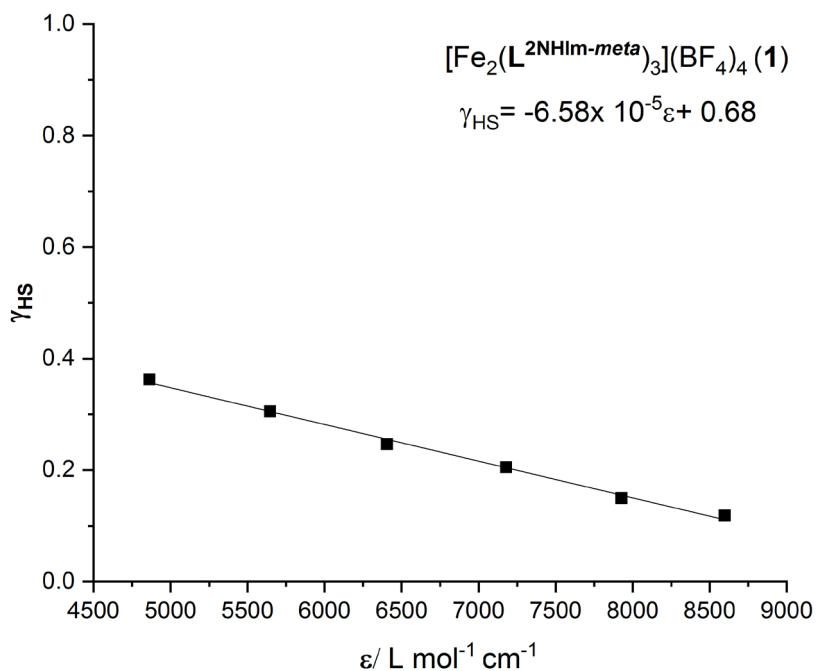


Figure S53. Plot of γ_{HS} (obtained from Evans method) vs extinction coefficient per metal ion (obtained from variable temperature UV-vis studies) of 446 nm band of complex **1** in 0.032 mM acetonitrile solution ($R^2 = 0.99$). The linear fit equation is further used to convert ϵ value into γ_{HS} for UV-vis studies.

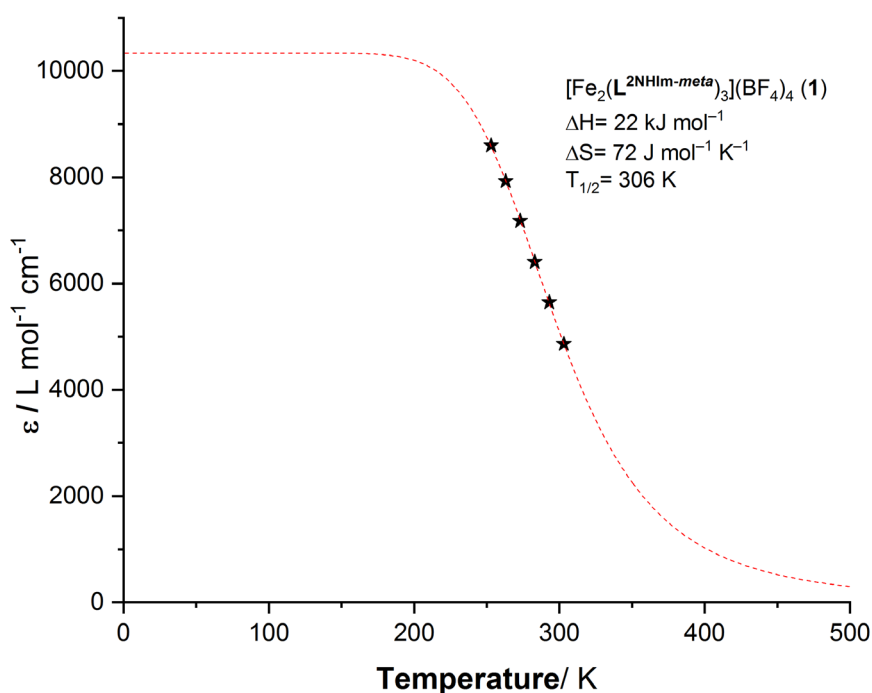


Figure S54. Temperature dependence of the molar extinction coefficients (ϵ) of the 446 nm charge transfer transition of **1** in acetonitrile solution. Red dotted curve represents fit to equation S3, $R^2 = 0.99$ (**1**) having set $\epsilon_{\text{LS}}(0) = 10334 \text{ L mol}^{-1} \text{cm}^{-1}$, see Figure S52).

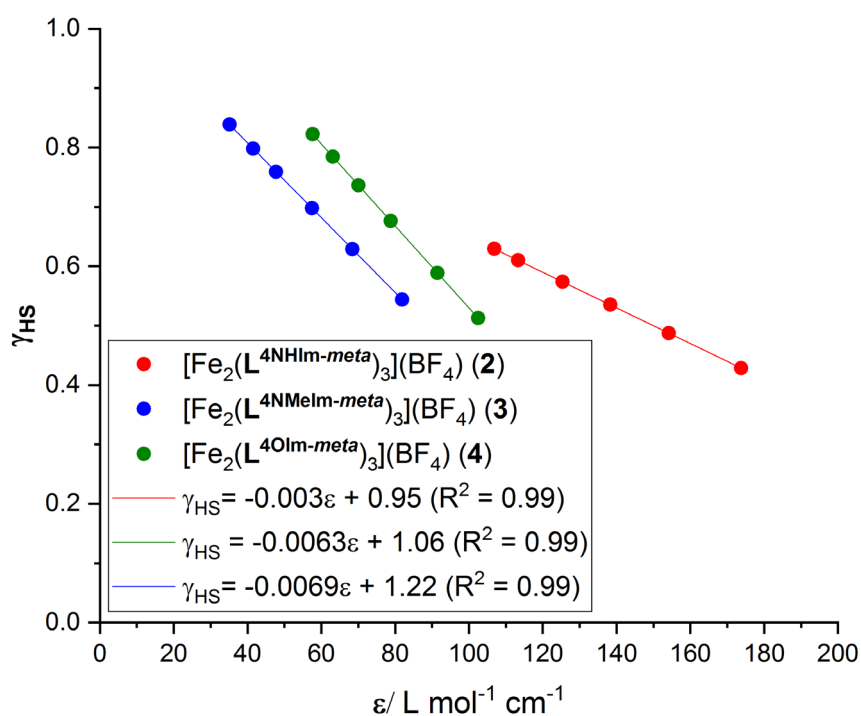


Figure S55. Plot of γ_{HS} (obtained from Evans method) vs extinction coefficient per metal ion (obtained from variable temperature UV-vis studies) of 540 nm band of complex **2** (1.6 mM), **3** (2 mM) and **4** (1.4 mM) acetonitrile solution. The linear fit equation is further used to convert ϵ value into γ_{HS} for UV-vis studies.

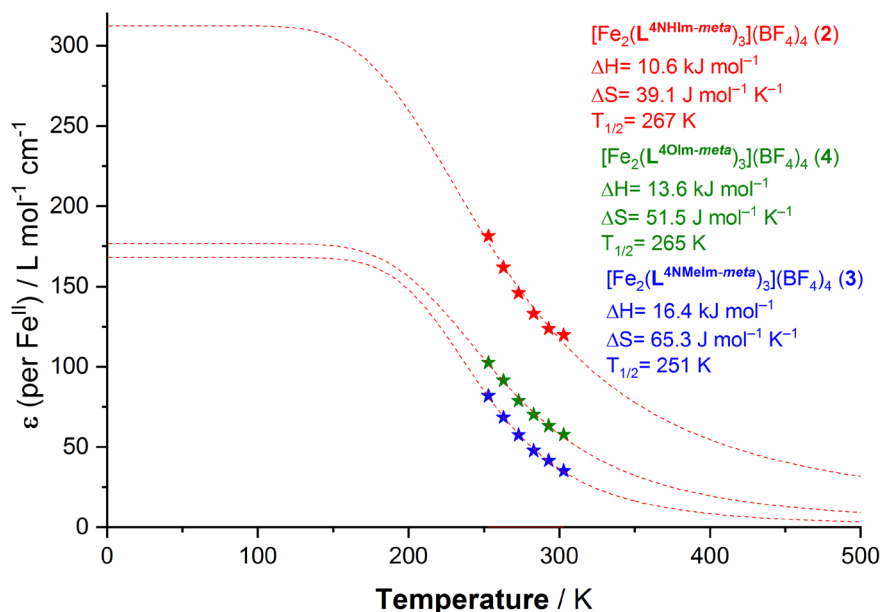


Figure S56. Temperature dependence of the molar extinction coefficients (ϵ) of the 540 nm LS Fe(II) $^1A_{1g} \rightarrow ^1T_{1g}$ band of **2**, **3** and **4** in acetonitrile solution. Red dotted curve represents fit to equation S3, $R^2 = 0.99$ (**2**), $R^2 = 0.99$ (**3**) and $R^2 = 0.99$ (**4**) having set $\epsilon_{\text{LS}}(0) = 316.6$ (**2**), 168.2 (**3**) and 176.8 (**4**) $\text{L mol}^{-1} \text{ cm}^{-1}$, see Figure S54).

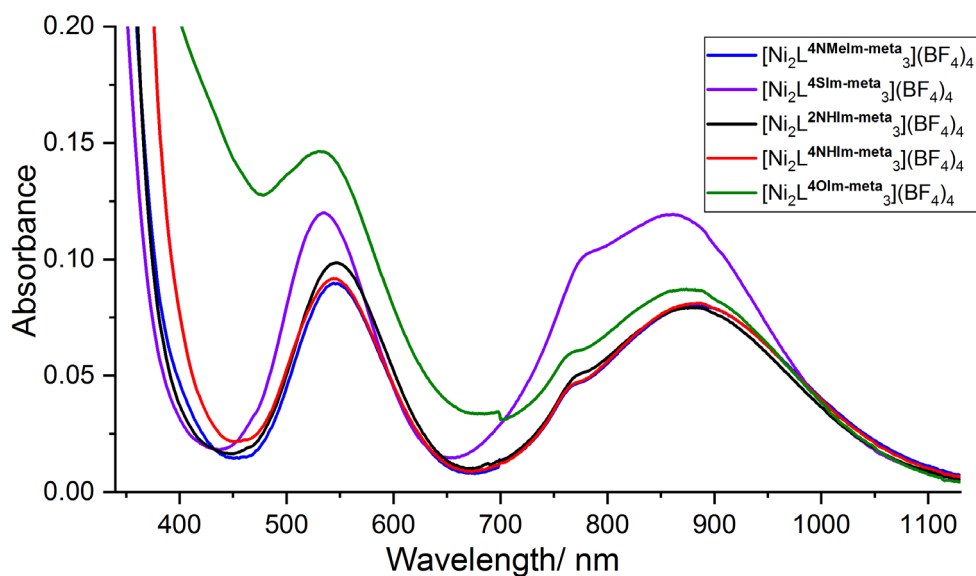


Figure S57. UV-vis spectra of accurately measured $\sim 3 \text{ mM}$ of analogous Ni(II) helicates in acetonitrile solution; **1**^{Ni}·6H₂O (black), **2**^{Ni}·4H₂O (red), **3**^{Ni}·5H₂O (blue) and **4**^{Ni}·2.5H₂O (green), and **5**^{Ni}·3H₂O (purple).

Table S12. Two of the three UV-vis transitions (λ_{\max} in nm/energy in cm^{-1}) of the accurately calculated ~ 3 mM of Ni(II) helicates in acetonitrile solution with ϵ per dinuclear complex ($\text{L mol}^{-1} \text{cm}^{-1}$) and corrected $\Delta_{0(\text{corr.})}$ calculated by using Hart, Boeyens and Hancock equation ($= 10630 + 1370\epsilon_1/\epsilon_2$).²⁹

Complexes	${}^3A_{2g} \rightarrow {}^3T_{1g}(\text{F})$	Shoulder/ cm^{-1} ($\epsilon_1 / \text{L mol}^{-1} \text{cm}^{-1}$)	Peak/ cm^{-1} ($\epsilon_2 / \text{L mol}^{-1} \text{cm}^{-1}$)	${}^3A_{2g} \rightarrow {}^3T_{2g}(\text{F})$ $\Delta_{0(\text{corr.})} / \text{cm}^{-1}$
1^{Ni}	547/18281 (28)	774/12919 (14)	879/11376 (23)	11505
2^{Ni}	544/18382 (25)	770/12987 (13)	884/11312 (22)	11420
3^{Ni}	544/18382 (27)	772/12953 (14)	880/11363 (24)	11430
4^{Ni}	530/18867 (41)	769/13003 (18)	874/11441 (26)	11516
5^{Ni}	535/18691 (26)	780/12820 (31)	862/11600 (36)	11804

Cyclic voltammetry

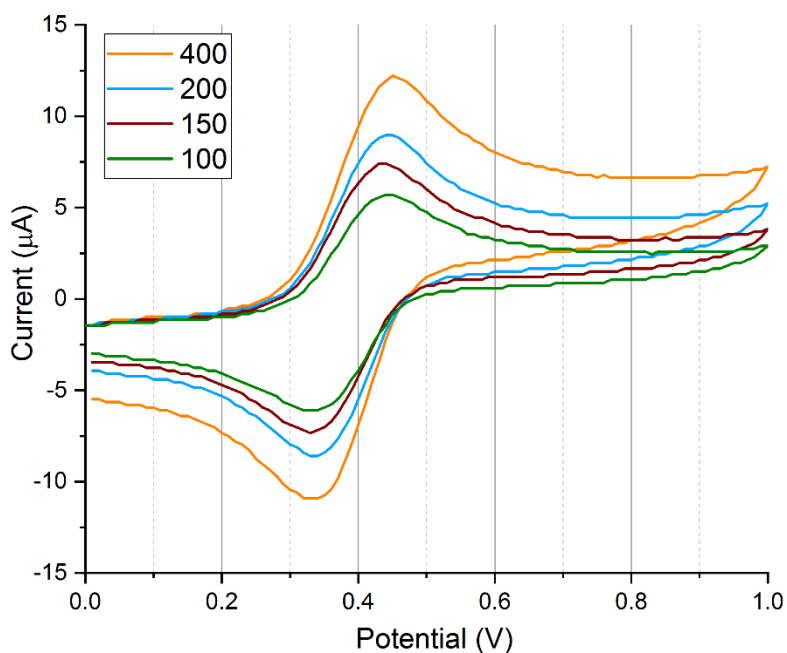


Figure S58. CVs of 1 mM of $[\text{Fe}_2(\text{L}^{2\text{NHIm-meta}})_3](\text{BF}_4)_4 \cdot 4\text{H}_2\text{O}$ in MeCN (0.1 M TBAClO_4), from $0 \rightarrow 1.0 \rightarrow 0$ V vs 0.01M Ag/AgNO_3 at scan rates 100, 150, 200 and 400 mV s^{-1} .

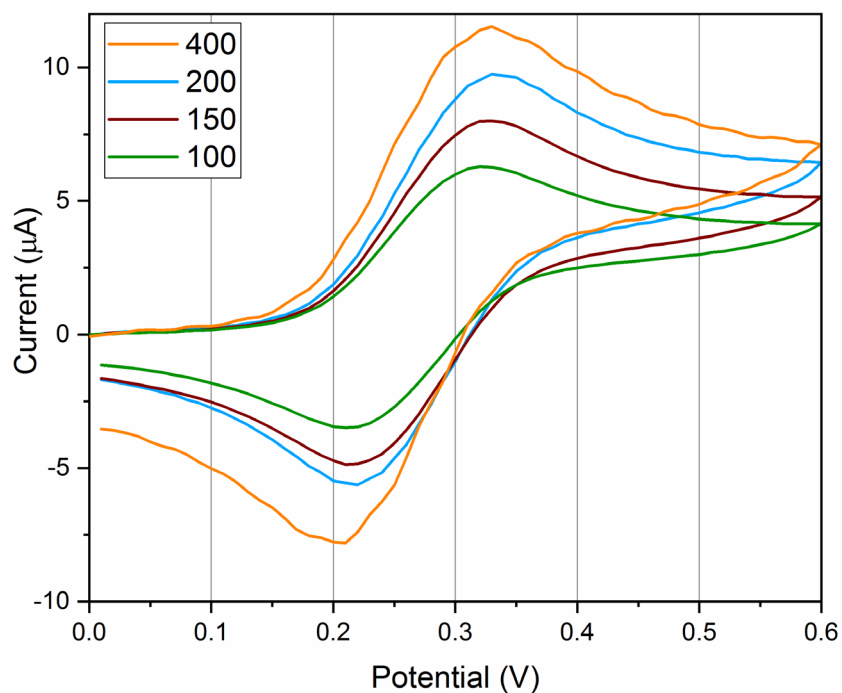


Figure S59. CVs of 1 mM of $[\text{Fe}_2(\text{L}^{4\text{NHIm-meta}})_3](\text{BF}_4)_4 \cdot 6\text{H}_2\text{O}$ in MeCN (0.1 M TBAClO₄), from 0 → 0.6 → 0 V vs 0.01M Ag/AgNO₃ at scan rates 100, 150, 200 and 400 mV s⁻¹.

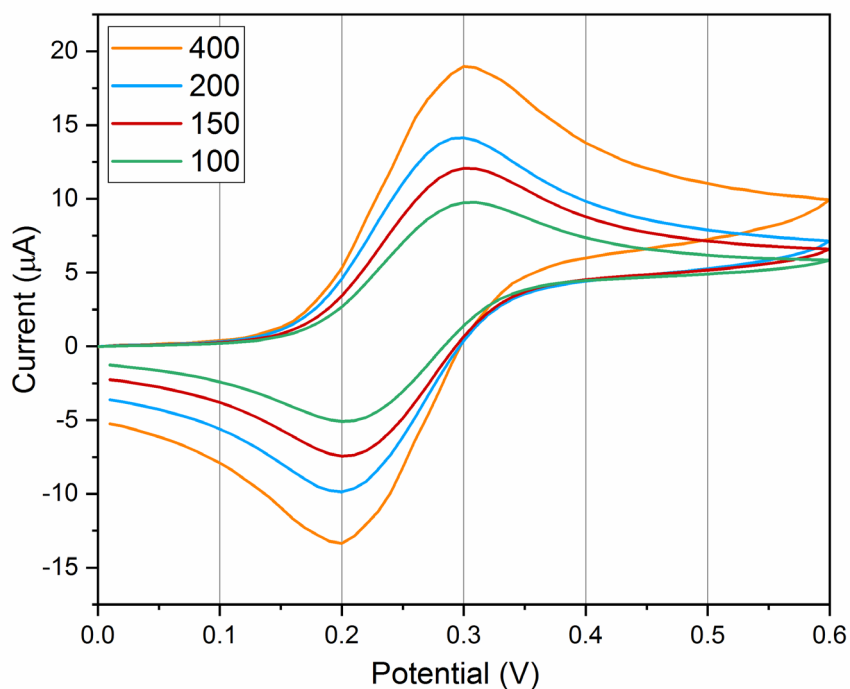


Figure S60. CVs of 1 mM of $[\text{Fe}_2(\text{L}^{4\text{NMeIm-meta}})_3](\text{BF}_4)_4 \cdot 5\text{H}_2\text{O}$ in MeCN (0.1 M TBAClO₄), from 0.0 → 0.6 → 0 V vs 0.01M Ag/AgNO₃ at scan rates 100, 150, 200 and 400 mV s⁻¹.

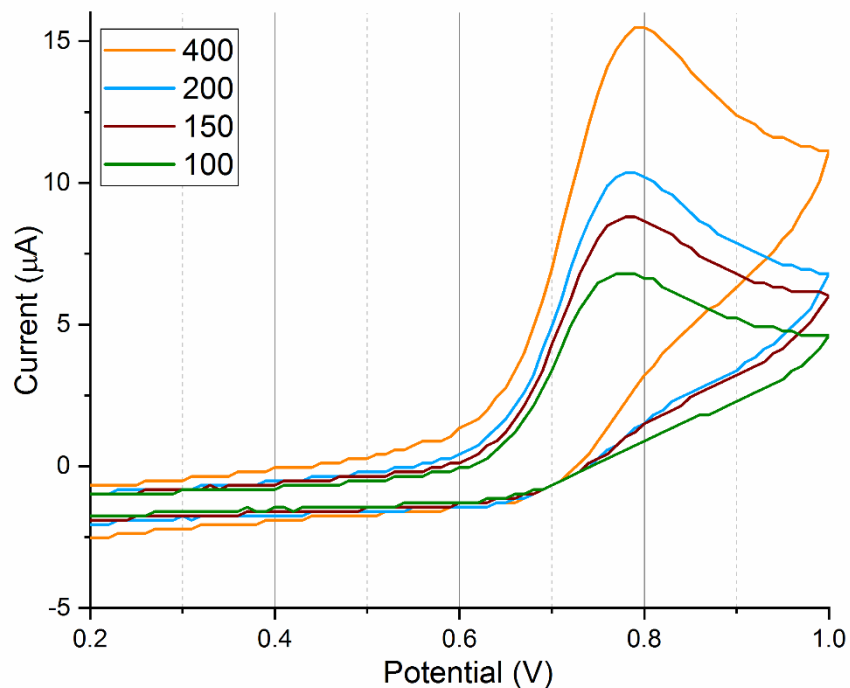


Figure S61. CVs of 1 mM of $[\text{Fe}_2(\text{L}^{40\text{Im-meta}})_3](\text{BF}_4)_4 \cdot 5\text{H}_2\text{O}$ in MeCN (0.1 M TBAClO₄), from 0.2 → 1.0 → 0.2 V vs 0.01M Ag/AgNO₃ at scan rates 100, 150, 200 and 400 mV s⁻¹.

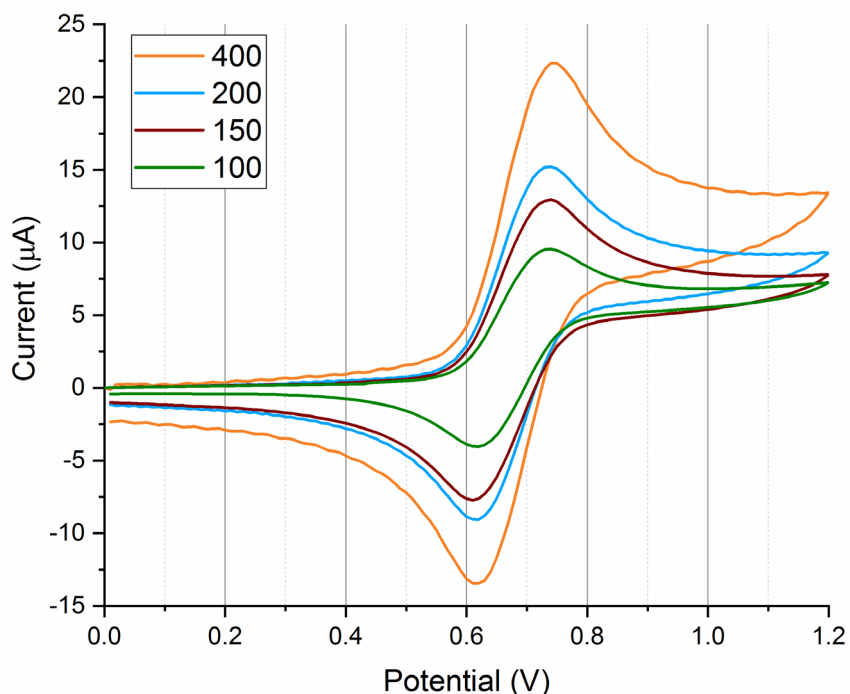


Figure S62. CVs of 1 mM of $[\text{Fe}_2(\text{L}^{45\text{Im-meta}})_3](\text{BF}_4)_4 \cdot 5\cdot 2.5\text{H}_2\text{O}$ in MeCN (0.1 M TBAPF₆, partially soluble), from 0 → 1.2 → 0 V vs 0.01M Ag/AgNO₃ at scan rates 100, 150, 200 and 400 mV s⁻¹.

^1H DOSY NMR spectra

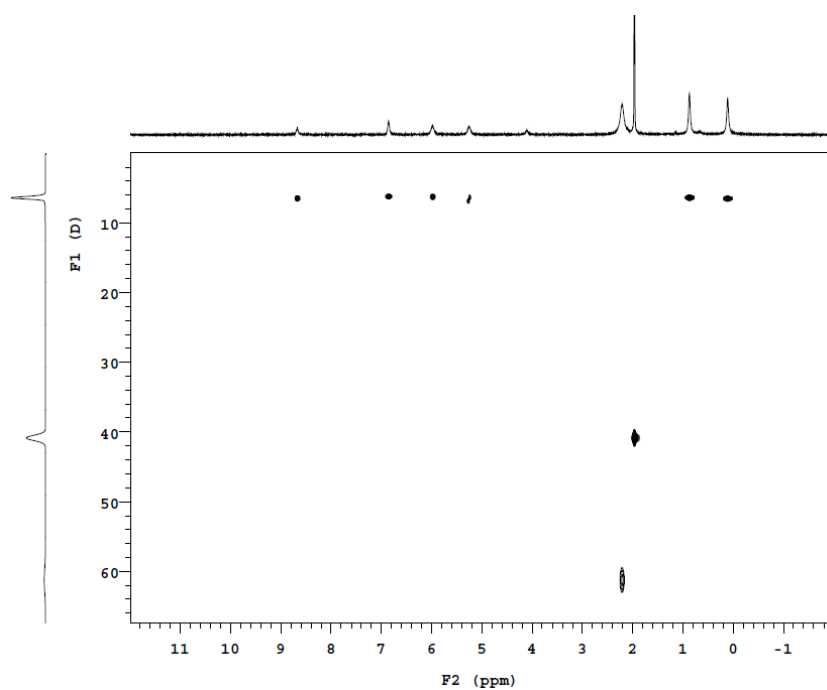


Figure S63. ^1H DOSY-NMR spectrum (500 MHz) of $\text{Fe}_2(\text{L}^{2\text{NHIm-meta}})_3(\text{BF}_4)_4$ (**1**) in CD_3CN at 25°C ; unit of D is $10^{-10} \text{ m}^2 \text{ s}^{-1}$.

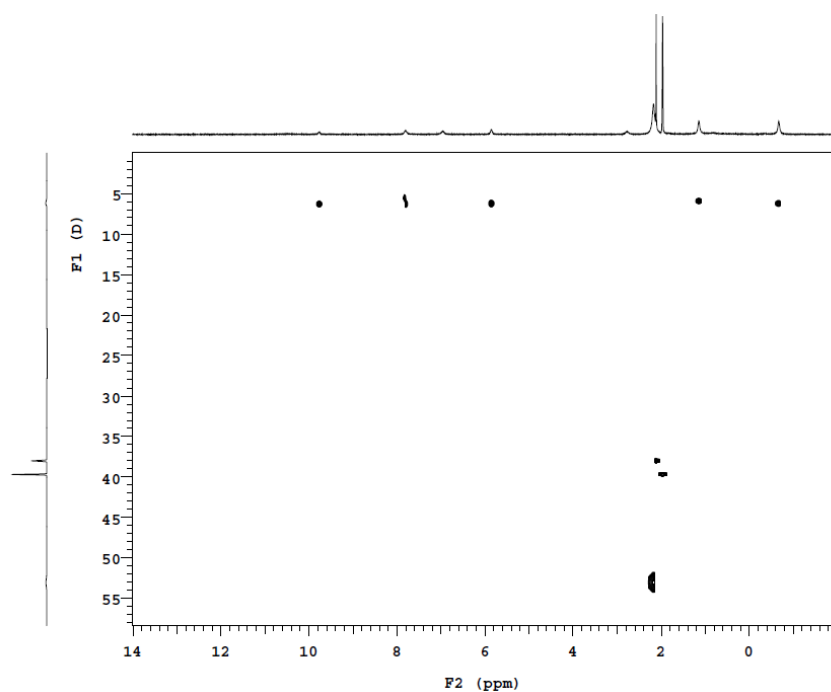


Figure S64. ^1H DOSY-NMR spectrum (500 MHz) of $\text{Fe}_2(\text{L}^{4\text{NHIm-meta}})_3(\text{BF}_4)_4$ (**2**) in CD_3CN at 25°C ; unit of D is $10^{-10} \text{ m}^2 \text{ s}^{-1}$.

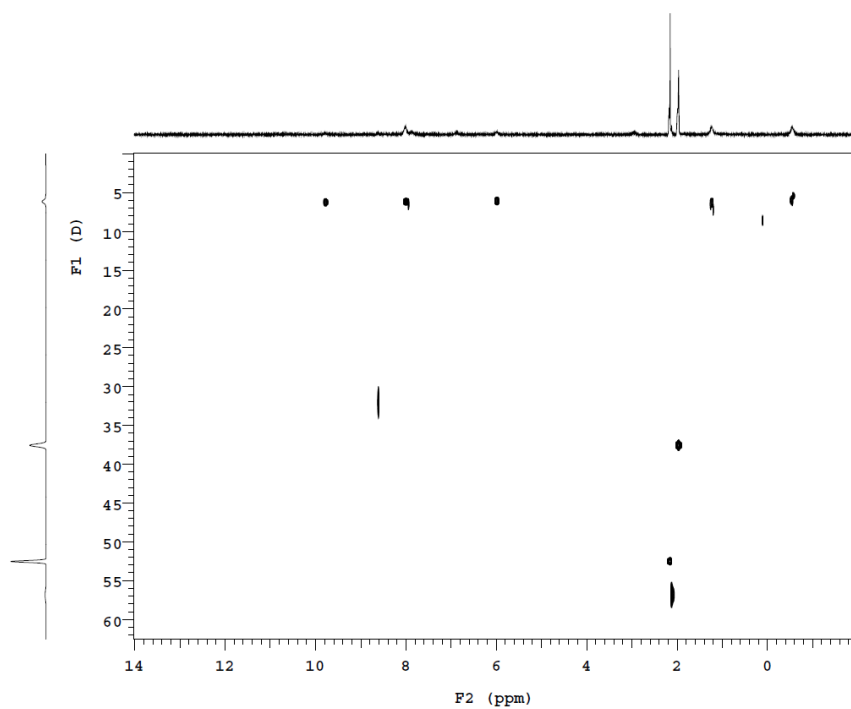


Figure S65. ^1H DOSY-NMR spectrum (500 MHz) of $\text{Fe}_2(\text{L}^{4\text{NMelm-meta}})_3(\text{BF}_4)_4$ (**3**) in CD_3CN at $25\text{ }^\circ\text{C}$; unit of D is $10^{-10}\text{ m}^2\text{s}^{-1}$.

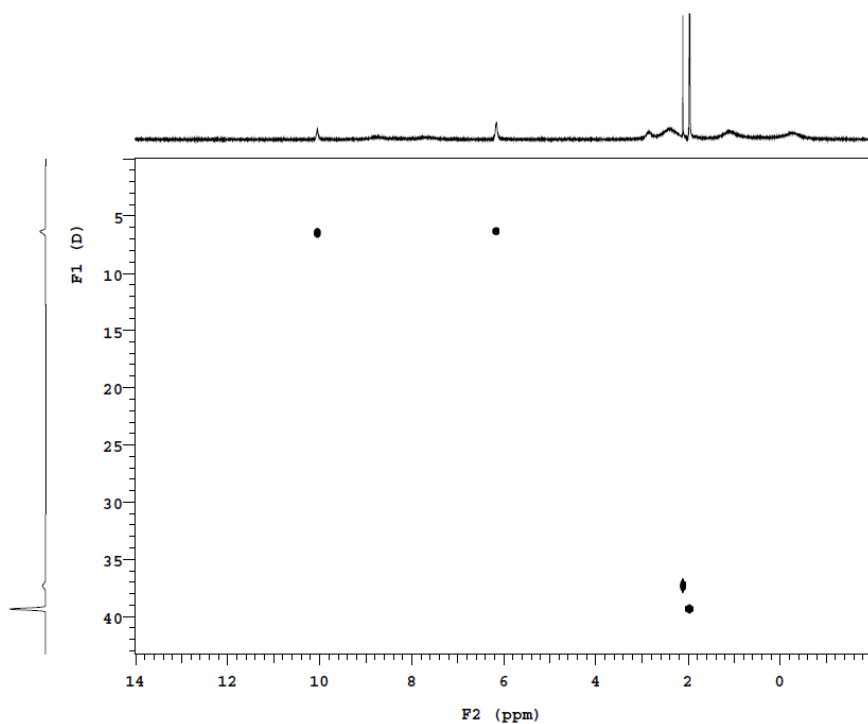


Figure S66. ^1H DOSY-NMR spectrum (500 MHz) of $\text{Fe}_2(\text{L}^{4\text{OIm-meta}})_3(\text{BF}_4)_4$ (**4**) in CD_3CN at $25\text{ }^\circ\text{C}$; unit of D is $10^{-10}\text{ m}^2\text{s}^{-1}$.

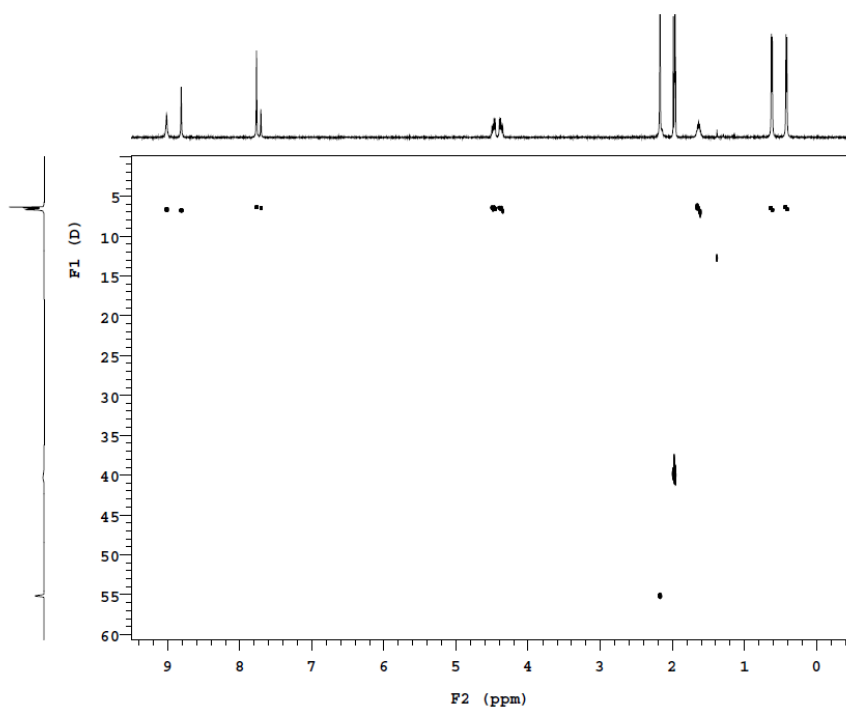


Figure S67. ^1H DOSY-NMR spectrum (500 MHz) of $\text{Fe}_2(\text{L}^{4\text{Sim-meta}})_3(\text{BF}_4)_4$ (**5**) in CD_3CN at $25\text{ }^\circ\text{C}$; unit of D is $10^{-10}\text{ m}^2\text{s}^{-1}$.

Mass spectra

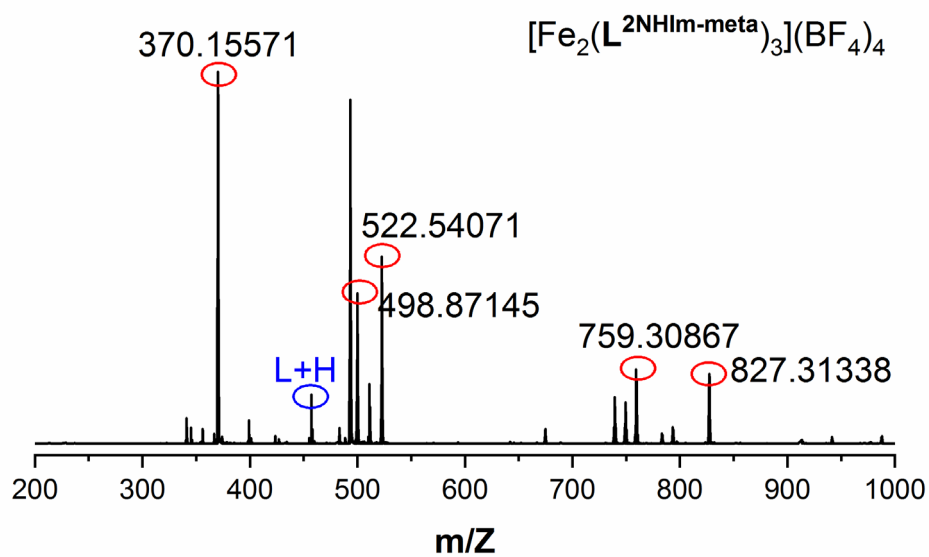


Figure S68. Mass spectrum of $[\text{Fe}_2(\text{L}^{2\text{NHIm-meta}})_3](\text{BF}_4)_4$ (**1**). Fits of the circled peaks are provided in the following figures.

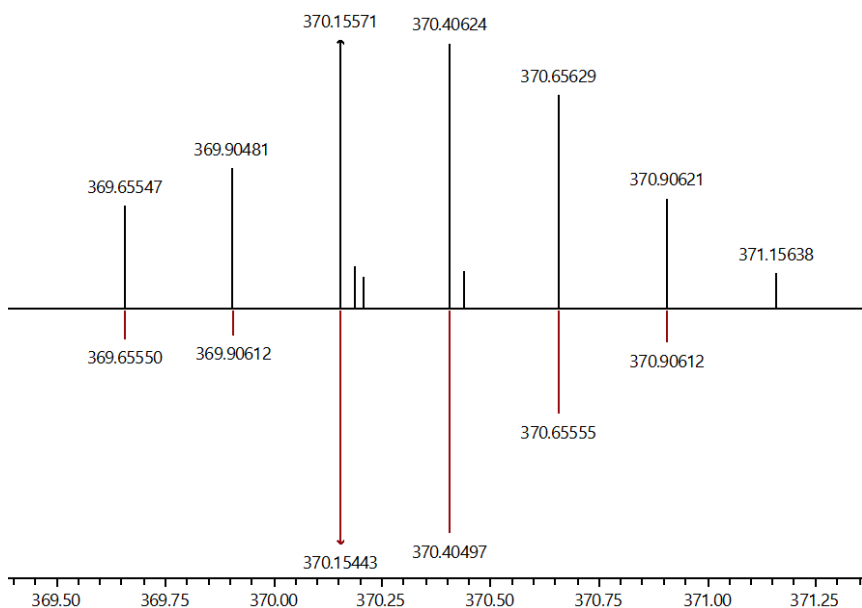


Figure S69. Fit of a peak in the mass spectrum of $[\text{Fe}_2(\text{L}^{2\text{NHIm-meta}})_3](\text{BF}_4)_4$ (**1**) (Figure S67): $[\text{Fe}_2(\text{L}^{2\text{NHIm-meta}})_3]^{4+}$ experimental (black) and simulated pattern (red).

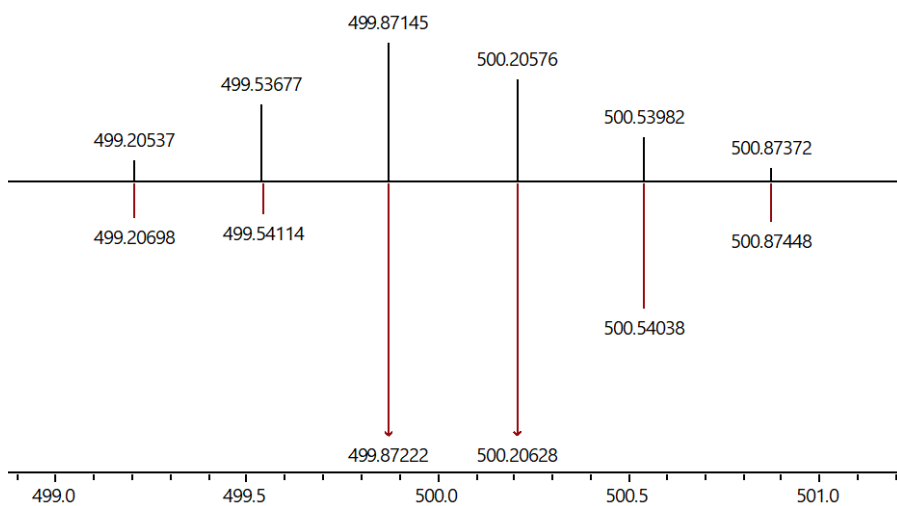


Figure S70. Fit of a peak in the mass spectrum of $[\text{Fe}_2(\text{L}^{2\text{NHIm-meta}})_3](\text{BF}_4)_4$ (**1**) (Figure S67): $[\text{Fe}_2(\text{L}^{2\text{NHIm-meta}})_3](\text{F})^{3+}$ experimental (black) and simulated pattern (red).

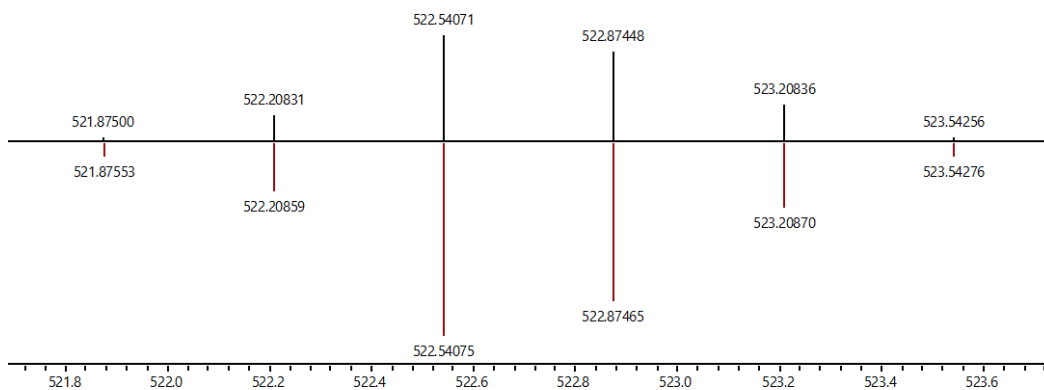


Figure S71. Fit of a peak in the mass spectrum of $[\text{Fe}_2(\text{L}^{2\text{NHIm-meta}})_3](\text{BF}_4)_4$ (**1**) (Figure S67): $[\text{Fe}_2(\text{L}^{2\text{NHIm-meta}})_3](\text{BF}_4)^{3+}$ experimental (black) and simulated pattern (red).

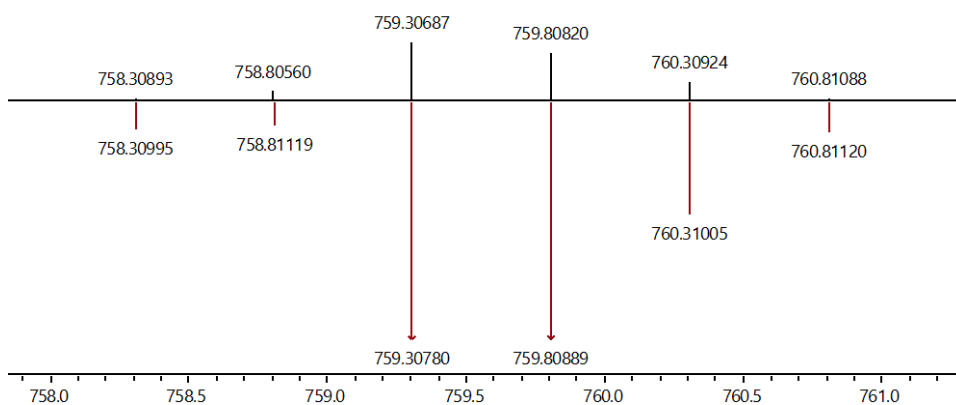


Figure S72. Fit of a peak in the mass spectrum of $[\text{Fe}_2(\text{L}^{2\text{NHIm-meta}})_3](\text{BF}_4)_4$ (**1**) (Figure S67): $[\text{Fe}_2(\text{L}^{2\text{NHIm-meta}})_3](\text{F}_2)^{2+}$ experimental (black) and simulated pattern (red).

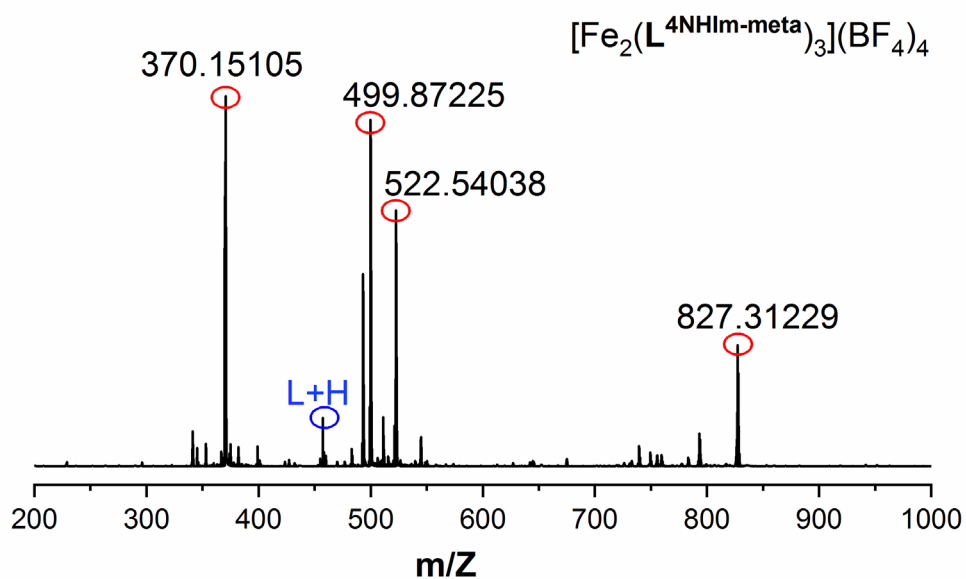


Figure S73. Mass spectrum of $[\text{Fe}_2(\text{L}^{4\text{NHIm-meta}})_3](\text{BF}_4)_4$ (**2**). Fits of the circled peaks are provided in the following figures.

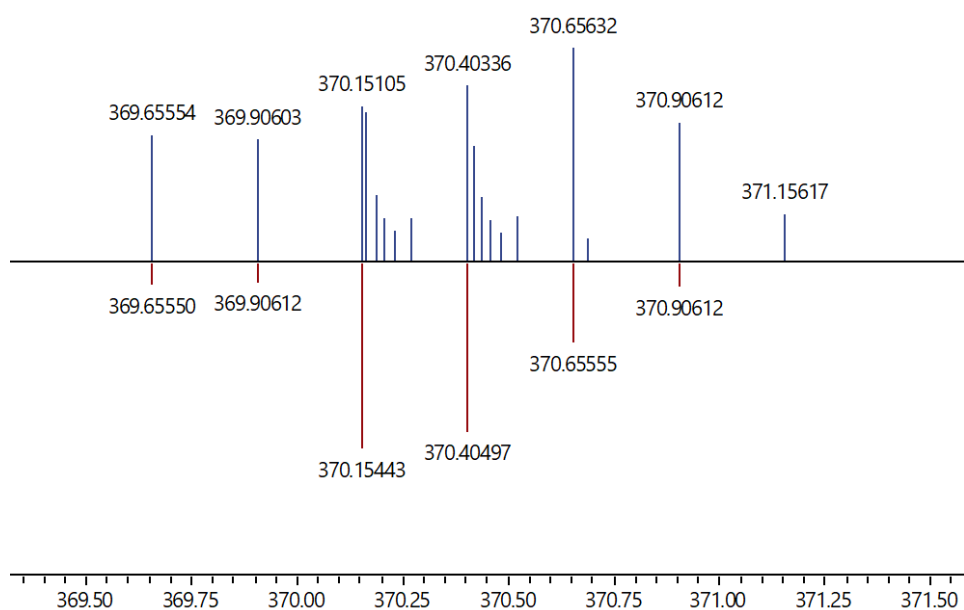


Figure S74. Fit of a peak in the mass spectrum of $[\text{Fe}_2(\text{L}^{4\text{NHIm-meta}})_3](\text{BF}_4)_4$ (**2**) (Figure S72): $[\text{Fe}_2(\text{L}^{4\text{NHIm-meta}})_3]^{4+}$ experimental (blue) and simulated pattern (red).

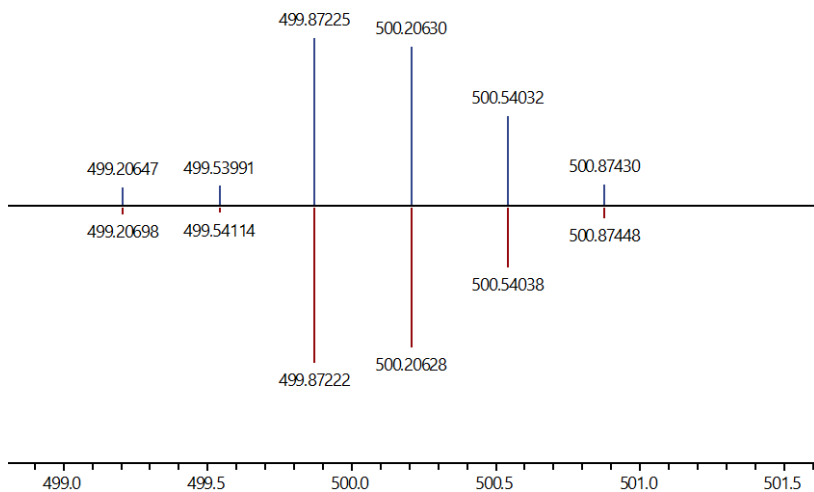


Figure S75. Fit of a peak in the mass spectrum of $[\text{Fe}_2(\text{L}^{4\text{NHIm-meta}})_3](\text{BF}_4)_4$ (**2**) (Figure S72): $[\text{Fe}_2(\text{L}^{4\text{NHIm-meta}})_3](\text{F}_1)^{3+}$ experimental (blue) and simulated pattern (red).

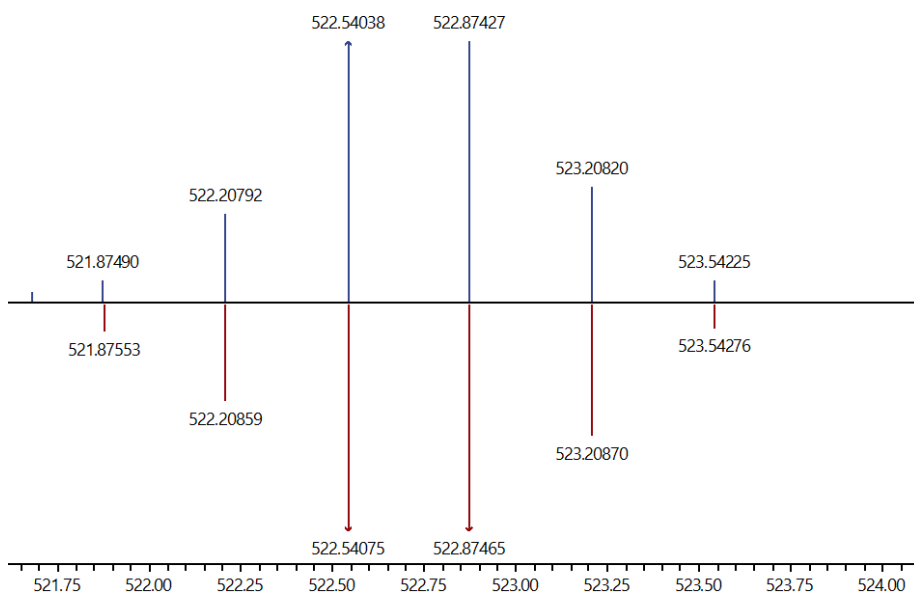


Figure S76. Fit of a peak in the mass spectrum of $[\text{Fe}_2(\text{L}^{4\text{NHIm-meta}})_3](\text{BF}_4)_4$ (**2**) (Figure S72): $[\text{Fe}_2(\text{L}^{4\text{NHIm-meta}})_3](\text{BF}_4)_1^{3+}$ experimental (blue) and simulated pattern (red).

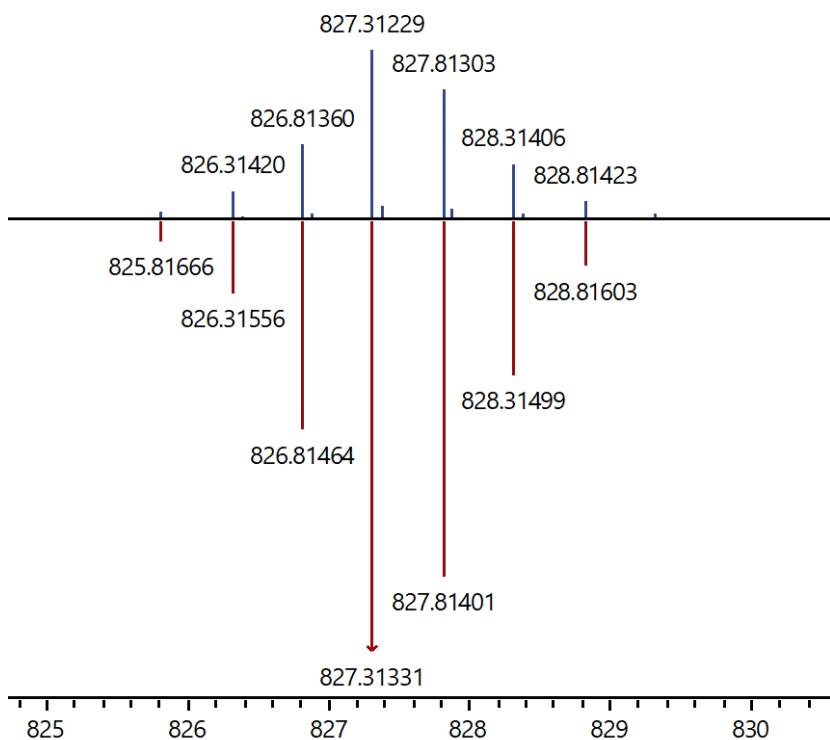


Figure S77. Fit of a peak in the mass spectrum of $[\text{Fe}_2(\text{L}^{4\text{NHIm-meta}})_3](\text{BF}_4)_4$ (**2**) (Figure S72): $[\text{Fe}_2(\text{L}^{4\text{NHIm-meta}})_3](\text{BF}_4)_2^{2+}$ experimental (blue) and simulated pattern (red).

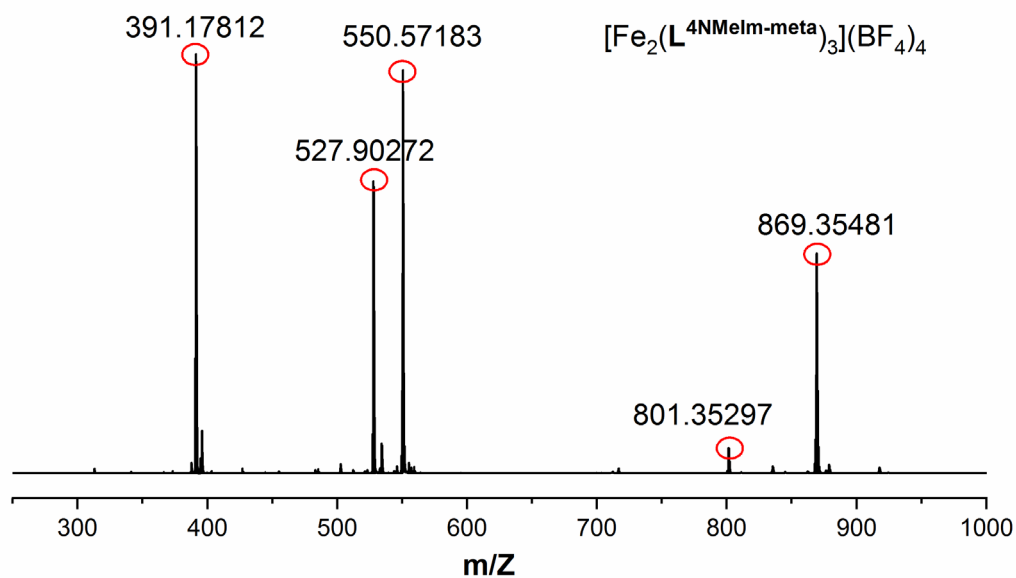


Figure S78. Mass spectrum of $[\text{Fe}_2(\text{L}^{4\text{NMeIm-meta}})_3](\text{BF}_4)_4$ (**3**). Fits of the circled peaks are provided in the following figures.

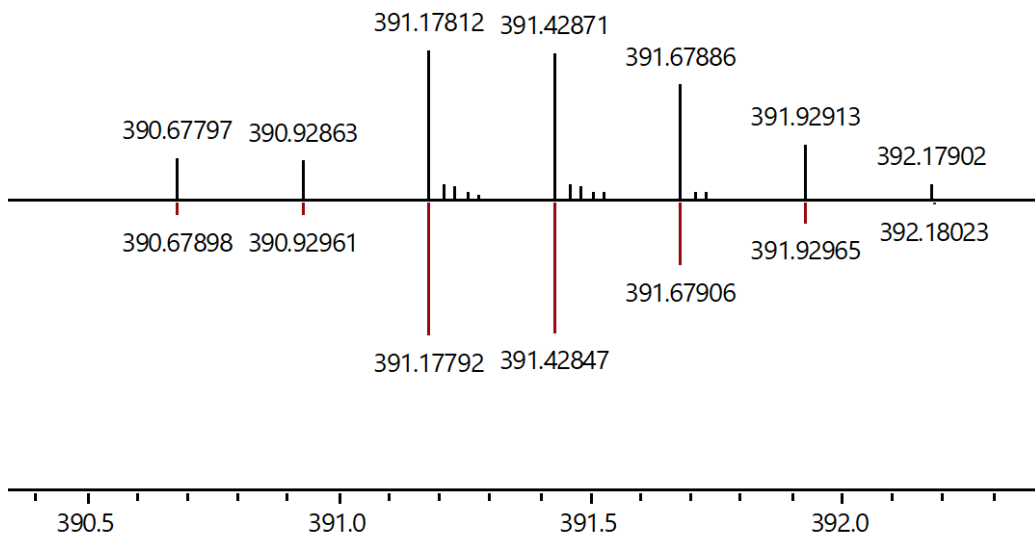


Figure S79. Fit of a peak in the mass spectrum of $[\text{Fe}_2(\text{L}^{4\text{NMelm-meta}})_3](\text{BF}_4)_4$ (**3**) (Figure S77): $[\text{Fe}_2(\text{L}^{4\text{NMelm-meta}})_3]^{4+}$ experimental (black) and simulated pattern (red).

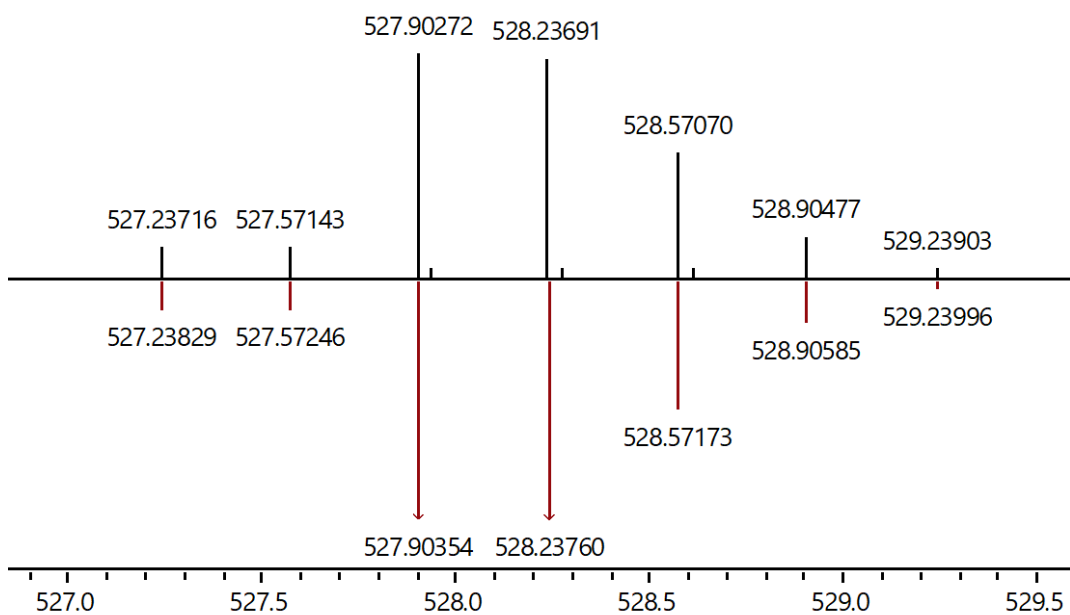


Figure S80. Fit of a peak in the mass spectrum of $[\text{Fe}_2(\text{L}^{4\text{NMelm-meta}})_3](\text{BF}_4)_4$ (**3**) (Figure S77): $[\text{Fe}_2(\text{L}^{4\text{NMelm-meta}})_3](\text{F})^{3+}$ experimental (black) and simulated pattern (red).

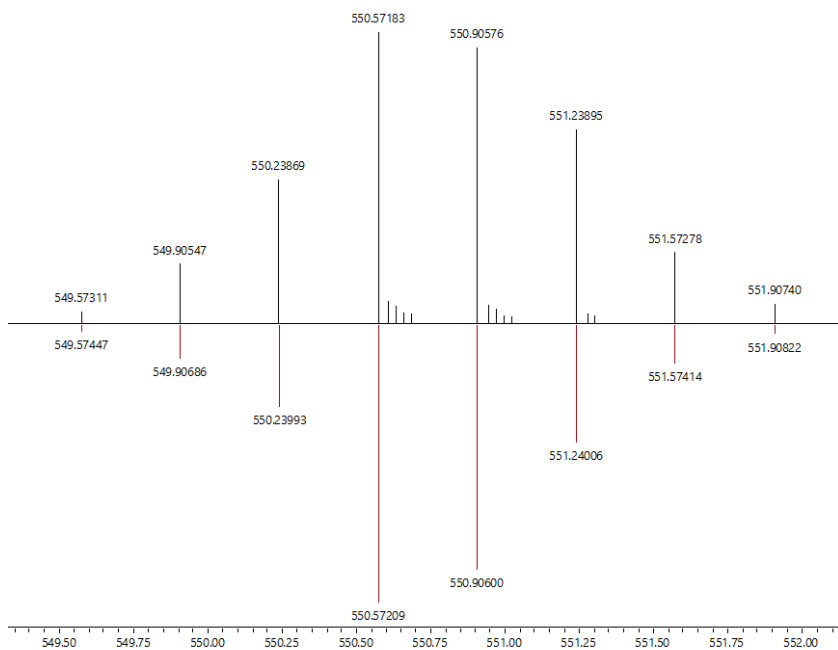


Figure S81. Fit of a peak in the mass spectrum of $[\text{Fe}_2(\text{L}^{4\text{NMeIm-meta}})_3](\text{BF}_4)_4$ (**3**) (Figure S77): $[\text{Fe}_2(\text{L}^{4\text{NMeIm-meta}})_3](\text{BF}_4)^{3+}$ experimental (black) and simulated pattern (red).

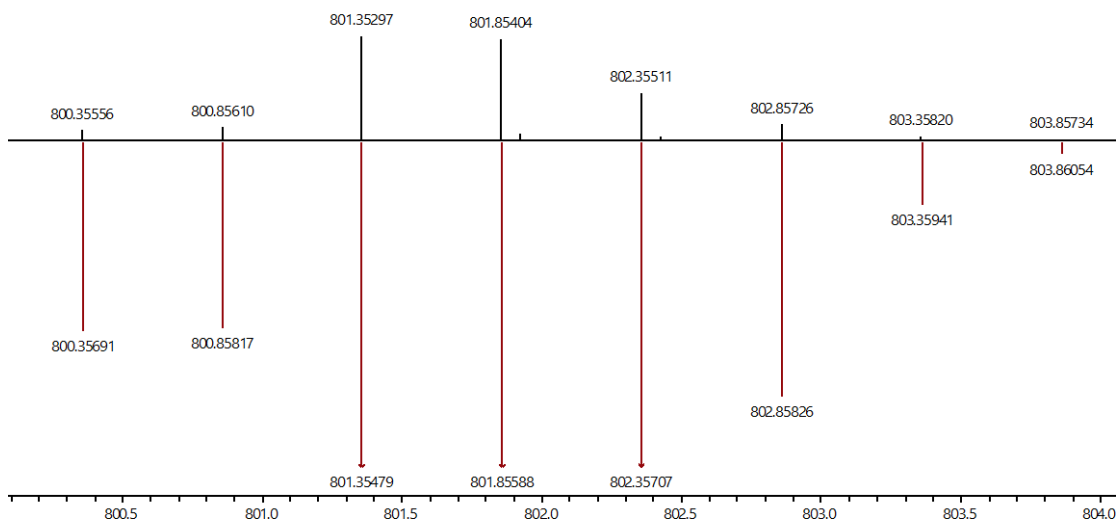


Figure S82. Fit of a peak in the mass spectrum of $[\text{Fe}_2(\text{L}^{4\text{NMeIm-meta}})_3](\text{BF}_4)_4$ (**3**) (Figure S77): $[\text{Fe}_2(\text{L}^{4\text{NMeIm-meta}})_3](\text{F}_2)^{2+}$ experimental (black) and simulated pattern (red).

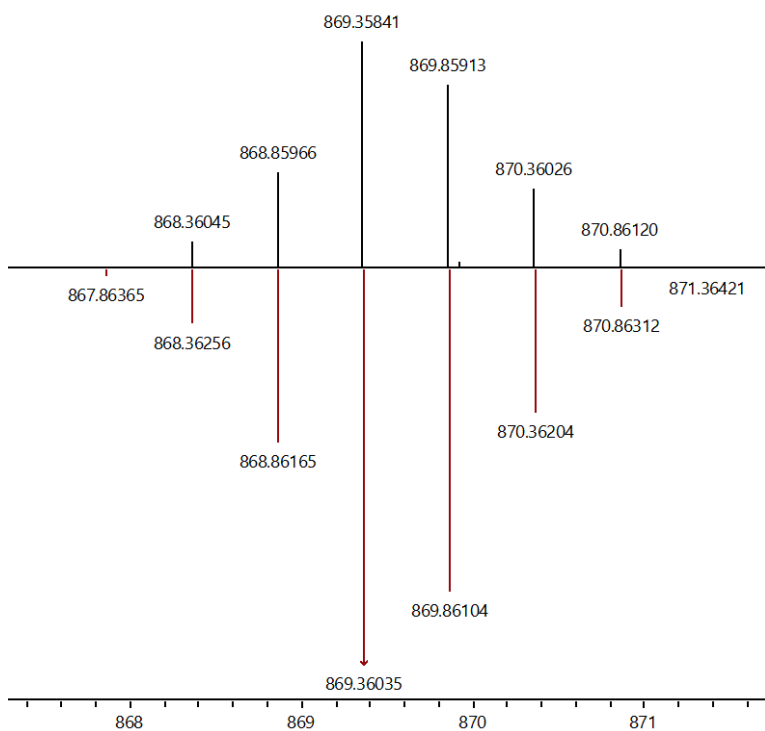


Figure S83. Fit of a peak in the mass spectrum of $[\text{Fe}_2(\text{L}^{4\text{NMelm-meta}})_3](\text{BF}_4)_4$ (**3**) (Figure S77): $[\text{Fe}_2(\text{L}^{4\text{NMelm-meta}})_3](\text{BF}_4)_2^{2+}$ experimental (black) and simulated pattern (red).

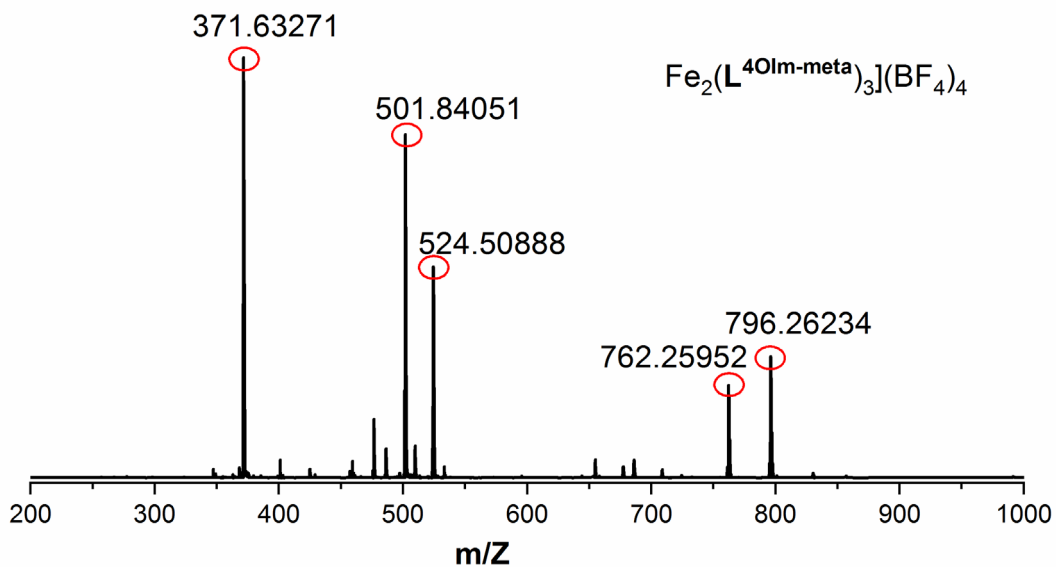


Figure S84. Mass spectrum of $[\text{Fe}_2(\text{L}^{4\text{OIm-meta}})_3](\text{BF}_4)_4$ (**4**). Fits of the circled peaks are provided in the following figures.

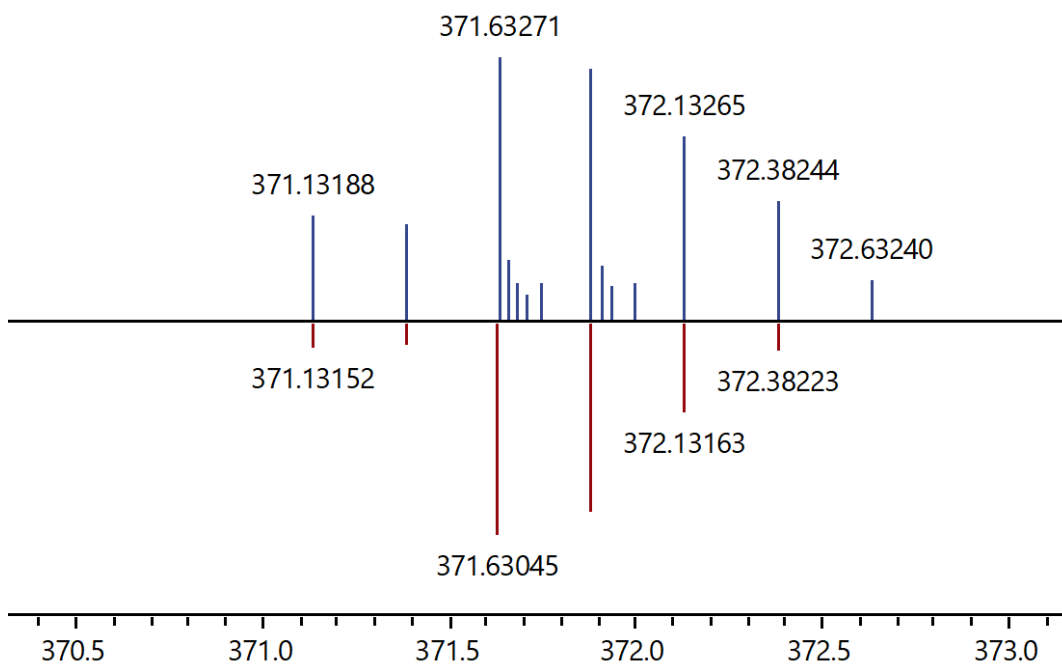


Figure S85. Fit of a peak in the mass spectrum of $[\text{Fe}_2(\text{L}^{40\text{Im-meta}})_3](\text{BF}_4)_4$ (**4**) (Figure S83): $[\text{Fe}_2(\text{L}^{40\text{Im-meta}})_3]^{4+}$ experimental (blue) and simulated pattern (red).

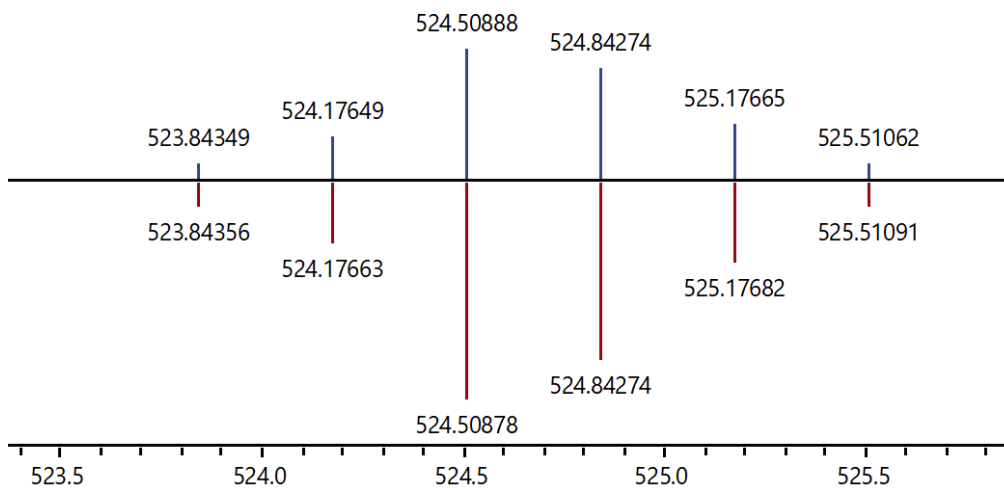


Figure S86. Fit of a peak in the mass spectrum of $[\text{Fe}_2(\text{L}^{40\text{Im-meta}})_3](\text{BF}_4)_4$ (**4**) (Figure S83): $[\text{Fe}_2(\text{L}^{40\text{Im-meta}})_3](\text{BF}_4)^{3+}$ experimental (blue) and simulated pattern (red).

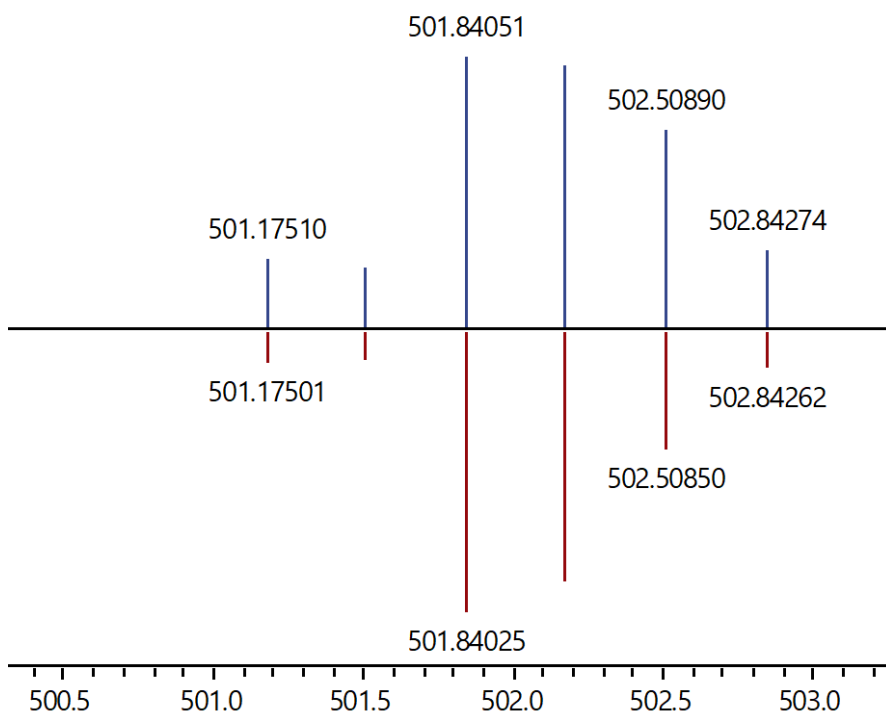


Figure S87. Fit of a peak in the mass spectrum of $[\text{Fe}_2(\text{L}^{40\text{Im-meta}})_3](\text{BF}_4)_4$ (**4**) (Figure S83): $[\text{Fe}_2(\text{L}^{40\text{Im-meta}})_3](\text{F})^{3+}$ experimental (blue) and simulated pattern (red).

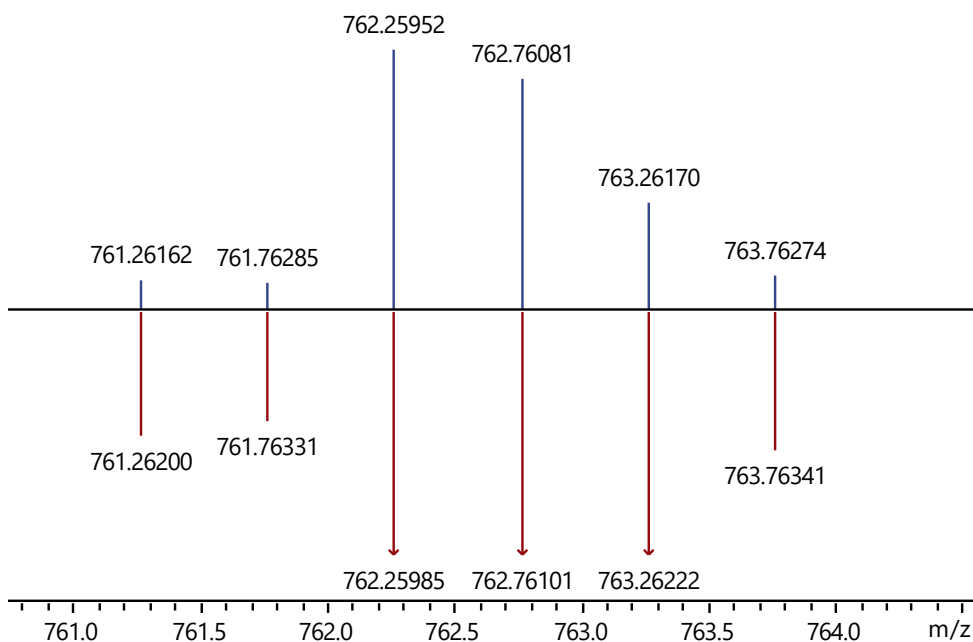


Figure S88. Fit of a peak in the mass spectrum of $[\text{Fe}_2(\text{L}^{40\text{Im-meta}})_3](\text{BF}_4)_4$ (**4**) (Figure S83): $[\text{Fe}_2(\text{L}^{40\text{Im-meta}})_3](\text{F}_2)^{2+}$ experimental (blue) and simulated pattern (red).

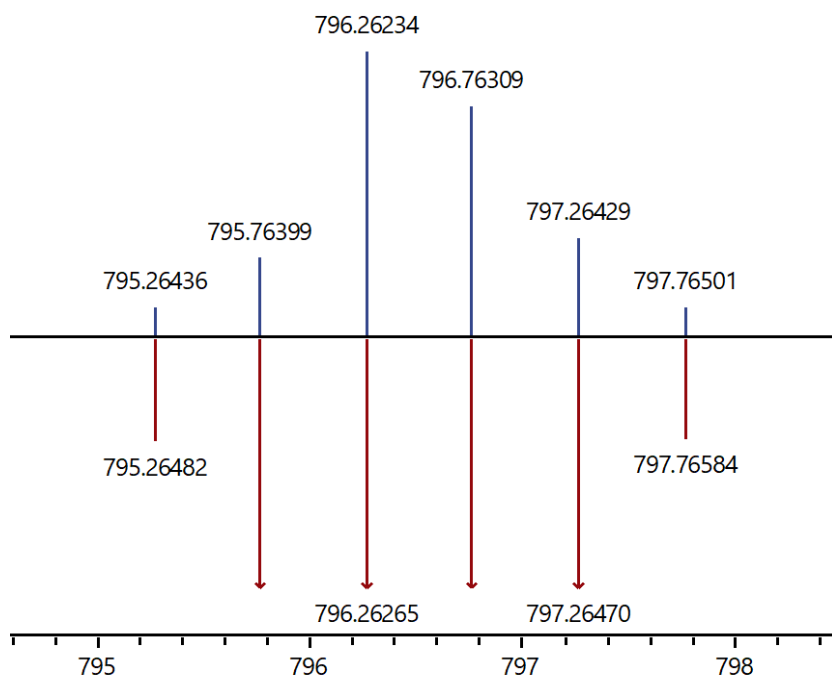


Figure S89. Fit of a peak in the mass spectrum of $[\text{Fe}_2(\text{L}^{4\text{OIm-meta}})_3](\text{BF}_4)_4$ (**4**) (Figure S83): $[\text{Fe}_2(\text{L}^{4\text{OIm-meta}})_3](\text{BF}_4)(\text{F})^{2+}$ experimental (blue) and simulated pattern (red).

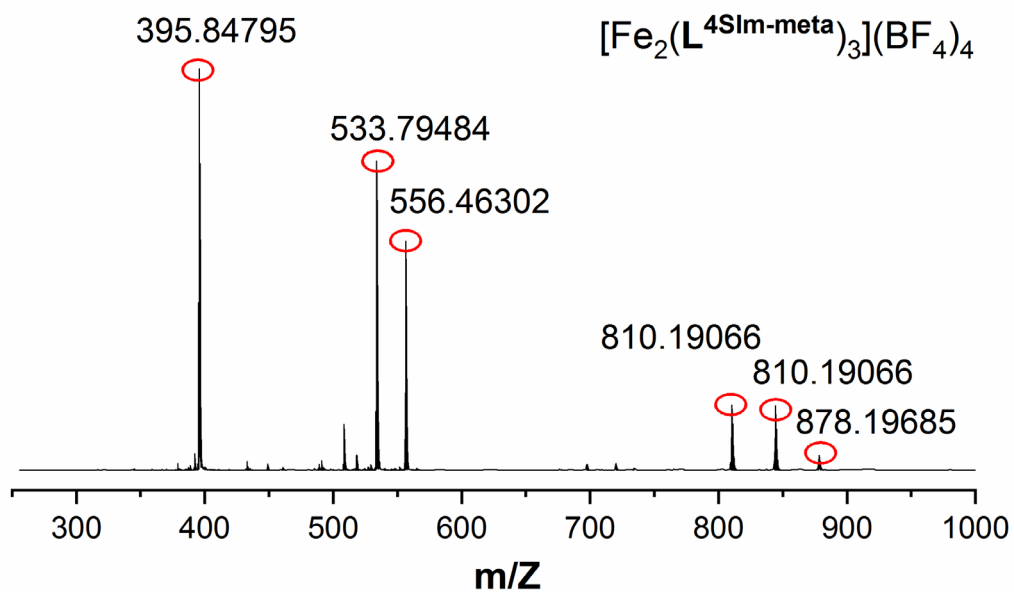


Figure S90. Mass spectrum of $[\text{Fe}_2(\text{L}^{4\text{Sim-meta}})_3](\text{BF}_4)_4$ (**5**). Fits of the circled peaks are provided in the following figures.

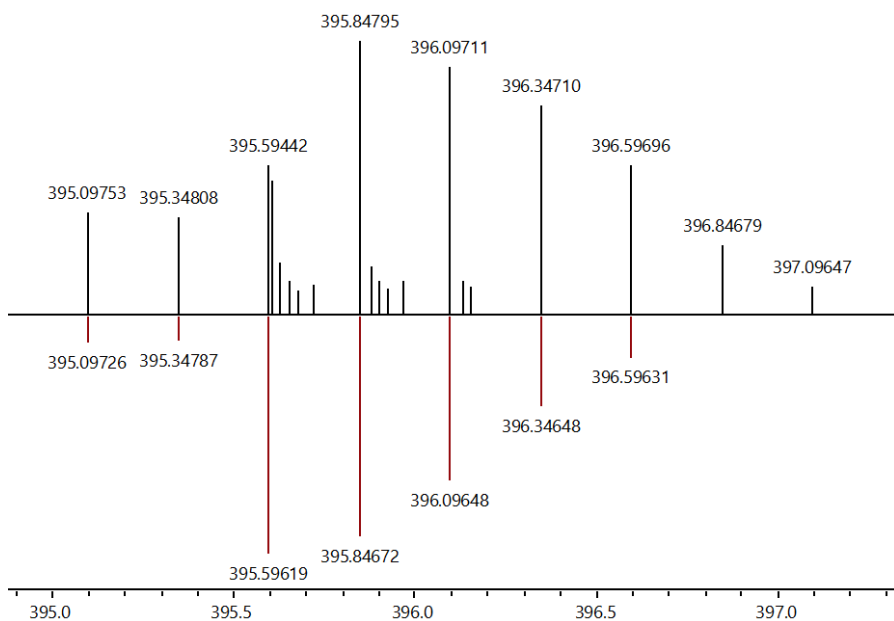


Figure S91. Fit of a peak in the mass spectrum of $[\text{Fe}_2(\text{L}^{4\text{Sim-meta}})_3](\text{BF}_4)_4$ (**5**) (Figure S89): $[\text{Fe}_2(\text{L}^{4\text{Sim-meta}})_3]^{4+}$ experimental (black) and simulated pattern (red).

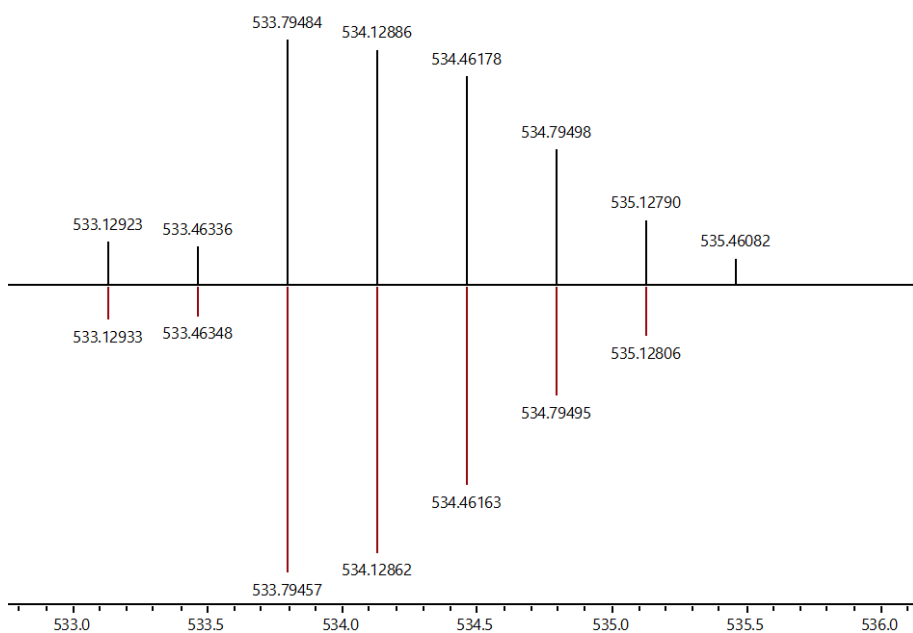


Figure S92. Fit of a peak in the mass spectrum of $[\text{Fe}_2(\text{L}^{4\text{Sim-meta}})_3](\text{BF}_4)_4$ (**5**) (Figure S89): $[\text{Fe}_2(\text{L}^{4\text{Sim-meta}})_3](\text{F})^{3+}$ experimental (black) and simulated pattern (red).

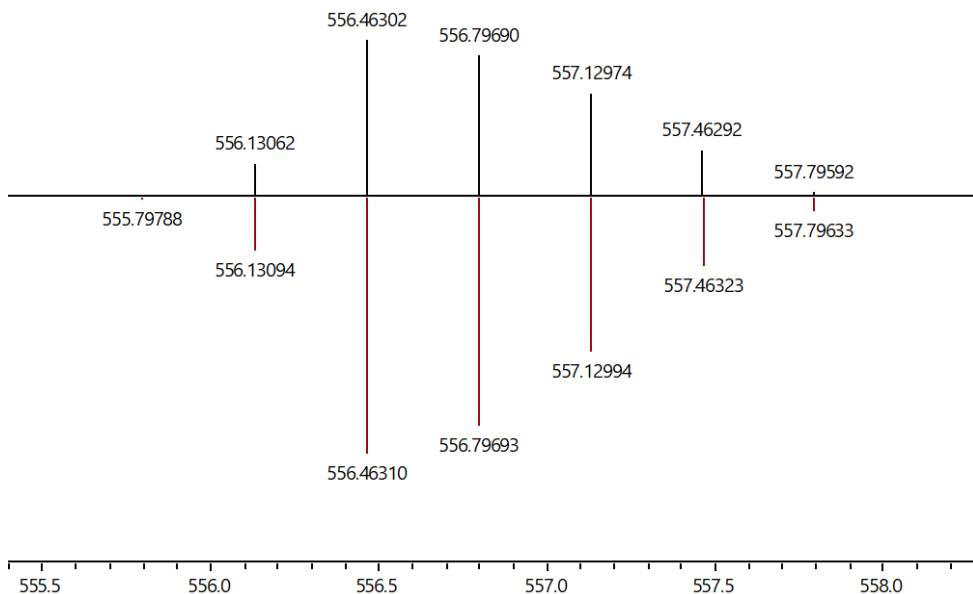


Figure S93. Fit of a peak in the mass spectrum of $[\text{Fe}_2(\text{L}^{4\text{Sim-meta}})_3](\text{BF}_4)_4$ (**5**) (Figure S89): $[\text{Fe}_2(\text{L}^{4\text{Sim-meta}})_3](\text{BF}_4)^{3+}$ experimental (black) and simulated pattern (red).

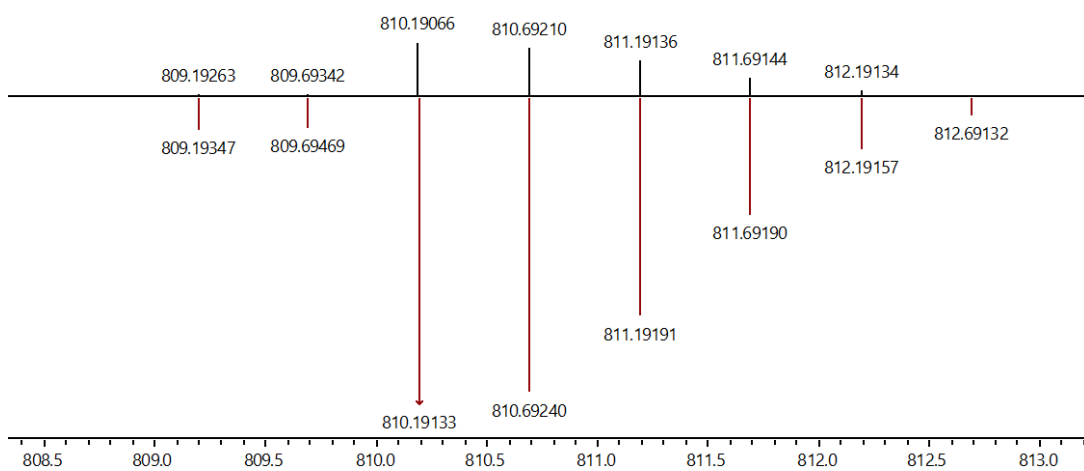


Figure S94. Fit of a peak in the mass spectrum of $[\text{Fe}_2(\text{L}^{4\text{Sim-meta}})_3](\text{BF}_4)_4$ (**5**) (Figure S89): $[\text{Fe}_2(\text{L}^{4\text{Sim-meta}})_3](\text{F}_2)^{2+}$ experimental (black) and simulated pattern (red).

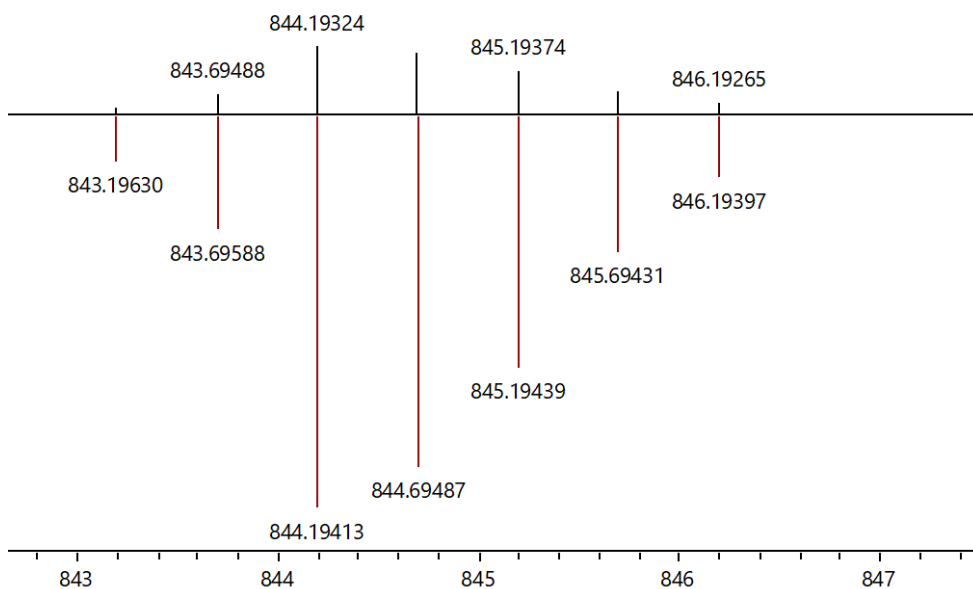


Figure S95. Fit of a peak in the mass spectrum of $[\text{Fe}_2(\text{L}^{4\text{Sim-meta}})_3](\text{BF}_4)_4$ (**5**) (Figure S89): $[\text{Fe}_2(\text{L}^{4\text{Sim-meta}})_3](\text{BF}_4)(\text{F})^{2+}$ experimental (black) and simulated pattern (red).

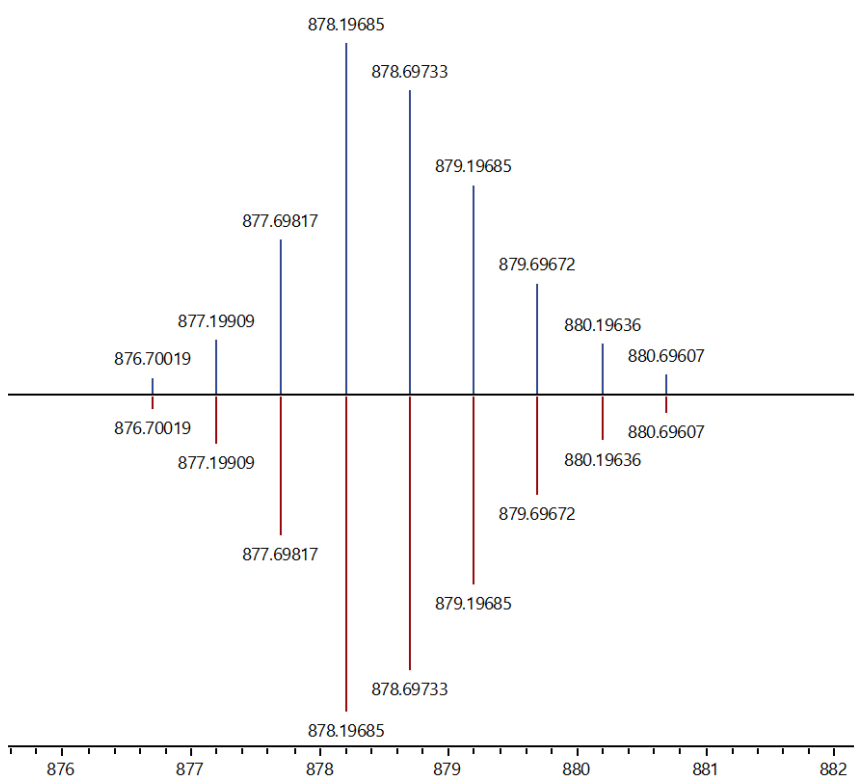


Figure S96. Fit of a peak in the mass spectrum of $[\text{Fe}_2(\text{L}^{4\text{Sim-meta}})_3](\text{BF}_4)_4$ (**5**) (Figure S89): $[\text{Fe}_2(\text{L}^{4\text{Sim-meta}})_3](\text{BF}_4)_2^{2+}$ experimental (black) and simulated pattern (red).

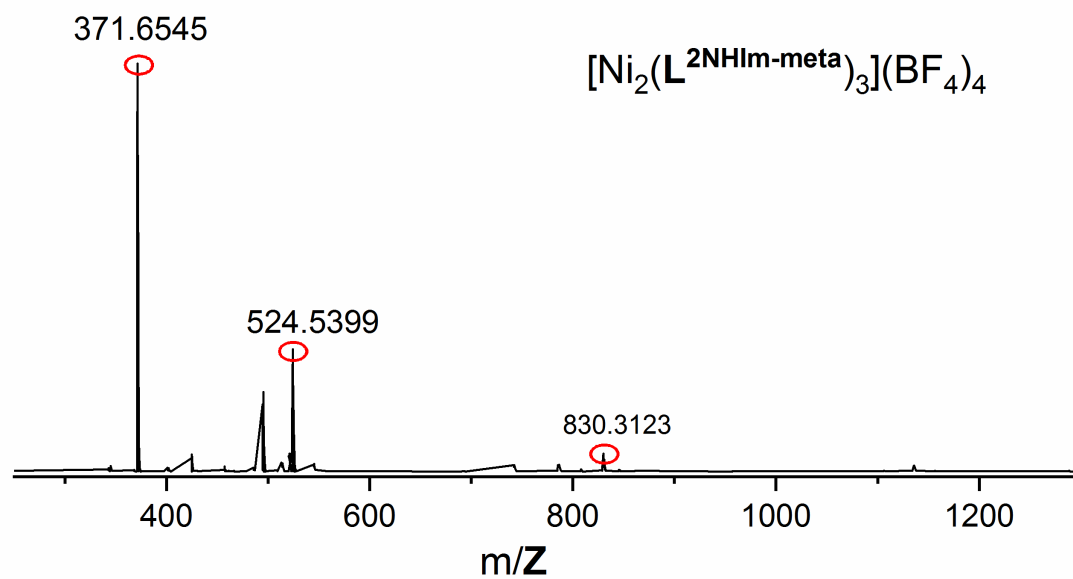


Figure S97. Mass spectrum of $[\text{Ni}_2(\text{L}^{2\text{NHIm-meta}})_3](\text{BF}_4)_4$ ($\mathbf{1}^{\text{Ni}}$). Fits of the circled peaks are provided in the following figures.

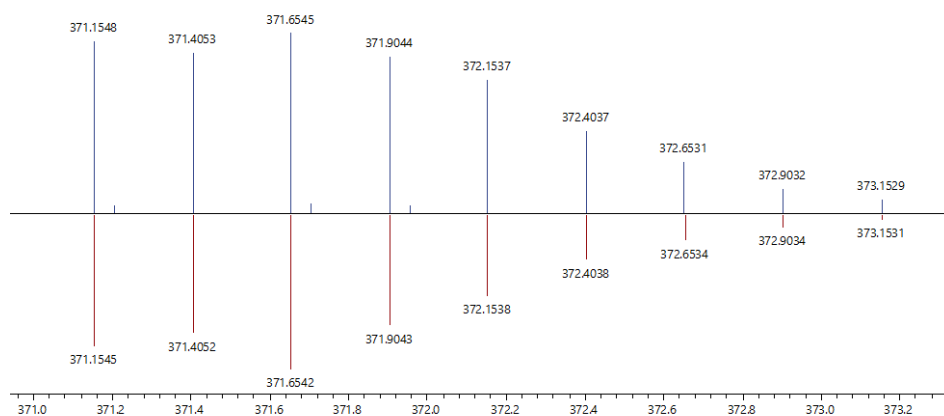


Figure S98. Fit of a peak in the mass spectrum of $[\text{Ni}_2(\text{L}^{2\text{NHIm-meta}})_3](\text{BF}_4)_4$ ($\mathbf{1}^{\text{Ni}}$) (Figure S96): $[\text{Ni}_2(\text{L}^{2\text{NHIm-meta}})_3]^{4+}$ experimental (blue) and simulated pattern (red).

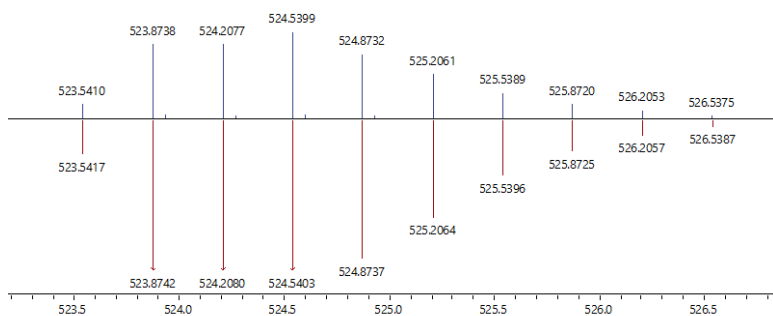


Figure S99. Fit of a peak in the mass spectrum of $[\text{Ni}_2(\text{L}^{2\text{NHIm-meta}})_3](\text{BF}_4)_4$ (1^{Ni}) (Figure S96): $([\text{Ni}_2(\text{L}^{2\text{NHIm-meta}})_3](\text{BF}_4)_4)^{3+}$ experimental (blue) and simulated pattern (red).

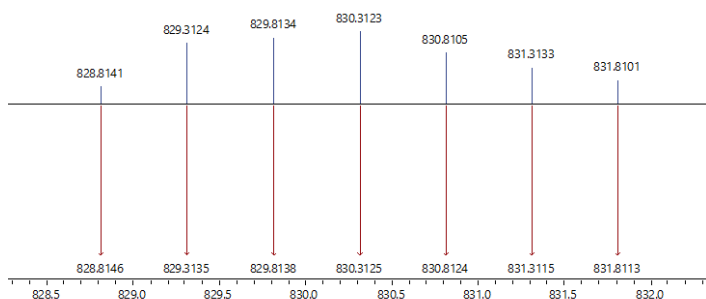


Figure S100. Fit of a peak in the mass spectrum of $[\text{Ni}_2(\text{L}^{2\text{NHIm-meta}})_3](\text{BF}_4)_4$ (1^{Ni}) (Figure S96): $([\text{Ni}_2(\text{L}^{2\text{NHIm-meta}})_3](\text{BF}_4)_4)^{2+}$ experimental (blue) and simulated pattern (red).

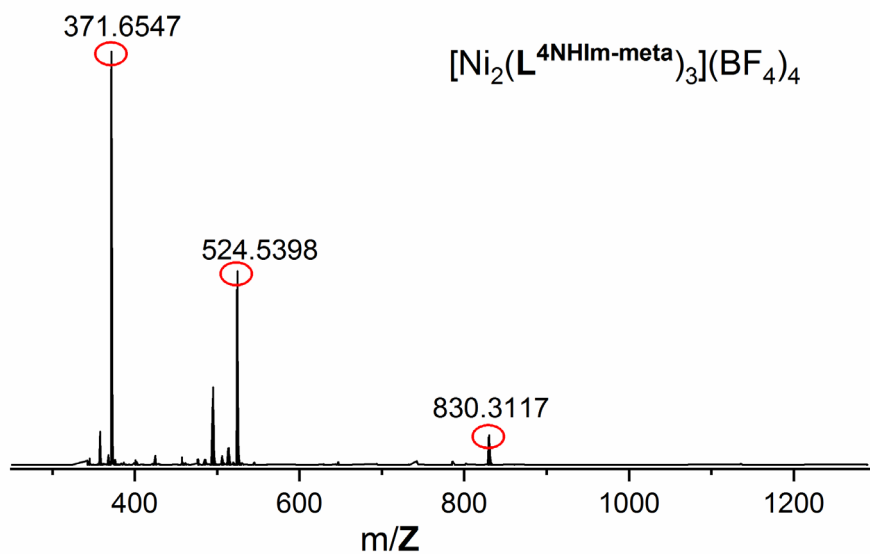


Figure S101. Mass spectrum of $[\text{Ni}_2(\text{L}^{4\text{NHIm-meta}})_3](\text{BF}_4)_4$ (2^{Ni}). Fits of the circled peaks are provided in the following figures.

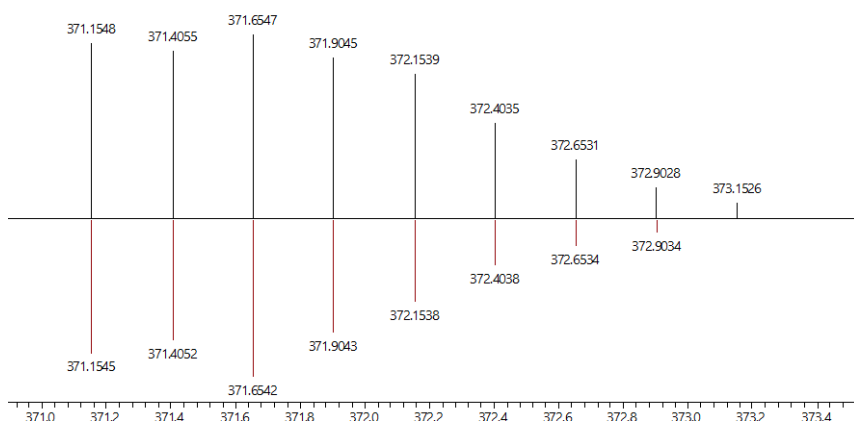


Figure S102. Fit of a peak in the mass spectrum of $[\text{Ni}_2(\text{L}^{4\text{NHIm-meta}})_3](\text{BF}_4)_4$ (2^{Ni}) (Figure S100): $([\text{Ni}_2(\text{L}^{4\text{NHIm-meta}})_3])^{4+}$ experimental (black) and simulated pattern (red).

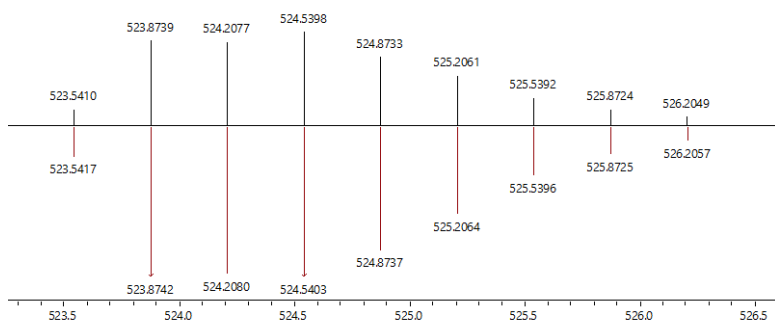


Figure S103. Fit of a peak in the mass spectrum of $[\text{Ni}_2(\text{L}^{4\text{NHIm-meta}})_3](\text{BF}_4)_4$ (2^{Ni}) (Figure S100): $([\text{Ni}_2(\text{L}^{4\text{NHIm-meta}})_3](\text{BF}_4))^{3+}$ experimental (black) and simulated pattern (red).

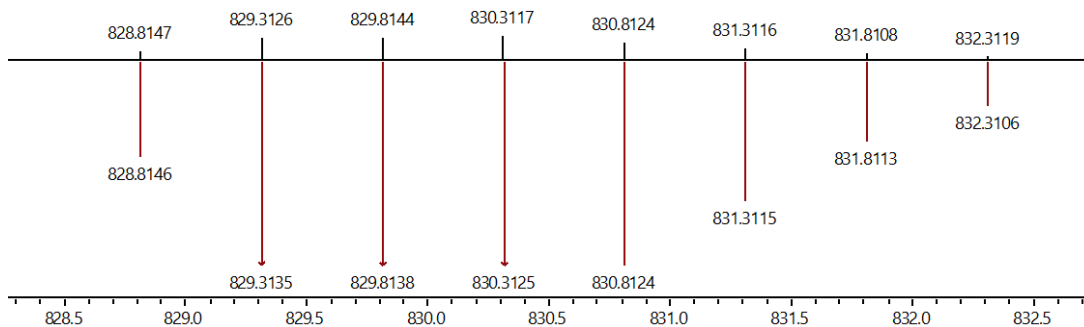


Figure S104. Fit of a peak in the mass spectrum of $[\text{Ni}_2(\text{L}^{4\text{NHIm-meta}})_3](\text{BF}_4)_4$ (2^{Ni}) (Figure S100): $([\text{Ni}_2(\text{L}^{4\text{NHIm-meta}})_3](\text{BF}_4)_2)^{3+}$ experimental (black) and simulated pattern (red).

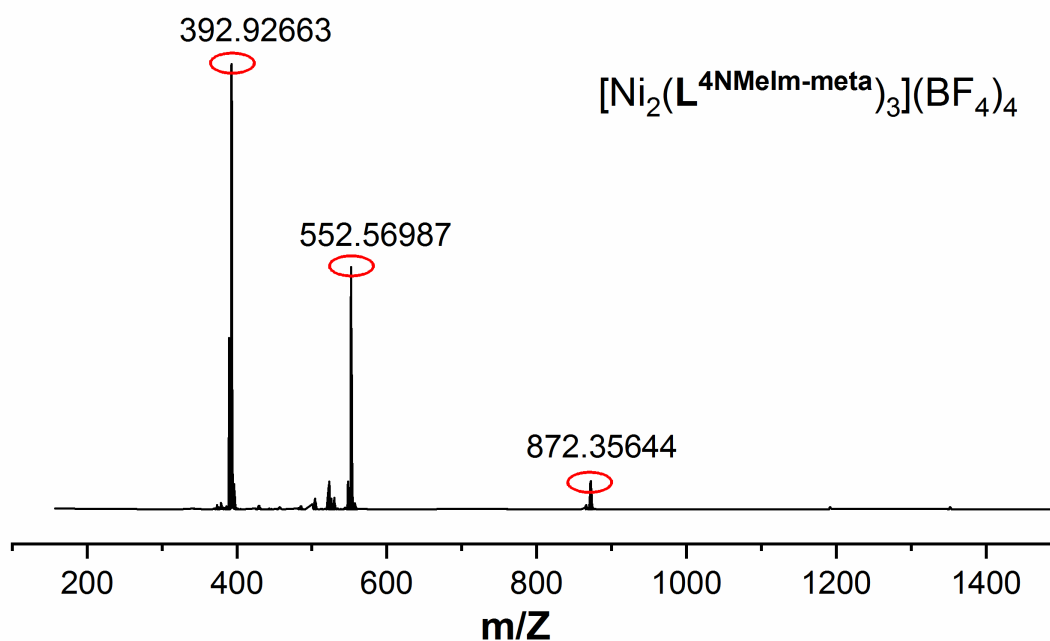


Figure S105. Mass spectrum of $[\text{Ni}_2(\text{L}^{4\text{NMelm-meta}})_3](\text{BF}_4)_4$ (3^{Ni}). Fits of the circled peaks are provided in the following figures.

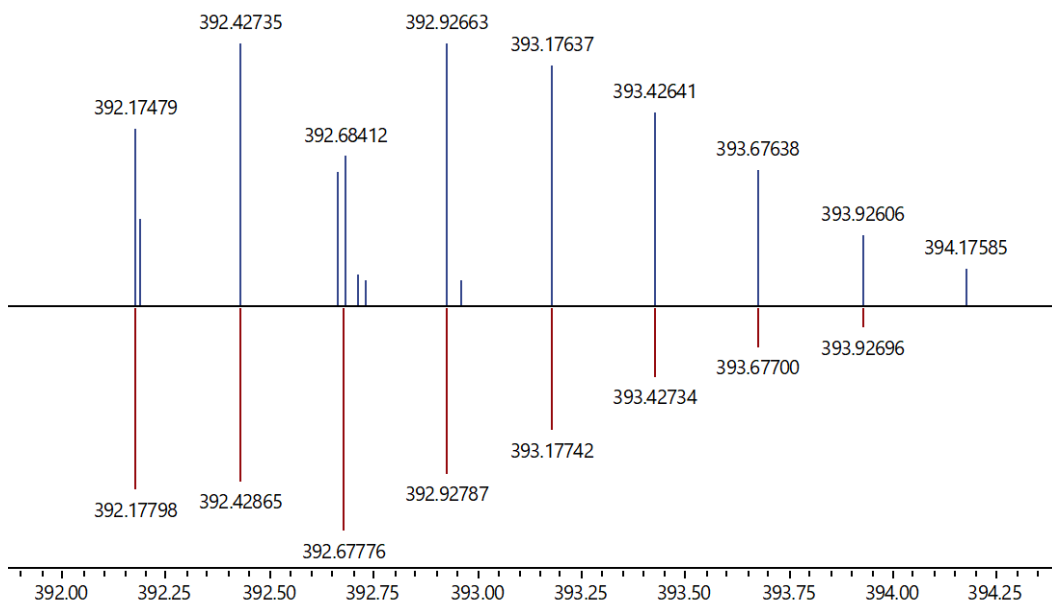


Figure S106. Fit of a peak in the mass spectrum of $[\text{Ni}_2(\text{L}^{4\text{NMelm-meta}})_3](\text{BF}_4)_4$ (3^{Ni}) (Figure S104): $[\text{Ni}_2(\text{L}^{4\text{NMelm-meta}})_3]^{4+}$ experimental (blue) and simulated pattern (red).

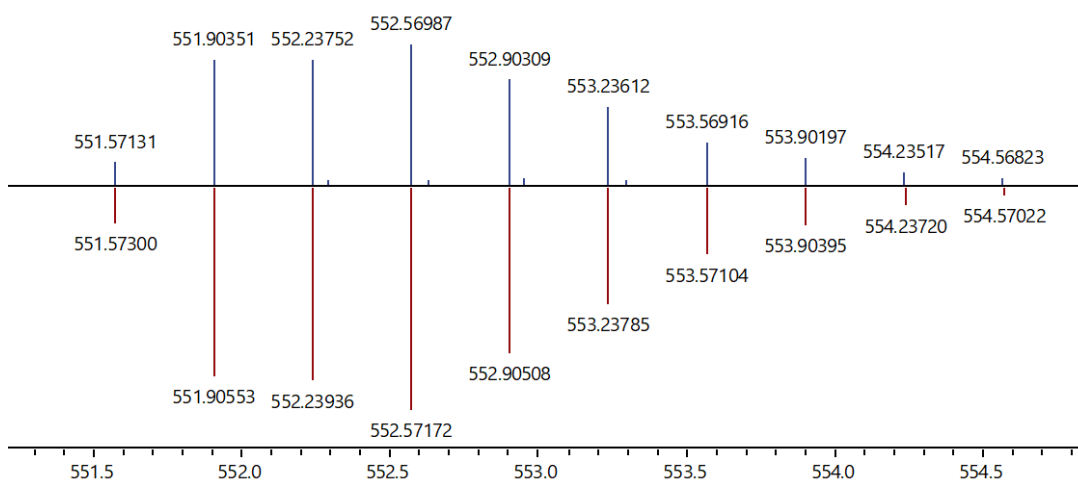


Figure S107. Fit of a peak in the mass spectrum of $[\text{Ni}_2(\text{L}^{4\text{NMelm-meta}})_3](\text{BF}_4)_4$ (3^{Ni}) (Figure S104): $[\text{Ni}_2(\text{L}^{4\text{NMelm-meta}})_3](\text{BF}_4)^{3+}$ experimental (blue) and simulated pattern (red).

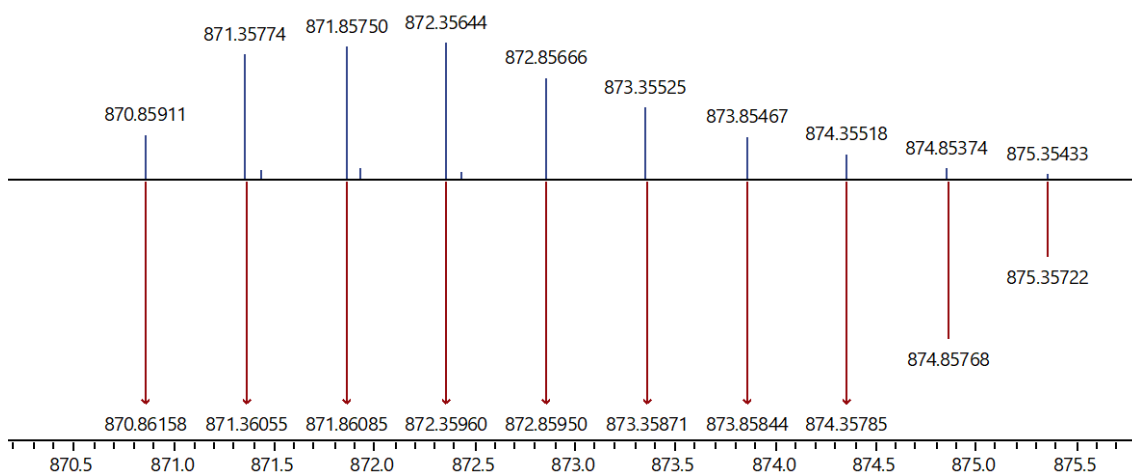


Figure S108. Fit of a peak in the mass spectrum of $[\text{Ni}_2(\text{L}^{4\text{NMelm-meta}})_3](\text{BF}_4)_4$ (3^{Ni}) (Figure S104): $[\text{Ni}_2(\text{L}^{4\text{NMelm-meta}})_3](\text{BF}_4)_2^{2+}$ experimental (blue) and simulated pattern (red).

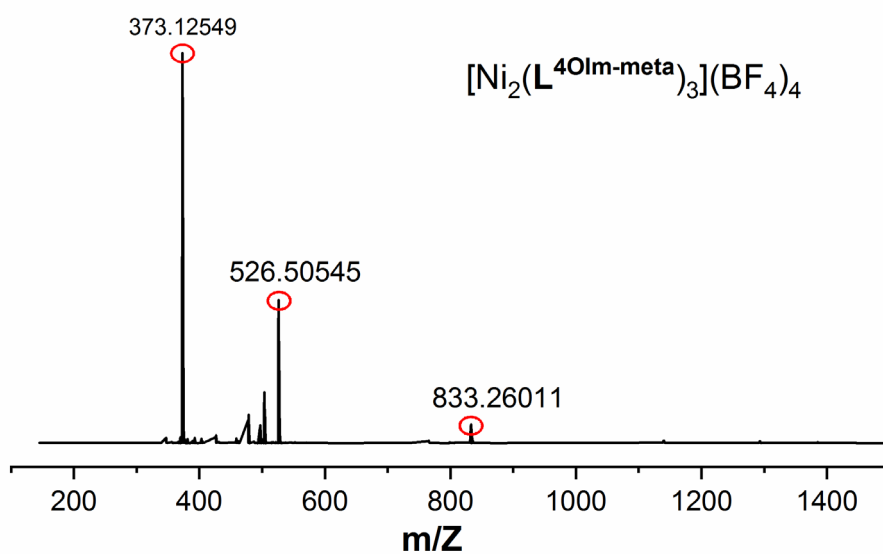


Figure S109. Mass spectrum of $[\text{Ni}_2(\text{L}^{4\text{OIm-meta}})_3](\text{BF}_4)_4$ (4^{Ni}). Fits of the circled peaks are provided in the following figures.

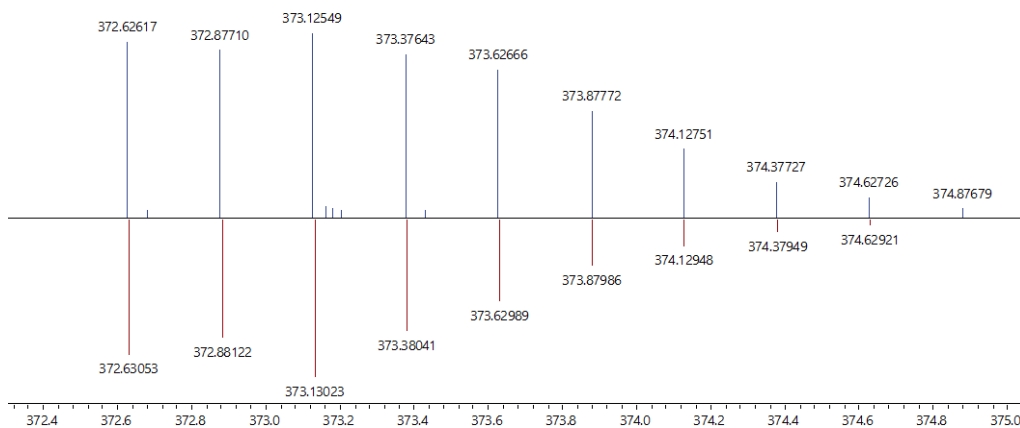


Figure S110. Fit of a peak in the mass spectrum of $[\text{Ni}_2(\text{L}^{4\text{OIm-meta}})_3](\text{BF}_4)_4$ (4Ni) (Figure S108): $[\text{Ni}_2(\text{L}^{4\text{OIm-meta}})_3]^{4+}$ experimental (blue) and simulated pattern (red).

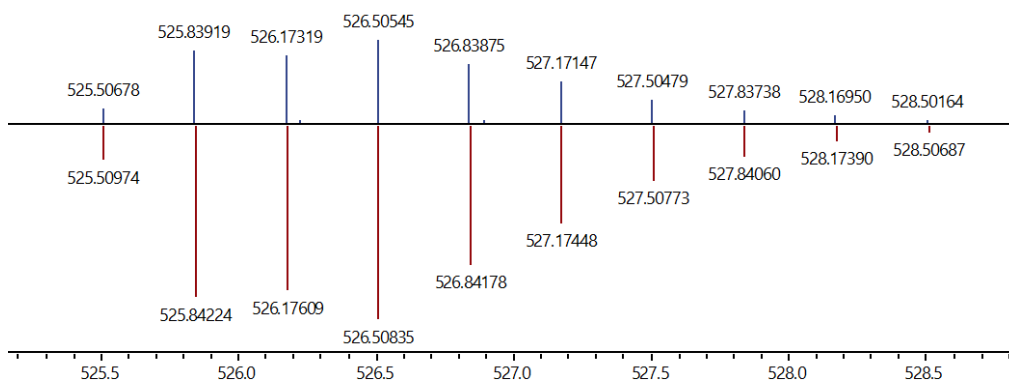


Figure S111. Fit of a peak in the mass spectrum of $[\text{Ni}_2(\text{L}^{4\text{OIm-meta}})_3](\text{BF}_4)_4$ (4Ni) (Figure S108): $[\text{Ni}_2(\text{L}^{4\text{OIm-meta}})_3](\text{BF}_4)^{3+}$ experimental (blue) and simulated pattern (red).

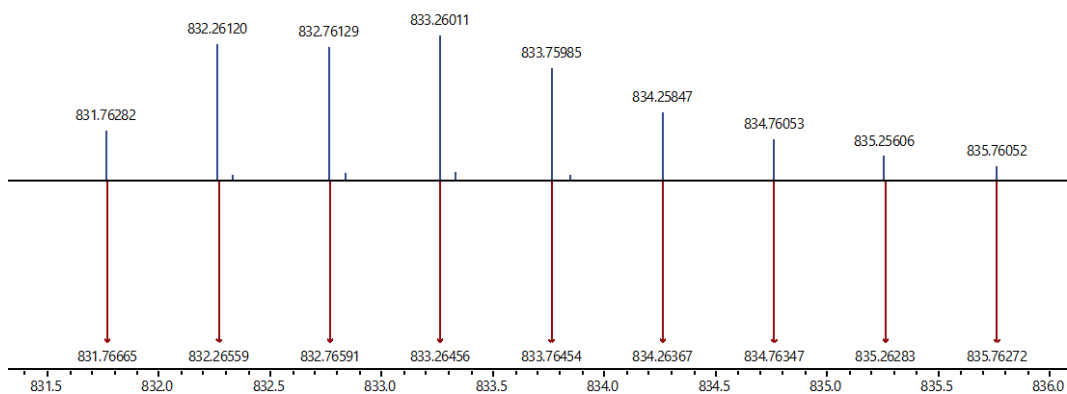


Figure S112. Fit of a peak in the mass spectrum of $[\text{Ni}_2(\text{L}^{4\text{OIm-meta}})_3](\text{BF}_4)_4$ (4^{Ni}) (Figure S108): $[\text{Ni}_2(\text{L}^{4\text{OIm-meta}})_3](\text{BF}_4)_2^{2+}$ experimental (blue) and simulated pattern (red).

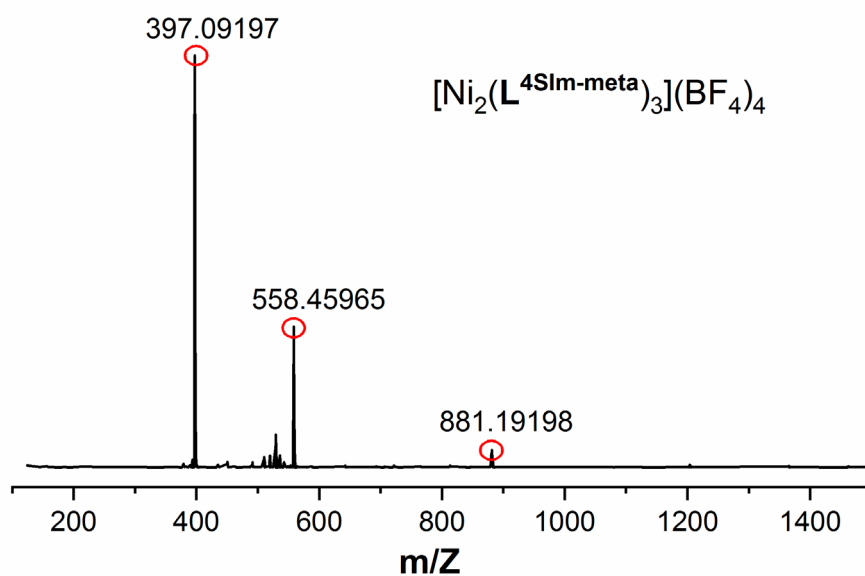


Figure S113. Mass spectrum of $[\text{Ni}_2(\text{L}^{4\text{SIm-meta}})_3](\text{BF}_4)_4$ (5^{Ni}). Fits of the circled peaks are provided in the following figures.

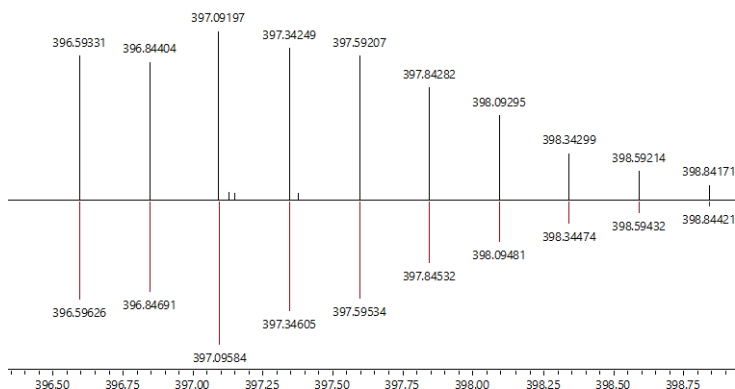


Figure S114. Fit of a peak in the mass spectrum of $[\text{Ni}_2(\text{L}^{4\text{Sim-meta}})_3](\text{BF}_4)_4$ (5^{Ni}) (Figure S112): $[\text{Ni}_2(\text{L}^{4\text{Sim-meta}})_3]^{4+}$ experimental (black) and simulated pattern (red).

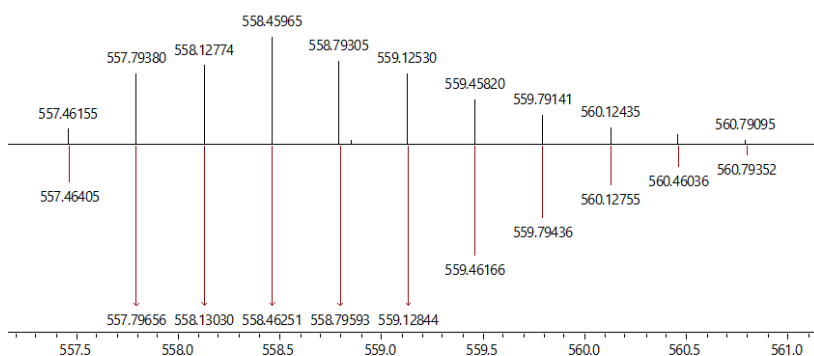


Figure S115. Fit of a peak in the mass spectrum of $[\text{Ni}_2(\text{L}^{4\text{Sim-meta}})_3](\text{BF}_4)_4$ (5^{Ni}) (Figure S112): $[\text{Ni}_2(\text{L}^{4\text{Sim-meta}})_3](\text{BF}_4)^{3+}$ experimental (black) and simulated pattern (red).

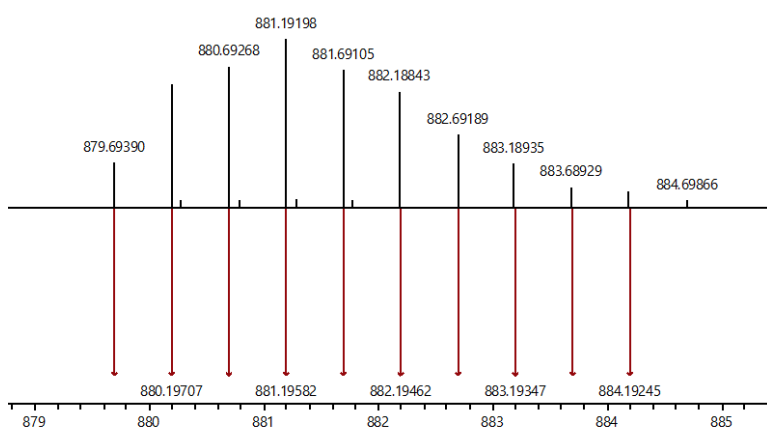


Figure S116. Fit of a peak in the mass spectrum of $[\text{Ni}_2(\text{L}^{4\text{Sim-meta}})_3](\text{BF}_4)_4$ (5^{Ni}) (Figure S112): $[\text{Ni}_2(\text{L}^{4\text{Sim-meta}})_3](\text{BF}_4)_2^{2+}$ experimental (black) and simulated pattern (red).

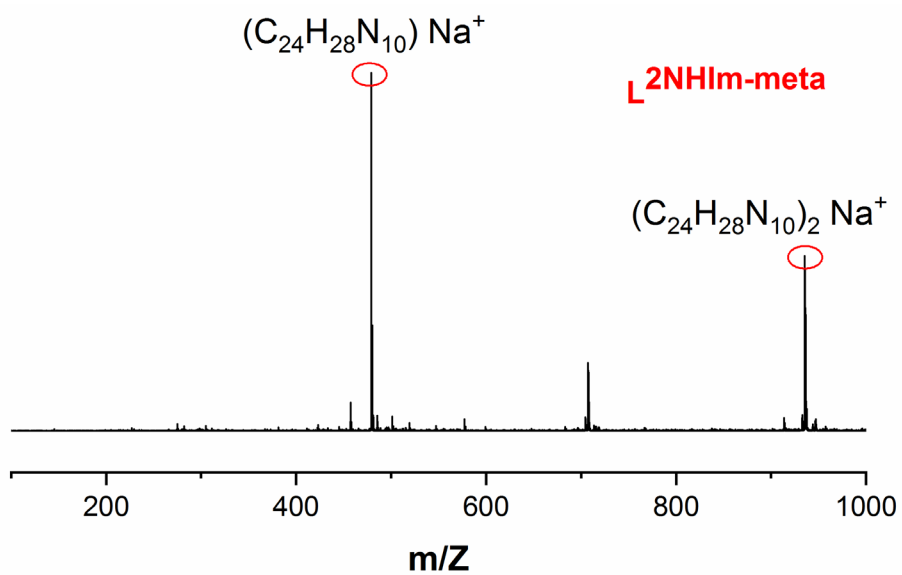


Figure S117. Mass spectrum of $L^{2NHIm-meta}$.

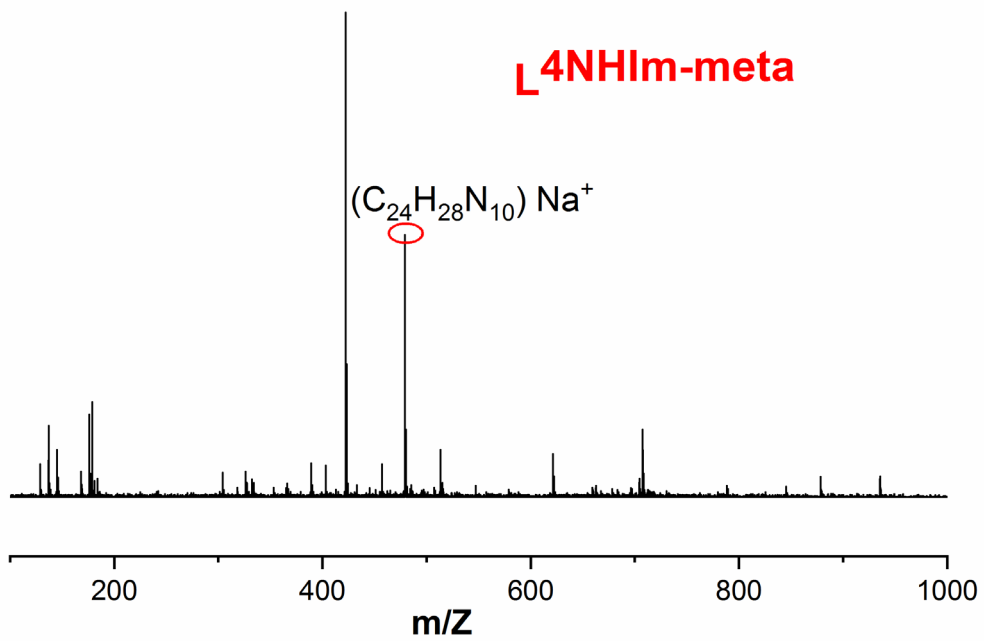


Figure S118. Mass spectrum of $L^{4NHIm-meta}$.

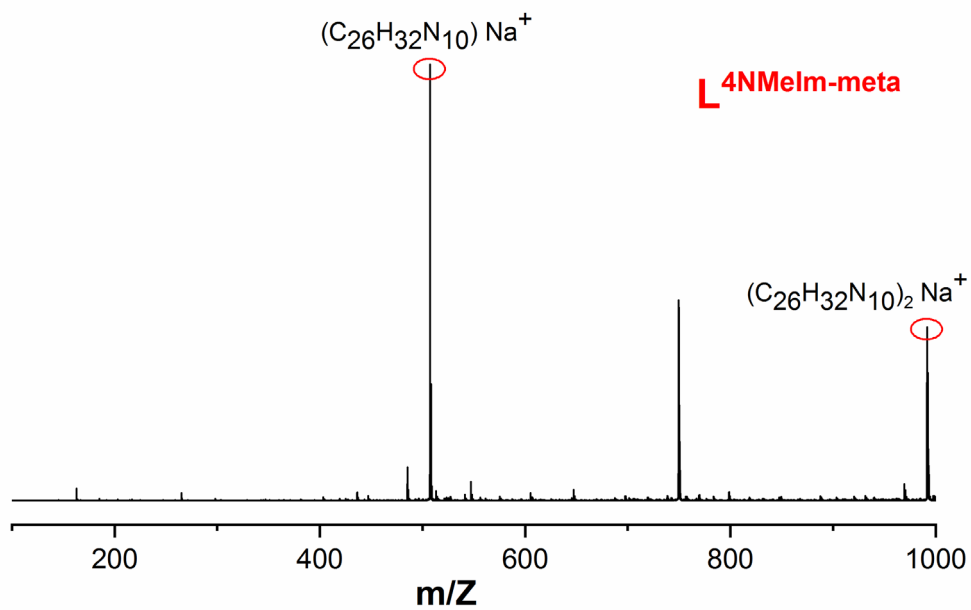


Figure S119. Mass spectrum of $L^{4NMelm-meta}$.

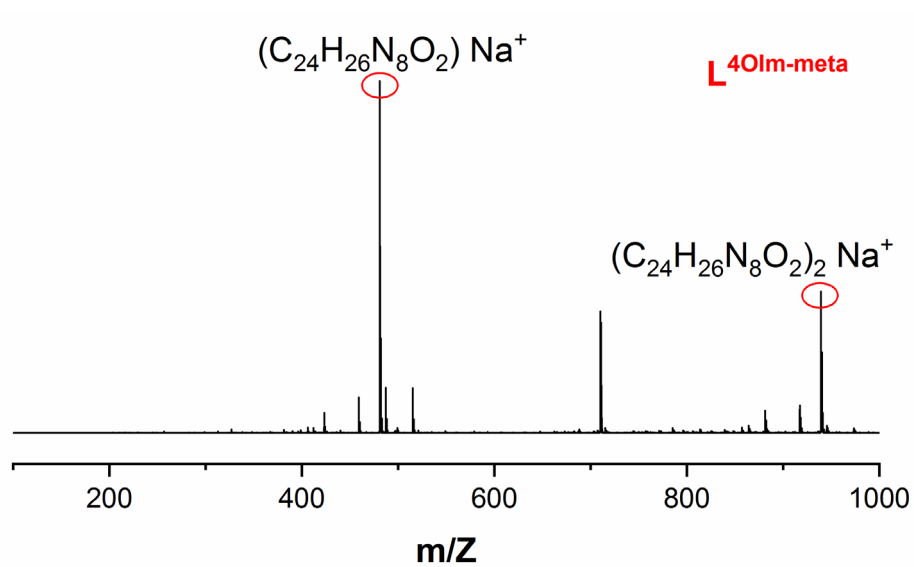


Figure S120. Mass spectrum of $L^{4OIm-meta}$.

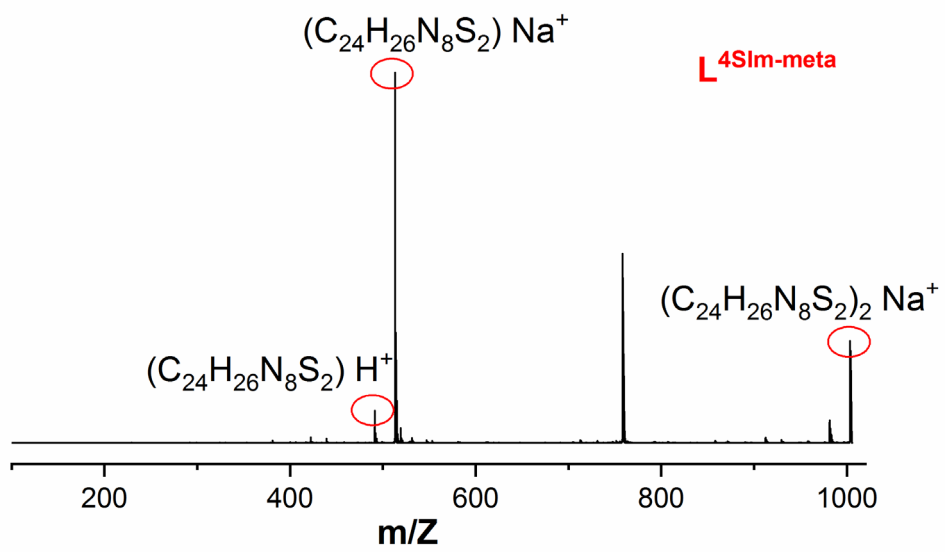


Figure S121. Mass spectrum of $L^{4SIm-meta}$.

NMR spectra

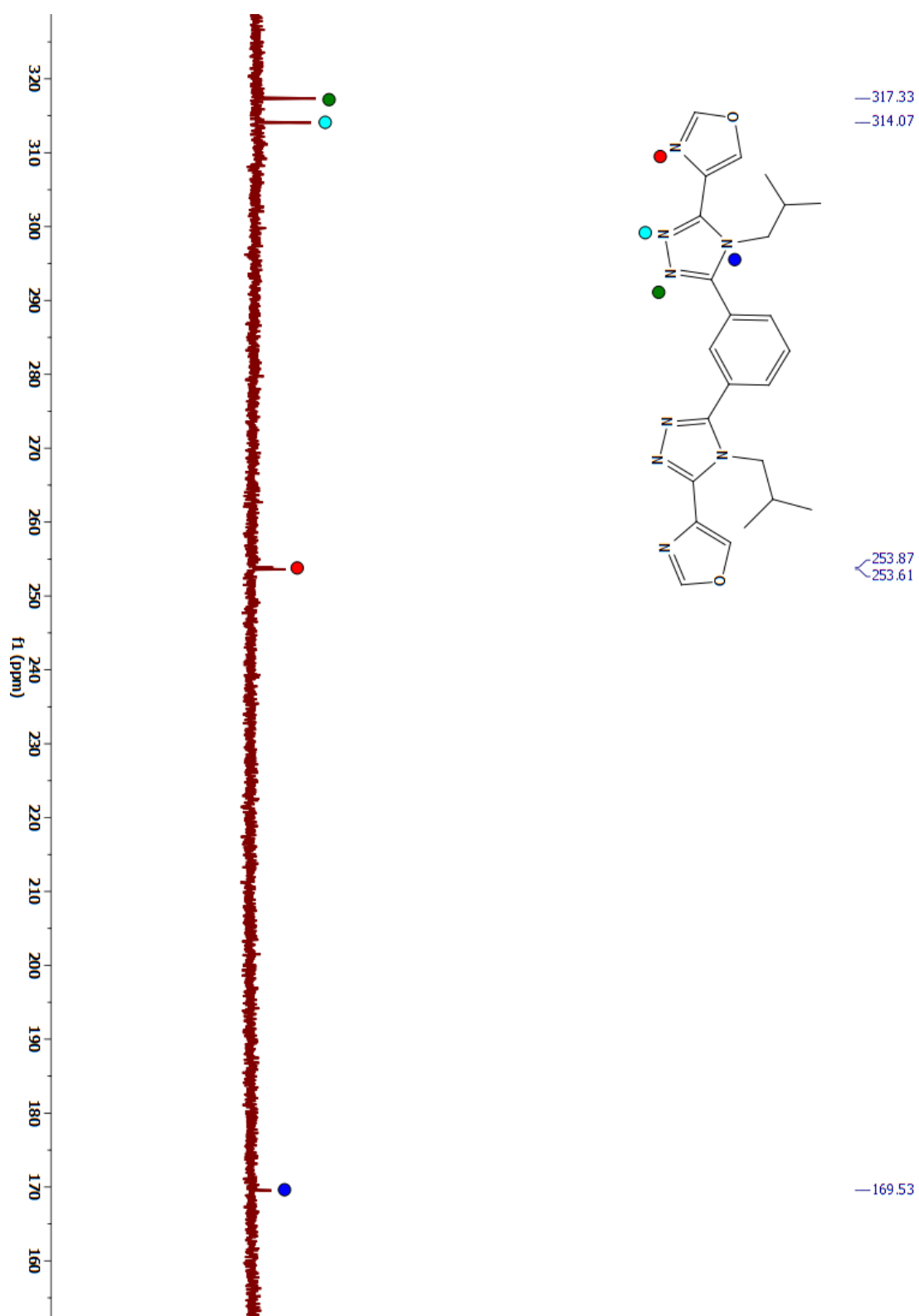


Figure S122. Direct ^{15}N NMR spectrum of $\text{L}^{40\text{Im-meta}}$ in CDCl_3 , referenced to NO_2CD_3 (+380 ppm).

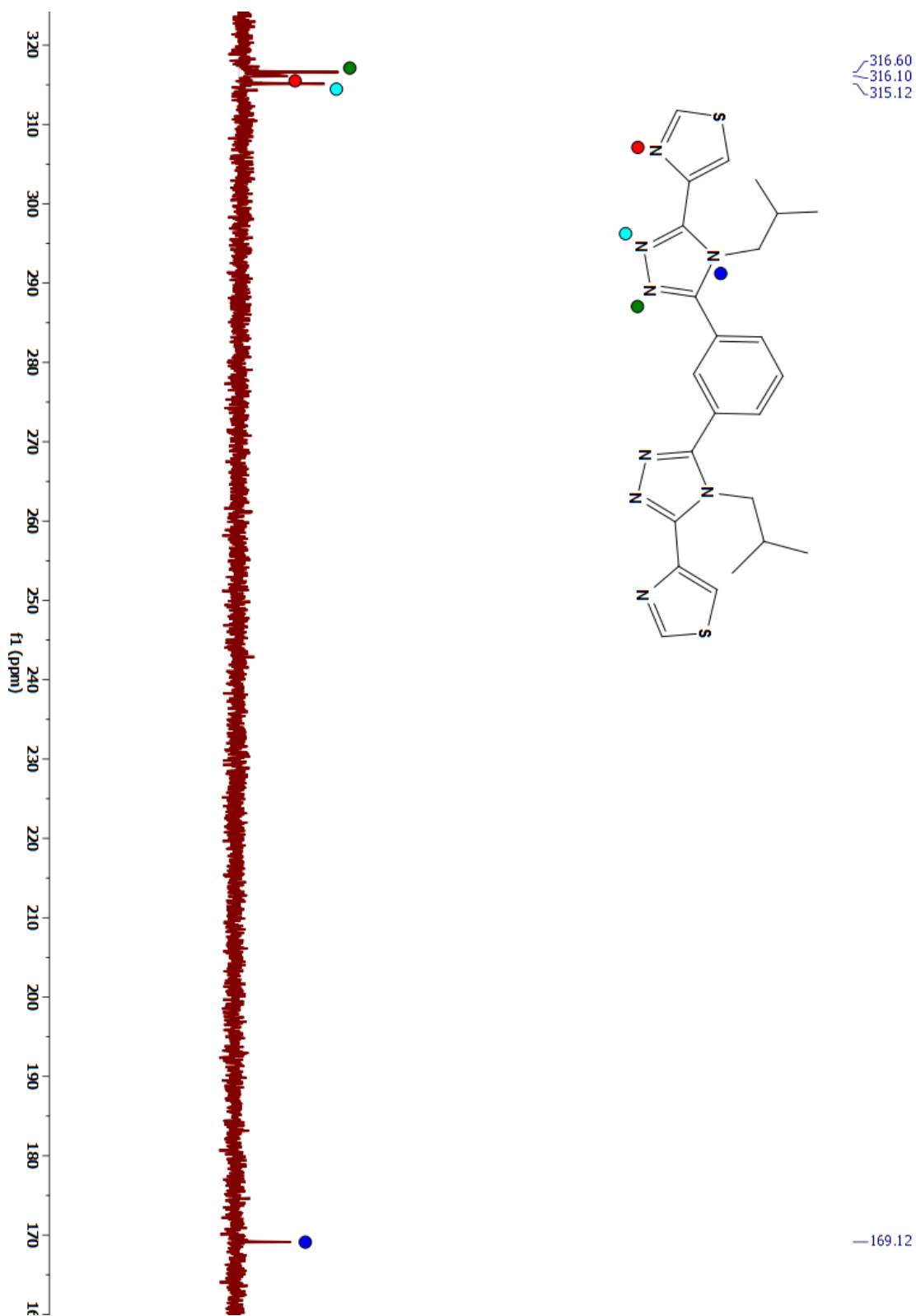


Figure S123. Direct ¹⁵N NMR spectrum of **L^{4Sim-meta}** in CDCl₃, referenced to NO₂CD₃ (+380 ppm).

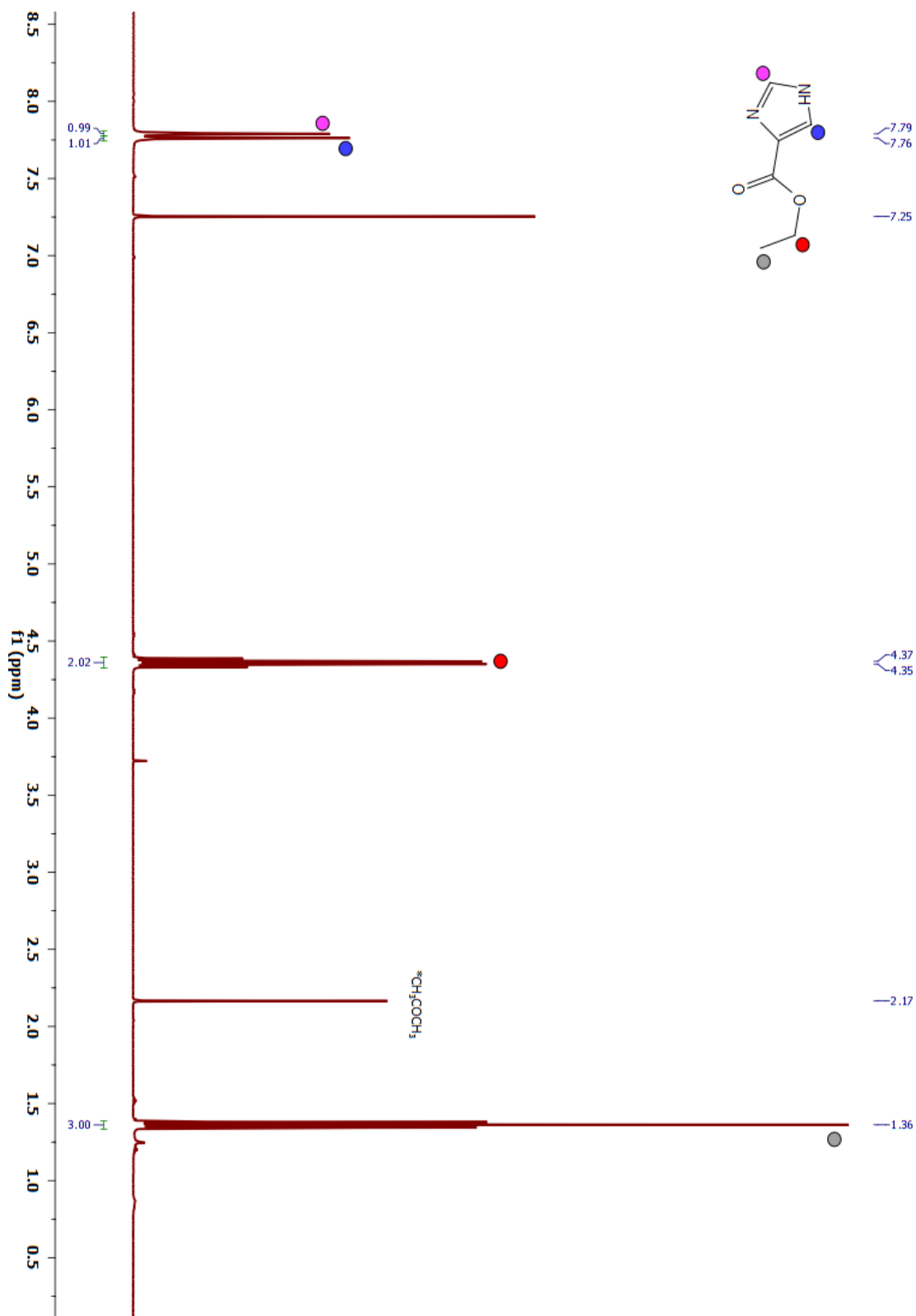


Figure S124. ¹H NMR spectrum (400 MHz) of Ethyl 1H-imidazole-4-carboxylate in CDCl₃.

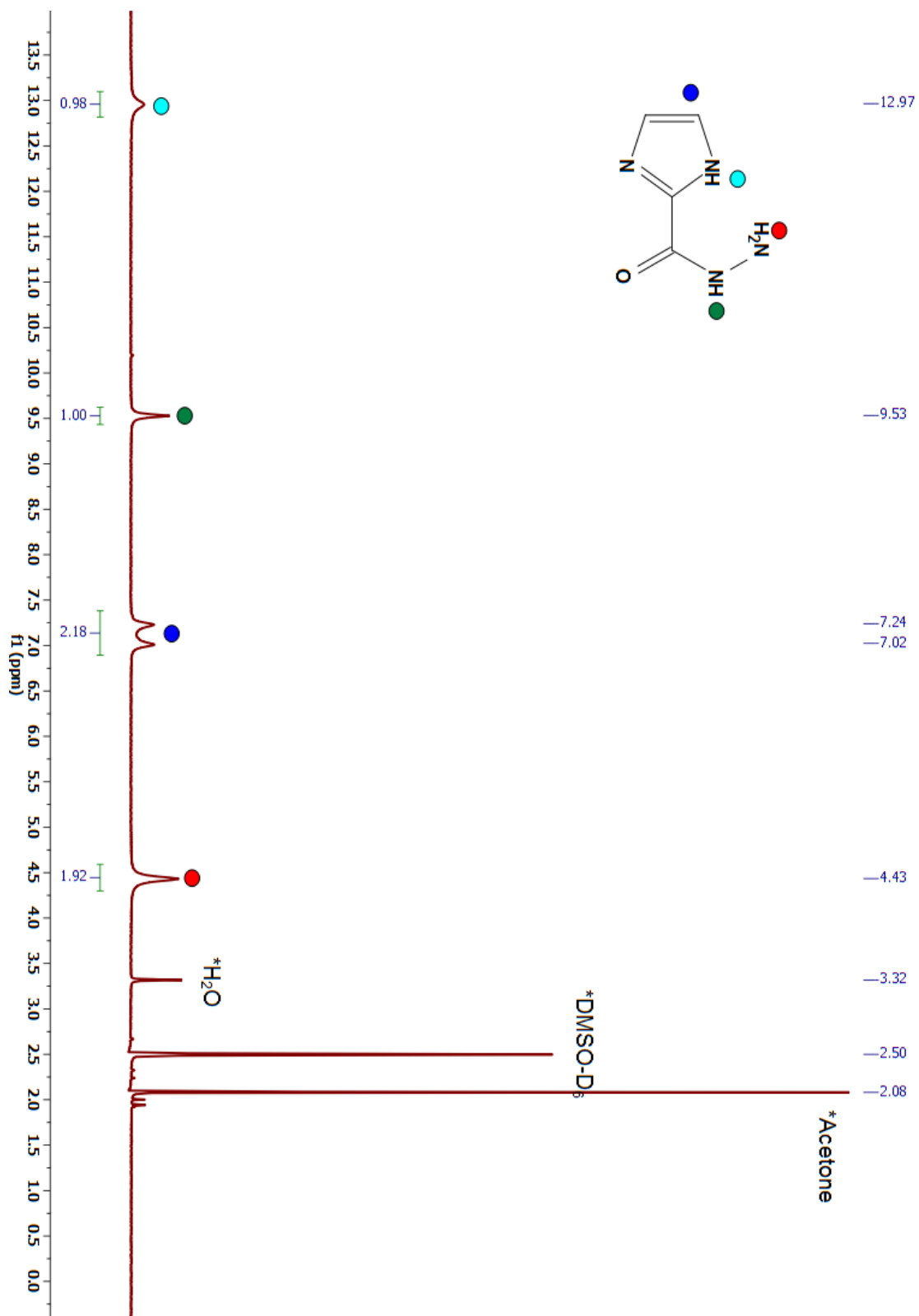


Figure S125. ^1H NMR spectrum (400 MHz) of 1H-imidazole-2-carbohydrazide in $\text{DMSO-}D_6$.

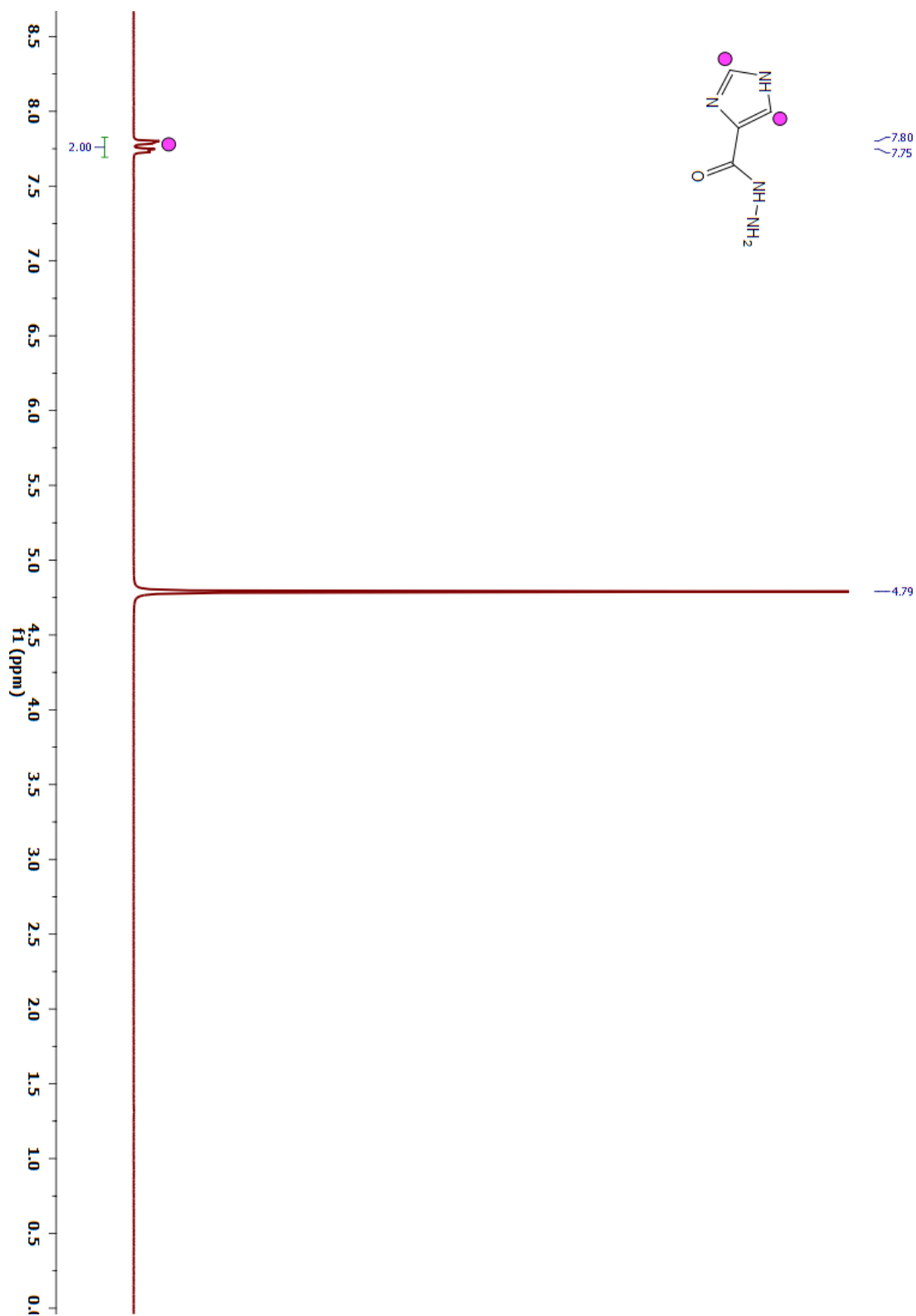


Figure S126. ^1H NMR spectrum (400 MHz) of 1H-imidazole-4-carbohydrazide in D_2O .

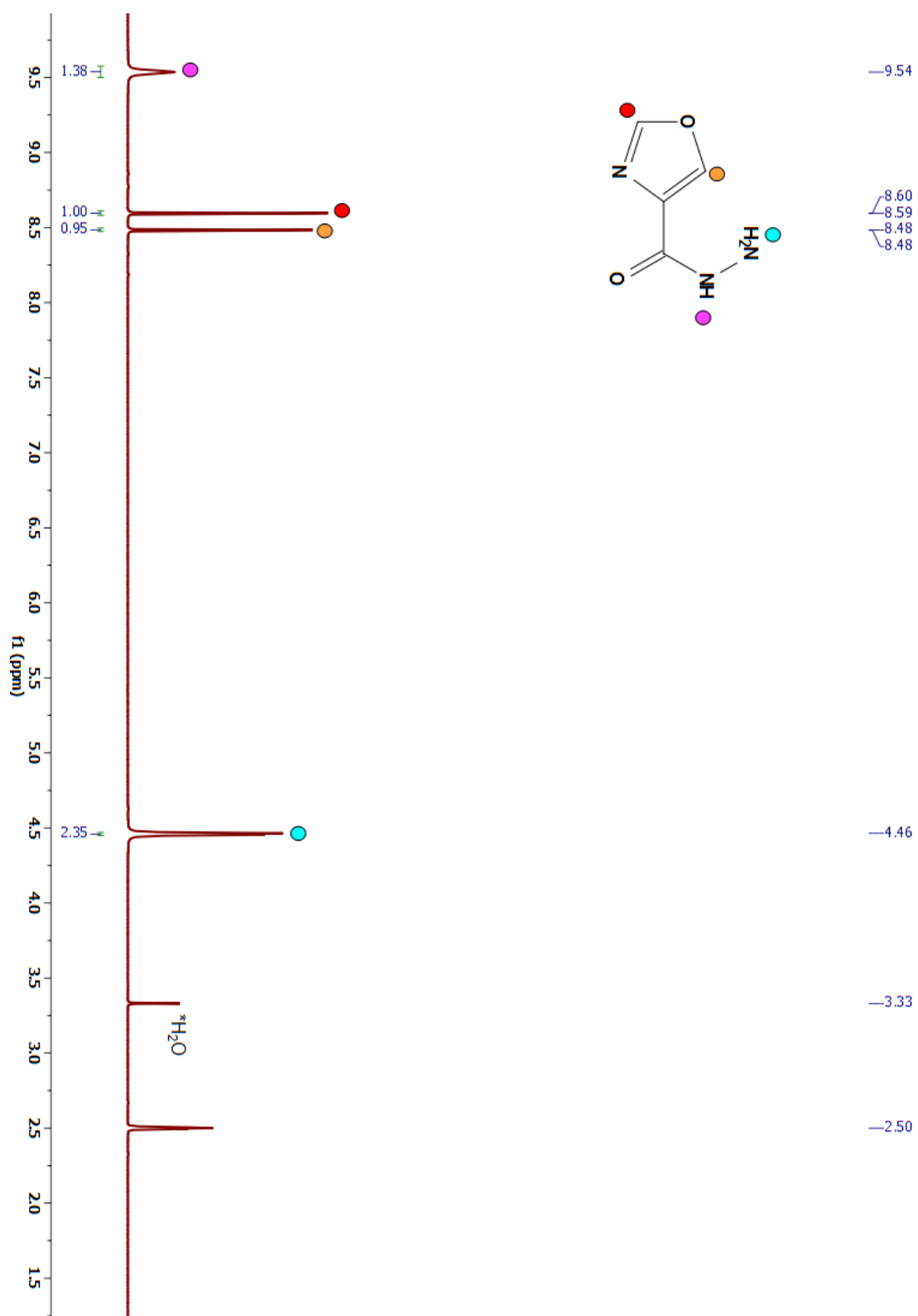


Figure S127. ^1H NMR spectrum (400 MHz) of oxazole-4-carbohydrazide in $\text{DMSO-}d_6$.

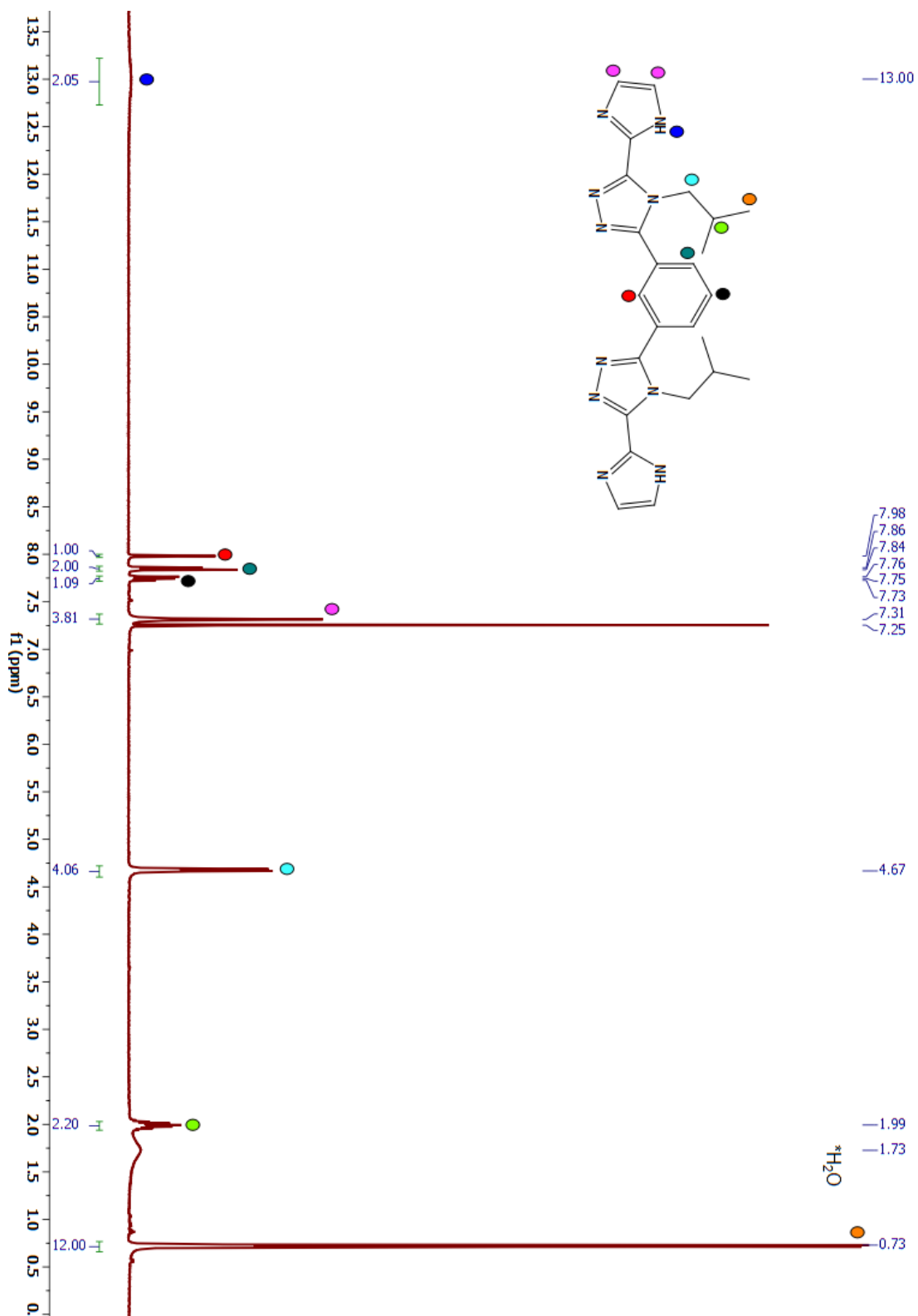


Figure S128. 1H NMR spectrum (400 MHz) of $L^{2NHIm-meta}$ in $CDCl_3$.

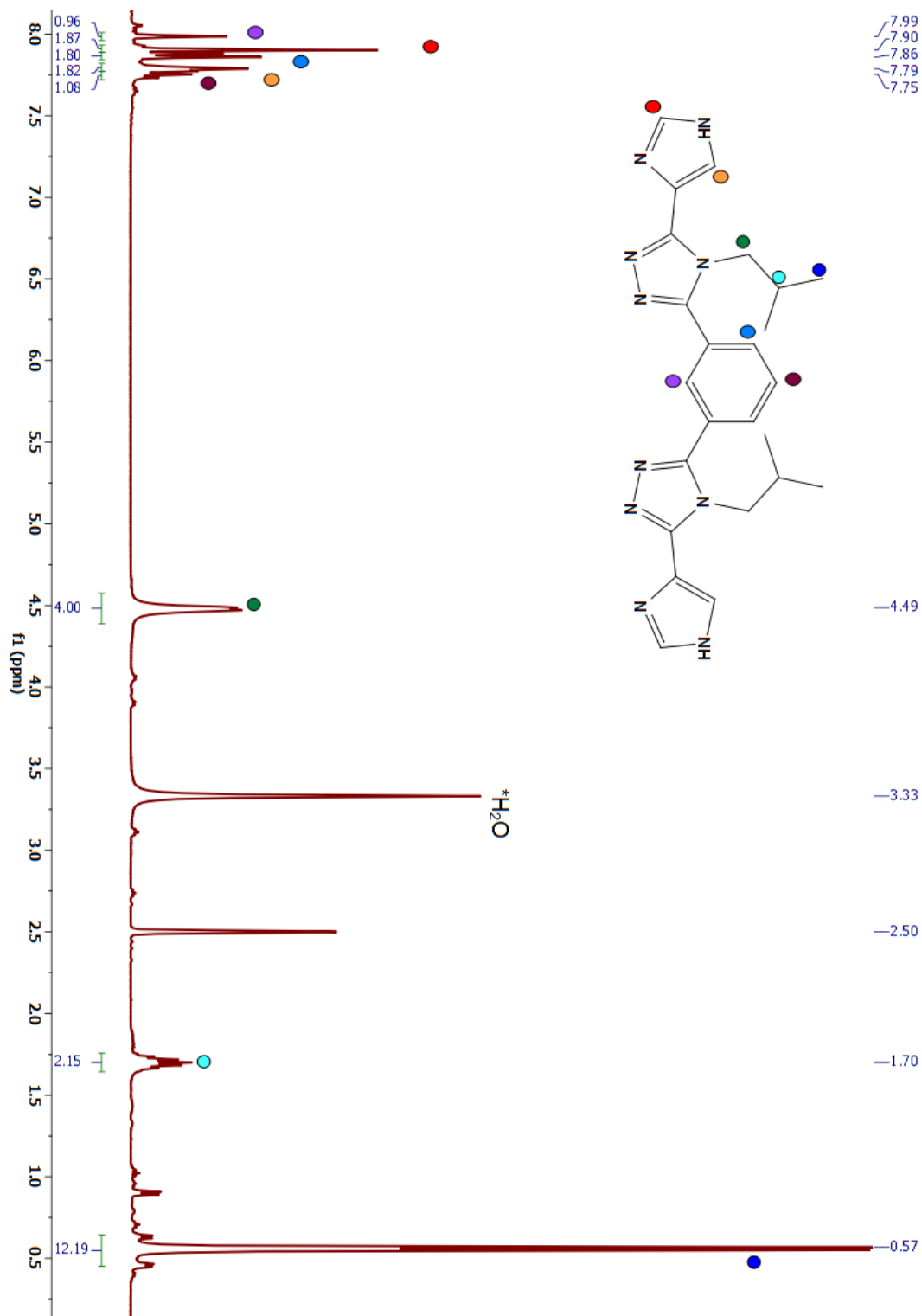


Figure S129. ^1H NMR spectrum (400 MHz) of $\text{L}^{4\text{NHIm-meta}}$ in $\text{DMSO-}d_6$.

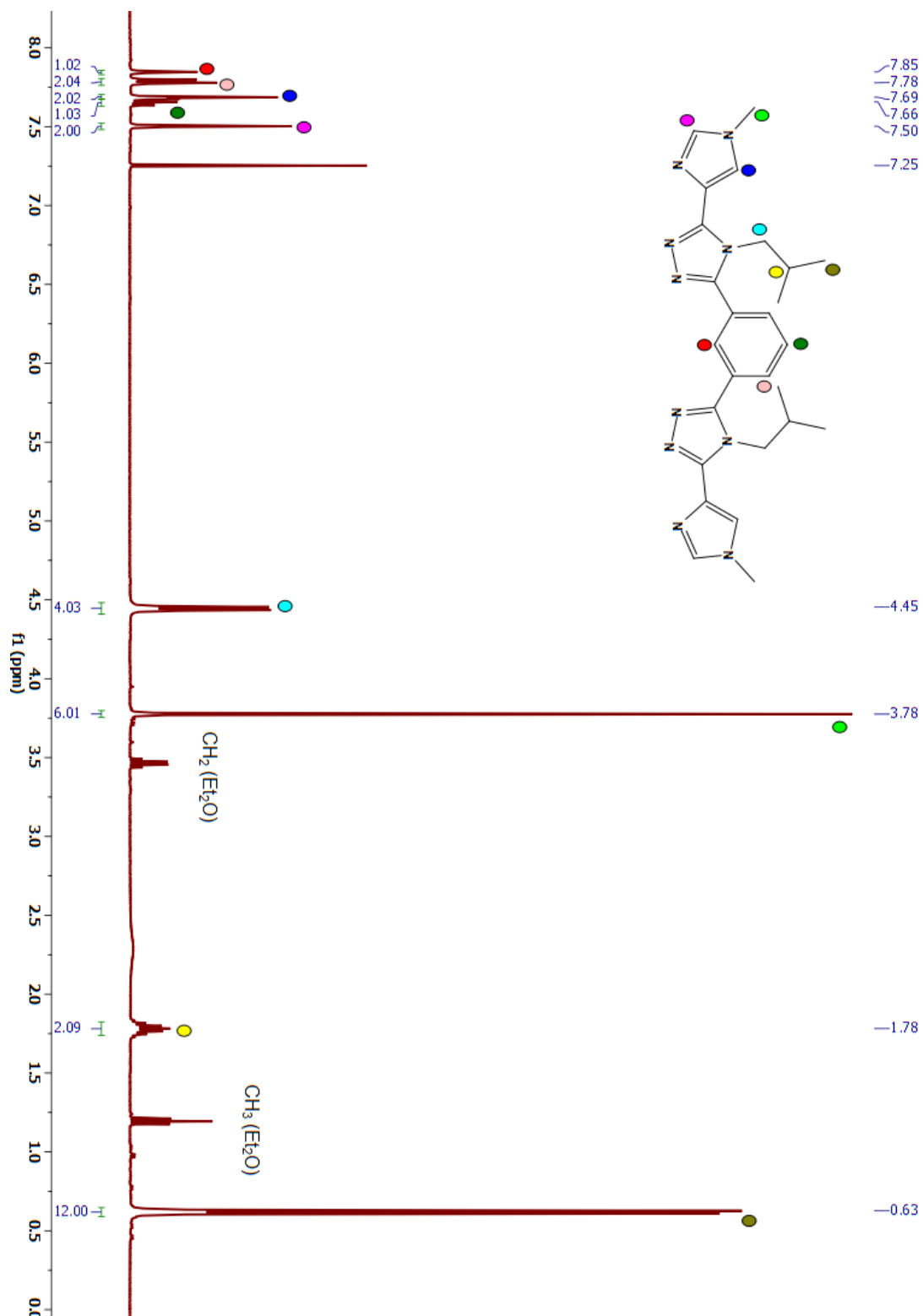


Figure S130. ^1H NMR spectrum (400 MHz) of $\text{L}^{2\text{NMeIm-meta}}$ in CDCl_3 .

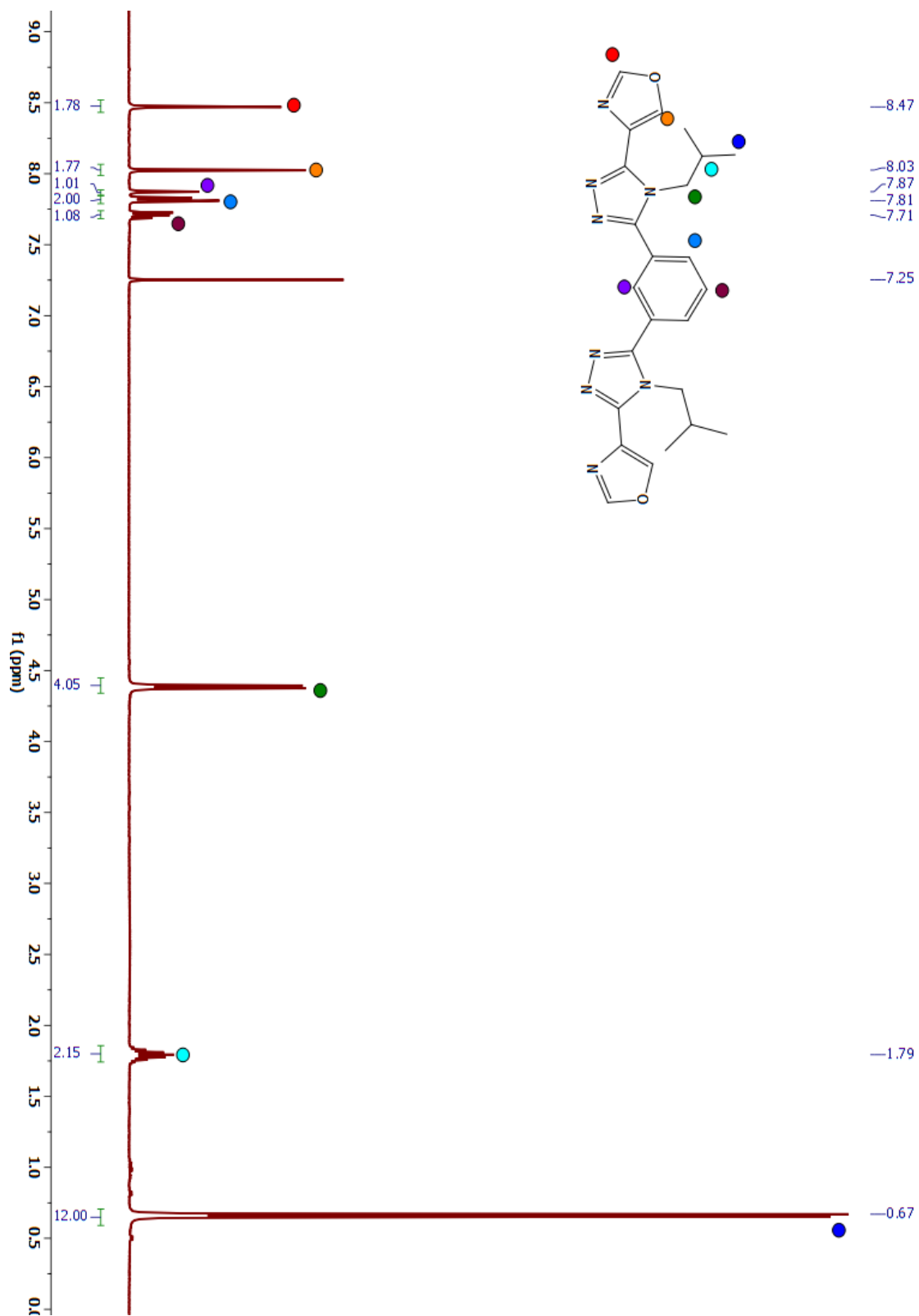


Figure S131. ^1H NMR spectrum (400 MHz) of $\text{L}^{40\text{Im-meta}}$ in CDCl_3 .

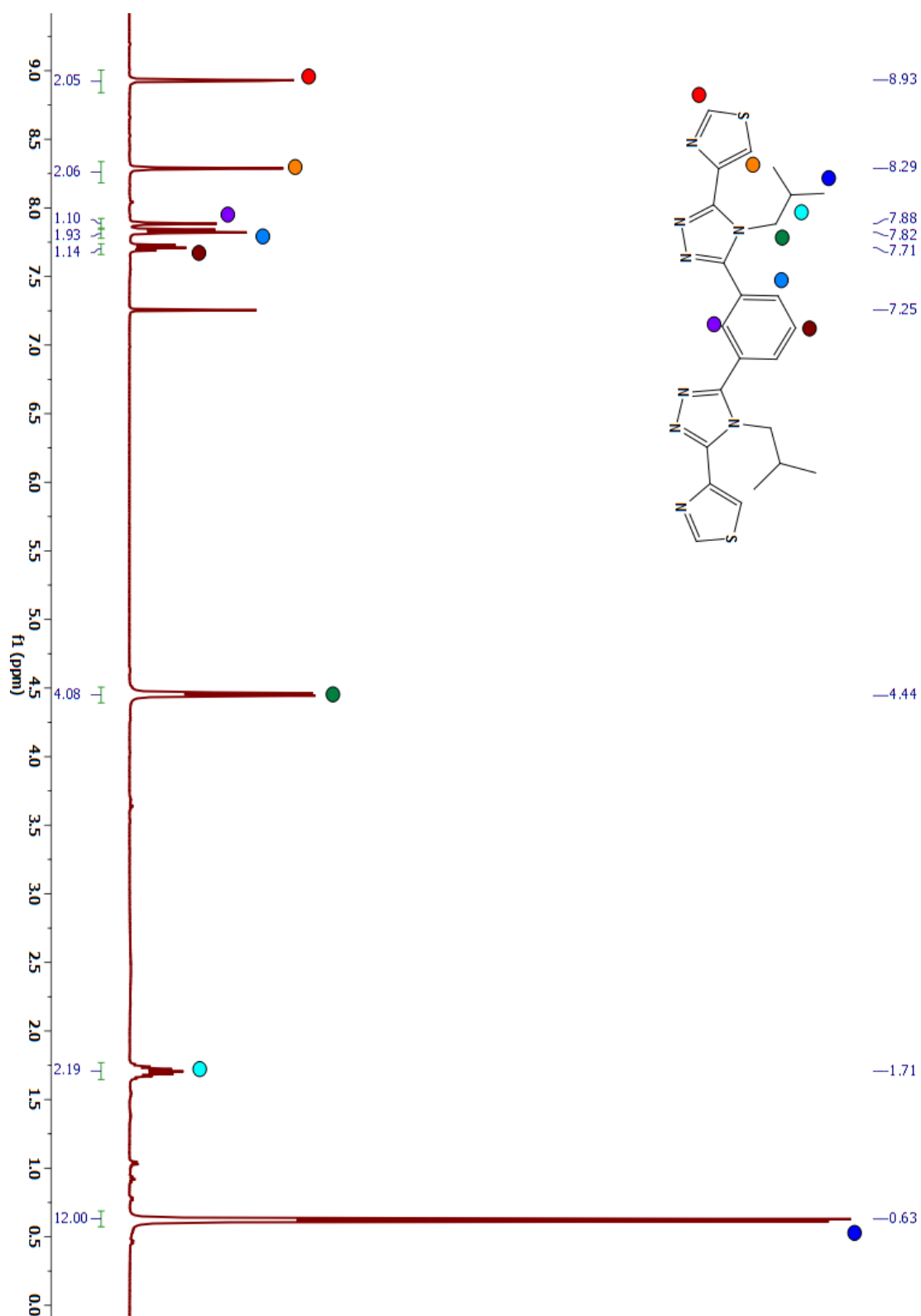


Figure S132. ^1H NMR spectrum (400 MHz) of $\text{L}^{4\text{SIm-meta}}$ in CDCl_3 .

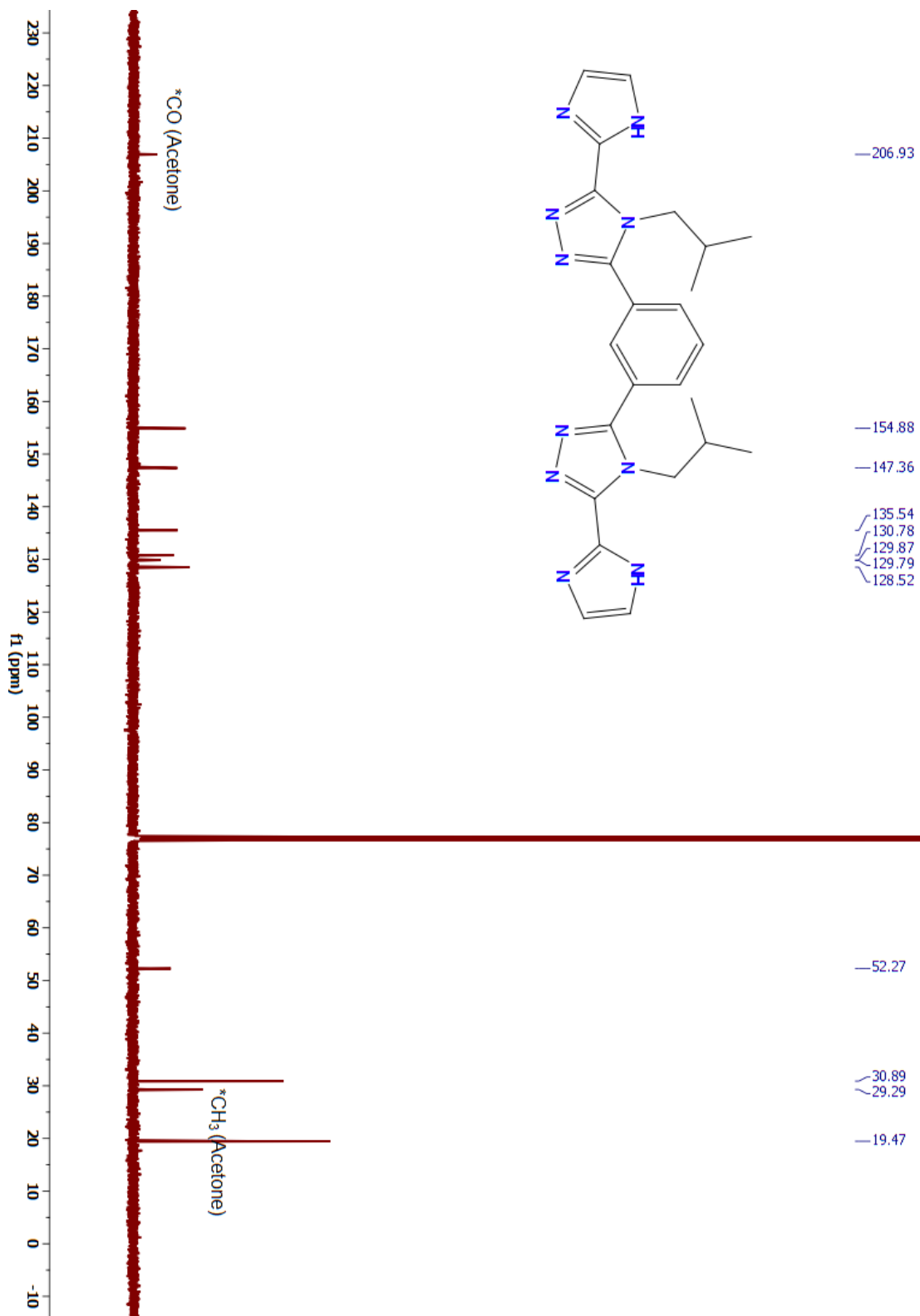


Figure S133. ¹³C NMR spectrum (100 MHz) of **L²NHIm-*meta*** in CDCl₃.

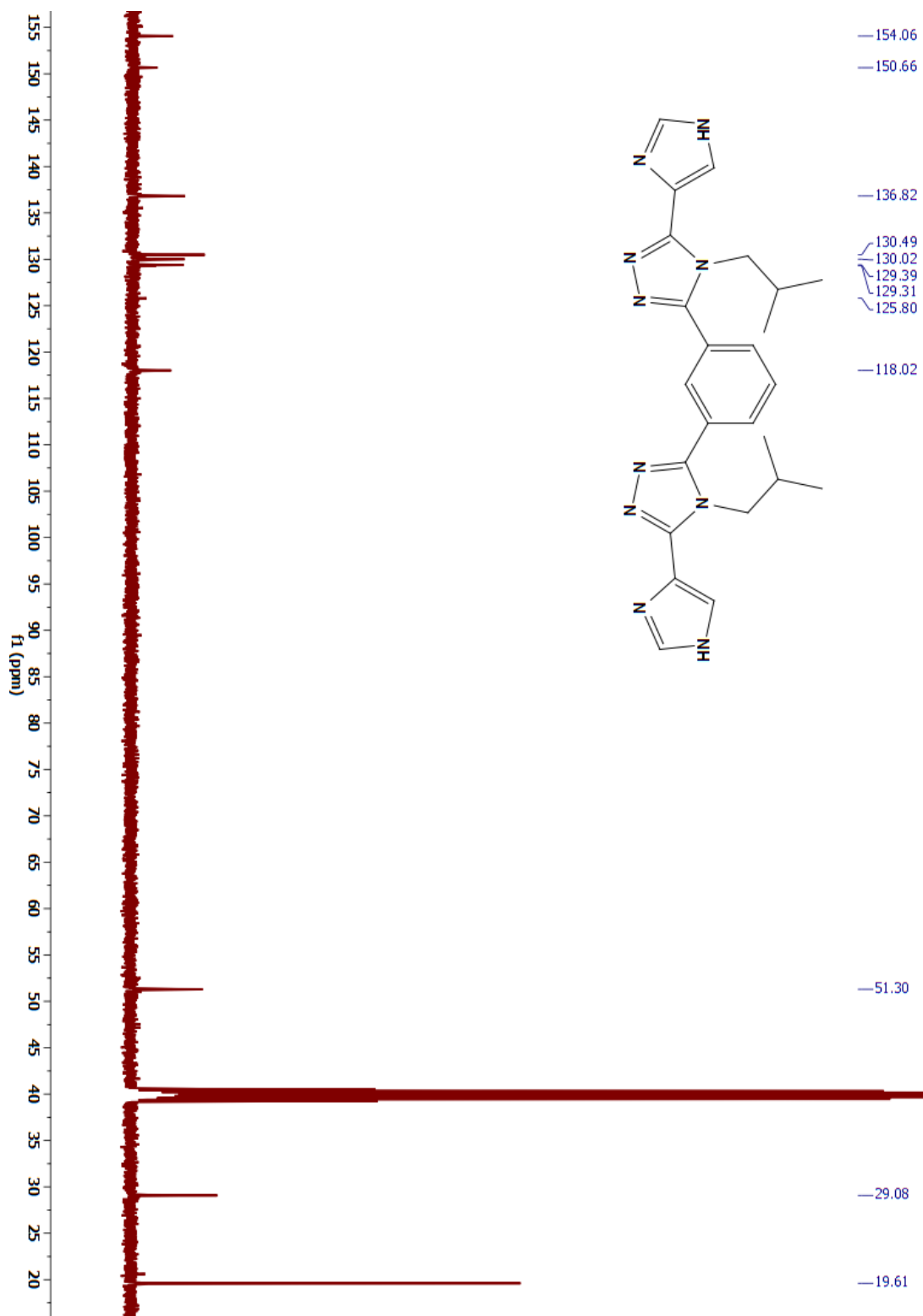


Figure S134. ^{13}C NMR spectrum (100 MHz) of $\text{L}^{4\text{NHIm-meta}}$ in $\text{DMSO-}D_6$.

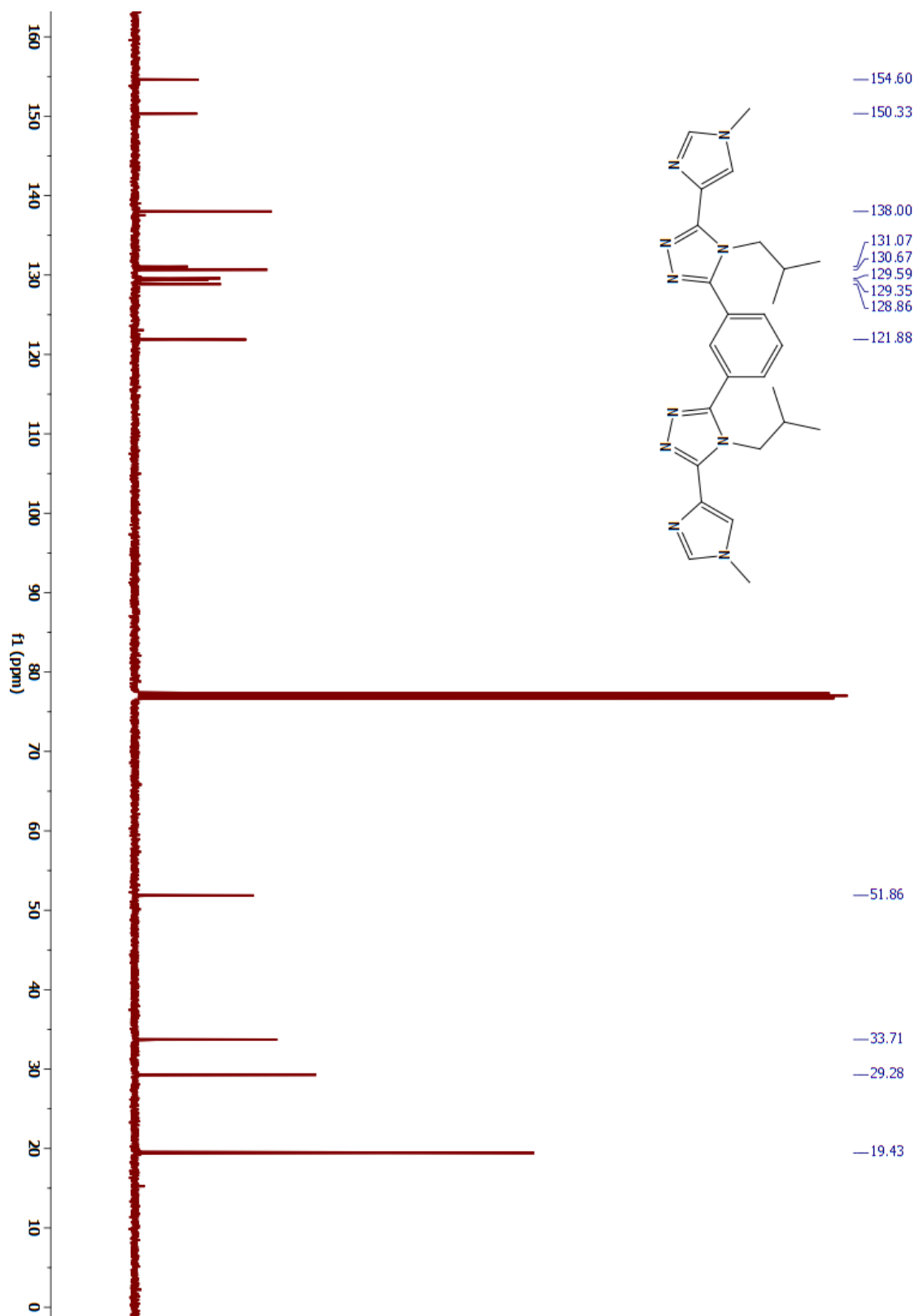


Figure S135. ^{13}C NMR spectrum (100 MHz) of $\text{L}^{4\text{NMelm-meta}}$ in CDCl_3 .

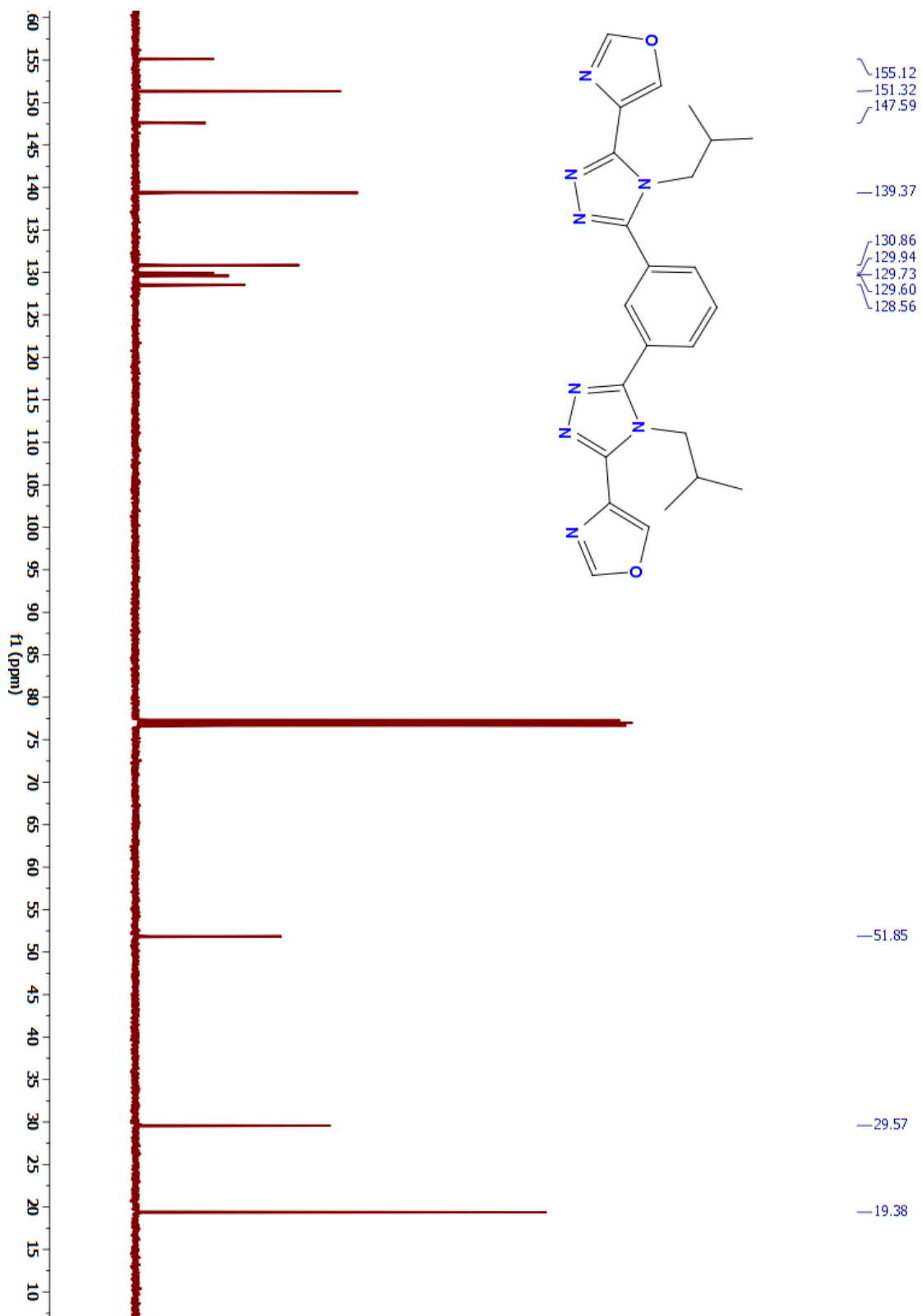


Figure S136. ^{13}C NMR spectrum (100 MHz) of $\text{L}^{40\text{Im-meta}}$ in CDCl_3 .

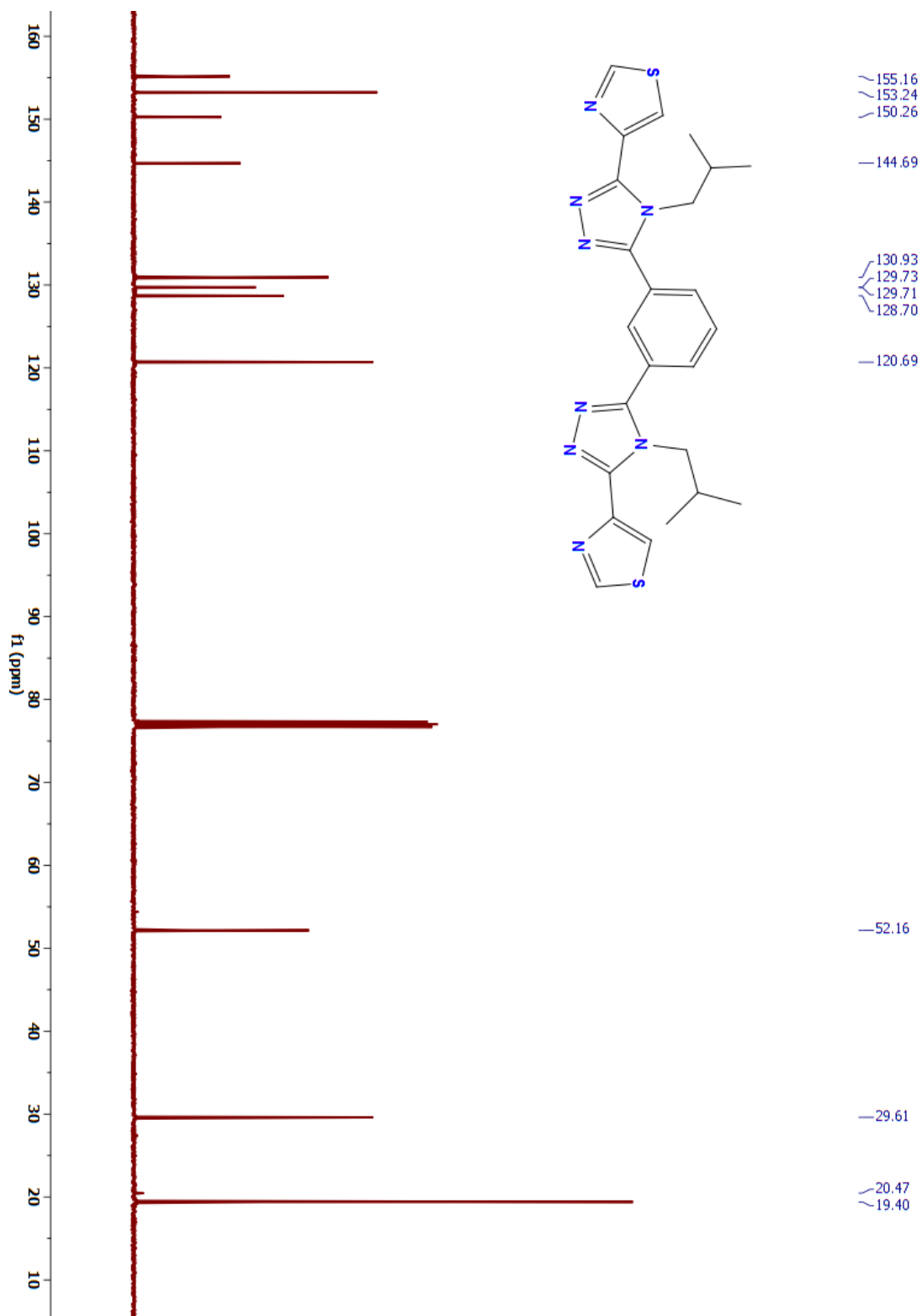


Figure S137. ^{13}C NMR spectrum (100 MHz) of $\text{L}^{4\text{Sim-meta}}$ in CDCl_3 .

Overlaid crystal structures

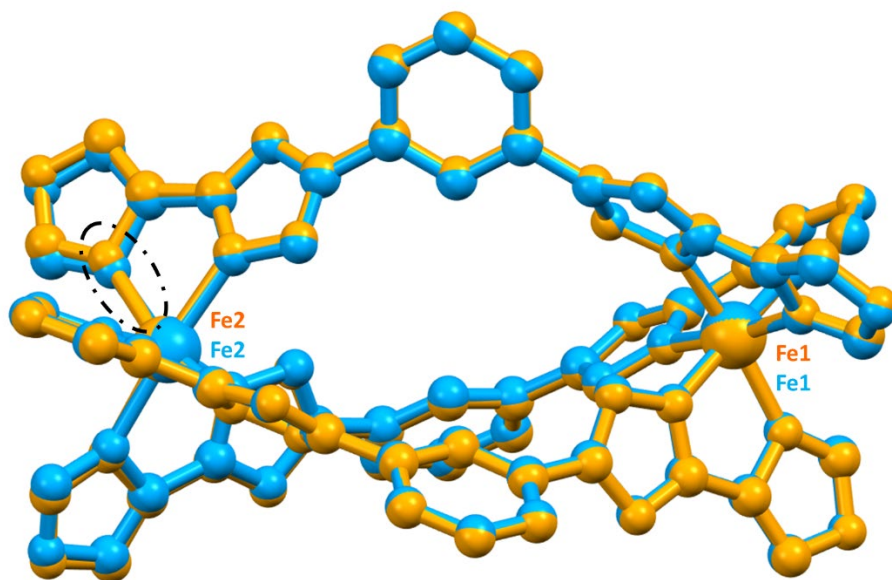


Figure S138. Overlay of structures (all atoms) of **4·5.5NO₂CH₃** (100 K, blue) and **4·5NO₂CH₃** (253 K, orange), emphasising on lengthening of Fe2-N bond (dashed ellipsoid).

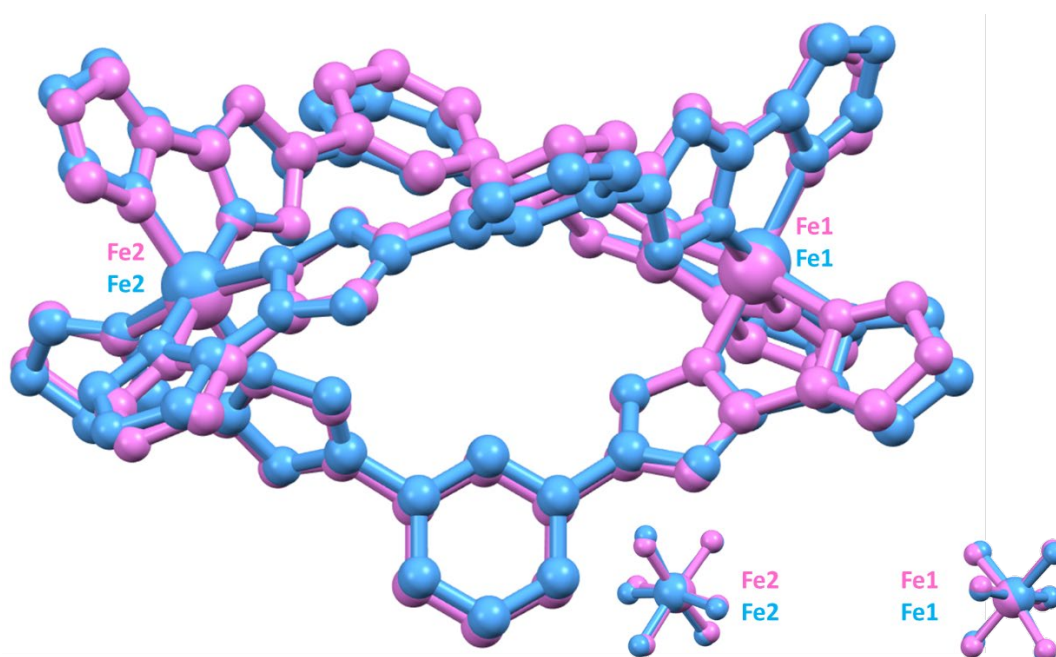


Figure S139. Overlay of structures (all atoms) of 4-oxazole helicites **4·5.5NO₂CH₃** (crystallised from nitromethane, blue) and **4·solvent** (crystallised from acetonitrile, pink) at 100K, emphasising on LS-LS Fe octahedral distortion (Σ°); higher number observed for former (62, 77.2°, blue) than latter (57.0, 56.8°, pink).

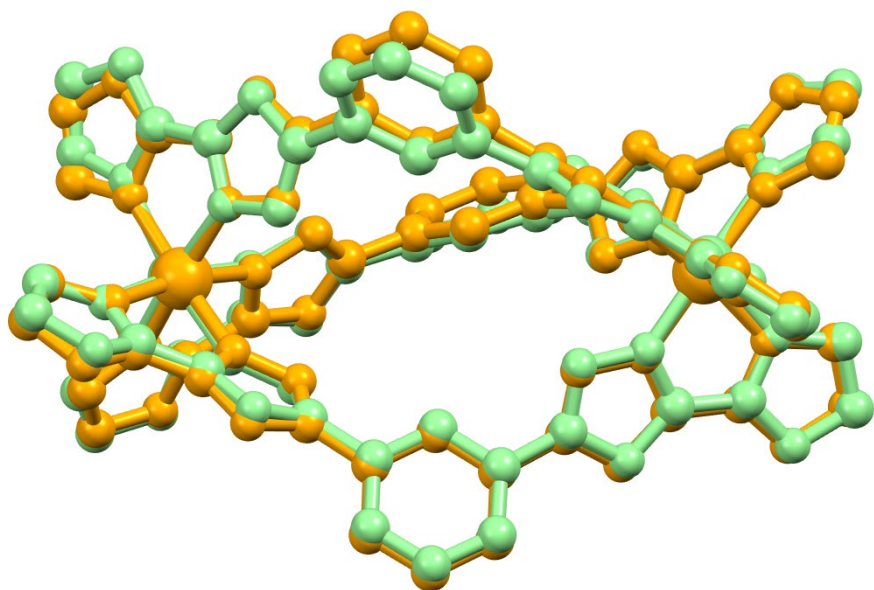


Figure S140. Overlay of structures (all atoms) of 2NH-imidazole helicate **1**·solvent (orange) and **1**^{Ni}·solvent (green), emphasising on comparison of distorted M(II) octahedral sphere.

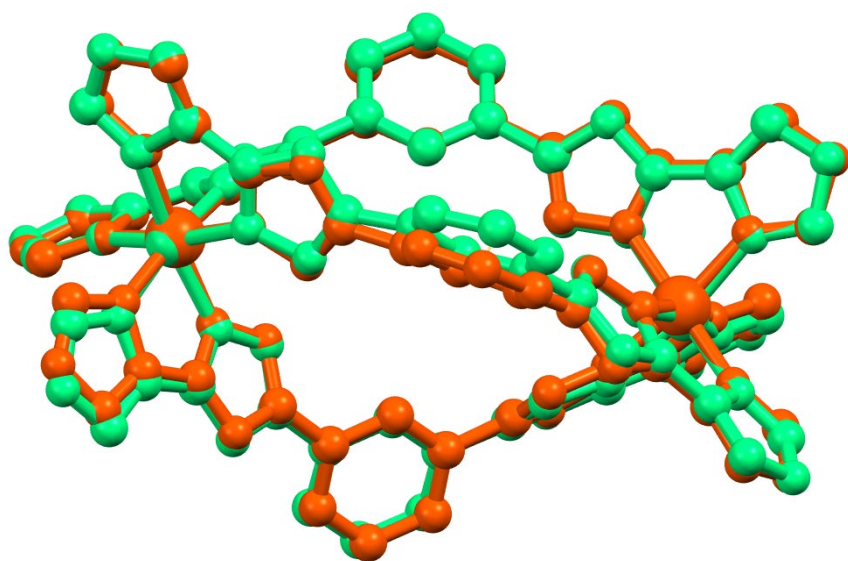


Figure S141. Overlay of structures (all atoms) of 4NH-imidazole helicate **2**·solvent (orange) and **2**^{Ni}·solvent (green), emphasising on comparison of distorted M(II) octahedral sphere.

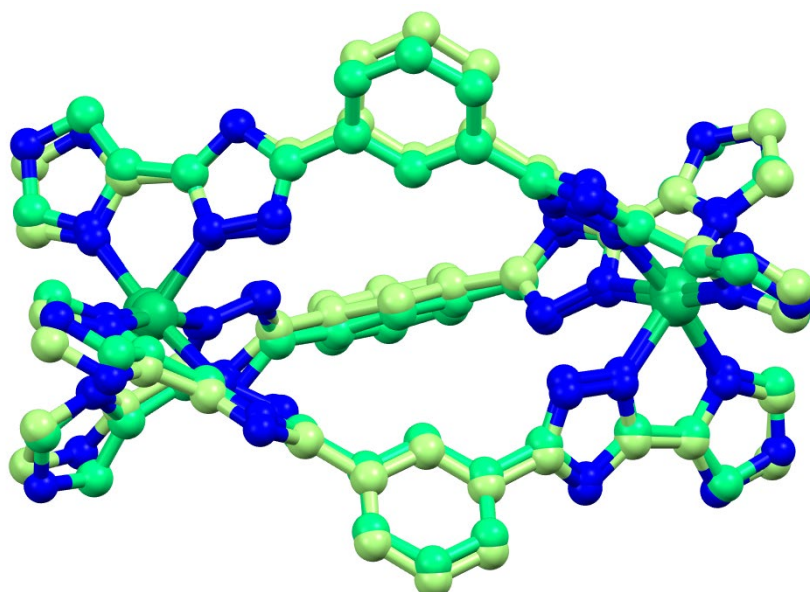


Figure S142. Overlay of structures (all atoms) of Ni(II) helicate of **1**^{Ni}-solvent (carbon: yellowish-green) and **2**^{Ni}-solvent (carbon: green).

Solid state magnetic studies

The solid state magnetic susceptibility vs temperature of the air dried crystalline samples **1-5** were monitored with scan speed of 5K/min in settle mode. On cooling from 300 K to 50 K, **1**·4H₂O remain LS whereas the small fraction of HS increased above 300 K, at 400 K ($\chi_m T = 0.79 \text{ cm}^3 \text{ K mol}^{-1}$). The SCO curve followed the same path over the next three cycles (Figure S143). On the contrast changing from 2NH-imidazole (**1**·4H₂O) to 4NH-imidazole (**2**·6H₂O), gradual and incomplete SCO (Figure S144) is observed. While heating from 50-400 K, γ_{HS} increased from 0.43 ($\chi_m T = 1.61 \text{ cm}^3 \text{ K mol}^{-1}$) to 0.86 ($\chi_m T = 3.17 \text{ cm}^3 \text{ K mol}^{-1}$). The $\chi_m T$ value for **3**·5H₂O at 50 K is $0.44 \text{ cm}^3 \text{ K mol}^{-1}$ which increased gradually upon heating to $3.86 \text{ cm}^3 \text{ K mol}^{-1}$ at 400 K with $T_{1/2}$ at 280 K (Figure S145). Compound **4**·6H₂O has undergone abrupt SCO at 230 K, the $\chi_m T$ value at 300 K of $3.43 \text{ cm}^3 \text{ K mol}^{-1}$, consistent with presence of 93% of HS fraction, dropped to $0.54 \text{ cm}^3 \text{ K mol}^{-1}$ at 50 K (Figure S146). On the other hand, **5**·2.5H₂O showed same behaviour as **1**·4H₂O, remains towards LS at 400 K ($\chi_m T = 1 \text{ cm}^3 \text{ K mol}^{-1}$), only 27 % fraction converted into HS (Figure S147).

Complex	T _{1/2} in solid state	T _{1/2} from NMR
[Fe ₂ (L ^{2NHIm-meta}) ₃](BF ₄) ₄ (1.4H ₂ O)	LS	331
[Fe ₂ (L ^{4NHIm-meta}) ₃](BF ₄) ₄ (2.6H ₂ O)	200	267
[Fe ₂ (L ^{4NMeIm-meta}) ₃](BF ₄) ₄ (3.5H ₂ O)	280	247
[Fe ₂ (L ^{4OIm-meta}) ₃](BF ₄) ₄ (4.6H ₂ O)	230	249
[Fe ₂ (L ^{4SIm-meta}) ₃](BF ₄) ₄ (5.2.5H ₂ O)	LS	471

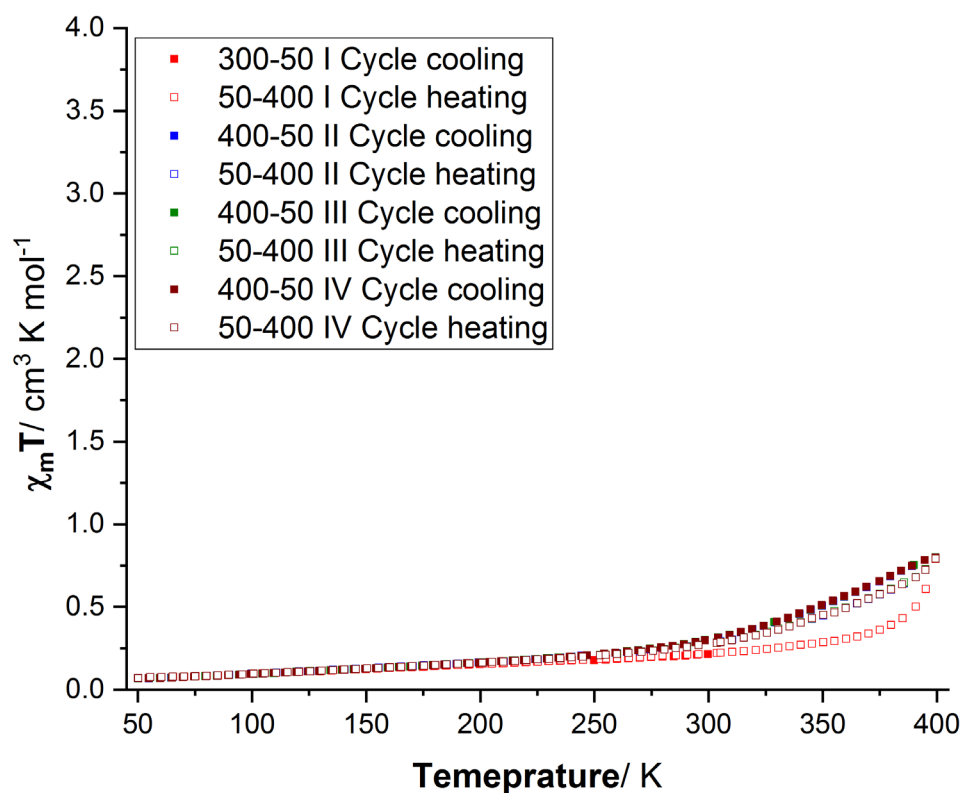


Figure S143. $\chi_M T$ versus T plot for $[\text{Fe}_2(\text{L}^{2\text{NHIm-meta}})_3](\text{BF}_4)_4 \cdot 4\text{H}_2\text{O}$ (1.4H₂O) over four successive cycles, 300-50-400, 400-50-400 K, 400-50-400 K and 400-50-400 K (cooling = filled squares; heating = open squares), in settle mode.

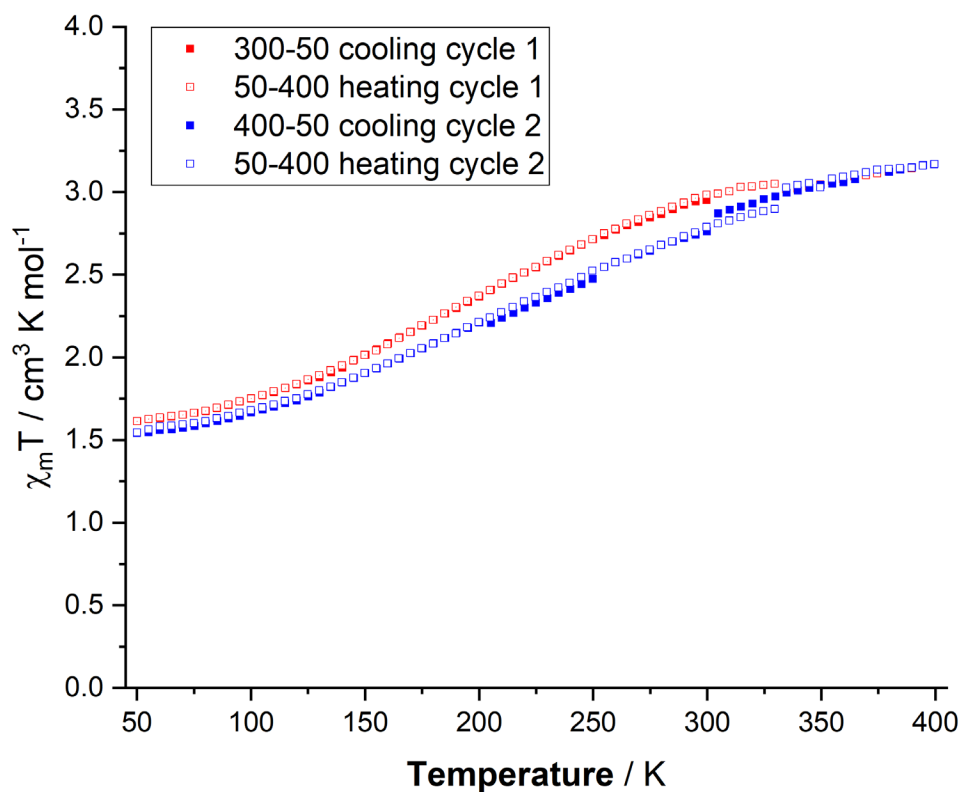


Figure S144. $\chi_M T$ versus T plot for $[\text{Fe}_2(\text{L}^{\text{4NHIm-meta}})_3](\text{BF}_4)_4 \cdot 6\text{H}_2\text{O}$ ($2 \cdot 6\text{H}_2\text{O}$) over two successive cycles, 300-50-400 and 400-50-400 K (cooling = filled squares; heating = open squares), in settle mode.

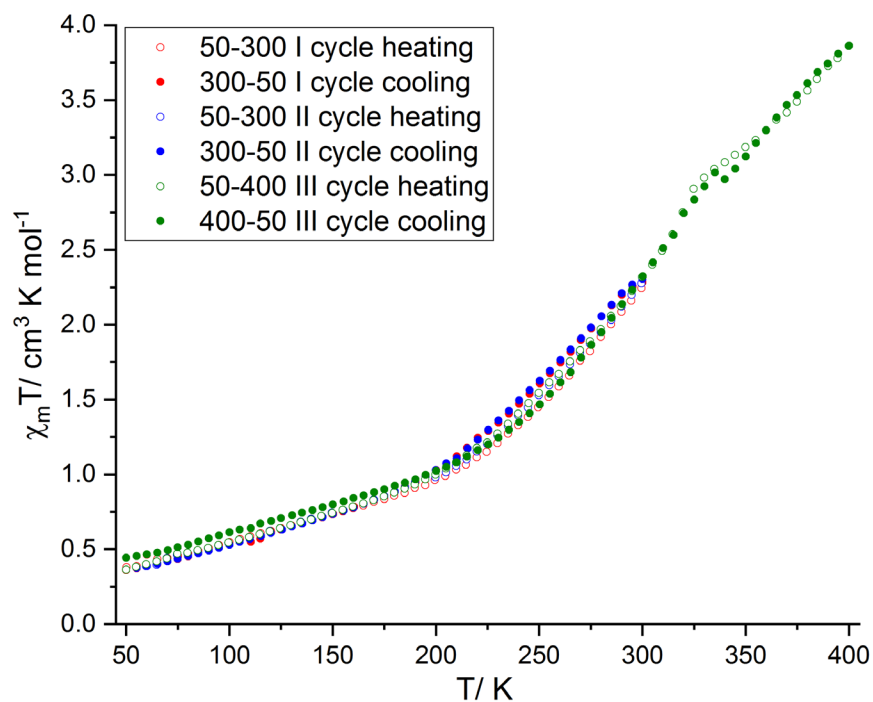


Figure S145. $\chi_M T$ versus T plot for $[\text{Fe}_2(\text{L}^{4\text{NMelm-meta}})_3](\text{BF}_4)_4 \cdot 5\text{H}_2\text{O}$ ($\mathbf{3} \cdot 5\text{H}_2\text{O}$) over three successive cycles, 50-300-50, 50-300-50 K and 50-400-50 K (cooling = filled circle; heating = open circle), in settle mode. TGA before the measurement calcd: 4.49, found: 5.27.

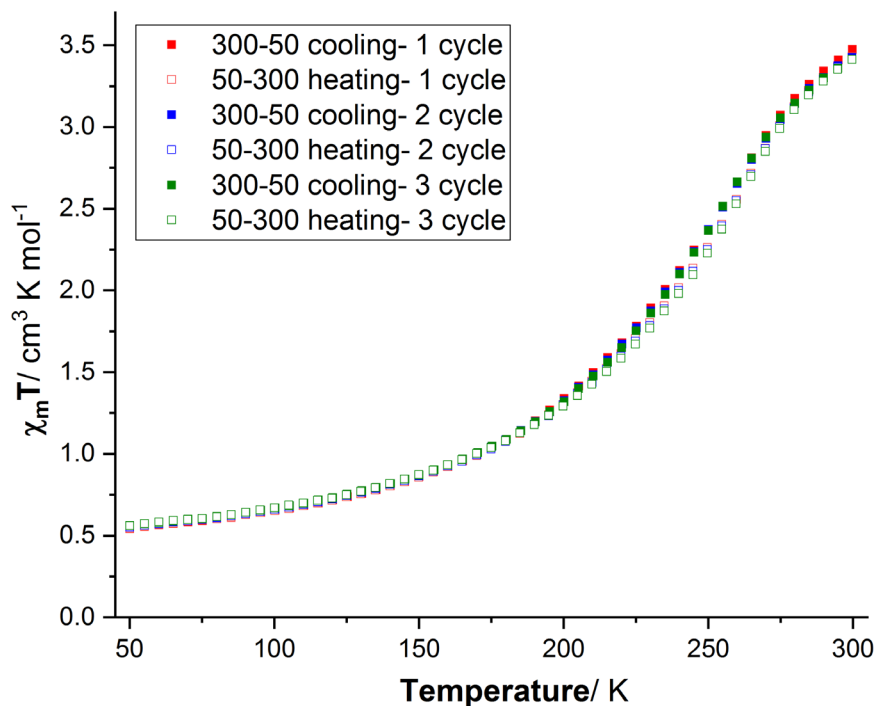


Figure S146. $\chi_M T$ versus T plot for $[\text{Fe}_2(\text{L}^{4\text{OIm-meta}})_3](\text{BF}_4)_4 \cdot 6\text{H}_2\text{O}$ ($4 \cdot 6\text{H}_2\text{O}$) over three successive cycles, 300-50-300, 300-50-300 K and 300-50-300 K (cooling = filled squares; heating = open squares), in settle mode. TGA before the measurement calcd: 5.56, found: 5.63.

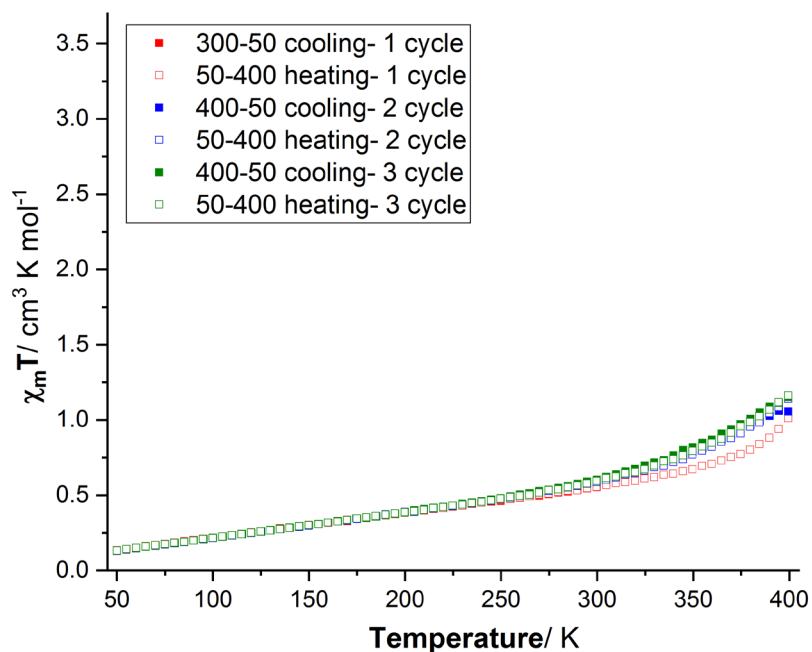


Figure S147. $\chi_M T$ versus T plot for $[\text{Fe}_2(\text{L}^{4\text{SIm-meta}})_3](\text{BF}_4)_4 \cdot 2.5\text{H}_2\text{O}$ ($5 \cdot 2.5\text{H}_2\text{O}$) over three successive cycles, 300-50-400, 400-50-400 K and 400-50-400 K (cooling = filled squares; heating = open squares), in settle mode.

References

- (1) Kahn, O., *Molecular Magnetism*. VCH Publishers Inc.: New York, 1993.
- (2) Sheldrick, G. M., SADABS, An Empirical Absorption Correction Program For Area Detector Data; University of Göttingen: Germany. **1996**.
- (3) Katoh, K.; Isshiki, H.; Komeda, T.; Yamashita, M., Multiple-decker phthalocyaninatoTb(III) single-molecule magnets and Y(III) complexes for next generation devices. *Coordination Chemistry Reviews*, **2011**, *255*, 2124-2148.
- (4) Sheldrick, G. M., SHELXT - Integrated space-group and crystal-structure determination. *Acta Crystallogr., Sect. A*, **2015**, *71*, 3-8.
- (5) Sheldrick, G. M., Crystal structure refinement with SHELXL. *Acta Crystallogr., Sect. C*, **2015**, *71*, 3-8.
- (6) Dolomanov, O. V.; Bourhis, L. J.; Gildea, R. J.; Howard, J. A. K.; Puschmann, H., OLEX2: a complete structure solution, refinement and analysis program. *J. Appl. Cryst.*, **2009**, *42*, 339-341.
- (7) Klingele, M. H.; Brooker, S., From *N*-substituted thioamides to symmetrical and unsymmetrical 3,4,5-trisubstituted 4*H*-1,2,4-triazoles: synthesis and characterisation of new chelating ligands. *Eur. J. Org. Chem.*, **2004**, 3422-3434.
- (8) Singh, S.; Hogue, R. W.; Feltham, H. L. C.; Brooker, S., Dinuclear helicate and tetranuclear cage assembly using appropriately designed ditopic triazole-azine ligands. *Dalton Trans.*, **2019**, 15435-15444.
- (9) Singh, S.; Brooker, S., Extension of azine-triazole synthesis to azole-triazoles reduces ligand field, leading to spin crossover in tris-L Fe(II). *Inorg. Chem.*, **2020**, *59*, 1265-1273.
- (10) Hogue, R. W.; Singh, S.; Brooker, S., Spin crossover in discrete polynuclear iron(II) complexes. *Chem. Soc. Rev.*, **2018**, *47*, 7303-7338 and inside front cover.
- (11) Charbonnière, L. J.; Williams, A. F.; Pigué, C.; Bernardinelli, G.; Rivara-Minten, E., Structural, Magnetic, and Electrochemical Properties of Dinuclear Triple Helices: Comparison with their Mononuclear Analogues. *Chem. Eur. J.*, **1998**, *4*, 485-493.
- (12) Craze, A.; Sciortino, N.; Badbhade, M.; Kepert, C.; Marjo, C.; Li, F., Investigation of the Spin Crossover Properties of Three Dinuclear Fe(II) Triple Helicates by Variation of the Steric Nature of the Ligand Type. *Inorganics*, **2017**, *5*, 62.
- (13) Pelleteret, D.; Clérac, R.; Mathonière, C.; Harte, E.; Schmitt, W.; Kruger, P. E., Asymmetric spin crossover behaviour and evidence of light-induced excited spin state trapping in a dinuclear iron(II) helicate. *Chem. Comm.*, **2009**, 221-223.
- (14) Li, L.; Craze, A. R.; Akiyoshi, R.; Tsukiashi, A.; Hayami, S.; Mustonen, O.; Bhadbhade, M. M.; Bhattacharyya, S.; Marjo, C. E.; Wang, Y.; Lindoy, L. F.; Aldrich-Wright, J. R.; Li, F., Direct monitoring of spin transitions in a dinuclear triple-stranded helicate iron(II) complex through X-ray photoelectron spectroscopy. *Dalton Trans.*, **2018**, *47*, 2543-2548.
- (15) Sunatsuki, Y.; Kawamoto, R.; Fujita, K.; Maruyama, H.; Suzuki, T.; Ishida, H.; Kojima, M.; Iijima, S.; Matsumoto, N., Structures and Spin States of Bis(tridentate)-Type Mononuclear and Triple Helicate Dinuclear Iron(II) Complexes of Imidazole-4-carbaldehyde azine. *Inorg. Chem.*, **2009**, *48*, 8784-8795.

- (16) Darawsheh, M.; Barrios, L. A.; Roubeau, O.; Teat, S. J.; Aromí, G., Guest-, light- and thermally-modulated spin crossover in [Fe^{II} 2] supramolecular helicates. *Chem. Eur. J.*, **2016**, *22*, 8635-8645.
- (17) Archer, R. J.; Scott, H.; Polson, M. I. J.; Williamson, B. E.; Mathoniere, C.; Rouzieres, M.; Clerac, R.; Kruger, P., Varied spin crossover behaviour in a family of dinuclear Fe(II) triple helicate complexes. *Dalton Trans.*, **2018**, *47*, 7965-7974.
- (18) Yukinari, S.; Hisashi, M.; Kunihiro, F.; Takayoshi, S.; Masaaki, K.; Naohide, M., Mononuclear Bis(tridentate)-Type and Dinuclear Triple Helicate Iron(II) Complexes Containing 2-Ethyl-5-methylimidazole-4-carbaldehyde Azine. *Bull. Chem. Soc. Jap.*, **2009**, *82*, 1497-1505.
- (19) Howard-Smith, K. J.; Craze, A. R.; Zenno, H.; Yagyu, J.; Hayami, S.; Li, F., A large dinuclear Fe(ii) triple helicate demonstrating a two-step spin crossover. *Chem. Commun.*, **2020**, *56*, 8838-8841.
- (20) Craze, A. R.; Bhadbhade, M. M.; Komatsumaru, Y.; Marjo, C. E.; Hayami, S.; Li, F., A Rare Example of a Complete, Incomplete, and Non-Occurring Spin Transition in a [Fe2L3]X4 Series Driven by a Combination of Solvent-and Halide-Anion-Mediated Steric Factors. *Inorg. Chem.*, **2020**, *59*, 1274-1283.
- (21) Tuna, F.; Lees, M. R.; Clarkson, G. J.; Hannon, M. J., Readily Prepared Metallo-Supramolecular Triple Helicates Designed to Exhibit Spin-Crossover Behaviour. *Chem. Eur. J.*, **2004**, *10*, 5737-5750.
- (22) Garcia, Y.; Grunert, M.; Reiman, S.; van Campenhoudt, O.; Gütllich, P., The two-step spin conversion in a supramolecular triple helicate dinuclear iron(II) complex studied by Mössbauer spectroscopy. *European Journal of Inorganic Chemistry*, **2006**, 3333-3339.
- (23) Archer, R. J.; Hawes, C. S.; Jameson, G. N. L.; McKee, V.; Moubaraki, B.; Chilton, N. F.; Murray, K. S.; Schmitt, W.; Kruger, P. E., Partial spin crossover behaviour in a dinuclear iron(II) triple helicate. *Dalton Trans.*, **2011**, *40*, 12368-12373.
- (24) Kadish, K. M.; Das, K.; Schaeper, D.; Merrill, C. L.; Welch, B. R.; Wilson, L. J., Spin state dependent redox properties of the [Fe(III)(X-sal)₂trien]⁺ spin-equilibrium system in solution. *Inorg. Chem.*, **1980**, *19*, 2816-2821.
- (25) Zhu, T.; Su, C. H.; Schaeper, D.; Lemke, B. K.; Wilson, L. J.; Kadish, K. M., Solvent and structure effects on the spin-crossover and electron-transfer properties of [Fe^{III}(X-Salmeen)₂](PF₆) and [Fe^{III}(X-Sal)₂trien](PF₆). *Inorg. Chem.*, **1984**, *23*, 4345-4349.
- (26) Hoselton, M. A.; Wilson, L. J.; Drago, R. S., Substituent effects on the spin equilibrium observed with hexadentate ligands on iron(II). *J. Am. Chem. Soc.*, **1975**, *97*, 1722-1729.
- (27) Kuroda-Sowa, T.; Isobe, R.; Yamao, N.; Fukumasu, T.; Okubo, T.; Maekawa, M., Variety of spin transition temperatures of iron(II) spin crossover complexes with halogen substituted Schiff-base ligands, HqsalX (X=F, Cl, Br, and I). *Polyhedron*, **2017**, *136*, 74-78.
- (28) Tanaka, T.; Sunatsuki, Y.; Suzuki, T., Synthesis and magnetic properties of tetrahedral tetranuclear iron(II) complexes with bis(bidentate)-type Schiff bases containing imidazole groups. *Inorganica Chim. Acta*, **2020**, *502*, 119373.
- (29) Spek, A., PLATON SQUEEZE: a tool for the calculation of the disordered solvent contribution to the calculated structure factors. *Acta Cryst. C*, **2015**, *71*, 9-18.

- (30) Kitchen, J. A.; White, N. G.; Boyd, M.; Moubaraki, B.; Murray, K. S.; Boyd, P. D. W.; Brooker, S., Iron(II) tris-[N^4 -substituted-3,5-di(2-pyridyl)-1,2,4-triazole] complexes: structural, magnetic, NMR and density functional theory studies. *Inorg. Chem.*, **2009**, *48*, 6670–6679.
- (31) Klingele, J.; Scherer, H.; Klingele, M. H., Mononuclear Low-Spin 3:1-Type Iron(II) Complexes of 4-Substituted 3,5-Bis(2-pyridyl)- and 3-Phenyl-5-(2-pyridyl)-4H-1,2,4-triazoles. *Z. Anorg. Allg. Chem.*, **2009**, *635*, 2279-2287.
- (32) Rodríguez-Jiménez, S.; Bondi, L.; Yang, M.; Garden, A. L.; Brooker, S., Predictable electronic tuning by choice of azine substituent in five iron(II) triazoles: redox properties and DFT calculations. *Chem. Asian J.*, **2019**, *14*, 1158–1166.
- (33) Lathion, T.; Guénée, L.; Besnard, C.; Bousseksou, A.; Piguet, C., Deciphering the Influence of Meridional versus Facial Isomers in Spin Crossover Complexes. *Chem. - Eur. J.*, **2018**, *24*, 16873-16888.
- (34) Rodríguez-Jiménez, S.; Barltrop, A. S.; White, N. G.; Feltham, H. L. C.; Brooker, S., Solvent polarity predictably tunes spin crossover $T_{1/2}$ in isomeric iron(II) pyrimidine triazoles. *Inorg. Chem.*, **2018**, *57*, 6266-6282.
- (35) Rodríguez-Jiménez, S.; Brooker, S., Qualitative guest sensing via iron(II) triazole complexes. *Inorg. Chem.*, **2019**, *58*, 8188-8197.
- (36) Rodríguez-Jiménez, S.; Yang, M.; Stewart, I.; Garden, A. L.; Brooker, S., A simple method of predicting spin state in solution. *J. Am. Chem. Soc.*, **2017**, *139*, 18392–18396.
- (37) Shores, M. P.; Klug, C. M.; Fiedler, S. R., Spin-state switching in solution. In *Spin-Crossover Materials: Properties and Applications*, John Wiley & Sons Ltd: Chichester, **2013**, pp 281-301.
- (38) Kershaw Cook, L. J.; Kulmaczewski, R.; Mohammed, R.; Dudley, S.; Barrett, S. A.; Little, M. A.; Deeth, R. J.; Halcrow, M. A., A unified treatment of the relationship between ligand substituents and spin state in a family of iron(II) complexes. *Angew. Chem. Int. Ed.*, **2016**, *55*, 4327-4331.
- (39) Rodríguez-Jiménez, S.; Brooker, S., Solid Versus Solution Spin Crossover and the Importance of Fe-N≡C(X) Angle. *Inorg. Chem.*, **2017**, *56*, 13697-13708.
- (40) Turner, J. W.; Schultz, F. A., Solution characterization of the iron(II) bis(1,4,7-triazacyclononane) spin-equilibrium reaction. *Inorg. Chem.*, **2001**, *40*, 5296-5298.
- (41) Hogue, R. W.; Feltham, H. L. C.; Miller, R. G.; Brooker, S., Spin crossover in dinuclear N_4S_2 iron(II) thioether-triazole complexes: access to [HS-HS], [HS-LS] and [LS-LS] states. *Inorg. Chem.*, **2016**, *55*, 4152–4165.